Cell Journal (Yakhteh)

Guide for Authors

Aims and Scope: The "Cell Journal (Yakhteh)**"** is a peer review and quarterly English publication of Royan Institute of Iran. The aim of the journal is to disseminate information through publishing the most recent scientific research studies on exclusively Cellular, Molecular and other related topics. **Cell J**, has been certified by the Ministry of Culture and Islamic Guidance since 1999 and also accredited as a scientific and research journal by HBI (Health and Biomedical Information) Journal Accreditation Commission since 2000 which is an open access journal. T**his journal holds the membership of the Committee on Publication Ethics (COPE).**

1. Types of articles

The articles in the field of Cellular and Molecular can be considered for publications in **Cell J.** These articles are as below:

A. Original articles Original articles are scientific reports of the original research studies. The article consists of English Abstract (structured), Introduction, Materials and Methods, Results, Discussion, Conclusion, Acknowledgements, Author's Contributions, and References **(Up to 40).**

B. Review articles Review articles are the articles written by well experienced authors and those who have excellence in the related fields. The corresponding author of the review article must be one of the authors of at least three published articles appearing in the references. The review article consists of English Abstract (unstructured), Introduction, Conclusion, Author's Contributions, and References **(Up to 70).**

C. Systematic Reviews

Systematic reviews are a type of literature review that collect and critically analyzes multiple research studies or papers. The Systematic reviews consist of English Abstract (unstructured), Introduction, Materials and Methods, Results, Discussion, Conclusion, Acknowledgements, Author's Contributions, and References **(Up to 70).**

D. Short communications: Short communications are articles containing new findings. Submissions should be brief reports of ongoing researches. The short communication consists of English Abstract (unstructured), the body of the manuscript (should not hold heading or subheading), Acknowledgements, Author's Contributions, and References **(Up to 30).**

E. Case reports: Case reports are short discussions of a case or case series with unique features not previously described which make an important teaching point or scientific observation. They may describe novel techniques or use equipment, or new information on diseases of importance. It consists of English Abstracts (Unstructured), Introduction, Case Report, Discussion, Acknowledgements, Author's Contributions, and References **(Up to 30).**

F. Editorial: Editorial should be written by either the editor in chief or the editorial board.

G. Imaging in biology: Images in biology should focus on a single case with an interesting illustration such as a photograph, histological specimen or investigation. Color images are welcomed. The text should be brief and informative.

H. Letter to the editors: Letter to editors are welcome in response to previously published **Cell J** articles, and may also include interesting cases that do not meet the requirement of being truly exceptional, as well as other brief technical or clinical notes of general interest.

I. Debate.

2. Submission process

It is recommended to see the guidelines for reporting different kinds of manuscripts here. This guide explains how to prepare the manuscript for submission. Before submitting, we suggest authors to familiarize themselves with **Cell J** format and content by reading the journal via the website (www.celljournal.com). The corresponding author ensures that all authors are included in the author list and agree with its order, and they must be aware of the manuscript submission.

A. Author contributions statements

It is essential for authors to include a statement of responsibility in the manuscript that specifies the contribution of every one of them. This participation must include conception and design of the manuscript, data acquisition or data analysis and interpretation, drafting of the manuscript and/or revising it for critically important intellectual content, revision and final approval of the manuscript and statistical analysis, obtaining funding, administrative, technical, or material support, or supervision. Authors who do not meet the above criteria should be acknowledged in the **Acknowledgments section.**

B. Cover letter

Each manuscript should be accompanied by a cover letter, signed by all authors specifying the following statement: "The

manuscript has been seen and approved by all authors and is not under active consideration for publication. It has neither been accepted for publication nor published in another journal fully or partially (except in abstract form). I hereby assign the copyright of the enclosed manuscript to **Cell J.** Corresponding author must confirm the proof of the manuscript before online publishing. Also, is it needed to suggest three peer reviewers in the field of their manuscript.

C. Manuscript preparation

Authors whose first language is not English encouraged to consult a native English speaker in order to confirm his manuscripts to American or British (not a mixture) English usage and grammar. It is necessary to mention that we will check the plagiarism of your manuscript by iThenticate Software. The manuscript should be prepared in accordance with the "International Committee of Medical Journal Editors (ICMJE)". Please send your manuscript in two formats Word and Pdf (including: title, name of all the authors with their degree, abstract, full text, references, tables and figures) and Also send tables and figures separately in the site. The abstract and text pages should have consecutive line numbers in the left margin beginning with the title page and continuing through the last page of the written text. Each abbreviation must be defined in the abstract and text when they are mentioned for the first time. Avoid using abbreviation in the title. Please use the international and standard abbreviations and symbols

It should be added that an essential step toward the integration and linking of scientific information reported in published literature is using standardized nomenclature in all fields of science and medicine. Species names must be italicized (*e.g., Homo sapiens*) and also the full genus and species written out in full, both in the title of the manuscript and at the first mention of an organism in a paper.

It is necessary to mention that genes, mutations, genotypes, and alleles must be indicated in italics. Please use the recommended name by consulting the appropriate genetic nomenclature database, e.g., HUGO for human genes. In another words; if it is a human gene, you must write all the letters in capital and italic (*e.g., OCT4, c-MYC*). If not, only write the first letter in capital and italic (*e.g., Oct4, c-Myc*). **In addition, protein designations are the same as the gene symbol but are not italicized.**

Of note, Cell J will only consider publishing genetic association study papers that are novel and statistically robust. Authors are advised to adhere to the recommendations outlined in the STREGA statement (http://www.strega-statement.org). The following criteria must be met for all submissions:

1. Hardy-Weinberg Equilibrium (HWE) calculations must be carried out and reported along with the P-values if applicable [see Namipashaki et al. 2015 (Cell J, Vol 17, N 2, Pages: 187-192) for a discussion].

2. Linkage disequilibrium (LD) structure between SNPs (if multiple SNPs are reported) must be presented.

3. Appropriate multiple testing correction (if multiple independent SNPs are reported) must be included.

Submissions that fail to meet the above criteria will be rejected before being sent out for review.

Each of the following manuscript components should begin in the following sequence:

Authors' names and order of them must be carefully considered (full name(s), highest awarded academic degree(s), email(s), and institutional affiliation(s) of all the authors in English. Also, you must send mobile number and full postal address of the corresponding author).

Changes to Authorship such as addition, deletion or rearrangement of author names must be made only before the manuscript has been accepted in the case of approving by the journal editor. In this case, the corresponding author must explain the reason of changing and confirm them (which has been signed by all authors of the manuscript). If the manuscript has already been published in an online issue, an erratum is needed.

Title is providing the full title of the research (do not use abbreviations in title).

Running title is providing a maximum of 7 words (no more than 50 characters).

Abstract must include Objective, Materials and Methods, Results, and Conclusion (no more than 300 words).

Keywords, three to five, must be supplied by the authors at the foot of the abstract chosen from the Medical Subject Heading (MeSH). Therefore; they must be specific and relevant to the paper.

The following components should be identified after the abstract:

Introduction: The Introduction should provide a brief background to the subject of the paper, explain the importance of the study, and state a precise study question or purpose.

Materials and Methods: It includes the exact methods or observations of experiments. If an apparatus is used, its manufacturer's name and address should be stipulated in parenthesis. If the method is established, give reference but if the method is new, give enough information so that another author can perform it. If a drug is used, its generic name, dose, and

route of administration must be given. Standard units of measurements and chemical symbols of elements do not need to be defined.

Statistical analysis: Type of study and statistical methods should be mentioned and specified by any general computer program used.

Ethical considerations*:* Please state that informed consent was obtained from all human adult participants and from the parents or legal guardians of minors and include the name of the appropriate institutional review board that approved the project. It is necessary to indicate in the text that the maintenance and care of experimental animals complies with National Institutes of Health guidelines for the humane use of laboratory animals, or those of your Institute or agency.

Clinical trial registration: All of the Clinical Trials performing in Iran must be registered in Iranian Registry of Clinical Trials (www.irct.ir). The clinical trials performed abroad, could be considered for publication if they register in a registration site approved by WHO or www.clinicaltrials.gov. If you are reporting phase II or phase III randomized controlled trials, you must refer to the CONSORT Statement for recommendations to facilitate the complete and transparent reporting of trial findings. Reports that do not conform to the CONSORT guidelines may need to be revised before peer-reviewing.

Results: They must be presented in the form of text, tables, and figures. Take care that the text does not repeat data that are presented in tables and/or figures. Only emphasize and summarize the essential features of the main results. Tables and figures must be numbered consecutively as appeared in the text and should be organized in separate pages at the end of the manuscript while their location should be mentioned in the main text.

Tables and figures: If the result of your manuscript is too short, it is better to use the text instead of tables & figures. Tables should have a short descriptive heading above them and also any footnotes. Figure's legend should contain a brief title for the whole figure and continue with a short explanation of each part and also the symbols used (no more than 100 words). All figures must be prepared based on cell journal's guideline in color (no more than 6 Figures and Tables) and also in GIF or JPEG format.

Of Note: Please put the tables & figures of the result in the results section not any other section of the manuscript.

Supplementary materials would be published on the online version of the journal. This material is important to the understanding and interpretation of the report and should not repeat material within the print article. The amount of supplementary material should be limited. Supplementary material should be original and not previously published and will undergo editorial and peer review with the main manuscript. Also, they must be cited in the manuscript text in parentheses, in a similar way as when citing a figure or a table. Provide a legend for each supplementary material submitted.

Discussion: It should emphasize the present findings and the variations or similarities with other researches done by other researchers. The detailed results should not be repeated in the discussion again. It must emphasize the new and important aspects of the study.

Conclusion: It emphasizes the new and important aspects of the study. All conclusions are justified by the results of the study.

Acknowledgements: This part includes a statement thanking those who contributed substantially with work relevant to the study but does not have authorship criteria. It includes those who provided technical help, writing assistance and name of departments that provided only general support. You must mention financial support in the study. Otherwise; write this sentence "There is no financial support in this study".

Conflict of interest: Any conflict of interest (financial or otherwise) and sources of financial support must be listed in the Acknowledgements. It includes providers of supplies and services from a commercial organization. Any commercial affiliation must be disclosed, regardless of providing the funding or not.

References: The references must be written based on the Vancouver style. Thus the references are cited numerically in the text and listed in the bibliography by the order of their appearance. The titles of journals must be abbreviated according to the style used in the list of Journals Indexed in PubMed. Write surname and initials of all authors when there are six or less. In the case of seven or more authors, the names of the first six authors followed by "et al." must be listed. You can download Endnote file for Journal references style: endnote file

The reference of information must be based on the following order:

Article:

Surname(s) and first letter of name &middle name(s) of author(s) .Manuscript title. Journal title (abbr).publication date (year); Volume & Issue: Page number.

Example: Manicardi GC, Bianchi PG, Pantano S, Azzoni P, Bizzaro D, Bianchi U, et al. Presence of endogenous nicks in DNA of ejaculated human spermatozoa and its relationship to chromomycin A3 accessibility. Biol Reprod. 1995; 52(4): 864-867.

Book:

Surname(s) and first letter of name & middle name(s) of author(s).Book title. Edition. Publication place: publisher name; publication date (year); Page number.

Example: Edelman CL, Mandle CL. Health promotion throughout the lifespan. 2nd ed. ST Louis: Mosby; 1998; 145-163.

Chapter of book:

Surname(s) and first letter of name & middle name(s) of author(s).Chapter title. In: Surname(s) and first letter of name & middle name(s) of editor(s), editors. Book title. Edition. Publication place: publisher name; publication date (year); Page number.

Example: Phillips SJ, Whisnant JP. Hypertension and stroke. In: Laragh JH, Brenner BM, editors. Hypertension: pathophysiology, diagnosis, and management. 2nd ed. New York: Raven Press; 1995; 465-478.

Abstract book:

Example: Amini rad O.The antioxidant effect of pomegranate juice on sperm parameters and fertility potential in mice. Cell J. 2008;10 Suppl 1:38.

Thesis:

Name of author. Thesis title. Degree. City name. University. Publication date (year).

Example: Eftekhari Yazdi P. Comparison of fragment removal and co-culture with Vero cell monolayers on development of human fragmented embryos. Presented for the Ph.D., Tehran. Tarbiyat Modarres University. 2004.

Internet references

Article:

Example: Jahanshahi A, Mirnajafi-Zadeh J, Javan M, Mohammad-Zadeh M, Rohani M. Effect of low-frequency stimulation on adenosineA1 and A2A receptors gene expression in dentate gyrus of perforant path kindled rats. Cell J. 2008; 10 (2): 87-92. Available from: http://www.celljournal.org. (20 Oct 2008).

Book:

Example: Anderson SC, Poulsen KB. Anderson's electronic atlas of hematology.[CD-ROM]. Philadelphia: Lippincott Williams & Wilkins; 2002.

D. Proofs are sent by email as PDF files and should be checked and returned within 72 hours of receipt. It is the authors' responsibility to check that all the text and data as contained in the page proofs are correct and suitable for publication. **We are requested to pay particular attention to author's names and affiliations as it is essential that these details be accurate when the article is published.**

E. Pay for publication: Authors do not have to pay any Manuscript Processing Charge or Open Access Publication Fee. **Before publishing author's article, it would be the author's responsibility to pay for the expenses, if the editor feels the level of English used in the manuscript requiresediting.**

F. Ethics of scientific publication: Manuscripts that have been published elsewhere with the same intellectual material will refer to duplicate publication. If authors have used their own previously published work or work that is currently under review, as the basis for a submitted manuscript, they are required to cite the previous work and indicate how their submitted manuscript offers novel contributions beyond those of the previous work. Research and publication misconduct is considered a serious breach of ethics.

The Journal systematically employs iThenticate, plagiarism detection and prevention software designed to ensure the originality of written work before publication. Plagiarism of text from a previously published manuscript by the same or another author is a serious publication offence. Some parts of text may be used, only where the source of the quoted material is clearly acknowledged.

3. General information

A. You can send your manuscript via online submission system which is available on our website. If the manuscript is not prepared according to the format of **Cell J**, it will be returned to authors.

B. The order of article appearance in the Journal is not demonstrating the scientific characters of the authors.

C. Cell J has authority to accept or reject the manuscript.

D. The received manuscript will be evaluated by associate editor. **Cell J** uses a single-blind peer review system and if the

manuscript suits the journal criteria, we select the reviewers. If three reviewers pass their judgments on the manuscript, it will be presented to the editorial board of **Cell J.** If the editorial board has a positive judgment about the manuscript, reviewers' comments will be presented to the corresponding author (the identification of the reviewers will not be revealed). The executive member of journal will contact the corresponding author directly within 3-4 weeks by email. If authors do not receive any reply from journal office after the specified time, they can contact journal office. Finally, executive manager will respond promptly to authors' request.

The Final Checklist

The authors must ensure that before submitting the manuscript for publication, they have to consider the following parts:

1. Title page should contain title, name of the author/coauthors, their academic qualifications, designation & institutions they are affiliated with, mailing address for future correspondence, email address, phone, and fax number.

2. Text of manuscript and References prepared as stated in the "guide for authors" section.

3. Tables and figures should be uploaded separately except in the main manuscript. Figures must be sent in color and also in GIF or JPEG format with 300 dpi resolutions.

4. Cover Letter should be uploaded with signature of all authors.

The Editor-in-Chief: Ahmad Hosseini, Ph.D.

Cell Journal (Yakhteh),

P.O. Box: 16635-148, Iran

Tel/Fax: + 98-21-22510895

Emails: Celljournal@royaninstitute.org

info@celljournal.org

Dr. Saeed Kazemi Ashtiani

IN THE NAME OF GOD

Gone But not Forgotten

In the memory of the late Director of Royan Institute, Founder of Stem Cells Research in Iran and Chairman of ***Cell Journal*** ***(Yakhteh)***. May he rest in peace.

PUBLISHED & SPONSORED BY:
Publication of Royan Institute (ACECR)

Indexed in:
1. Thomson Reuters (ISI); *Impact Factor: 2.046*
2. PubMed
3. PubMed Central (PMC)
4. National Library Medicine (NLM)
5. Biosis Preview
6. Index Medicus for the Eastern Mediterranean Region (IMEMR)
7. Regional Information Center for Sciences and Technology (RICeST)
8. Index Copernicus International
9. Cambridge Scientific Abstract (CSA)
10. EMBASE
11. Scopus
12. Cinahl Database
13. Google Scholar
14. Chemical Abstract Service (CAS)
15. Proquest
16. Directory of Open Access Journals (DOAJ)
17. Open Academic Journals Index (OAJI)
18. Directory of Research Journals Indexing (DRJI)
19. Scientific Information Database (SID)
20. Iranmedex
21. Islamic World Science Citation Center (ISC)
22. Magiran
23. Science Library Index

ACECR

Editorial Office Address (Dr. Ahmad Hosseini):
Royan Institute, P.O.Box: 16635-148,
Tehran, Iran
Tel & Fax: (+9821)22510895
Website: www.celljournal.org
Emails: info@celljournal.org
celljournal@royaninstitute.org

Printing Company:
Naghshe e Johar Co.
No. 103, Fajr alley, Tehranpars Street,
Tehran, Iran.

Cell Journal (Yakhteh), Vol 22, No 3, October-December (Autumn) 2020, Serial Number: 87, Pages: 253-400

CONTENTS

Original Articles

Original Article

Effects of Sorafenib and Arsenic Trioxide on U937 and KG-1 Cell Lines: Apoptosis or Autophagy?

Atousa Haghi, M.Sc.[1, 2#], Mahdieh Salami, M.Sc.[1, 3#], Mahnaz Mohammadi Kian, M.Sc.[1, 3], Mohsen Nikbakht, Ph.D.[1, 3*], Saeed Mohammadi, Ph.D.[1, 3*], Bahram Chahardouli, Ph.D.[1, 3], Shaharbano Rostami, Ph.D.[1, 3], Kianoosh Malekzadeh, Ph.D.[4]

1. Hematology, Oncology and Stem Cell Transplantation Research Center, Tehran University of Medical Sciences, Tehran, Iran
2. Young Researchers and Elite Club, Tehran Medical Sciences, Islamic Azad University, Tehran, Iran
3. Hematologic Malignancies Research Center, Tehran University of Medical Sciences, Tehran, Iran
4. Molecular Medicine Research Center (MMRC), Hormozgan University of Medical Science (HUMS), Bandar Abbass, Iran

#The first two authors equally contributed to this work.

**Corresponding Address: P.O.Box: 1411713135, Hematology, Oncology and Stem Cell Transplantation Research Center, Tehran University of Medical Sciences, Tehran, Iran*
Emails: m-nikbakht@sina.tums.ac.ir, smohammadi@sina.tums.ac.ir

Received: 19/January/2019, Accepted: 23/April/2019

Abstract

Objective: Acute myeloid leukemia (AML) is a clonal disorder of hemopoietic progenitor cells. The Raf serine/threonine (Ser/Thr) protein kinase isoforms including B-Raf and RAF1, are the upstream in the MAPK cascade that play essential functions in regulating cellular proliferation and survival. Activated autophagy-related genes have a dual role in both cell death and cell survival in cancer cells. The cytotoxic activities of arsenic trioxide (ATO) were widely assessed in many cancers. Sorafenib is known as a multikinase inhibitor which acts through suppression of Ser/Thr kinase Raf that was reported to have a key role in tumor cell signaling, proliferation, and angiogenesis. In this study, we examined the combination effect of ATO and sorafenib in AML cell lines.

Materials and Methods: In this experimental study, we studied *in vitro* effects of ATO and sorafenib on human leukemia cell lines. The effective concentrations of compounds were determined by MTT assay in both single and combination treatments. Apoptosis was evaluated by annexin-V FITC staining. Finally, mRNA levels of apoptotic and autophagy genes were evaluated using real-time polymerase chain reaction (PCR).

Results: Data demonstrated that sorafenib, ATO, and their combination significantly increase the number of apoptotic cells. We found that the combination of ATO and sorafenib significantly reduces the viability of U937 and KG-1 cells. The expression level of selective autophagy genes, *ULK1* and *Beclin1* decreased but LC3-II increased in U937.

Conclusion: The expression levels of apoptotic and autophagy activator genes were increased in response to treatment. The crosstalk between apoptosis and autophagy is a complicated mechanism and further investigations seem to be necessary.

Keywords: Acute Myeloid Leukemia, Apoptosis, Arsenic Trioxide, Cell Proliferation, Sorafenib

Cell Journal(Yakhteh), Vol 22, No 3, October-December (Autumn) 2020, Pages: 253-262

Citation: Haghi A, Salami M, Mohammadi Kian M, Nikbakht M, Mohammadi S, Chahardouli B, Rostami Sh, Malekzadeh K. Effects of sorafenib and arsenic trioxide on U937 and KG-1 cell lines: apoptosis or autophagy? Cell J. 2020; 22(3): 253-262. doi: 10.22074/cellj.2020.6728.

Introduction

Acute myeloid leukemia (AML) as a malignant disease of the bone marrow, is caused by acquired somatic mutations and chromosomal rearrangements which occur in a hematopoietic progenitor. Regardless of its etiology, the AML pathogenesis involves extraordinary differentiation and proliferation of a clonal population of myeloid stem cells. Different processes involved in leukemia are controlled by signaling pathways initiated by activated receptor tyrosine kinases (RTKs) (1).

RAS is a downstream factor for various RTKs. Activation of RAS signaling pathway has a critical function in the development of human malignancies (2). Fundamental activity of the RAS pathways arises from downstream effectors of RAS, activating mutations in the RAS, or even overexpression of a variety of RTKs, including vascular endothelial growth factor receptors (VEGFRs), epidermal growth factor receptor (EGFR) or platelet-derived growth factor receptor (PDGFR) (3). Therefore, RAS mutations or activation in human tumors could lead to cell survival and proliferation. RAS adjusts multiple pathways such as RAF/MEK/ERK pathway which remarkably activate cellular transformation.

RAF kinases are serine/threonine protein kinases which act as a downstream effector of RAS. The Raf serine/threonine protein kinase isoforms including A-Raf, B-Raf and Raf1, are the upstream in the MAPK cascade (4) and they regulate cellular proliferation and survival. Moreover, it was recently demonstrated that wild-type Raf1 could, independently of MAPK signaling, promote cell survival, through interactions with apoptosis and anti-apoptosis regulatory proteins (5).

Beclin1 (which is encoded by *BCNG 1* gene) is one of the core autophagy-regulating elements and a haploinsufficient tumor suppressor gene which is directly

associated with BCL-2 (6). ULK1 is a serine/threonine-protein kinase that is involved in autophagy pathways (7). LC3 (an ubiquitin-like protein) is a soluble protein that is distributed in cultured cells and tissues. During autophagy activation, LC3-I is found in the cytoplasm and it is also conjugated with phosphatidylethanolamine via LC3-phosphatidylethanolamine conjugate (LC3-II) that induces formation and elongation of the autophagosome (8). PTEN as a tumor suppressor is one of the most commonly deleted, mutated or promoter methylated genes in various cancers. PTEN is able to control autophagy based upon lipid phosphatase activity that opposes the function of PI3K and also deactivates Akt and mTOR signaling (9).

Sorafenib is known as a multikinase inhibitor which has effective roles in tumor cell signaling, proliferation, and angiogenesis (Fig.1A) (10). Arsenic trioxide (ATO) targets various cellular functions through multiple molecular factors (Fig.1B). ATO plays dual roles in acute promyelocytic leukemia (APL) cells, and at low concentrations, it activates differentiation while at high concentrations, it promotes apoptosis (11). The aim of the present study was to appraise the combination effect of ATO and sorafenib on *VEGFA*, *B-RAF*, *MEK1*, *MEK2*, *Beclin1*, *LC3-II*, *ULK1*, *RAF1*, *BCL-2* and *PTEN* gene expression and apoptosis in leukemic cell lines.

Material and Methods

Reagents

In this *in vitro* experimental study, annexin-V-FITC apoptosis detection kit, 3-(4, 5-dimethylthiazol-2-yl)-2, 5-diphenyltetrazolium bromide (MTT), dimethylsulfoxide (DMSO) and diethyl pyrocarbonate (DEPC)-treated water were obtained from Sigma-Aldrich (St. Louis, MO), and sorafenib was purchased from Santa Cruz (Dallas, Texas). ATO was provided by Sigma-Aldrich, St. Louis, MO, and dissolved in distilled water. RPMI 1640 medium and fetal bovine serum (FBS) were purchased from Gibco, Carlsbad, CA. The cDNA synthesis kit was purchased from Takara Bio Inc. (Otsu, Japan). TRI pure (used as the isolation reagent) was obtained from Roche Applied Science (Germany).

Cell lines and treatments

We purchased U937 and KG-1 cell lines from the National Cell Bank of Iran (Pasteur Institute, Iran). Cell lines were cultured and expanded in RPMI 1640 supplemented with 10 and 20% heat-inactivated FBS for U937 and KG-1 cell line, respectively, 100 IU/ml penicillin and 100 µg/ml streptomycin. Cells were cultured in a CO_2 incubator at 37˚C with 5% CO_2 in a humidified atmosphere. Cells were seeded at 1×10^5 cells/mL. For treatment experiments, prior to each assay, 80-90% confluent flask was centrifuged, the supernatant was discarded and each cell pellet was resuspended separately in 1-2 ml of media and completely pipetted to prevent cell clumping. Then, 10 µL of cell solution including cell and media, was pipetted and cells were counted. Afterward, the cells were treated with the selected concentrations.

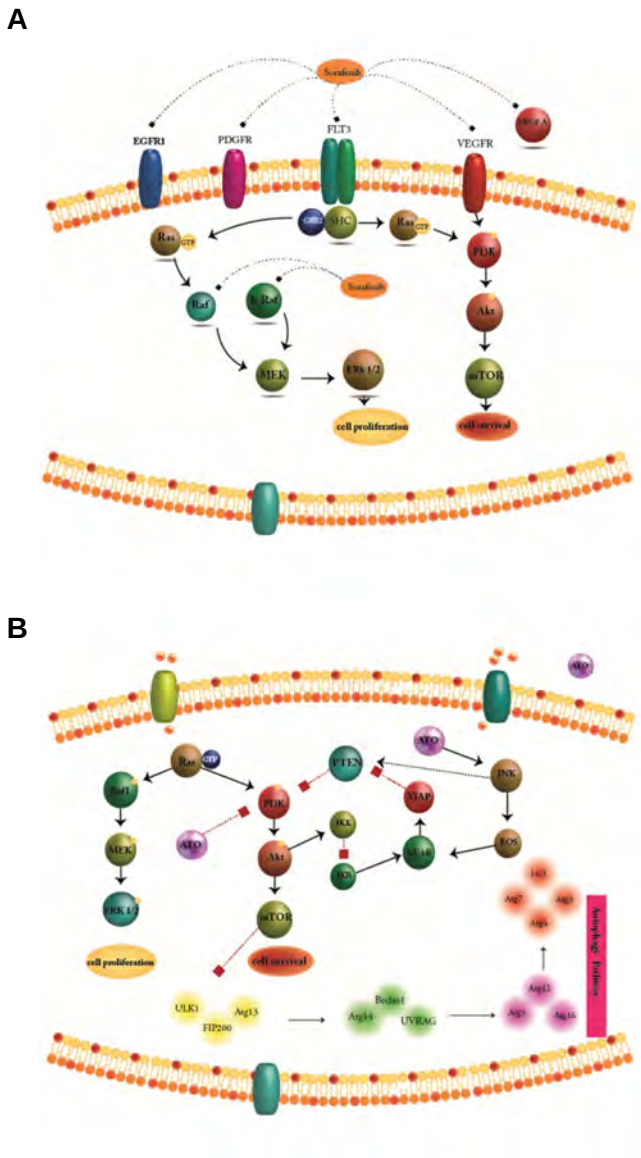

Fig.1: Molecular target of sorafenib and arsenic trioxide (ATO). **A.** Sorafenib is known as a multikinase inhibitor which acts through suppressing Ser/Thr kinase Raf that is known to have important roles in tumor cell signaling and proliferation and **B.** ATO as a single agent, targets various cellular functions through affecting multiple molecular factors. ATO activates both autophagy and apoptosis.

Proliferation assay

The antiproliferative activity of ATO (0.5-5 µM) and sorafenib (2-12 µM) was assessed using MTT assay at 24, 48 and 72 hours, to distinguish optimal conditions with maximum effects, in KG-1 and U937 cells. In order to determine the growth inhibitory effects of ATO and sorafenib, KG-1 and U937 cells were seeded into 96-well plates at a primary density of 5×10^3 per well (100 µl). After that, cells were treated with ATO, sorafenib and their combinations for 24, 48 and 72 hours. Control cells were treated with 0.1% DMSO alone. The proliferation rate of cells was analyzed by MTT assay and results are expressed as proliferation rate.

Apoptosis assay

To assess the percentage of apoptosis induced by the above-noted compounds, fluorescein-conjugated annexin-V (annexin-V-FITC) staining assay was accomplished based on the manufacturer's protocol. We treated KG-1 and U937 cells with ATO (1.618 and 2 μM for KG-1 and 1 μM for U937) and sorafenib (7 μM for KG-1 and 5 μM for U937) and their combination for 48 hours. Data acquisition and analysis of apoptosis by a Becton Dickinson (BD, America) flow cytometer and percentage of the annexin-V^+/PI^- cells was recorded; finally, we used flowJo program to analyze our data.

Cell cycle analysis

Here, U937 and KG-1 cell population were treated with specific concentrations of ATO and sorafenib for 48 hours, then fixed in cold 70% ethanol and stained with propidium iodide (PI). Cells were evaluated by BD flow cytometer instrument and data were analyzed by flowJo program. The apoptotic cell fraction was calculated based on hypodiploid G0/G1 DNA fraction.

RNA isolation and real-time polymerase chain reaction

We treated KG-1 and U937 cells with ATO (1.618 and 2 μM for KG-1 and 1 μM for U937) and sorafenib (7 μM for KG-1 and 5 μM for U937) and their combination for 48 hours. Treated cells were harvested and dissolved in 1 ml of TRI pure (Roche Applied Science, Germany), based on the manufacturer's instructions. DEPC-treated water was used to reconstitute the RNA pellets. The quantity and quality of total RNA were analyzed spectrophotometrically using Nanodrop ND-1000 (Nanodrop Technologies, Wilmington, DE) at 260 and 280 nm. Then, complementary DNAs (cDNAs) were reverse transcribed from 1-2 μg of total RNA by use of a cDNA synthesis kit (Takara Bio Inc., Japan) according to the manufacturer's instructions. The concentration of cDNA was normalized in series of PCR through using *HPRT* and *GAPDH* primers. The normalized cDNAs were subjected to amplification, using Step One Plus™ ABI instrument (Applied Biosystems, USA). The levels of *HPRT* mRNA expression were used to evaluate the relative expression levels of the genes. The comparative Ct method was used to compute relative expression values. The primers and their corresponding amplicon lengths are provided in Table 1.

Statistical analysis

Data were analyzed using GraphPad Prism 5 software by using one/two way ANOVA and for post-test evaluations, we used t test. All data represent the results obtained from triplicate independent experiments and expressed as mean ± standard errors of the mean (SE). Asterisks (*, **, and ***) in the Figures indicate $P<0.05$, $P<0.01$, and $P<0.001$, respectively.

Table 1: Real-time polymerase chain reaction primer

Gene	Primer sequence (5′-3′)	Reference
GAPDH	F: TGAACGGGAAGCTCACTGG	(12)
	R: TCCACCACCCTGTTGCTGTA	
HPRT	F: GCTATAAATTCTTTGCTGACCTGCTG	(13)
	R: AATTACTTTTATGTCCCCTGTTGACTGG	
VEGFA	F: AGGGCAGAATCATCACGAAGT	(14)
	R: AGGGTCTCGATTGGATGGCA	
VEGFB	F: GAGATGTCCCTGGAAGAACACA	(15)
	R: GAGTGGGATGGGTGATGTCAG	
VEGFC	F: GAGGAGCAGTTACGGTCTGTG	(16)
	R: TCCTTTCCTTAGCTGACACTTGT	
VEGF-R1	F: CAGGCCCAGTTTCTGCCATT	(14)
	R: TTCCAGCTCAGCGTGGTCGTA	
VEGF-R2	F: CCAGCAAAAGCAGGGAGTCTGT	(14)
	R: TGTCTGTGTCATCGGAGTGATATCC	
LC3-II	F: GATGTCCGACTTATTCGAGAGC	(17)
	R: TTGAGCTGTAAGCGCCTTCTA	
Beclin1	F: AGCTGCCGTTATACTGTTCTG	(17)
	R: ACTGCCTCCTGTGTCTTCAATCTT	
ULK1	F: TCGAGTTCTCCCGCAAGG	(18)
	R: CGTCTGAGACTTGGCGAGGT	
BCL-2	F: CTGCACCTGACGCCCTTCACC	(19)
	R: CACATGACCCCACCGAACTCAAAGA	
PTEN	F: TGGATTCGACTTAGACTTGACCT	(13)
	R: TTTGGCGGTGTCATAATGTCTT	
AKT	F: AGCGACGTGGCTATTGTGAAG	(13)
	R: GTACTCCCCTCGTTTGTGCAG	
mTOR	F: AACTCCGAGAGATGAGTCAAGA	(13)
	R: AGTTGGTCATAGAAGCGAGTAGA	
PI3K	F: AACACAGAAGACCAATACTC	(20)
	R: TTCGCCATCTACCACTAC	
B-RAF	F: CTCGAGTGATGATTGGGAGATTCCTGATGG	(21)
	R: CTGCTGAGGTGTAGGTGCTGTCAC	
RAF-1	F: CAG CCC TGT CCA GTA GC	(21)
	R: GCG TGA CTT TAC TGT TGC	
MEK1	F: ACCAGCCCAGCACACCAA	(22)
	R: GGGACTCGCTCTTTGTTGCTT	
MEK2	F: TGCTCACAAACCACACCTTCA	(22)
	R: ACACAACCAGCCGGCAAA	

Result

Evaluation of cell proliferation using MTT test

Metabolic activity can be detected through measuring the activity of succinate dehydrogenase as a mitochondrial enzyme via MTT assay. We applied the MTT assay to determine the anti-proliferative activity of ATO and sorafenib (alone and in combination) in U937 and KG-1 cell lines.

We perceived both time- and dose-dependent effect of compounds. As seen in Figure 2, we did not see a significant difference between 48 and 72 hours treatment as assessed by two way ANOVA. Our data indicated that combination effect of ATO and sorafenib ($P<0.001$ for both cell lines) compared to the control or even single-compound treatment ($P<0.001$ for KG-1 and $P<0.01$ for U937), could significantly decrease cell proliferation at 48 hours in both U937 and KG-1 cell lines (Fig.2).

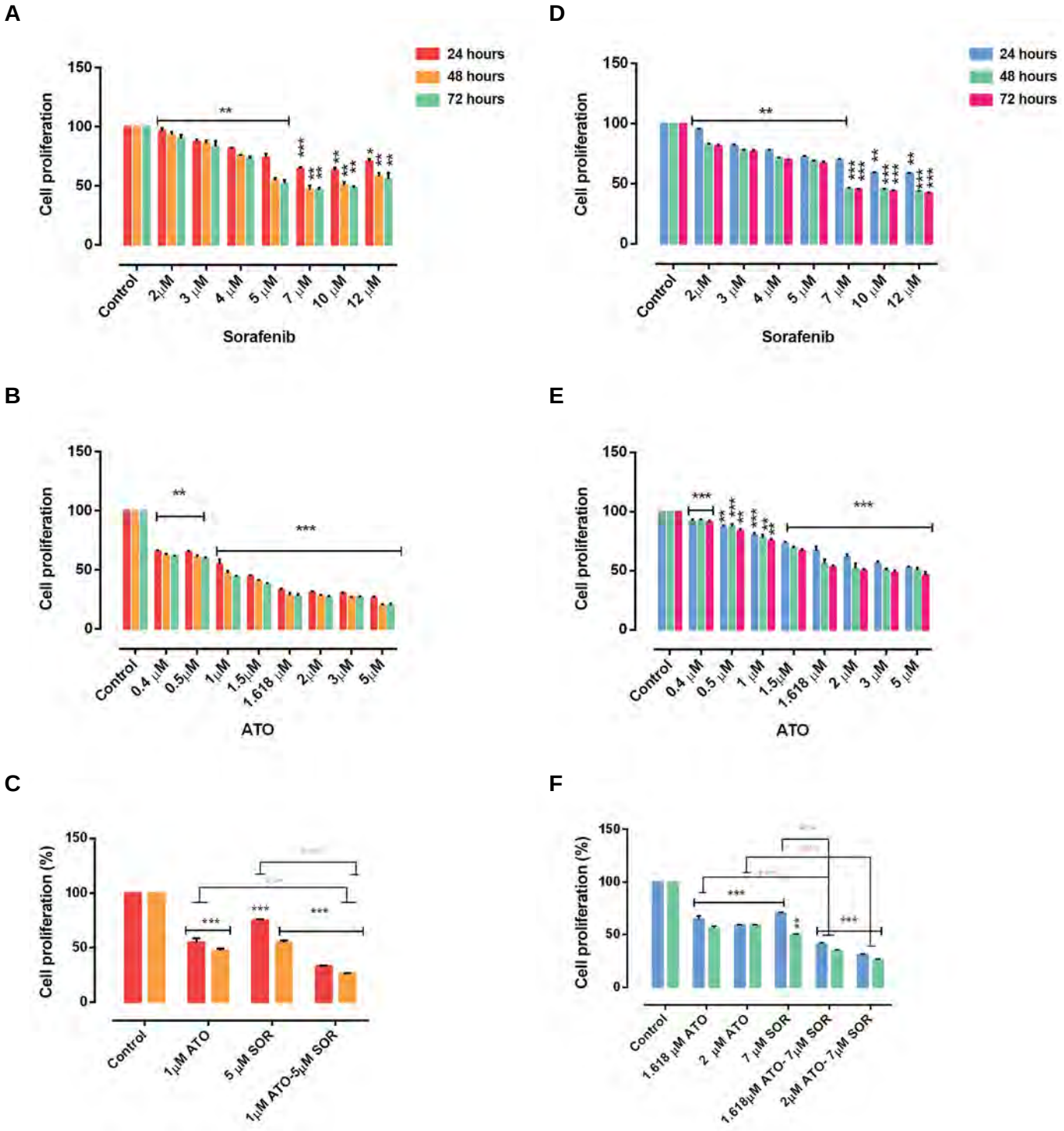

Fig.2: U937 and KG-1 cells proliferation. In U937 **A.** The anti-proliferative effects of sorafenib, **B.** Arsenic trioxide (ATO) and **C.** Their combinations. In KG-1 **D.** The anti-proliferative effects of sorafenib, **E.** ATO, and **F.** Their combinations were assessed by MTT assay after 24, 48, and 72 hours treatment. Combination of ATO and sorafenib compared to the control or each compound alone, could significantly decrease cell proliferation in both cell lines. Data are expressed as mean ± SE of three independent experiments. Statistical significance was defined at *; $P<0.05$, **; $P<0.01$ and ***; $P<0.001$ compared to corresponding control and red star compared to combination therapy, by using two way ANOVA and t test.

Apoptosis assay

To investigate apoptosis and necrosis, we performed flow cytometry assay using annexin-V FITC/PI staining for both U937 and KG-1 cell lines following 48h treatment. As seen in Figures 3A and B, our result indicated an increase in apoptotic cells (annexin^{+}/PI^{-}) and minimum percentage of necrosis in treated cells compared to control, in both U937 and KG-1 cells. Moreover, we observed a significant increase (up to 70% in KG-1 and around 80% in U937 cells) in combination doses ($P<0.001$). The percentages of apoptotic cells in treated KG-1 and U937 cell lines were significantly higher than those of the control groups.

Cell cycle assay

DNA content of U937 and KG-1 cells was assessed by flow cytometry. To specify the apoptosis activating role of ATO and sorafenib, U937 and KG-1 cells were treated with chosen doses for 48 hours. Our result indicated that combination of ATO and sorafenib increased hypodiploid G0/G1 DNA fraction in a dose-dependent manner (1.13 to 8.3% for KG-1 cell and 9.21 to 16.1% for U937 cell) (Fig.4).

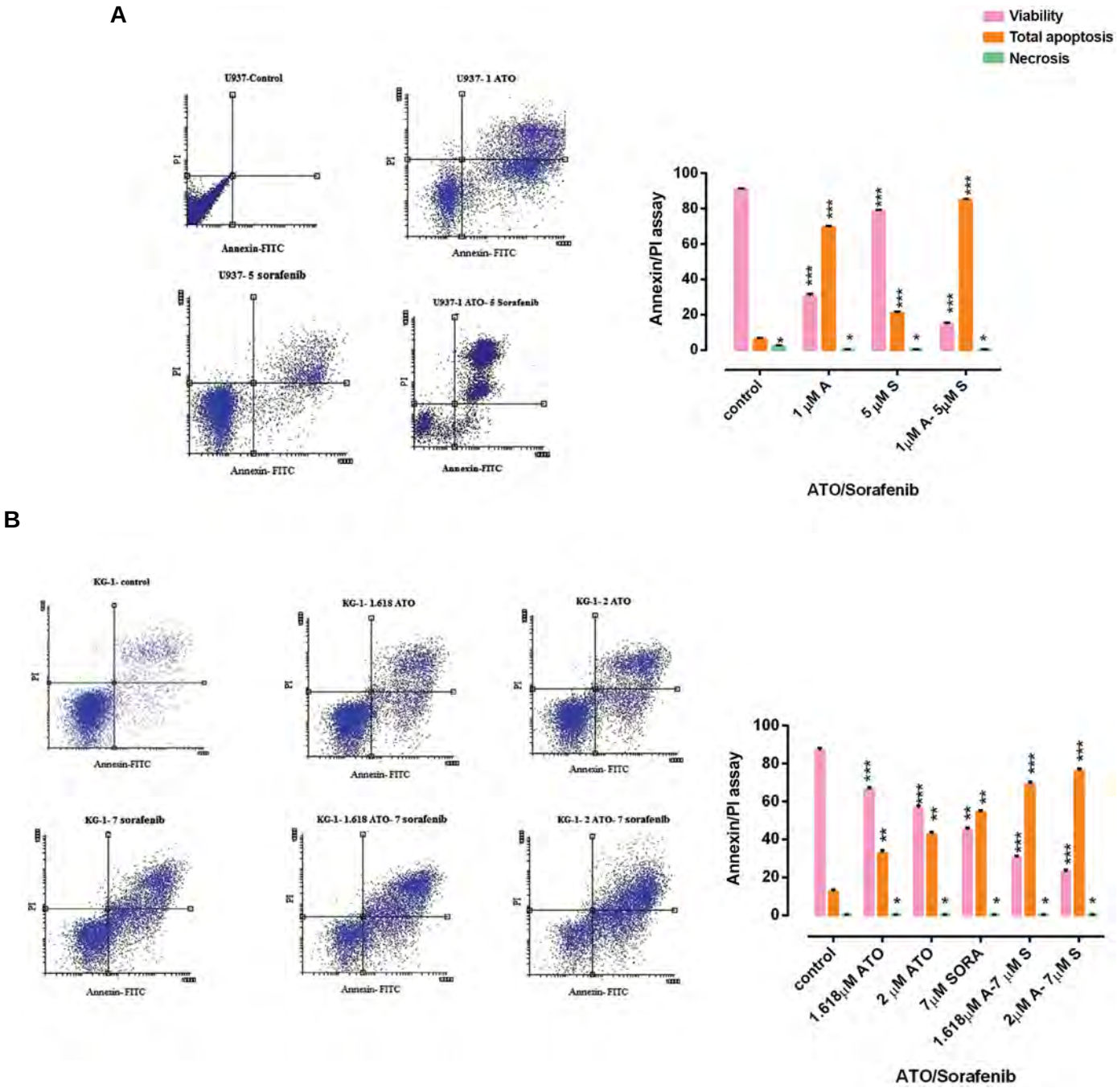

Fig.3: The rate of apoptosis and necrosis by flow cytometry. Investigation of apoptosis in **A.** U937 and **B.** KG-1 cell lines after 48 hours. Cells in the lower right quadrant show apoptosis while in the upper right quadrant show post-apoptotic necrosis. Data are expressed as mean ± SE of three independent experiments. Statistical significance was defined at *; $P<0.05$, **; $P<0.01$ and ***; $P<0.001$ compared to corresponding control, by using two way ANOVA.

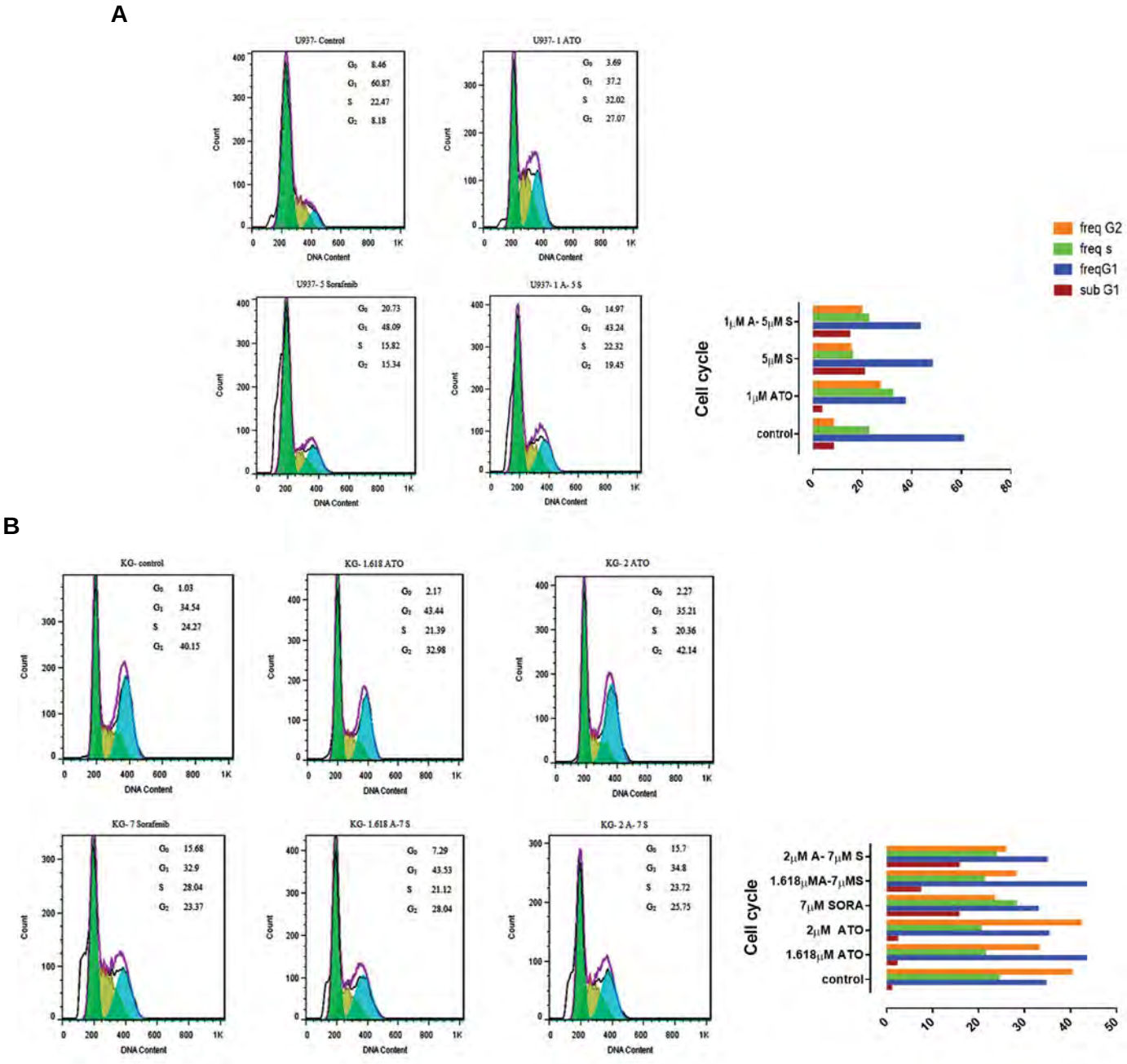

Fig.4: Cell cycle analysis. **A.** Cell cycle analysis for U937. Combination of arsenic trioxide (ATO) and sorafenib increased sub G1. **B.** Cell cycle analysis for KG-1. Effect of ATO and sorafenib on KG-1 increased sub-G0/G1 DNA population.

Real-time polymerase chain reaction assay

In order to investigate the mechanisms underlying the synergy observed for ATO and sorafenib, we analyzed gene expression of *B-RAF*, *MEK1*, *MEK2*, *Beclin1*, *LC3-II*, *ULK1*, *RAF1*, *BCL-2*, *PTEN*, *PI3K*, *AKT*, *mTOR*, and *VEGF* isoforms and its receptors (*VEGFR1* and *VEGFR2*) by real-time PCR.

U937 cells were treated with specific concentrations of ATO (1 μM), sorafenib (5 μM) and their combination for 48 hours. We observed that the expression of *B-RAF* and *MEK1* decreased when cells were treated with a single compound ($P<0.05$) while increased when treated with the combination dose ($P<0.001$) in comparison with the control. But, the expression of *MEK2* decreased following treatment with chosen doses (both single and combination) ($P<0.05$). Moreover, in this pathway, the expression of *RAF1* was markedly decreased following treatment with the combination dose ($P<0.01$). Furthermore, the expression of *BCL-2* decreased while cells were treated with a single compound ($P<0.05$), but slightly increased following treatment with the combination dose ($P<0.01$). The expression of *PTEN* as a tumor suppressor significantly increased after treatment with the combination dose. In addition, expression of *PI3/AKT/mTOR* decreased following treatment with the combination dose ($P<0.001$). Among the autophagy-related genes, we observed that the level of expression of *ULK1* ($P<0.01$) and *Beclin1*

(P<0.05) decreased after combination treatment while the expression of *LC3-II* increased (P<0.01) following treatment with the combination dose (Fig.5A-D).

KG-1 cells were treated with ATO (1.618 and 2 µM), sorafenib (7 µM) and their combination for 48 hours. Our data indicated that the expression of *B-RAF* (P<0.001), *MEK*1 (P<0.05), *MEK*2 (P<0.001), and *RAF1* (P<0.001) increased following treatment with the combination doses. Furthermore, the expression of *BCL-2* slightly increased (P<0.05) following treatment with the combination doses. The expression of *PTEN* significantly increased after treatment with combination dose (P<0.05). Moreover, the expression of *AKT* (P<0.01) and *mTOR* (P<0.05) slightly increased following treatment with the combination of ATO and sorafenib. In addition, the expression of *Beclin1* (P<0.05), *LC3-II* (P<0.001 for the combination of ATO 2 µM and sorafenib 7 µM) and *ULK1* (P<0.01 for the combination of ATO 2 µM and sorafenib 7 µM) as autophagy activators, increased in KG-1 cells. Since autophagy signaling pathway plays a dual role in cancer cells, activation of this pathway may promote programmed cell death (Fig.5E-H).

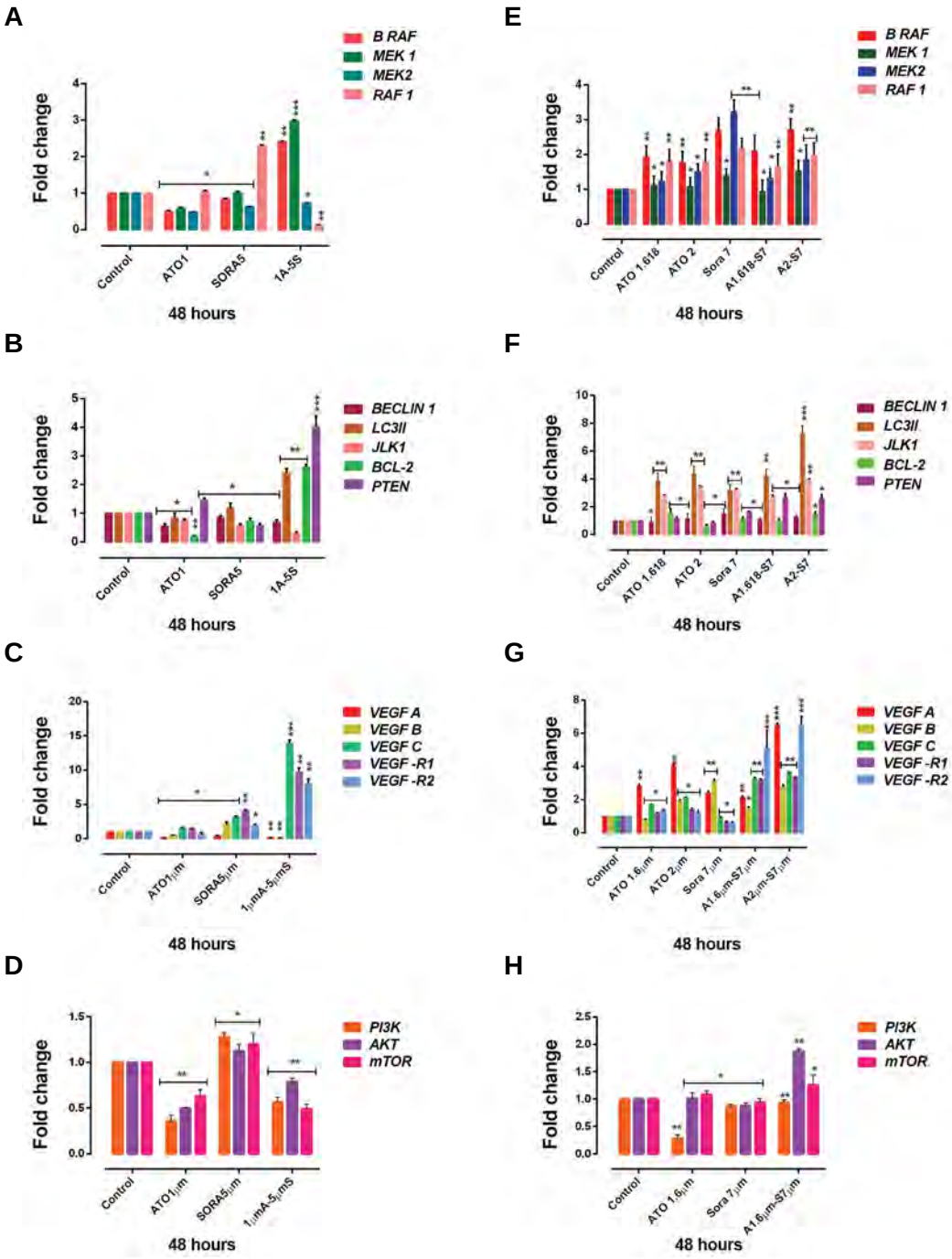

Fig.5: The effects of arsenic trioxide (ATO) and sorafenib on the mRNA level of indicated genes in U937 and KG-1 cells. In U937 cell line **A.** The effects of ATO and sorafenib on expression levels of cell proliferation genes, **B.** Autophagy genes, **C.** VEGF, **D.** Cell survival genes, and in KG-1 cells, **E.** The effects of ATO and sorafenib on expression levels of cell proliferation genes, **F.** Autophagy genes, **G.** VEGF, and **H.** Cell survival genes, were determined by real-time polymerase chain reaction (PCR) analysis. Values are given as mean ± SE of three independent experiments. Statistical significance was defined at *; P<0.05, **; P<0.01, ***; P<0.001 compared to corresponding control by using two way ANOVA and t test, and VEGF; Vascular endothelial growth factor.

Discussion

In the present research, we tried to assess the *in vitro* activity of sorafenib and ATO, alone and in combination, in AML cell lines. AML is known as a heterogeneous disorder. Despite advanced treatment options which have to promote overall survival, AML still remains as a life-threating disease (23). In the current article, we studied the effect of ATO and sorafenib on the expression pattern of *VEGFA* (24), *B-RAF*, *MEK1*, *MEK2*, *Beclin1*, *LC3-II*, *ULK1*, *RAF1*, *BCL-2* and *PTEN* in leukemic cell lines. We focused not only on apoptosis but also on autophagy. Previous studies demonstrated that angiogenesis factors such as VEGF-A play a vital role in cancer progression and metastasis (25). Autophagy is a major protein degradation process that contributes to maitainence of intercellular hemostasis (26). The critical and dual role of autophagy has been confirmed in various studies. Any dysfunction of this pathway may contribute to cancer progression, and metastasis or drug resistance.

ATO as a multi-target agent is able to activate apoptosis and autophagy (27) through various molecular pathways in numerous cancers including solid tumor cells and hematological malignancies. In this study, we observed ATO cytotoxic and apoptosis-inducing effects in both U937 and KG-1 cell lines in a dose and time-dependent manner. Our data indicated that ATO can influence cell proliferation and cell death pathway. We examined a wide range of ATO concentrations in both resistant and sensitive cell lines. We observed that 1.618 and 2 μM of ATO has a significant effect as compared to its lower concentrations in KG-1 (as a resistant cell line). Chiu et al. (28) reported that ATO in combination with ionizing radiation may enhance programmed cell death by activating both autophagy and apoptosis in human fibrosarcoma cells. Also, Chiu et al. (29) confirmed that ATO can synergistically activate both apoptosis and autophagy.

Sorafenib is known as a multikinase inhibitor which act through suppression of Ser/Thr kinase Raf that is known to have an important role in tumor cell signaling and proliferation, and various RTKs involved in angiogenesis, such as VEGF (30). However, sorafenib was shown to be more effective in leukemia with the FLT3-ITD mutation, and its antileukemic function was clarified in several patients with AML and wild-type form of FLT3 (31). In our previous study, we demonstrated that sorafenib downregulates the gene expression of *VEGFR-1/2* in KG-1 cell line and downregulates the gene expression of *VEGF-A* in U937 cell line (32).

The RAF/MEK/ERK signaling pathway was shown to be activated in various processes in cancer. In the present study, we observed that the expression of *B-RAF*, *MEK1*, *MEK2*, and *RAF1* increased as a result of treatment with ATO, sorafenib and their combination in KG-1 cell line. In addition, the expression level of *MEK2*, *RAF1*, *Beclin1*, *ULK1*, *VEGFA* and *VEGFB* decreased following treatment with the combination dose in U937 cell line while the expression of *LC3-II* incresed. Various studies reported that blockade of the MEK/ERK pathway by ATO treatment, induces apoptotic cell death. Fecteau et al. (33) reported that sorafenib downregulates VEGFR and the RAF/MEK/ERK signaling pathways.

We observed that the expression of *Beclin1*, *LC3-II* and *ULK1* as autophagy activators increased following treatment with ATO, sorafenib and their combination in KG-1 cell line. Our data indicated increases in the expression of *LC3-II* and *PTEN* which may lead to activation of both autophagy and apoptosis. Consistent with our result, a group of scientists reported that ATO decreased the gene expression level of *Beclin1*, *LC3-II* and *MAPK* signaling pathways in U118-MG cells (29). Li et al. (34) by studying Beclin 1 and LC3 Ⅱ, indicated that inhibiting autophagy promotes the cytotoxic effect of ATO in glioblastoma cells. Goussetis et al. (35) reported that ATO can activate autophagy in the leukemic cells; induction of autophagy process seems to involve activation of the ERK pathway. Chiu et al. (36) demonstrated that ATO in combination with ionizing radiation, could initiate autophagy through activation of ERK and inhibition of PI3K/AKT signaling pathway. Wang et al. (37) showed that mice xenografted with FLT3-ITD MOLM13 cell line and treated with a combination of sorafenib and ATO have remarkably promoted survival. This combination has the potential to prosper the therapeutic effect of FLT3-ITD in patients with AML.

Tai et al. (38) reported that sorafenib-induced autophagy signaling pathway through significant induction of LC3-II in HCC cell lines. Shimizu et al. (39) demonstrated increased expression of *LC3-II* which led to autophagosome formation and autophagy activation while expression of Beclin 1 did not change under sorafenib treatment. Amantini et al. (40) using bladder cancer cells, reported that sorafenib induces apoptosis through blocking Akt and activating PTEN.

Conclusion

In this study, we found that combination of ATO and sorafenib significantly reduced the viability of U937 and KG-1 cells. In addition, the crosstalk between apoptosis and autophagy is complicated and varies among different cell types. Similar stimuli may activate both pathways as they share various signaling. ATO with antileukemic activity in AML cell lines, enhances the antitumor activity of sorafenib in both U937 and KG-1 cells. Our study indicated a potential mechanism underlying the interaction between ATO and sorafenib in U937 and KG-1 cell lines.

Acknowledgements

This study had financial support by the Hematology, Oncology and Stem Cell Transplantation Research Center, Tehran University of Medical Sciences. The authors declare no conflicts of interest.

Authors' Contributions

A.H., M.N., S.M.; Contributed to conception

and design. A.H., M.S., M.M.K., B.C., S.R., K.M.; Contributed to all experimental work, data and statistical analysis, and interpretation of data. M.N., S.M.; Were responsible for overall supervision. A.H.; Drafted the manuscript. All authors read and approved the final manuscript.

References

1. De Kouchkovsky I, Abdul-Hay M. Acute myeloid leukemia: a comprehensive review and 2016 update. Blood Cancer J. 2016; 6(7): e441.
2. Martinelli E, Morgillo F, Troiani T, Ciardiello F. Cancer resistance to therapies against the EGFR-RAS-RAF pathway: the role of MEK. Cancer Treat Rev. 2017; 53: 61-69.
3. Zaniboni A, Formica V. The Best. First. Anti-EGFR before anti-VEGF, in the first-line treatment of RAS wild-type metastatic colorectal cancer: from bench to bedside. Cancer Chemother Pharmacol. 2016; 78(2): 233-244.
4. Li P, Xue WJ, Feng Y, Mao QS. Long non-coding RNA CASC2 suppresses the proliferation of gastric cancer cells by regulating the MAPK signaling pathway. Am J Transl Res. 2016; 8(8): 3522-3529.
5. Sun Y, Liu W-Z, Liu T, Feng X, Yang N, Zhou H-F. Signaling pathway of MAPK/ERK in cell proliferation, differentiation, migration, senescence and apoptosis. J Recept Signal Transduct Res. 2015; 35(6): 600-6004.
6. De Amicis F, Guido C, Santoro M, Giordano F, Donà A, Rizza P, et al. Ligand activated progesterone receptor B drives autophagy-senescence transition through a Beclin-1/Bcl-2 dependent mechanism in human breast cancer cells. Oncotarget. 2016; 7(36): 57955-57969.
7. Russell RC, Tian Y, Yuan H, Park HW, Chang Y-Y, Kim J, et al. ULK1 induces autophagy by phosphorylating Beclin-1 and activating VPS34 lipid kinase. Nat Cell Biol. 2013; 15(7): 741-750.
8. Martinez J, Malireddi RK, Lu Q, Cunha LD, Pelletier S, Gingras S, et al. Molecular characterization of LC3-associated phagocytosis reveals distinct roles for Rubicon, NOX2 and autophagy proteins. Nat Cell Biol. 2015; 17(7): 893-906.
9. Xia P, Xu X-Y. PI3K/Akt/mTOR signaling pathway in cancer stem cells: from basic research to clinical application. Am J Cancer Res. 2015; 5(5): 1602-1609.
10. Cao G, Li X, Qin C, Li J. Prognostic value of VEGF in hepatocellular carcinoma patients treated with sorafenib: a meta-analysis. Med Sci Monit. 2015; 21: 3144-3151.
11. Abaza Y, Kantarjian H, Garcia-Manero G, Estey E, Borthakur G, Jabbour E, et al. Long-term outcome of acute promyelocytic leukemia treated with all-trans-retinoic acid, arsenic trioxide, and gemtuzumab. Blood. 2017; 129(10): 1275-1283.
12. Kong X, Xu X, Yan Y, Guo F, Li J, Hu Y, et al. Estrogen regulates the tumour suppressor MiRNA-30c and its target gene, MTA-1, in endometrial cancer. PLoS One. 2014; 9(3): e90810.
13. Mohammadi S, Ghaffari SH, Shaiegan M, Zarif MN, Nikbakht M, Akbari Birgani S, et al. Acquired expression of osteopontin selectively promotes enrichment of leukemia stem cells through AKT/mTOR/PTEN/β-catenin pathways in AML cells. Life Sci. 2016; 152: 190-198.
14. Hiramatsu A, Miwa H, Shikami M, Ikai T, Tajima E, Yamamoto H, et al. Disease-specific expression of VEGF and its receptors in AML cells: possible autocrine pathway of VEGF/type1 receptor of VEGF in t (15;17) AML and VEGF/type2 receptor of VEGF in t (8;21) AML. Leuk Lymphoma. 2006; 47(1): 89-95.
15. Yang S, Dong Q, Yao M, Shi M, Ye J, Zhao L, et al. Establishment of an experimental human lung adenocarcinoma cell line SPC-A-1BM with high bone metastases potency by (99m) Tc-MDP bone scintigraphy. Nucl Med Biol. 2009; 36(3): 313-321.
16. Awad KS, Elinoff JM, Wang S, Gairhe S, Ferreyra GA, Cai R, et al. Raf/ERK drives the proliferative and invasive phenotype of BMPR2-silenced pulmonary artery endothelial cells. Am J Physiol Lung Cell Mol Physiol. 2016; 310(2): L187-L201.
17. Zhao Y, Yang J, Liao W, Liu X, Zhang H, Wang S, et al. Cytosolic FoxO1 is essential for the induction of autophagy and tumour suppressor activity. Nat Cell Biol. 2010; 12(7): 665-675.
18. Gao W, Shen Z, Shang L, Wang X. Upregulation of human autophagy-initiation kinase ULK1 by tumor suppressor p53 contributes to DNA-damage-induced cell death. Cell Death Differ. 2011; 18(10): 1598-1607.
19. Cianfrocca R, Tocci P, Semprucci E, Spinella F, Di Castro V, Bagnato A, et al. β-Arrestin 1 is required for endothelin-1-induced NF-κB activation in ovarian cancer cells. Life Sci. 2014; 118(2): 179-184.
20. Fan B, Yu Y, Zhang Y. PI3K-Akt1 expression and its significance in liver tissues with chronic fluorosis. Int J Clin Exp Pathol. 2015; 8(2): 1226-1236.
21. Gronych J, Korshunov A, Bageritz J, Milde T, Jugold M, Hambardzumyan D, et al. An activated mutant BRAF kinase domain is sufficient to induce pilocytic astrocytoma in mice. J Clin Invest. 2011; 121(4): 1344-1348.
22. Lin DA, Boyce JA. IL-4 regulates MEK expression required for lysophosphatidic acid-mediated chemokine generation by human mast cells. J Immunol. 2005; 175(8): 5430-5438.
23. Döhner H, Weisdorf DJ, Bloomfield CD. Acute myeloid leukemia. N Engl J Med. 2015; 373(12): 1136-1152.
24. Mohammadi Kian M, Mohammadi S, Tavallaei M, Chahardouli B, Rostami S, Zahedpanah M, et al. Inhibitory Effects of arsenic trioxide and thalidomide on angiogenesis and vascular endothelial growth factor expression in leukemia cells. Asian Pac J Cancer Prev. 2018; 19(4): 1127-1134.
25. Zhao D, Pan C, Sun J, Gilbert C, Drews-Elger K, Azzam D, et al. VEGF drives cancer-initiating stem cells through VEGFR-2/Stat3 signaling to upregulate Myc and Sox2. Oncogene. 2015; 34(24): 3107-3119.
26. Wei J, Long L, Yang K, Guy C, Shrestha S, Chen Z, et al. Autophagy enforces functional integrity of regulatory T cells by coupling environmental cues and metabolic homeostasis. Nat Immunol. 2016; 17(3): 277-285.
27. Zhang G, Liu J, Zhang Y, Qu J, Xu L, Zheng H, et al. Cbl-b-dependent degradation of FLIP(L) is involved in ATO-induced autophagy in leukemic K562 and gastric cancer cells. FEBS Lett. 2012; 586(19): 3104-3110.
28. Chiu HW, Lin JH, Chen YA, Ho SY, Wang YJ. Combination treatment with arsenic trioxide and irradiation enhances cell-killing effects in human fibrosarcoma cells in vitro and in vivo through induction of both autophagy and apoptosis. Autophagy. 2010; 6(3): 353-365.
29. Chiu HW, Ho YS, Wang YJ. Arsenic trioxide induces autophagy and apoptosis in human glioma cells in vitro and in vivo through downregulation of survivin. J Mol Med (Berl). 2011; 89(9): 927-941.
30. Yildiz C, Kacan T, Akkar OB, Karakus S, Kacan SB, Ozer H, et al. Effects of pazopanib, sunitinib, and sorafenib, anti-VEGF agents, on the growth of experimental endometriosis in rats. Reprod Sci. 2015; 22(11): 1445-1451.
31. Crump M, Hedley D, Kamel-Reid S, Leber B, Wells R, Brandwein J, et al. A randomized phase I clinical and biologic study of two schedules of sorafenib in patients with myelodysplastic syndrome or acute myeloid leukemia: a NCIC (National Cancer Institute of Canada) Clinical Trials Group Study. Leuk Lymphoma. 2010; 51(2): 252-260.
32. Haghi A, Mohammadi S, Heshmati M, Ghavamzadeh A, Nikbakht M. Anti-vascular endothelial growth factor effects of sorafenib and arsenic trioxide in acute myeloid leukemia cell lines. Asian Pac J Cancer Prev. 2017; 18(6): 1655-1661.
33. Fecteau JF, Bharati IS, O'Hayre M, Handel TM, Kipps TJ, Messmer D. Sorafenib-induced apoptosis of chronic lymphocytic leukemia cells is associated with downregulation of RAF and myeloid cell leukemia sequence 1 (Mcl-1). Mol Med. 2012; 18: 19-28.
34. Li C, Liu Y, Liu H, Zhang W, Shen C, Cho K, et al. Impact of

autophagy inhibition at different stages on cytotoxic effect of autophagy inducer in glioblastoma cells. Cell Physiol Biochem. 2015; 35(4): 1303-1316.
35. Goussetis DJ, Gounaris E, Platanias LC. BCR-ABL1-induced leukemogenesis and autophagic targeting by arsenic trioxide. Autophagy. 2013; 9(1): 93-94.
36. Chiu HW, Ho SY, Guo HR, Wang YJ. Combination treatment with arsenic trioxide and irradiation enhances autophagic effects in U118-MG cells through increased mitotic arrest and regulation of PI3K/Akt and ERK1/2 signaling pathways. Autophagy. 2009; 5(4): 472-483.
37. Wang R, Li Y, Gong P, Gabrilove J, Waxman S, Jing Y. Arsenic trioxide and sorafenib induce synthetic lethality of FLT3-ITD acute myeloid leukemia cells. Mol Cancer Ther. 2018; 17(9): 1871-1880.
38. Tai WT, Shiau CW, Chen HL, Liu CY, Lin CS, Cheng AL, et al. Mcl-1-dependent activation of Beclin 1 mediates autophagic cell death induced by sorafenib and SC-59 in hepatocellular carcinoma cells. Cell Death Dis. 2013; 4: e485.
39. Shimizu S, Takehara T, Hikita H, Kodama T, Tsunematsu H, Miyagi T, et al. Inhibition of autophagy potentiates the antitumor effect of the multikinase inhibitor sorafenib in hepatocellular carcinoma. Int J Cancer. 2012; 131(3): 548-557.
40. Amantini C, Morelli MB, Santoni M, Soriani A, Cardinali C, Farfariello V, et al. Sorafenib induces cathepsin B-mediated apoptosis of bladder cancer cells by regulating the Akt/PTEN pathway. The Akt inhibitor, perifosine, enhances the sorafenib-induced cytotoxicity against bladder cancer cells. Oncoscience. 2015; 2(4): 395-409.

Original Article

The Combination of Metformin and Disulfiram-Cu for Effective Radiosensitization on Glioblastoma Cells

Narges Rezaei, M.Sc.[1, 2], Ali Neshasteh-Riz, Ph.D.[1, 2*], Zohreh Mazaheri, Ph.D.[3], Fereshteh Koosha, Ph.D.[1, 4], Mahmood Hoormand, M.D.[5]

1. Radiation Biology Research Center, Iran University of Medical Sciences, Tehran, Iran
2. Department of Radiation Sciences, School of Paramedicine, Iran University of Medical Sciences, Tehran, Iran
3. Department of Anatomical Sciences, Medical Sciences Faculty, Tarbiat Modares University, Tehran, Iran
4. Department of Medical Physics and Biomedical Engineering, Faculty of Medicine, Tehran University of Medical Sciences, Tehran, Iran
5. Department of Pharmacology, Faculty of Medicine, Iran University of Medical Sciences, Tehran, Iran

**Corresponding Address: P.O.Box: 1449614535, Department of Radiation Sciences, School of Paramedicine, Iran University of Medical Sciences, Tehran, Iran*
Email: neshastehriz@yahoo.com

Received: 9/April/2019, Accepted: 22/May/2019

Abstract

Objective: Glioblastoma (GBM) is one of the devastating types of primary brain tumors with a negligible response to standard therapy. Repurposing drugs, such as disulfiram (DSF) and metformin (Met) have shown antitumor properties in different cell lines, including GBM. In the present study, we focused on the combinatory effect of Met and DSF-Cu on the induction of apoptosis in U87-MG cells exposed to 6-MV X-ray beams.

Materials and Methods: In this experimental study, the MTT assay was performed to evaluate the cytotoxicity of each drug, along with the combinatory use of both. After irradiation, the apoptotic cells were assessed using the flow cytometry, western blot, and real-time polymerase chain reaction (RT-PCR) to analyze the expression of some cell death markers such as *BAX* and *BCL-2*.

Results: The synergistic application of both Met and DSF had cytotoxic impacts on the U87-MG cell line and made them sensitized to irradiation. The combinatory usage of both drugs significantly decreased the cells growth, induced apoptosis, and caused the upregulation of *BAX, P53, CASPASE-3,* and it also markedly downregulated the expression of the anti-apoptotic protein BCL-2 at the gene and protein levels.

Conclusion: It seems that the synergistic application of both Met and DSF with the support of irradiation can remarkably restrict the growth of the U87-MG cell line. This may trigger apoptosis via the stimulation of the intrinsic pathway. The combinatory use of Met and DSF in the presence of irradiation could be applied for patients afflicted with GBM.

Keywords: Apoptosis, Disulfiram, Glioblastoma, Irradiation, Metformin

Cell Journal(Yakhteh), Vol 22, No 3, October-December (Autumn) 2020, Pages: 263-272

Citation: Rezaei N, Neshasteh-Riz A, Mazaheri Z, Koosha F, Hoormand M. The combination of metformin and disulfiram-cu for effective radiosensitization on glioblastoma cells. Cell J. 2020; 22(3): 263-272. doi: 10.22074/cellj.2020.6798.

Introduction

Glioblastoma (GBM) is a grade IV astrocytoma, regarded as one of the most aggressive and devastating cancers of the central nervous system with a dismal prognosis (1, 2). Despite the improvements in therapeutic options, treatment modalities have recently improved overall survival up to 14.6 months (3). GBM is characterized by the uncontrolled proliferation of astrocytes along with the increased rate of angiogenesis, making the disease incurable with a high recurrence rate (4, 5). Since GBM is highly resistant to recent therapies, new approaches are required to improve the treatment outcomes. Upon treatment of cancer cells with ionizing radiation and cytotoxic agents, the cell signaling pathways involved in the vital biological functions such as cell division, gene expression, and protein synthesis are effectively influenced. Ionizing radiation could cause damages to DNA and dysregulate the expression of a group of essential proteins, such as P53 and DNA-dependent kinases (6).

Radiation stimulates the expression of P53 via the post-translational mechanism. P53 regulates the expression level of several genes and proteins that are located in the downstream of the P53 signaling pathway such as *BAX* and *P21* (7). The Bcl-2 family proteins play a significant role in the regulation of apoptosis, and they consisted of two groups of proteins, namely pro-apoptotic (BAX) and anti-apoptotic (BCL2) proteins which are capable of modulating the mitochondrial permeabilization. After irradiation, BCL2 and the caspase cascade are fully activated, and the process of apoptosis would be initiated (8).

During the last decades, molecular targeting agents, such as disulfiram (DSF) and metformin (Met), which are known as repurposing drugs, exert antitumor properties when used for the induction of cell death in different types of cancers, such as GBM (9). DSF is an Food and Drug Administration (FDA) approved drug which is a member of the carbamate family, and it has been prescribed as a safe drug for the treatment of alcohol abusers (10). Recently, researchers have highlighted DSF as an anti-cancer agent for different kinds of malignancies, including hematological cancers, breast cancer, melanoma, and especially GBM (11, 12). DSF is a safe and non-toxic compound which can easily penetrate the blood-brain barrier (BBB) (13).

Met, an FDA-approved drug, belongs to the family of biguanide agents, and it is commonly prescribed for patients who have type 2 diabetes (14). Different studies have shown that Met exerts antitumor potential against many types of tumors; however, the mechanisms underlying the anti-tumor characteristic of Met is still unknown (15-17).

Furthermore, Met could show anti-neoplastic properties via the prevention of the electron transport chain complex I (ETCI) and activation of the pathways responsible for energy homeostasis. Met is also capable of stimulating the expression of adenosine monophosphate-activated protein (AMPK) and preventing the activation of the mammalian target of rapamycin complex I (mTOR). It has been shown that Met confines the synthesis of proteins and suppresses cancer stem cells via the inhibition of the production of Foxo-3 and AKT. Some reports indicated that Met could increase the sensitivity of tumor cells to common anti-cancer drugs such as paclitaxel and temozolomide (TMZ) (18). To date, numerous clinical trials and retrospective studies have been conducted to elucidate how Met can extend the survival of patients afflicted with cancer (19, 20). Several lines of evidence demonstrated that Met and DSF could prevent the proliferation, invasion, and metastasis of tumor cells in the pancreas (21, 22).

According to the above evidence, we hypothesized that the combination of DSF-Cu and Met with irradiation could induce apoptosis in the U87-MG cell line. Therefore, we investigated the effect of combinatory treatment with Met and DSF-Cu in the presence of radiation on the induction of apoptosis thereby the measurement of B*AX*, *CASPASE3*, *P53* and *BCL2* levels in the U87-MG cell line. Our findings could be a promising approach for the treatment of GBM patients.

Materials and Methods

Cell culture

In this experimental study, the U87-MG cell line was purchased from the Pasteur Institute, Tehran, Iran. Cells were cultured in high-glucose Dulbecco's modified Eagle Medium (DMEM, Atocel, Austria) supplemented with 10% fetal bovine serum (FBS, Biowest, France) and 1% Penicillin-Streptomycin (Atocel, Austria). Cells were then incubated at 37˚C in a humidified atmosphere containing 5% CO_2 and 95% O_2.

This research was performed after receiving the ethics approval from the Ethics Communication of Iran University of Medical Science (IUMS, Number: 28594).

Preparation of drugs and application of irradiation

DSF, Copper chloride ($CuCl_2$), and Met (1,1-dimethyl biguanide-hydrochloride) were procured from Sigma Aldrich (Dorset-UK). DSF was then dissolved in dimethyl sulfoxide [DMSO, maximum DMSO concentration was 0.1% (v/v)]. Met and $CuCl_2$ were diluted in double distilled water to reach the desired concentrations and kept at -20˚C until analysis Afterward, drugs were diluted with DMEM to adjust the required concentrations. Cells were treated with various types of drugs and then assigned into seven groups as follows: Met group; cells received only Met, Met+IR group; cells were treated with Met plus irradiation, DSF-Cu group; cells received only DSF, DSF-Cu+IR group; cells were treated with DSF-Cu along with irradiation, Met+DSF-Cu group; cells received the combination of Met and DSF-Cu, Met+DSF-Cu+IR; cells were treated with the combination of Met and DSF-Cu with the support of irradiation, and Control group; cells received no treatment. The 3-(4, 5-Dimethylthiazol-2-yl)-2, 5-diphenyltetrazolium bromide (MTT, Atocel, Austria) assay was applied to evaluate the cytotoxicity of the drugs. Cells were treated with various concentrations of Met (1-15000 μM) and DSF-Cu (0.1-5 μM). Also, the impact of combinatory treatment was also examined by the MTT assay. Briefly, 24 hours after the cell-seeding, cells were pre-treated with Met for 24 hours and then treated with DSF-Cu for another 24 hours. Afterward, cells were exposed to a dose of 2Gy X-ray and incubated for 24 hours. Finally, the flow cytometry, western blot, and real-time polymerase chain reaction (RT-PCR) analyses were performed. Irradiation was carried out using a linear accelerator (Siemens, Germany) at a dose rate of 2Gy/minutes, with a field size of 40×40 cm^2 to determine the radiosensitivity of the U87-MG cells. In accordance with treatment methods, the maximum dose of 6 MV X-ray was applied at a 1.5 cm depth of tissue. Thus, we used three layers of 0.5 cm tissue-equivalent, which were placed under the plates to ensure the electronic equilibrium. The cells were exposed to a dose of 2Gy from the posterior side of the flasks. The required dose of irradiation was calculated by the treatment planning software by which the dose of irradiation was determined as 2Gy/minutes,

Cell survival inhibition assay

The cell viability was measured using MTT to evaluate the cytotoxicity of each drug along with the combination of both. Briefly, U87-MG cells at a concentration of 1×10^4 were seeded on the 96-well plates and incubated at 37˚C overnight to allow the cells to adhere. The cells were then treated with Met, DSF, Cu, DSF-Cu, and the combination of both drugs. After the determination of the incubation times, cells were incubated with the MTT solution (5 mg/ml) at 37˚C for 4 hours, and then the medium was removed to solubilize the formazan crystals. Next, 100 μl DMSO was added to each well, and the absorbance was measured using an ELISA reader (Bio-rad laboratories, USA) at an excitation wavelength of 570 nm. The percentage of viability was calculated utilizing the comparison of the absorbance of treated cells with untreated cells. Thus, the following formula was employed to compute the percentage of viability:

Viability=treated cell absorbance/untreated cell absorbance×100.

Flow cytometry

The Annexin-V kit was purchased from Biosciences Inc. (BD, e-Biosciences, USA). The rate of apoptosis in

U87-MG cells was assessed using the Annexin-PI detection kit (BD-ebioscience) according to the manufacturer's protocols. Briefly, 3×10^5 cells were seeded on the 6-well plates for 24 hours and pre-treated with10 mM Met. After 24 hours, they were exposed to 1:1 µM DSF-Cu and finally irradiated with 6 MV X-Rays at the dose of 2 Gy. The cells were then harvested and then resuspended in 100 µl binding buffer. The FITC-conjugated Annexin V-PI were added and incubated for 15 minutes at room temperature. After that, the percentage of apoptotic cells was determined using the flow cytometry (BD FACS Caliber, BD Biosciences, Sanjose, CA, USA) analysis, and the obtained data were analyzed using the FlowJo software (version 7.6.1). The degree of apoptosis was detected in the FL-1 channel (green fluorescence) while necrosis was recorded in the FL-3 channel (red fluorescence). Finally, cells stained with only Annexin-V were at the early stage of apoptosis, while those double-stained with Annexin-V and PI were at the late step of the apoptosis process. Each sample had a negative control that was $Annexin^-$- PI^- and the quadrant was set based on this sample. Samples of each group were compared with their control counterparts.

Western blot analysis

First off, the protein contents of the cells were extracted using RIPA-buffer (Cell Signal, Germany). Next, about 20 µg of the extracted proteins (BioRad Bradford Assay, BioRad, Germany) was mixed with loading buffer (Carl Roth, Germany), and then run on sodium dodecyl sulfate-polyacrylamide gel electrophoresis (SDS-PAGE, BioRad Mini-Protean II Cell; BioRad, Germany). After the electrophoresis process, proteins were transferred onto PVDF that was located in transfer buffer containing 192 mM glycine, 10% methanol, 25 mM Tris, and pH=8.2. The membrane was blocked by 4% non-fat milk powder in phosphate-buffered saline (PBS)-0.05% Tween for 2 hours. The primary antibodies were added in blocking buffer and incubated at 4˚C overnight (1:2000 dilution, Cell Signaling Technology, Danvers, MA, USA), according to the manufacturer's instructions. The membranes were incubated with primary antibodies against rabbit anti-BCL-2 and rabbit anti-BAX (All obtained from the Cell Signaling Technology Company). The equal protein lane loading was corroborated, utilizing a monoclonal antibody against the GAPDH protein (Sigma-Aldrich, USA). The membranes were rinsed three times with PBS-T [0.1% (v/v) Triton-X100] buffer for 30 minutes and probed with horseradish peroxidase (HRP)-conjugated secondary antibodies for 2 hours. When the washing process with PBS-T buffer was performed, the protein bands were visualized using the Odyssey Infrared Imaging System (LI-COR).

Real time- quantitative polymerase chain reaction

The RNA isolation kit was obtained from Qiagen (USA), and the cDNA synthesis kit was purchased from Thermo Scientific (USA). In this study, total RNA was extracted from all experimental groups using Qiazol (Qiazol lysis reagent, USA), according to the manufacturer's instructions. The integrity and concentration of the extracted RNA were determined using a Nanodrop (Thermo Scientific, USA) apparatus, by which the absorbance of the samples is read at wavelengths of 260 and 280 nm. Soon after, cDNA was synthesized using the Revert Aid™ First Strand cDNA Synthesis Kit (Thermo Scientific, MA, USA), based on the manufacturer's recommendations. Primers were designed for *GAPDH* (internal control), *CASPASE3, BAX, BCL-2*, and *P53* by Pishgam Company (Iran, Tehran). Table 1 shows the sequences of primers, the accession number, and the melting temperature of primers. The suitability of the primers was confirmed using BLAST (http://blast.ncbi.nlm.gov/Blast.cgi) to identify the amplified fragment length and show that there were no non-specific binding sites on the same gene or positions of the similar sequences in other species. The relative expression of the above genes was assessed using the $2^{-\Delta\Delta ct}$ method for all groups. RT-qPCR was performed on an Applied Bio-System.

Table 1: List of primer sequences of apoptosis-related genes

Official name	Primer sequences (5´-3´)	Accession number	TM (˚C)
GAPDH	F: GCAGGGATGATGTTCTGG	001289745/2	86.6
	R: CTTTGGTATCGTGGAAGGAC		
P53	F: TTCCGTCTGGGCTTCTTG	001126118/1	88.1
	R: TGCTGTGACTGCTTGTAGAT		
CASPASE3	F: GGACTGTGGCATTGAGAGAG	001354779/1	81.25
	R: GGAGCCATCCTTTGAACTTC		
BAX	F: CGCCCTTTTCTACTTTGACA	001291430/1	86.61
	R: GTGACGAGGCTTGAGGAG		
BCL2	F: TGGTCTTCTTTGAGTTCGG	000633/2	86.61
	R: GGCTGTACAGTTCCACAA		

Statistical analysis

Statistical analysis was performed using the independent-sample t test and one-way analysis of variance (ANOVA) via the SPSS software version 16. The error bars represent the standard error among the different experiments. All analyses were conducted at a significance level of $P<0.05$. All experiments were performed in triplicate.

Results

Metformin and Disulfiram-Cu are individually cytotoxic to U87-MG cells and inhibit cell growth

At first, the MTT assay was performed to evaluate the effect of Met and DSF-Cu on U87-MG cell viability. Cells were exposed to different concentrations of DSF, Cu (0.1-5μM) and Met (0.1-15000 μM). Treatment with DSF or Cu alone had no significant effect on cell viability. Interestingly, as shown in Figure 1A, the combination of DSF-Cu with different concentrations decreased cell viability ($P<0.05$). The cytotoxicity of DSF was dependent on Cu. Met significantly reduced the cell viability in a dose-dependent manner (Fig.1B).

Disulfiram-Cu enhanced the cytotoxicity effect of metformin on U87-MG cells in a dose-dependent manner

To assess the cytotoxicity of Met in combination with drugs that are activated in reducing environments first, cells were pre-treated with 10 mM Met for 24 hours and then treated with different concentrations of DSF along with 1 μM Cu for 24 hours. Finally, the MTT assay was conducted to assess the toxicity of each compound or the combination of them. Figure 1C shows that there was no significant difference among 0.25, 0.5 and 1 μM DSF when combined with 1 μM Cu ($P>0.05$), and the highest toxicity was observed in equimolar (1:1) ratio of DSF to Cu. Furthermore, the morphology of the cells changed as they became more rounded-shape. Thus, junctions between the cells were not observed.

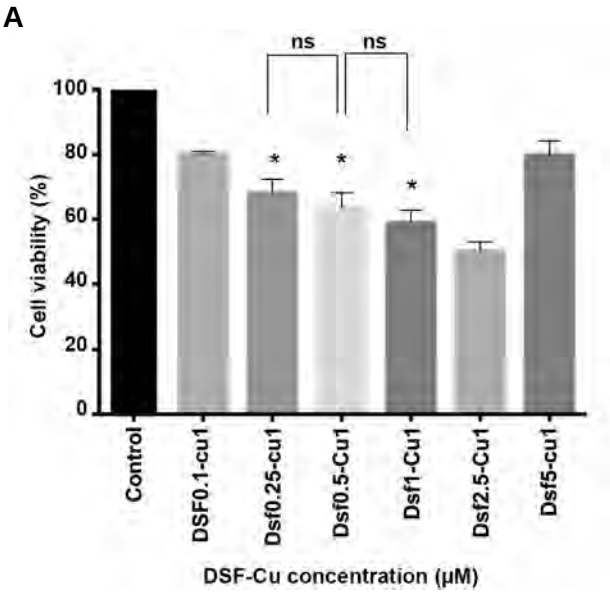

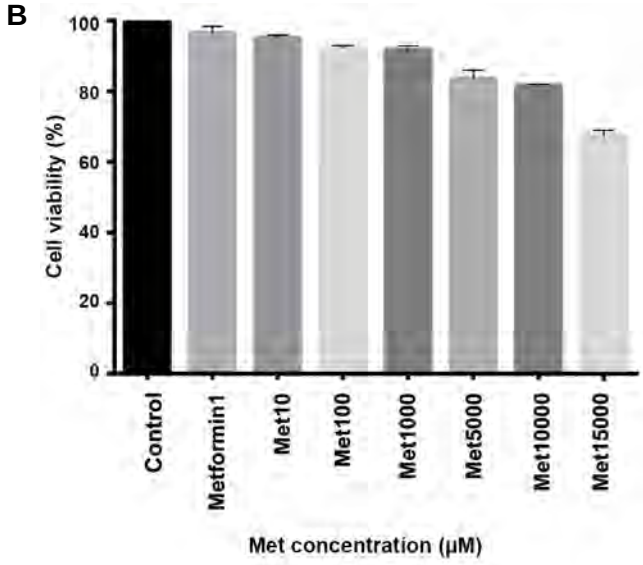

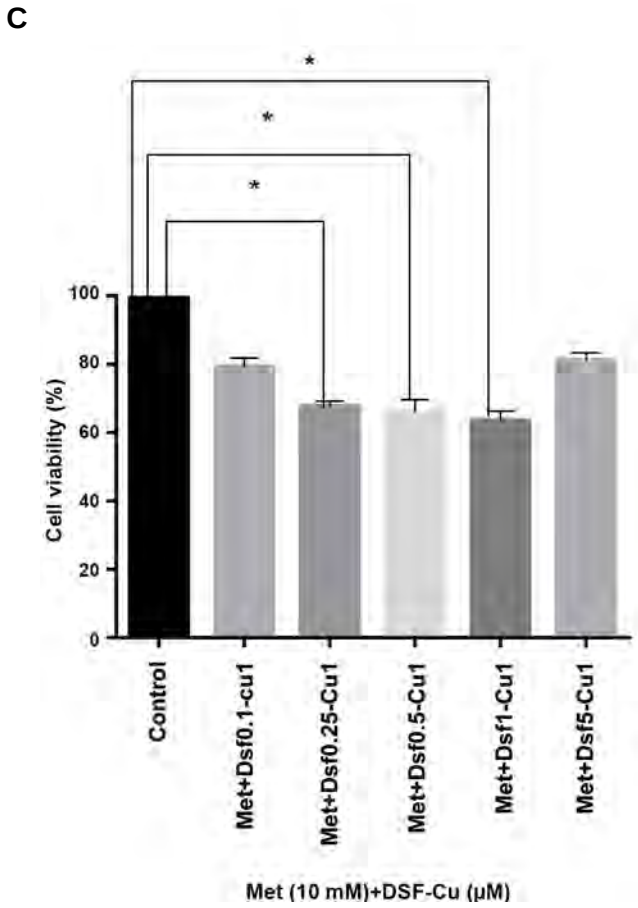

Fig.1: Metformin and DSF-Cu are cytotoxic to U87-MG cells when used alone and inhibit cell viability. **A.** The effect of different concentrations of DSF-Cu on U87-MG cells; DSF (0.1-5 μM), Cu 1 μM, **B.** The impact of different doses of Met (1-15000 μM) on U87-MG cells. Cells were treated and incubated with Met and DSF-Cu for 24 hours, and the MTT assay was performed at least three times, **C.** DSF-Cu increases the cytotoxic effect of Met on U87-MG cells *in vitro* in a dose-dependent manner. The MTT assay was carried out to assess the combinatory effects of Met and DSF-Cu (0.1-5 μM) and Cu (1 μM). Cells were pretreated with 10 mM Met, and after 24 hours, treated with DSF-Cu. Afterward, the MTT assay was performed 24 hours later. The error bars represent the standard error of the mean (SEM) from three repetitions for the experiments. Some error bars are too small to be seen. *; Indicates a statistically significant difference between the control and drug-treated groups at $P<0.05$ vs. the control group, DSF; Disulfiram, Met; Metformin, and ns; Non-significant.

Disulfiram-Cu and metformin as well as their combination, induced apoptosis in U87-MG cells

Apoptosis was evaluated in cells treated with Met, DSF-Cu, and a combination of both drugs. For this aim, cells were exposed to 10 mM Met, and DSF-Cu at a ratio of 1:1 µM for 24 hours. The combinatory effect of both drugs was assessed with Annexin/PI staining that is measured by the flow cytometry analysis. As shown in Figure 2A, a single treatment with Met or DSF-Cu induced cell death in U87-MG cells. As compared with the control or single treatment, the percentage of apoptosis was significantly increased when the synergistic usage of both drugs was applied ($P<0.05$). In cells treated with Met, the percentage of apoptosis was 10.62 ± 1.60% ($P<0.05$), whereas the rate of apoptosis was 14.34 ± 1.29% in cells treated with DSF-Cu ($P<0.05$). Also, the percentage of cell death was 27.31 ± 1.37% when the combined treatment strategy was used ($P<0.05$).

Radiation enhances apoptosis in U87- MG cells

The radiosensitization effect of Met and DSF-Cu was determined when they were used alone or in combination with each other on cells was in the presence of 6 MV X-ray at a dose of 2 Gy. After 24 hours of irradiation, the rate of apoptosis was measured in cells. As compared with the control group and the groups treated with single drugs, apoptosis was significantly ($P<0.05$) increased in the Met+IR group (16.72 ± 1.79%). The percentage of cell death was 22.48 ± 1.79% ($P<0.05$) in the DSF-Cu+IR group whereas the rate of apoptosis was reported 42.35 ± 1.73% in the Met+DSF-Cu+IR group. The radiosensitization effect was more pronounced ($P<0.05$) in the Met+DSF-Cu+IR group when compared with other treatment groups. As a whole, the synergistic role of Met and DSF-Cu considerably inhibited the rate of cell growth in U87-MG cells. Besides, the combination of both drugs promoted irradiation mediated cytotoxicity (Fig.2A, B).

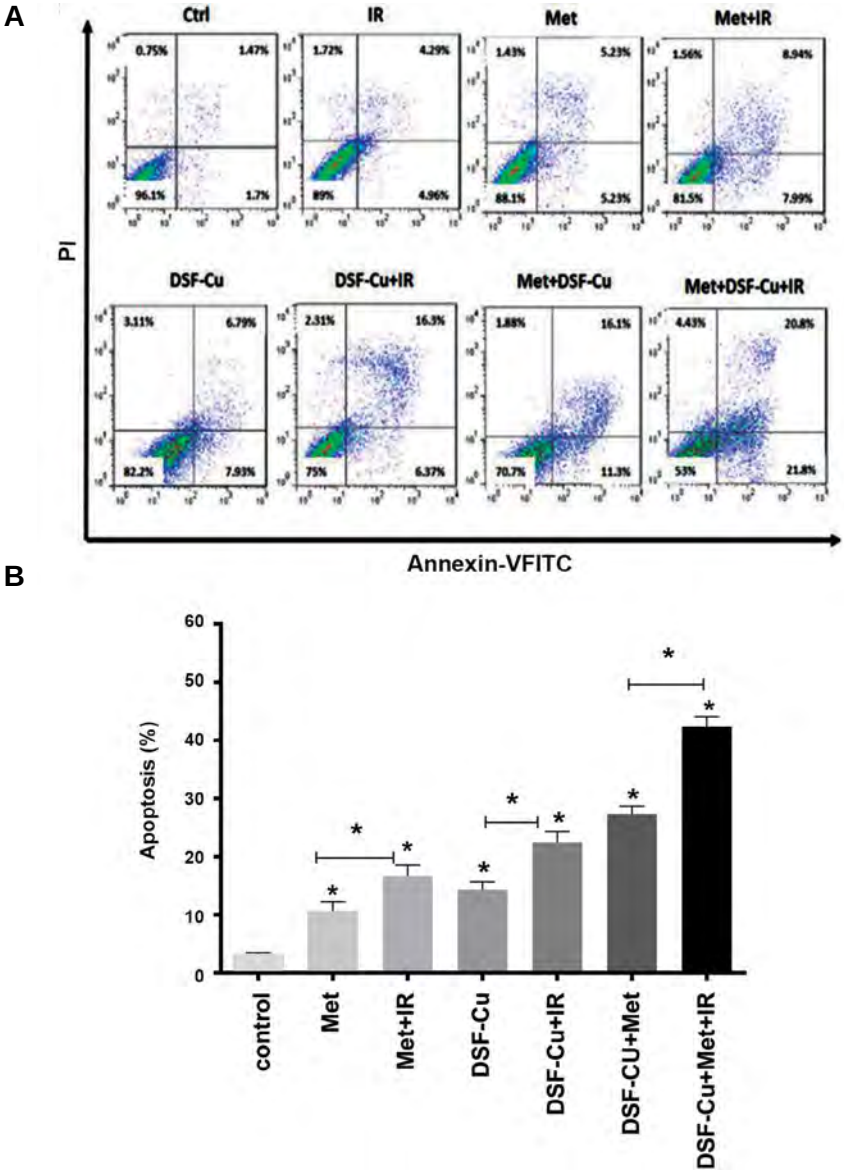

Fig.2: DSF-Cu, Met, and the combination of both promote apoptosis in U87-MG cells. Cells were treated with 10 mM Met at a ratio of 1:1 µM DSF-Cu and irradiation at a dose of 2 Gy. Apoptosis assay was performed 24 hours after the treatment with drugs and IR exposure. **A.** The flow cytometry plots show the early and late apoptosis in the treated groups and **B.** Total apoptosis in different treatment groups. Data are expressed as the mean ± SEM deduced from experiments performed in triplicate, *; $P<0.05$ versus the control group, DSF; Disulfiram, Met; Metformin, and IR; Irradiation.

Metformin, Disulfiram-Cu, and the combination of drugs reduced BCL2 protein levels and increased BAX levels in U87-MG cells

To investigate the mechanisms underlying the apoptotic role of DSF-Cu, Met, and the combination of both, the levels of apoptosis-related proteins, such as BCL_2 and BAX were assessed by the western blot analysis 24 hours after the treatment periods and irradiation (Fig.3A). The western blot assay demonstrated that the expression of BCL_2 was markedly ($P<0.05$) decreased when cells treated with drugs alone or in combination with each other (Fig.3B). Also, the levels of BAX was significantly ($P<0.05$) increased between each treatment group and the control group (Fig.3C). The increase in the expression of Bax and the reduction in the expression of BCL_2 were remarkable ($P<0.05$, Met: 0.002, Met+IR: 0.020, DSF-Cu: 0.004, DSF-Cu+IR: 0.020, Combination: 0.018, Combination+IR: 0.035) higher in the cells treated with the combination of both drugs with the support of irradiation in comparison with other treatment groups.

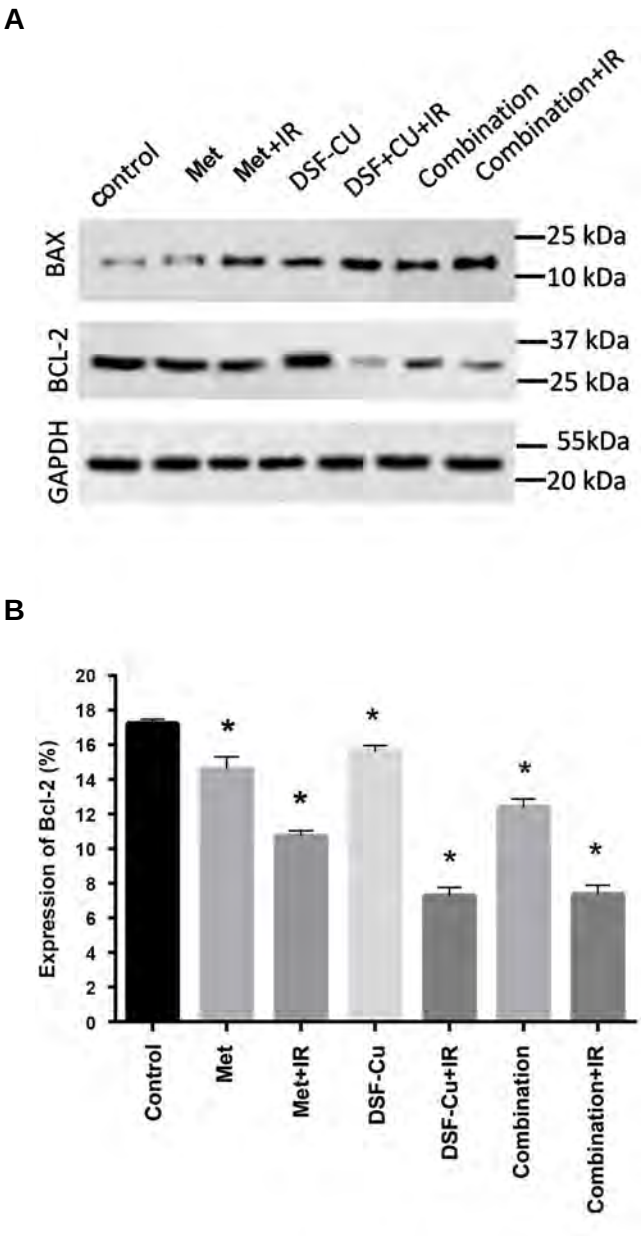

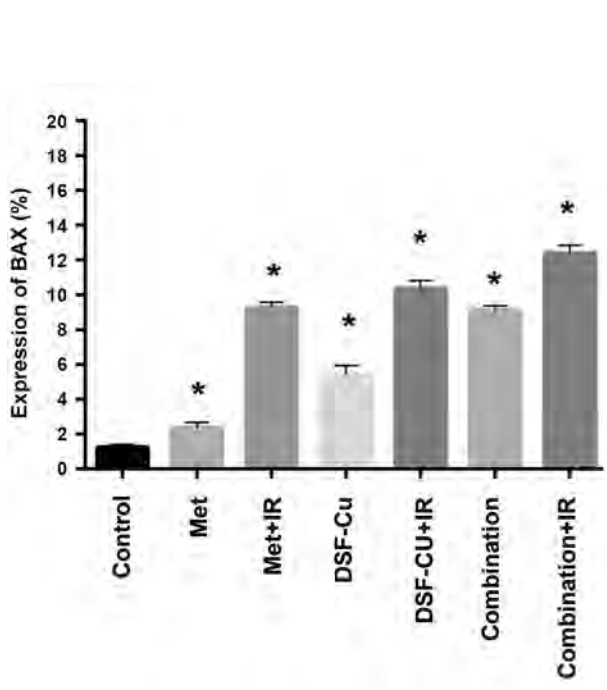

Fig.3: Met, DSF-Cu, and the combination of both suppress BCL-2 protein levels and increase BAX levels in U87-MG cells. **A.** The expression levels of BCL-2 and BAX proteins were measured in U87-MG cells by the western blot analysis 24 hours after treatment with 10 mM Met at a ratio of 1:1 µM DSF-Cu and 2Gy IR, **B.** Western blot of BAX, BCL-2 with and GAPDH. BCL-2 expression was significantly decreased, and **C.** While the expression of BAX was markedly increased in all treatment groups. *; $P<0.05$ vs. the control group, Met; Metformin, DSF; Disulfiram, and IR; Irradiation.

Metformin Disulfiram-Cu and the combination of both with irradiation regulate anti-apoptotic and pro-apoptotic markers in U87-MG cells

The gene expression levels of anti-apoptotic and pro-apoptotic genes that regulate the intrinsic pathway of apoptosis were evaluated using the RT-PCR method. The incubation of U87-MG cells with Met, DSF-Cu, and the combination of both drugs caused the overexpression of *BAX*, *P53*, and *CASPASE3*, but decreased the expression of *BCL2*, as compared with the control or untreated group. The expression of *BCL2* was significantly ($P<0.05$) diminished in all groups as depicted in Figure 4A. *BAX* expression was considerably increased between the treatment groups and the control group ($P<0.05$). However, in cells treated with Met, the expression of *BAX* remained unchanged ($P>0.05$) as displayed in Figure 4B. Figure 4C shows that, as compared with the control group, the expression of *CASPASE3* significantly substantially elevated in all treated groups ($P<0.05$). As shown in Figure 4D, the expression of *P53*, as compared with the control group, was significantly increased in all treated groups ($P<0.05$).

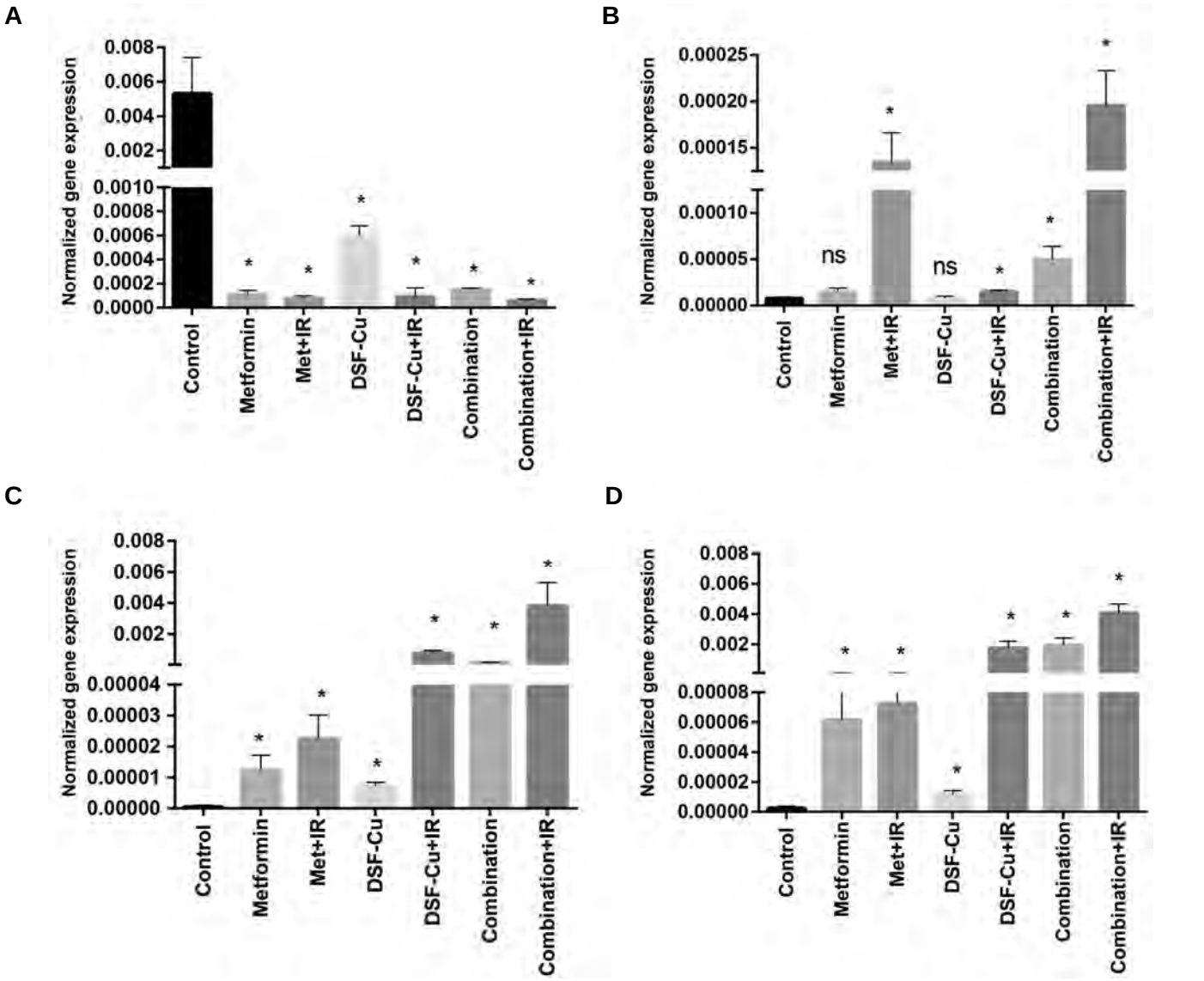

Fig.4: Regulation of anti-apoptotic and pro-apoptotic genes. U87-MG cells were treated with 10 mM Met at a ratio of 1:1 µM DSF-Cu, and the combination of both drugs in the presence/absence of irradiation at a dose of 2 Gy. Then, RT-qPCR was performed to evaluate the expression levels of apoptosis-related genes. **A.** The relative expression level of *BCL-2*, **B.** The relative expression of *BAX*, **C.** The relative expression of *CASPASE-3*, and **D.** The relative expression of *P53*, 24 hours after the incubation times. The internal control was *GAPDH*, and the relative gene expression was compared with the untreated control group. Some error bars are too small to be detected. Data are expressed as the mean ± SEM. *; P<0.05 versus the control group, Met; Metformin, DSF; Disulfiram, ns; Non significant, and RT-qPCR; Real time-quantitative polymerase chain reaction.

Discussion

In recent decades, studies dealing with repurposing drugs, such as DSF and Met possessing the anti-tumor properties are rapidly increasing with the hope of seeking new strategies to fight cancer cells (9). The available treatment strategies have a poor prognosis for the cure of glioblastoma, which is a lethal brain cancer in humans; therefore; new treatment modalities for the therapy of GBM are warranted. The application of drugs that target the metabolism of cells in combination with conventional treatment may yield satisfactory results (23, 24). Based on the results of the present study, the combination of Met and DSF-Cu with the support of radiation had cytotoxic effects on U87-MG cells in which significantly decreased proliferation and increased rate of apoptosis was observed in cells. In other words, the combination of Met and DSF-Cu in the presence of irradiation was more effective in the suppression of cell proliferation and promotion of apoptosis than the single use of radiation, Met or DSF-Cu. Jivan et al. (25) showed that Met in combination with DSF-Cu had cytotoxic effects on oesophageal squamous cell carcinoma (Oscc) and Met empowered the cytotoxicity of DSF-Cu.

Additionally, Met augmented Cu transport into Oscc cells and caused a substantial increase in the number of apoptotic cells and cell death (25). We have also demonstrated that DSF and Cu had no cytotoxic impact on U87-MG cells when used alone, but the synergistic use of both drugs dramatically decreased cell growth

and viability even in the presence of 1 µM DSF. Above this concentration, the viability of cells was increased up to 5 µM.

Some previous studies indicated the biphasic cytotoxic effect of DSF on U87-MG cells in which the cells underwent apoptosis when the compound was used at the concentrations of 0.25, 0.5, and 1 µM. The concentrations above 10 µM did not show any signs of cytotoxicity (22, 26). Several lines of evidence implicated that repurposing drugs, such as Met and DSF-Cu are capable of preventing cell growth, arresting cell cycle progression, as well as triggering autophagy and apoptosis via intrinsic pathway when employed individually in tumor cells especially in GBM (17, 27). Met and DSF-Cu can penetrate the BBB without causing any significant side effects; thus exhibiting low cytotoxicity even when combined with irradiation to act as radiosensitizers (28, 29).

A large body of *in vivo* and *in vitro* research demonstrated that Met and DSF-Cu could increase the potency of chemotherapeutic agents and radiotherapy when added to the therapeutic regimen as the addition of these two drugs are capable of elevating the levels of *BAX*, *P53*, *CASPASE-3*, as well as decreasing the level of *BCL-2* in some types of malignancies such as pancreas, lung, and breast cancers (30-32). The precise mechanism(s) by which Met and DSF-Cu exert anticancer potential is still opaque. It is thought that DSF could prevent the activation of the proteasome, as well as the expression/activation of aldehyde dehydrogenase (ALDH) and nuclear factor B (NF-kB). Besides, these effects, when DSF is combined with Cu can serve to stimulate the production of reactive oxygen species (ROS) (33, 34). In a study performed by Haji et al. (35), they reported that DSF could incite the initiation of cell death pathway by the overexpression of *P21* and *BAX* genes within pancreatic cancer cells. Correspondingly, Feng et al. (36) showed that treatment of GBM cells with DSF-Cu increased the levels of Bax and Caspase-3, and also decreased the Bcl-2 level.

Thus, it seems that apoptosis is mediated via the intrinsic pathway in response to the exposure of the cells to DSF-Cu (36). Sesen et al. (29) indicated that Met at a dose of 300 mg/kg did not induce any significant cell toxicity when administered to the mice *in vivo*. Of note, the administration of Met at a dose prescribed for diabetic patients is not the allowed drug dosage; rather, the lowest side effects were observed when administrated for patients with diabetes. In the case of malignancies, the concentration of Met could be increased up to 10mM as we employed this dose in our experiments (14). In one distinct investigation conducted in Iran, it has been shown that the administration of Met altered the expression of caspase-8, -9, and *PARP-1* in breast cancer cells; however, the expression of *CASPASE-3* remained unchanged (37). Also, different studies have demonstrated that treatment of pancreatic and breast cancer cells with Met, induced apoptosis via the intrinsic pathway in which the expression of BAX was elevated while BCL-2 expression was proteins diminished (30, 32). Apoptosis regulates the proliferation of cells (38), and the Bcl-2 family proteins play a vital role in the modulation of apoptosis in different cells (8). When the regulation of the BCL2 family proteins is impaired, cytochrome c is released from the mitochondria, leading to the activation of a caspase cascade in which some caspases such as CASPASE-9 and -3 are fully activated and can initiate the process of cell death (39). Moreover, P53, when present in the cytoplasm, regulates the permeability of mitochondrial membrane as a pro-apoptotic protein which causes the release of cytochrome c and induces caspase cascade activation which is required for cell death (7). According to our the flow cytometry analyses of the present study, the combinatory treatment significantly induced apoptosis in U87-MG cells as approved by the western blot results, showing a significant reduction in the expression of the B-2 and an increase in pro-apoptotic proteins such as BAX. Different death inducing and survival genes contribute to the control of the apoptosis process, and these genes are capable of regulating via internal or external signals (40). It is apparent that the combination of Met and DSF-Cu can induce apoptosis, led to the overexpression of BAX and P53, as well as the activation of CASPASE3 and decreasing the expression of BCL2. At the same time, in the presence of irradiation, these effects were amplified, and in comparison with the combinatory treatment, we can conclude that the combination of both drugs with irradiation can act as a radiosensitizer and induce apoptosis through the intrinsic pathway. The contradictory results obtained from other investigations may be due to discrepancies in the experimental conditions, diverse cell origin, and/or cell function and, empirical method models that need complementary investigations. It seems that the synergistic use of both drugs effectively stimulated the apoptotic pathways within the cells; however, we cannot rule out the involvement of other death pathways such as autophagy as they share common protein when activated in response to external and internal insults. Further studies are required to illuminate whether the induction of apoptosis is not the sole pathway for the efficacy of the combinatory treatment with Met and DSF-Cu.

Conclusion

Our findings showed that the combined treatment with Met and DSF-Cu with the support of radiation could be an advantageous method for the prevention of U87-MG cells

growth in comparison with treatment with Met, DSF-Cu or irradiation alone. The molecular mechanism of action can be related to the changes in the expression level of proteins and genes involved in the intrinsic pathway of apoptosis. This study is the first preclinical evidence evaluating the combined impact of Met and DSF-Cu with the aid of radiation on the growth of U87-MG cells as this approach increased the sensitivity of U87-MG cells to radiation. Altogether, these findings provide hope for the cure of GBM patients who are resistant to conventional therapies. Further investigations should be carried out to determine the precise mechanism of action and therapeutic potency of the combination of Met and DSF-Cu.

Acknowledgements

This work was financially supported under a research grant (number: 28594) provided by the Iran University of Medical Sciences. The authors declare no conflicts of interest.

Authors' Contributions

N.R., Z.M., F.K.; Conceived and designed the experiment, performed the experiments, analyzed the data, contributed to providing reagents/materials, prepared the figures and /or tables, and drafts of the manuscript. A.N.-R.; Was responsible for the overall supervision, contributed to design and implementation of study. M.H.; Was responsible for the pharmaceutical consulting, determined accuracy of drugs concentration. All authors read and approved the final manuscript.

References

1. Tanaka S, Louis DN, Curry WT, Batchelor TT, Dietrich J. Diagnostic and therapeutic avenues for glioblastoma: no longer a dead end? Nat Rev Clin Oncol. 2013; 10(1): 14-26.
2. Cloughesy TF, Cavenee WK, Mischel PS. Glioblastoma: from molecular pathology to targeted treatment. Annu Rev Pathol. 2014; 9: 1-25.
3. Stupp R, Mason WP, van den Bent MJ, Weller M, Fisher B, Taphoorn MJ, et al. Radiotherapy plus concomitant and adjuvant temozolomide for glioblastoma. N Engl J Med. 2005; 352(10): 987-996.
4. Nicholas MK, Lukas RV, Chmura S, Yamini B, Lesniak M, Pytel P, editors. Molecular heterogeneity in glioblastoma: therapeutic opportunities and challenges. Seminars in oncology; 2011: Elsevier.
5. Garber K. Cancer's copper connections. Science. 2015; 349(6244): 129.
6. Degterev A, Boyce M, Yuan J. A decade of caspases. Oncogene. 2003; 22(53): 8543-8567.
7. Watters D. Molecular mechanisms of ionizing radiation-induced apoptosis. Immunol Cell Biol. 1999; 77(3): 263-271.
8. Peña Blanco A, García Sáez AJ. Bax, Bak and beyond-mitochondrial performance in apoptosis. FEBS J. 2018; 285(3): 416-431.
9. Würth R, Barbieri F, Florio T. New molecules and old drugs as emerging approaches to selectively target human glioblastoma cancer stem cells. Biomed Res Int. 2014; 2014: 126586.
10. Johansson B. A review of the pharmacokinetics and pharmacodynamics of disulfiram and its metabolites. Acta Psychiatr Scand Suppl. 1992; 369: 15-26.
11. Cvek B. Targeting malignancies with disulfiram (Antabuse): multidrug resistance, angiogenesis, and proteasome. Curr Cancer Drug Targets. 2011; 11(3): 332-337.
12. Kast RE, Boockvar JA, Brüning A, Cappello F, Chang WW, Cvek B, et al. A conceptually new treatment approach for relapsed glioblastoma: coordinated undermining of survival paths with nine repurposed drugs (CUSP9) by the International Initiative for Accelerated Improvement of Glioblastoma Care. Oncotarget. 2013; 4(4): 502-530.
13. Huang J, Campian JL, Gujar AD, Tran DD, Lockhart AC, DeWees TA, et al. A phase I study to repurpose disulfiram in combination with temozolomide to treat newly diagnosed glioblastoma after chemoradiotherapy. J Neurooncol. 2016; 128(2): 259-266.
14. Zhao Y, Zhang E, Lv N, Ma L, Yao S, Yan M, et al. Metformin and FTY720 Synergistically induce apoptosis in multiple myeloma cells. Cell Physiol Biochem. 2018; 48(2): 785-800.
15. Pollak M. Potential applications for biguanides in oncology. J Clin Invest. 2013; 123(9): 3693-3700.
16. Pollak MN. Investigating metformin for cancer prevention and treatment: the end of the beginning. Cancer Discov. 2012; 2(9): 778-790.
17. Isakovic A, Harhaji L, Stevanovic D, Markovic Z, Sumarac-Dumanovic M, Starcevic V, et al. Dual antiglioma action of metformin: cell cycle arrest and mitochondria-dependent apoptosis. Cell Mol Life Sci. 2007; 64(10): 1290-1302.
18. Kalender A, Selvaraj A, Kim SY, Gulati P, Brûlé S, Viollet B, et al. Metformin, independent of AMPK ,inhibits mTORC1 in a rag GTPase-dependent manner. Cell Metab. 2010; 11(5): 390-401.
19. Esteva FJ, Moulder SL, Gonzalez-Angulo AM, Ensor J, Murray JL, Green MC, et al. Phase I trial of exemestane in combination with metformin and rosiglitazone in nondiabetic obese postmenopausal women with hormone receptor–positive metastatic breast cancer. Cancer Chemother Pharmacol. 2013; 71(1): 63-72.
20. MacKenzie MJ, Ernst S, Johnson C, Winquist E. A phase I study of temsirolimus and metformin in advanced solid tumours. Invest New Drugs. 2012; 30(2): 647-652.
21. Emami Riedmaier A, Fisel P, Nies AT, Schaeffeler E, Schwab M. Metformin and cancer: from the old medicine cabinet to pharmacological pitfalls and prospects. Trends Pharmacol Sci. 2013; 34(2): 126-135.
22. Wickström M, Danielsson K, Rickardson L, Gullbo J, Nygren P, Isaksson A, et al. Pharmacological profiling of disulfiram using human tumor cell lines and human tumor cells from patients. Biochem Pharmacol. 2007; 73(1): 25-33.
23. Feng Y, Ke C, Tang Q, Dong H, Zheng X, Lin W, et al. Metformin promotes autophagy and apoptosis in esophageal squamous cell carcinoma by downregulating Stat3 signaling. Cell Death Dis. 2014; 5: e1088.
24. Janjetovic K, Vucicevic L, Misirkic M, Vilimanovich U, Tovilovic G, Zogovic N, et al. Metformin reduces cisplatin-mediated apoptotic death of cancer cells through AMPK-independent activation of Akt. Eur J Pharmacol. 2011; 651(1-3): 41-50.
25. Jivan R, Damelin LH, Birkhead M, Rousseau AL, Veale RB, Mavri Damelin D. Disulfiram/copper disulfiram damages multiple protein degradation and turnover pathways and cytotoxicity is enhanced by metformin in oesophageal squamous cell carcinoma cell lines. J Cell Biochem. 2015; 116(10): 2334-2343.
26. Yip NC, Fombon IS, Liu P, Brown S, Kannappan V, Armesilla AL, et al. Disulfiram modulated ROS-MAPK and NFκB pathways and targeted breast cancer cells with cancer stem cell-like properties. Br J Cancer. 2011; 104(10): 1564-1574.
27. Sato A, Sunayama J, Okada M, Watanabe E, Seino S, Shibuya K, et al. Glioma Initiating cell elimination by metformin activation of FOXO3 via AMPK. Stem Cells Transl Med. 2012; 1(11): 811-824.
28. Rae C, Tesson M, Babich JW, Boyd M, Sorensen A, Mairs RJ. The role of copper in disulfiram-induced toxicity and radiosensitization of cancer cells. J Nucl Med. 2013; 54(6): 953-960.
29. Sesen J, Dahan P, Scotland SJ, Saland E, Dang VT, Lemarié A, et al. Metformin inhibits growth of human glioblastoma cells and enhances therapeutic response. PLoS One. 2015; 10(4): e0123721.
30. Zhu M, Zhang Q, Wang X, Kang L, Yang Y, Liu Y, et al. Metformin potentiates anti-tumor effect of resveratrol on pancreatic cancer by down-regulation of VEGF-B signaling pathway. On-

cotarget. 2016; 7(51): 84190-84200.
31. Chen X, Li C, He T, Mao J, Li C, Lyu J, et al. Metformin inhibits prostate cancer cell proliferation, migration, and tumor growth through upregulation of PEDF expression. Cancer Biol Ther. 2016; 17(5): 507-514.
32. Gao ZY, Liu Z, Bi MH, Zhang JJ, Han ZQ, Han X, et al. Metformin induces apoptosis via a mitochondria-mediated pathway in human breast cancer cells in vitro. Exp Ther Med. 2016; 11(5): 1700-1706.
33. Cen D, Brayton D, Shahandeh B, Meyskens FL Jr, Farmer PJ. Disulfiram facilitates intracellular Cu uptake and induces apoptosis in human melanoma cells. J Med Chem. 2004; 47(27): 6914-6920.
34. Yip NC, Fombon IS, Liu P, Brown S, Kannappan V, Armesilla AL, et al. Disulfiram modulated ROS–MAPK and NFκB pathways and targeted breast cancer cells with cancer stem cell-like properties. Br J Cancer. 2011; 104(10): 1564-1574.
35. Haji HA, Sheibak H, Khosravi M, Asadi J. The Effect of Metformin on the Expression of Caspase 3, 8, 9 and PARP-1 in Human Breast Cancer Cell Line T47D. International Journal of Health Studies. 2016; 2(2).
36. Feng Y, Xu X, Zhang Y, Ding J, Wang Y, Zhang X, et al. HPIP is upregulated in colorectal cancer and regulates colorectal cancer cell proliferation, apoptosis and invasion. Sci Rep. 2015; 5: 9429.
37. Willis SN, Adams JM. Life in the balance: how BH3-only proteins induce apoptosis. Curr Opin Cell Biol. 2005; 17(6): 617-625.
38. Zhang J, Yao T, Wang Y, Yu J, Liu Y, Lin Z. Long noncoding RNA MEG3 is downregulated in cervical cancer and affects cell proliferation and apoptosis by regulating miR-21. Cancer Biol Ther. 2016; 17(1): 104-113.
39. Dastjerdi MN, Babazadeh Z, Rabbani M, Gharagozloo M, Esmaeili A, Narimani M. Effects of disulfiram on apoptosis in PANC-1 human pancreatic cancer cell line. Res Pharm Sci. 2014; 9(4): 287-294.
40. Liu P, Kumar IS, Brown S, Kannappan V, Tawari PE, Tang JZ, et al. Disulfiram targets cancer stem-like cells and reverses resistance and cross-resistance in acquired paclitaxel-resistant triple-negative breast cancer cells. Br J Cancer. 2013; 109(7): 1876-1885.

Original Article

Cardiac Differentiation of Adipose Tissue-Derived Stem Cells Is Driven by BMP4 and bFGF but Counteracted by 5-Azacytidine and Valproic Acid

Sanaz Hasani, M.Sc.[1, 2], Arash Javeri, M.D., Ph.D.[1], Asadollah Asadi, Ph.D.[2], Masoumeh Fakhr Taha, Ph.D.[1]*

1. Department of Stem Cells and Regenerative Medicine, Institute for Medical Biotechnology, National Institute of Genetic Engineering and Biotechnology (NIGEB), Tehran, Iran
2. Department of Biology, Faculty of Science, University of Mohaghegh Ardabili, Ardabil, Iran

Corresponding Address: P.O.Box: 14965-161, Department of Stem Cells and Regenerative Medicine, Institute for Medical Biotechnology, National Institute of Genetic Engineering and Biotechnology (NIGEB), Tehran, Iran
Email: mftaha@nigeb.ac.ir

Received: 14/December/2018, Accepted: 14/July/2019

Abstract

Objective: Bone morphogenetic protein 4 (BMP4) and basic fibroblast growth factor (bFGF) play important roles in embryonic heart development. Also, two epigenetic modifying molecules, 5´-azacytidine (5´-Aza) and valproic acid (VPA) induce cardiomyogenesis in the infarcted heart. In this study, we first evaluated the role of BMP4 and bFGF in cardiac trans-differentiation and then the effectiveness of 5´-Aza and VPA in reprogramming and cardiac differentiation of human adipose tissue-derived stem cells (ADSCs).

Materials and Methods: In this experimental study, human ADSCs were isolated by collagenase I digestion. For cardiac differentiation, third to fifth-passaged ADSCs were treated with BMP4 alone or a combination of BMP4 and bFGF with or without 5´-Aza and VPA pre-treatment. After 21 days, the expression of cardiac-specific markers was evaluated by reverse transcription polymerase chain reaction (RT-PCR), quantitative real-time PCR, immunocytochemistry, flow cytometry and western blot analyses.

Results: BMP4 and more prominently a combination of BMP4 and bFGF induced cardiac differentiation of human ADSCs. Epigenetic modification of the ADSCs by 5´-Aza and VPA significantly upregulated the expression of OCT4A, *SOX2, NANOG, Brachyury/T* and *GATA4* but downregulated *GSC* and *NES* mRNAs. Furthermore, pre-treatment with 5´-Aza and VPA upregulated the expression of *TBX5, ANF, CX43* and *CXCR4* mRNAs in three-week differentiated ADSCs but downregulated the expression of some cardiac-specific genes and decreased the population of cardiac troponin I-expressing cells.

Conclusion: Our findings demonstrated the inductive role of BMP4 and especially BMP4 and bFGF combination in cardiac trans-differentiation of human ADSCs. Treatment with 5´-Aza and VPA reprogrammed ADSCs toward a more pluripotent state and increased tendency of the ADSCs for mesodermal differentiation. Although pre-treatment with 5´-Aza and VPA counteracted the cardiogenic effects of BMP4 and bFGF, it may be in favor of migration, engraftment and survival of the ADSCs after transplantation.

Keywords: Adipose Tissue-Derived Stem Cells, Basic Fibroblast Growth Factor, BMP4, Cardiomyocyte, Small Molecules

Cell Journal(Yakhteh), Vol 22, No 3, October-December (Autumn) 2020, Pages: 273-282

Citation: Hasani S, Javeri A, Asadi A, Taha MF. Cardiac differentiation of adipose tissue-derived stem cells is driven by BMP4 and bFGF but counteracted by 5-azacytidine and valproic acid. Cell J. 2020; 22(3): 273-282. doi: 10.22074/cellj.2020.6582.

Introduction

Cardiovascular diseases are the most common causes of deaths worldwide (1). Despite the great advances in medical and surgical therapies, functional recovery of the infarcted heart remains elusive. A novel strategy for the treatment of advanced myocardial infarction is transplantation of stem cells or stem cell-derived cardiac progenitor cells into the damaged heart with the expectation that these cells can produce or stimulate generation of new cardiomyocytes and blood vessels in the injured tissue (2).

Adipose tissue has been considered as a valuable source of autologous mesenchymal stem cells for heart tissue engineering and cardiac repair. Beneficial role of adipose tissue-derived stem cells (ADSCs) in regeneration of ischemic heart disease is emanated from several properties, including differentiation to cardiomyocytes, endothelial cells and smooth muscle cells (3, 4), secretion of several angiogenic and anti-apoptotic factors (3, 5) and recruitment of endogenous stem cells into the damaged area (6). Although accumulating evidence has shown the capability of ADSCs for differentiation into cardiomyocytes and improvement of ventricular function in animal models of myocardial infarction (7-9), a highly efficient protocol for cardiac differentiation of human ADSCs is yet to be reported. Further studies are required to develop optimal media formulations which generate a large number of functional cardiomyocytes for embryology, toxicology, pharmacology and transplantation therapy purposes. In this regard, better understanding of the role of cardiogenic growth factors and small molecules which can reprogram somatic cells toward a more undifferentiated state is of utmost importance.

Bone morphogenetic protein 4 (BMP4) and basic fibroblast growth factor (bFGF) signaling play important roles in embryonic heart development (10, 11). A combination of bFGF and BMP2/4 has been shown necessary to induce Nkx2.5 expression and contractile phenotype in non-precardiac mesoderm of chicken embryos (12). In fact, BMPs and FGFs have complementary roles in cardiac development; BMP induces the specification of non-precardiac mesoderm cells to cardiac cell lineage, while FGF supports terminal differentiation of cardiomyocytes (13, 14).

5′-azacytidine (5′-Aza) and valproic acid (VPA) are two small molecules which regulate chromatin remodeling through inhibition of DNA methyltransferases and histone deacetylases, respectively (14). The positive role of 5′-Aza and VPA in cardiac differentiation has been demonstrated by different groups (14-16), although contradictory results have also been reported (17, 18). In an attempt by Thal and colleagues (14), treatment of the endothelial progenitor cells with 5′-Aza and VPA significantly upregulated the expression of pluripotency and cardiac-specific genes and increased the cardiogenic potential of the reprogrammed cells. However, this should be kept in mind that reactivation of previously silent genes by epigenetic modifiers like 5′-Aza and VPA is not limited to pluripotency-associated or cardiac-specific genes but is rather indicative of a global gene transcription. So, an appropriate culture condition is necessary to direct the fate of reprogrammed cells towards a cardiogenic lineage (14).

Despite the available evidence demonstrating the inductive role of BMP4 and bFGF growth factors (10-12) as well as small molecules like 5′-Aza and VPA (14-16) in cardiac differentiation, there is no report regarding the impact of these factors on cardiac differentiation of hADSCs. We previously showed that BMP4 treatment induces the expression of cardiac-specific markers in mouse ADSCs (19). In the current study, we first evaluated the role of BMP4 individually, and then in combination with bFGF in cardiac trans-differentiation of human ADSCs and finally examined the impact of 5′-Aza and VPA on reprogramming and cardiac differentiation of the ADSCs.

Materials and Methods

Isolation and culture of human adipose tissue-derived stem cells

In this experimental study, adipose tissue samples were harvested from five 40-45 years old women undergoing elective abdominoplasty after obtaining informed consent. The study was approved by the Ethics Committee of National Institute of Genetic Engineering and Biotechnology (7-8-93/NIGEB).

Isolation and characterization of the ADSCs was performed as described previously (20). Briefly, adipose tissue was minced and digested by 2 mg/ml collagenase I (Thermo Fisher Scientific, USA) in PBS containing 2% bovine serum albumin (BSA, Sigma Aldrich, USA). The stromal vascular fraction (SVF) was plated at 5×10^4 cells/ml in tissue culture flasks. Growth medium contained Dulbecco's Modified Eagle's Medium (DMEM), 20% fetal bovine serum (FBS), 100 U/ml penicillin and 100 µg/ml streptomycin (all from Gibco, Thermo Fisher Scientific, USA). Medium was changed every other day, and the cells were subcultured after reaching 80-90% confluency.

Cardiac differentiation of human adipose tissue-derived stem cells

For cardiac differentiation, third to fifth-passaged ADSC were seeded into 0.1% gelatin-coated 6-well tissue culture plates with a density of 10^5 cell/ml (2 ml per each well). After 24 hours, the cells were induced for cardiac differentiation with 10 ng/ml bFGF (Sigma-Aldrich, USA) and 20 ng/ml BMP4 (Thermo Fisher Scientific, USA) for four days. After the induction stage, growth factors were omitted completely and differentiation of the cells was continued in 10% FBS-containing medium up to three weeks. The ADSCs that were cultured in the same medium without bFGF and BMP4 treatment were used as the control group.

To investigate the impact of DNA methyltransferase and histone deacetylase inhibitors on cardiac differentiation of ADSCs, the cells were pre-treated with 10 µM 5′-Azacitidine (Sigma-Aldrich, USA) and 500 nM VPA (Sigma-Aldrich, USA) for 24 hours and then were treated with 10 ng/ml bFGF and 20 ng/ml BMP4 as described above.

Gene expression analysis

Total RNAs were extracted from three-week differentiated ADSCs using High Pure RNA Isolation Kit (Roche Applied Science, Germany). Briefly, cDNA was synthesized from 1 µg of total RNA using cDNA Synthesis Kit (Thermo Fisher Scientific, USA). PCR amplification on the cDNA samples was performed using PCR master mix (Ampliqon, Denmark) and specific primers, as described in Table S1 (See Supplementary Online Information at www.celljournal.org).

RealQ PCR Master (Ampliqon, Denmark) were used for quantitative assessment of gene expression by real-time polymerase chain reaction (qPCR) on a Rotor-Gene™ 6000 (Corbett Research, Australia) real-time analyzer. β2 microglobulin (*B2M*) and β-actin (*ACTB*) were used as the internal reference genes. The size of the qPCR products were assessed both by melting

curve analysis and also by agarose gel electrophoresis.

Comparative quantification was performed using REST 2009 (Relative Expression Software Tool, Qiagen) based on Pair Wise Fixed Reallocation Randomization Test® (21). At least, three biological replicates of each group were included in the qPCR experiments, and *B2M* and *ACTB* were used to normalize the quantitative data.

Immunocytochemistry

Since cell density of three-week differentiated ADSCs was too high, the cells were dissociated using trypsin-EDTA (Gibco, USA) and cultured at half the density in gelatin-coated 4-well tissue culture plates. After 24 hours, the cells were fixed using 4% paraformaldehyde and permeabilized with 0.2% Triton X-100. 10% goat serum was used to block non-specific binding sites. Next, the cells were incubated with the primary monoclonal antibodies against α-actinin (Sigma-Aldrich, USA) and cardiac troponin I (Santa Cruz Biotechnology, USA) and then with goat anti-mouse FITC-conjugated IgG (Sigma-Aldrich, USA). The stained cells were observed by a fluorescence microscope (Nikon, Japan).

Flow cytometry analysis

Three-week differentiated cells were dissociated using trypsin-EDTA and fixed in cold 70% ethanol. The cells were permeabilized with 0.2% Triton X-100. After washing, the cells were incubated with the primary antibody against cardiac troponin I (Santa Cruz Biotechnology, USA) and then with fluorescein isothiocyanate (FITC)-conjugated goat anti-mouse IgG (Sigma-Aldrich, USA). Some cells were only stained with the secondary antibody and were used as the negative control. Flow cytometry was performed using an Attune® Acoustic Focusing Cytometer (Applied Biosystems, Thermo Fisher Scientific, USA). FlowJo vX.0.6 software (Tree Star Inc., Ashland, USA) was used for analysis of the results.

Western blot analysis

For protein analysis by western blot, three-week differentiated ADSCs were homogenized in ice-cold Radioimmunopercipitation assay (RIPA) lysis buffer and were centrifuged at 13000 g for 15 minutes at 4˚C. After collecting the supernatant, protein concentration was determined by Bradford assay. For each sample, 50 µg of protein was separated using sodium dodecyl sulphate-polyacrylamide gel electrophoresis (SDS-PAGE) and transferred to polyvinylidene difluoride (PVDF, Roche) membranes. Blocking of non-specific binding sites was achieved by 5% non-fat dried milk in Tris-buffered saline containing 0.1% Tween-20 (TBST). After blocking, the membranes were incubated with the diluted primary antibodies against glyceraldehyde 3-phosphate dehydrogenase (GAPDH, Sigma-Aldrich, G8795), α-actinin (Sigma-Aldrich, USA), desmin (Sigma-Aldrich, USA) and connexion 43 (Sigma-Aldrich, USA) overnight at 4˚C. Then, the membranes were incubated with goat anti-mouse horseradish peroxidase (HRP)-conjugated secondary IgG for 1 hour at room temperature. Enhanced chemiluminescence (ECL) kit (Najm Biotech Co., Iran) was used to detect the immunoreactive bands.

Results

Isolation, culture and differentiation of human adipose tissue-derived stem cells

Within 3-4 hours, the ADSCs attached to the growth surfaces of tissue culture plates. The ADSCs proliferated rapidly and were passaged 2-3 times a week. The undifferentiated cells showed a fibroblast-like morphology (Fig.1A). The mesenchymal stem cell feature and multipotential differentiation capability of the ADSCs was determined as described previously by our team (20, 22, 23). Third-passaged ADSCs expressed cardiac transcription factors, *GATA4*, *MEF2C* and *TBX5*, and cardiac-specific genes, *MLC2A*/*MYL7* and *MLC2V*/*MYL2* (Fig.1B) which possibly indicate the capability of these cells for cardiac differentiation.

After three weeks cardiac differentiation in different experimental groups, including control (no treatment, Fig.1C), BMP4 alone (Fig.1D) and a combination of bFGF and BMP4 with or without pre-treatment with 5-Aza and VPA (Fig.1E, F, respectively), differentiating ADSCs showed an elongated morphology.

BMP4 induces cardiac trans-differentiation of human adipose tissue-derived stem cells

We previously showed that BMP4 induces the expression of cardiac-specific genes in mouse ADSCs (19). In the current study, treatment of human ADSCs with 20 ng/ml BMP4 upregulated the expression of *GATA4*, *TBX5*, *MEF2C*, *MLC2A* and *MLC2V* mRNAs by 4.31, 1.88, 1.63, 2.03 and 3.4 folds compared to the control group, respectively (Fig.2A).

A combination of BMP4 and bFGF augments cardiac trans-differentiation of human ADSCs

To investigate the synergistic effect of BMP4 and bFGF in cardiac differentiation of human ADSCs, third to fifth-passaged ADSCs were simultaneously treated with 10 ng/ml bFGF and 20 ng/ml BMP4 for the first four days of differentiation. The expression levels of *GATA4*, *MEF2C*, *MLC2A* and *MLC2V* mRNAs were upregulated respectively by 10.46, 2.09, 4.16 and 4.21 folds in the BMP4 and bFGF combination treatment group compared to the BMP4 treatment alone (Fig.2B).

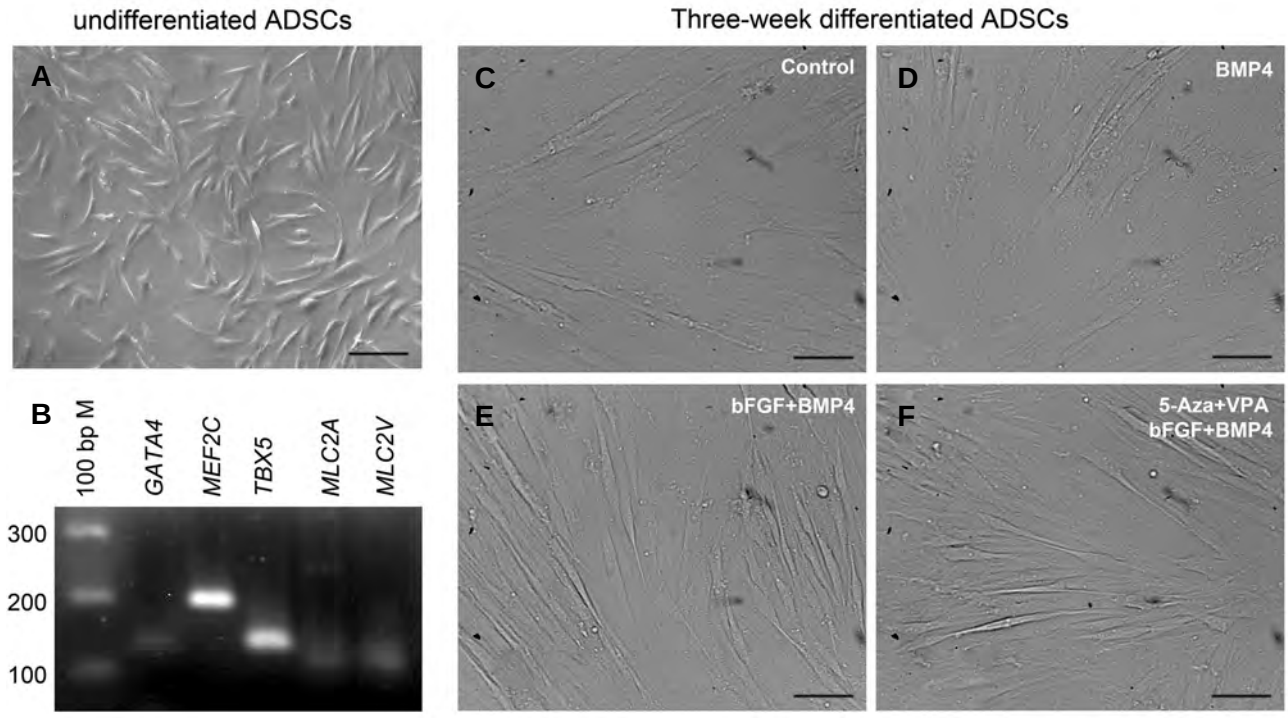

Fig.1: The undifferentiated and three-week differentiated ADSCs. **A.** Third-passaged ADSCs showed a fibroblast-like morphology, **B.** Expressed some cardiac-specific genes, **C.** After cardiac differentiation in the control (no treatment), **D.** BMP4 alone, **E,** and **F.** A combination of bFGF and BMP4 with or without pre-treatment with 5-Aza and VPA, differentiating ADSCs showed an elongated morphology (scale bar: 50 µm). ADSCs; Adipose tissue-derived stem cells, BMP4; Bone morphogenetic protein 4, bFGF; basic fibroblast growth factor, 5´-Aza; 5´-azacytidine, and VPA; Valproic acid (scale bar: 50 µm).

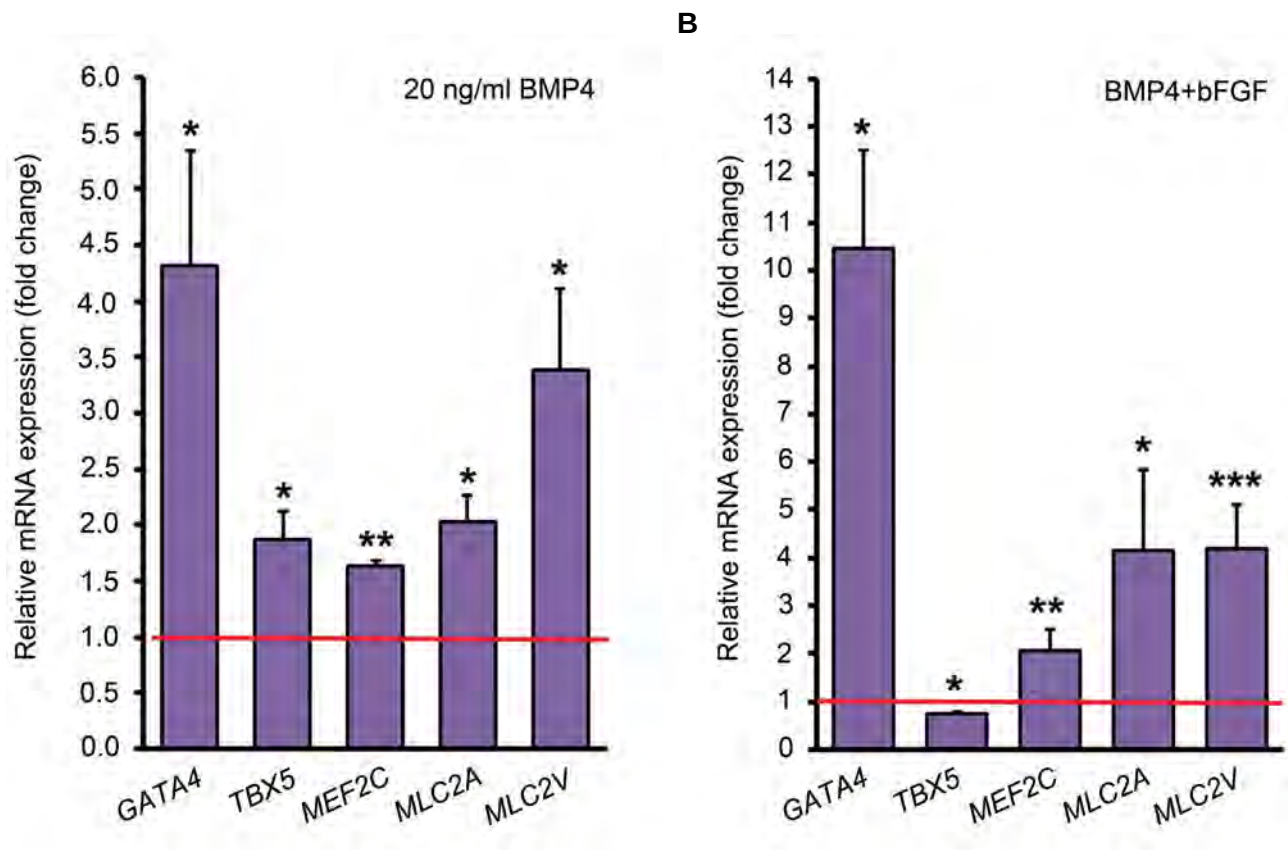

Fig.2: Quantitative analysis of some cardiac-specific genes by comparative method. **A.** The expression level of each gene in the control group (untreated ADSCs) has been assumed 1 (indicated by the red line) and its expression in BMP4 treatment group was compared to that and **B.** The expression level of each gene in the BMP4 treatment group has been assumed 1 (indicated by the red line) and its expression in BMP4 plus bFGF treatment group was compared to that. *; P<0.05, **; P<0.01, ***; P<0.001 (Pair Wise Fixed Reallocation Randomization Test® performed by REST 2009 software), ADSCs; Adipose tissue-derived stem cells, BMP4; Bone morphogenetic protein 4, and bFGF; Basic fibroblast growth factor.

Treatment of the ADSCs with 5′-Aza and VPA upregulated the expression of some pluripotency and mesodermal genes

24 hours treatment of the undifferentiated ADSCs with 5′-Aza and VPA upregulated the expression of *OCT4A*, *SOX2* and *NANOG* by 1.69 (P=0.009), 1.6 (P=0.015) and 1.93 folds (P=0.029), respectively. Goosecoid (*GSC*) and Nestin (*NES*) were downregulated by half after 5′-Aza and VPA treatment. *Brachyury*/*T* and *GATA4* expression in the ADSCs treated with 5′-Aza and VPA were respectively 18.33 folds and 1.95 folds higher than the untreated ADSCs, while the expression of *MEF2C* and *TBX5* was not changed significantly (Fig.3).

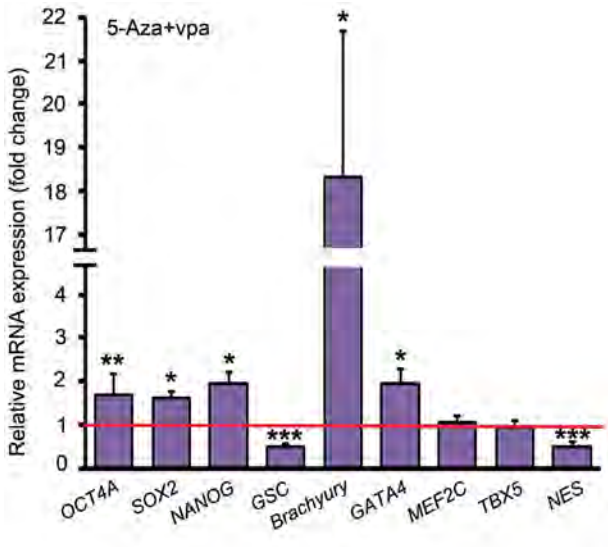

Fig.3: Quantitative analysis of some genes involved in the maintenance of pluripotency or early development by comparative method; the expression level of each gene in the control ADSCs has been assumed 1 (indicated by the red line) and its expression in the ADSCs treated with 5′-Aza and VPA was compared to that. *; P<0.05, **; P<0.01, ***; P<0.001 (Pair Wise Fixed Reallocation Randomization Test® performed by REST 2009 software), ADSCs; Adipose tissue-derived stem cells, 5´-Aza; 5´-azacytidine, and VPA; Valproic acid.

Pre-treatment with 5′-Aza and VPA affected cardiac differentiation of human ADSCs

To elucidate the influence of DNA methyltransferase and histone deacetylase inhibitors on cardiac differentiation of human ADSCs, the cells were pre-treated with 10 µM 5′-Aza and 0.5 µM VPA for 24 hours and then were induced with 10 ng/ml bFGF and 20 ng/ml BMP4 in 10% FBS-containing medium. As revealed by qPCR analysis, pre-treatment with 5′-Aza and VPA downregulated the expression of *GATA4*, *MEF2C*, *MLC2A* and *MLC2V* by mean factors of 0.5, 0.35, 0.34 and 0.66, respectively. However, *TBX5*, *ANF*, *CX43* and *CXCR4* were upregulated after pre-treatment with 5-Aza and VPA by 1.3, 5.4, 1.94 and 2.6 folds, respectively (Fig.4).

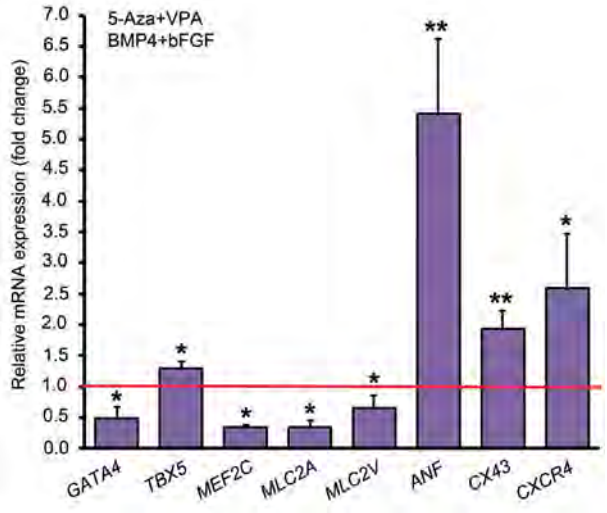

Fig.4: Quantitative analysis of some cardiac-specific genes by comparative method. The expression of each gene in the group with BMP4 and bFGF treatment but without 5-Aza and VPA pre-treatment has been assumed 1 (indicated by the red line) and gene expression levels in the group with 5-Aza and VPA pre-treatment was compared to that. *; P<0.05, **; P<0.01 (Pair Wise Fixed Reallocation Randomization Test® performed by REST 2009 software). BMP4; Bone morphogenetic protein 4, bFGF; basic fibroblast growth factor, 5´-Aza; 5´-azacytidine, and VPA; Valproic acid.

Protein expression analysis

BMP4 treatment group and the groups which received a combination of BMP4 and bFGF with or without 5′-Aza and VPA pre-treatment were assessed for the expression of α-actinin and cardiac troponin I as two cardiac-specific proteins. As revealed by immunocytochemistry, after trypsinization and re-plating the differentiated cells, ADSC-derived cardiomyocyte-like cells tend to form aggregations which showed positive immunostaining for α-actinin (Fig.5A-F) and cardiac troponin I (Fig.5G-L) proteins.

Western blot analysis demonstrated the expression of α-actinin, desmin and connexin 43 proteins in the differentiated cells. α-actinin and connexin 43 showed their maximum expression in the cells pre-treated with 5-Aza and VPA and followed by BMP4 and bFGF treatment (Fig.6A). Based on flow cytometry analysis, about 21% of the cells in the BMP4 treatment group, 39% of the cells which treated with BMP4 and bFGF combination without 5-Aza and VPA pre-treatment and 18% of the cells pre-treated with 5-Aza and VPA and induced with BMP4 and bFGF combination showed positive staining for cardiac troponin I protein. In the control group, about 1.5% of the cells expressed cardiac troponin I protein (Fig.6B).

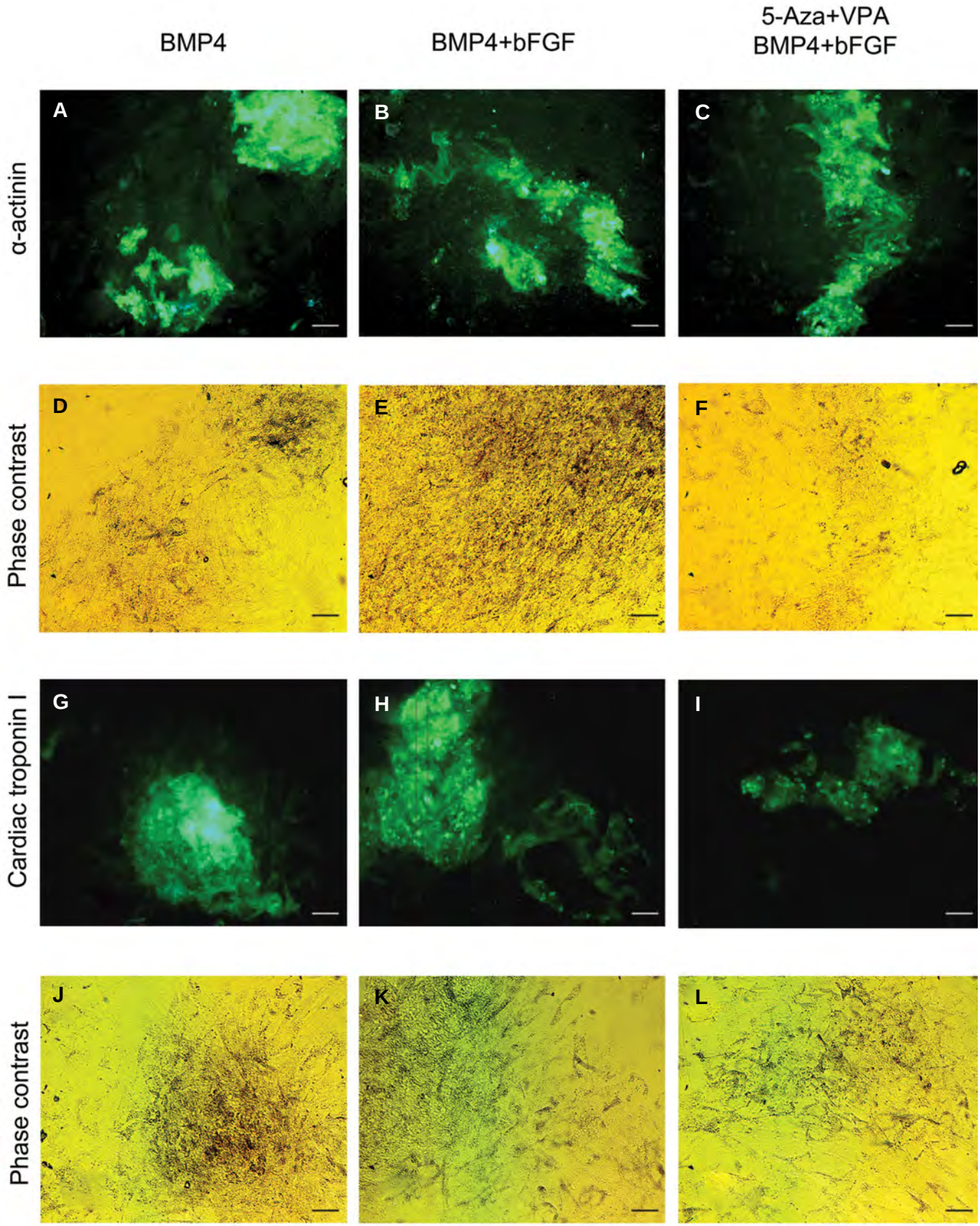

Fig.5: Immunocytochemical staining of three-week differentiated ADSCs. **A-C.** Immunostaining for α-actinin in the BMP4 treatment group and the groups which received a combination of BMP4 and bFGF with or without 5′-Aza and VPA pre-treatment, **D-F.** Phase contrast images of A to C, respectively, **G-I.** Immunostaining for cardiac troponin I in the BMP4 treatment group and the groups which received a combination of BMP4 and bFGF with or without 5′-Aza and VPA pre-treatment, and **J-L.** Phase contrast images of G to I, respectively (scale bar: 50 µm).

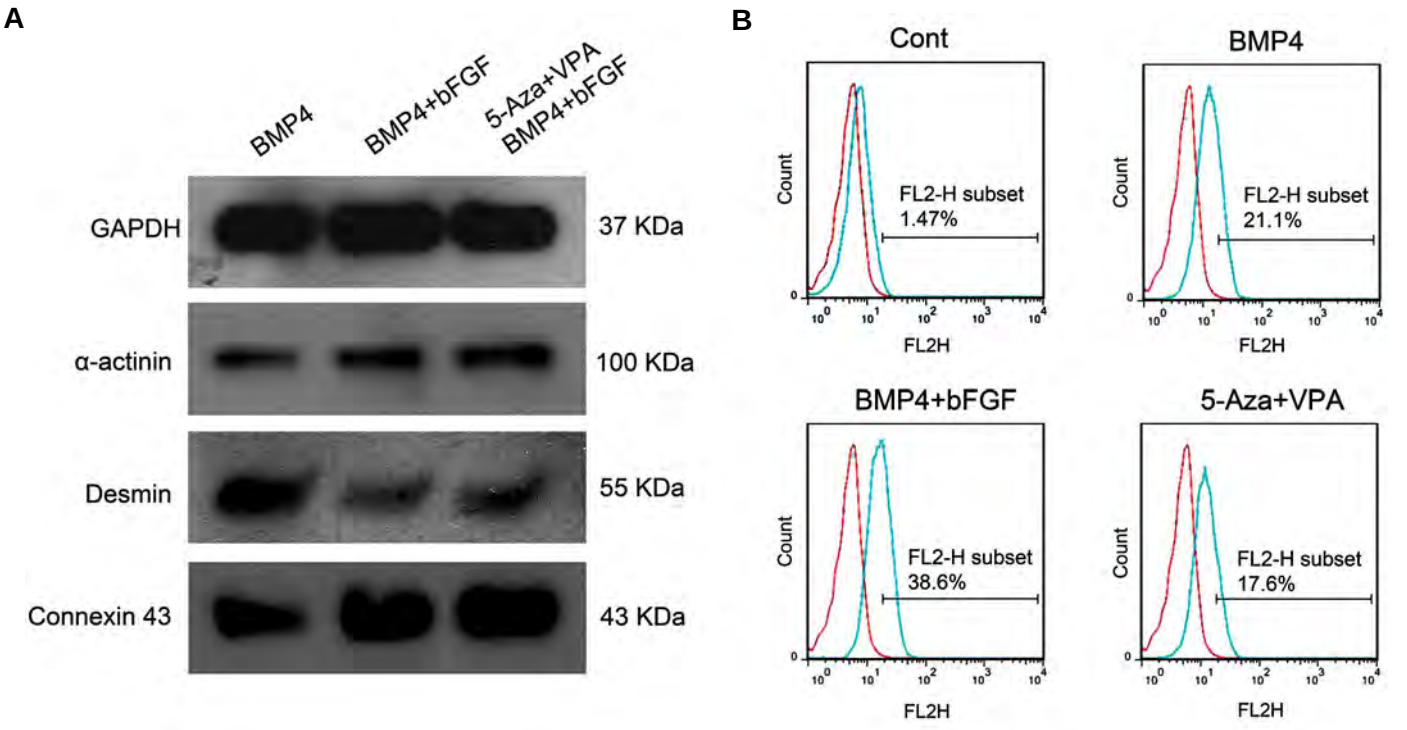

Fig.6: Western blot and flow cytometry analyses. **A.** Western blot analysis for the expression of α-actinin, desmin and connexin 43 proteins and **B.** Flow cytometry analysis for the expression of cardiac troponin I protein in three-week differentiated ADSCs of the control group, BMP4 treatment group and the groups which received a combination of BMP4 and bFGF with or without 5′-Aza and VPA pre-treatment. ADSCs; Adipose tissue-derived stem cells, BMP4; Bone morphogenetic protein 4, bFGF; basic fibroblast growth factor, 5′-Aza; 5′-azacytidine, and VPA; Valproic acid.

Discussion

In the current study, we first examined the influence of BMP4 on cardiomyocyte trans-differentiation of human ADCSs. BMPs are members of TGFβ superfamily with essential roles in both mesoderm induction and embryonic heart development (11). While increasing evidence support the inductive role of BMPs in cardiac differentiation, some studies point to the temporally and spatially regulated expression of BMPs and BMP antagonists during heart development (24). BMP2 and BMP4 inhibit cardiomyogenesis during gastrula stage of chicken embryos (25). In mouse, noggin show a transient but strong expression in the anterolateral plate mesoderm and has a critical role in cardiac differentiation (26). Similar contradictory results have been obtained during cardiac differentiation of embryonic and adult stem cells. As reported by Yuasa et al. (26), inhibition of BMP signalling in a period between the undifferentiated state and early phase of embryoid body formation increases the incidence of beating EBs and the expression of cardiac transcription factors. We showed previously that BMP4 treatment inhibits cardiac differentiation of mouse embryonic stem cells (ESCs) in serum-containing media (27), although the complete removal of serum is not in favour of cardiomyocyte development (28). Some other investigators have demonstrated the inductive role of BMP4 in cardiac differentiation of human ESCs in a serum-based condition (29). Treatment of human bone marrow-derived mesenchymal stem cells (BM-MSCs) with BMP4 shifts the fate of cells toward a cardiac phenotype rather than the skeletal-like myocytes (30). We previously showed that BMP4 treatment of mouse ADSCs, especially in a knockout serum replacement (KoSR)-containing medium, induces the expression of cardiac-specific markers (19). In the current study, we examined the effect of BMP4 on cardiac differentiation of human ADSCs and showed that treatment of the ADSCs with 20 ng/ml BMP4 increases the expression of *GATA4*, *MEF2C*, *TBX5*, *MLC2A* and *MLC2V* mRNAs.

bFGF is a paracrine FGF with significant roles in development and pathophysiology of the heart (10). Barron et al. (12) showed that treatment of non-precardiac mesoderm of stage 6 chicken embryos with a combination of bFGF and BMP2/4 is necessary to induce Nkx2.5 expression and to promote contractile phenotype. In fact, both BMPs and FGFs act as cardiac specification factors; BMP specifies non-precardiac mesoderm cells to cardiac lineage (12), while FGF functions as a survival factor and supports their terminal differentiation (13). Here we examined the role of bFGF-BMP4 combination in cardiac differentiation of human ADSCs and showed that except for *TBX5* all tested cardiac markers, including *GATA4*, *MEF2C*, *MLC2A* and *MLC2V* mRNAs and CX43 and α-actinin proteins, were upregulated. Also, combined application of bFGF-BMP4 increased the population of cardiac troponin I-expressing cells to about 37% compared to 21% in BMP4 treatment alone.

In this study, *TBX5* was downregulated in the ADSCs treated with bFGF-BMP4 combination compared to BMP4

alone. In human, *TBX5* transcription factor is expressed in all developing heart chambers, but its expression in the atria is significantly higher than the ventricles (31). Also, ventricular expression of *TBX5* decreases at late embryonic stage and after birth (32). The known target genes for *TBX5* are atrial natriuretic factor (ANF) and connexin 40 (CX40) which are normally expressed in the atria and trabeculae (33). Therefore, lower expression of *TBX5* in the cells treated with bFGF-BMP4 combination than the BMP4-treated cells may be due to a reduction in atrial specification of myocytes.

Previous human clinical trials demonstrate the safety and efficacy of ADSCs for regeneration of myocardial infarction (34). However, a significant portion of this reparative function is emanated from secretion of several angiogenic and anti-apoptotic factors (3, 5) and recruitment of endogenous stem cells into the injury site (6). ADSCs rarely differentiate into cardiomyocytes *in vivo* (35), and even when collected from aged patients, they have a diminished capability for proliferation and differentiation (36). Epigenetic modification of ADSCs by small molecules may reprogram ADSCs towards a more pluripotent state, enhance their functional properties and improve their functionality after transplantation. In this study, we examined effectiveness of two epigenetic modifying molecules, 5′-Aza and VPA, for reprogramming of human ADSCs towards a more undifferentiated state. 5′-Aza and VPA, which are inhibitors of DNA methyltransferases and histone deacetylases respectively, have been used in generation of induced pluripotent stem cells (iPSCs) to improve reprogramming efficiency (37).

24 hours treatment of the undifferentiated ADSCs with a combination of 5′-Aza and VPA upregulated the expression of some pluripotency transcription factors, including *OCT4A*, *SOX2* and *NANOG*. Also, treatment of the ADSCs with 5′-Aza and VPA resulted in downregulation of definitive endoderm marker *GSC* and early neuroectoderm marker *NES*, and upregulation of mesendodermal marker *Brachyury/T* and cardiac transcription factor *GATA4*. Altogether, these findings suggest a delicate alteration in gene expression profile of the ADSCs and tendency of the reprogrammed cells for differentiation towards mesodermal lineages.

We assessed the influence of 5′-Aza and VPA on cardiac differentiation of human ADSCs. It has been shown that both chemical factors remodel chromatin to allow expression of transcriptionally inactivated genes and to induce differentiation toward cardiomyocytes (15, 16). In 2012, Thal et al. (14) showed that epigenetic reprogramming of endothelial progenitor cells with 5′-Aza and VPA improves repair of infarcted hearts by both cardiomyogenesis and vascularization. In contrast, we showed here that pre-treatment with a combination of 5′-Aza and VPA downregulated the expression of *GATA4*, *MEF2C*, *MLC2A* and *MLC2V* which indicates the suppressive impact of these combination on cardiac differentiation of human ADSCs. Flow cytometry analysis for cardiac troponin I protein supports this conclusion since the population of immunostained cells decreased from 39% in the group which only received BMP4 and bFGF combination to about 18% in the BMP4 and bFGF combination group with 5′-Aza and VPA pre-treatment. Of course, these findings do not contradict the stimulatory role of 5′-Aza and VPA on cardiac differentiation and may just reflect the consequence of using these two agents at the same time. Perhaps, if the cells were initially treated with VPA for 24 hours and then with 5′-Aza for 24 hours, as shown by Thal et al. (14), this might have a positive effect on cardiac differentiation. The other concentrations of these two small molecules can also be tested. However, pre-treatment with 5′-Aza and VPA upregulated the expression of *TBX5*, *ANF* and *CX43* mRNAs and CX43 and α-actinin proteins. The reason for this discrepancy in the expression of cardiac-specific genes is not clear, but it is interesting to note that not only the expression of *ANF* is regulated by *TBX5* (33) but also *CX43* has been identified as a target for *TBX* factors (38). So, the simultaneous increase in the expression of these three genes is not far from the mind. Altogether, the upregulated expression of *TBX5* and *ANF* genes may be due to an increased differentiation of atrial myocytes after 5′-Aza and VPA pre-treatment. On the other hand, previous studies have demonstrated that *CX43* increases the survival of MSCs after transplantation into the ischemic heart and so may improve therapeutic efficacy of transplanted cells (9).

Stromal cell-derived factor (SDF)-1 and its membrane receptor, CXCR4, play pivotal roles in the migration, homing and engraftment of multiple stem cell types. At the injury site, SDF-1 expression increases and recruits circulating CXCR4-expressing MSC. Strategies to induce CXCR4 upregulation increases the migration and engraftment of MSCs *in vivo* (39). In the present study, pre-treatment with a combination of 5′-Aza and VPA significantly upregulated the expression of CXCR4 in the ADSCs. This finding is in agreement with previous studies showing that 5-Aza and VPA significantly increase *CXCR4* expression in other types of stem cells (40).

Conclusion

Our findings demonstrated that cardiac differentiation of human ADSCs can be induced by BMP4 but more significantly by a combination of BMP4 and bFGF. Treatment of the ADSCs with a combination of 5′-Aza and VPA, which are respectively DNA methyltransferase and histone deacetylase inhibitors, significantly upregulated the expression of pluripotency transcription factors which indicates reprogramming of the ADSCs towards a more undifferentiated state. Downregulation of *GSC* and *NES* and upregulation of Brachyury/*T* and *GATA4* mRNAs in the ADSCs treated with 5′-Aza and VPA suggests improved potential of the reprogrammed cells for mesodermal differentiation. However, pre-treatment with 5′-Aza and VPA compromised the cardiogenic effects of BMP4 and bFGF which was determined by downregulation of some cardiac-specific genes and a decrease in the population of cardiac troponin I-expressing cells. Nevertheless,

5′-Aza and VPA upregulated the expression of *TBX5*, *ANF*, *CX43* and *CXCR4* mRNAs which may improve migration, engraftment and survival of the ADSCs after transplantation into the injury site.

Acknowledgements

There is no financial support and conflict of interest in this study.

Authors' Contributions

S.H.; Performed the experiments and wrote the draft. A.J.; Performed gene expression and flow cytometry analyses and contributed to editing and approving the manuscript for submission. A.A.; Contributed to the project as co-supervisor and participated in drafting. M.F.T.; Designed the study, supervised the project, performed western blot analysis and edited and approved the final version of manuscript for submission. All authors read and approved the final manuscript.

References

1. Benjamin EJ, Virani SS, Callaway CW, Chamberlain AM, Chang AR, Cheng S, et al. Heart disease and stroke statistics-2018 update: a report from the american heart association. Circulation. 2018; 137(12): e67-e492.
2. Michler RE. Stem cell therapy for heart failure. Methodist Debakey Cardiovasc J. 2013; 9(4): 187-194.
3. Miranville A, Heeschen C, Sengenès C, Curat CA, Busse R, Bouloumié A. Improvement of postnatal neovascularization by human adipose tissue-derived stem cells. Circulation. 2004; 110(3): 349-355.
4. Miyahara Y, Nagaya N, Kataoka M, Yanagawa B, Tanaka K, Hao H, et al. Monolayered mesenchymal stem cells repair scarred myocardium after myocardial infarction. Nat Med. 2006; 12(4): 459-465.
5. Rehman J, Traktuev D, Li J, Merfeld-Clauss S, Temm-Grove CJ, Bovenkerk JE, et al. Secretion of angiogenic and antiapoptotic factors by human adipose stromal cells. Circulation. 2004; 109(10): 1292-1298.
6. Gimble JM, Katz AJ, Bunnell BA. Adipose-derived stem cells for regenerative medicine. Circ Res. 2007; 100(9): 1249-1260.
7. He Y, Guo Y, Xia Y, Guo Y, Wang R, Zhang F, et al. Resistin promotes cardiac homing of mesenchymal stem cells and functional recovery after myocardial ischemia/reperfusion via the ERK1/2-MMP-9 pathway. Am J Physiol Heart Circ Physiol. 2019; 316(1): H233-H244.
8. Valina C, Pinkernell K, Song YH, Bai X, Sadat S, Campeau RJ, et al. Intracoronary administration of autologous adipose tissue-derived stem cells improves left ventricular function, perfusion, and remodelling after acute myocardial infarction. Eur Heart J. 2007; 28(21): 2667-2677.
9. Wang D, Shen W, Zhang F, Chen M, Chen H, Cao K. Connexin43 promotes survival of mesenchymal stem cells in ischaemic heart. Cell Biol Int. 2010; 34(4): 415-423.
10. Itoh N, Ohta H, Nakayama Y, Konishi M. Roles of FGF signals in heart development, health, and disease. Front Cell Dev Biol. 2016; 4: 110.
11. van Wijk B, Moorman AF, van den Hoff MJ. Role of bone morphogenetic proteins in cardiac differentiation. Cardiovasc Res. 2007; 74(2): 244-255.
12. Barron M, Gao M, Lough J. Requirement for BMP and FGF signaling during cardiogenic induction in non-precardiac mesoderm is specific, transient, and cooperative. Dev Dyn. 2000; 218(2): 383-393.
13. Sugi Y, Lough J. Activin-A and FGF-2 mimic the inductive effects of anterior endoderm on terminal cardiac myogenesis in vitro. Dev Biol. 1995; 168(2): 567-574.
14. Thal MA, Krishnamurthy P, Mackie AR, Hoxha E, Lambers E, Verma S, et al. Enhanced angiogenic and cardiomyocyte differentiation capacity of epigenetically reprogrammed mouse and human endothelial progenitor cells augments their efficacy for ischemic myocardial repair. Circ Res. 2012; 111(2): 180-190.
15. Burlacu A, Rosca AM, Maniu H, Titorencu I, Dragan E, Jinga V, et al. Promoting effect of 5-azacytidine on the myogenic differentiation of bone marrow stromal cells. Eur J Cell Biol. 2008; 87(3): 173-184.
16. Morez C, Noseda M, Paiva MA, Belian E, Schneider MD, Stevens MM. Enhanced efficiency of genetic programming toward cardiomyocyte creation through topographical cues. Biomaterials. 2015; 70: 94-104.
17. Na L, Wartenberg M, Nau H, Hescheler J, Sauer H. Anticonvulsant valproic acid inhibits cardiomyocyte differentiation of embryonic stem cells by increasing intracellular levels of reactive oxygen species. Birth Defects Res A Clin Mol Teratol. 2003; 67(3): 174-180.
18. Liu Y, Song J, Liu W, Wan Y, Chen X, Hu C. Growth and differentiation of rat bone marrow stromal cells: does 5-azacytidine trigger their cardiomyogenic differentiation? Cardiovasc Res. 2003; 58(2): 460-468.
19. Khaleghi M, Taha MF, Jafarzadeh N, Javeri A. Atrial and ventricular specification of ADSCs is stimulated by different doses of BMP4. Biotechnol Lett. 2014; 36(12): 2581-2589.
20. Faghih H, Javeri A, Taha MF. Impact of early subcultures on stemness, migration and angiogenic potential of adipose tissue-derived stem cells and their resistance to in vitro ischemic condition. Cytotechnology. 2017; 69(6): 885-900.
21. Pfaffl MW, Horgan GW, Dempfle L. Relative expression software tool (REST) for group-wise comparison and statistical analysis of relative expression results in real-time PCR. Nucleic Acids Res. 2002; 30(9): e36.
22. Salehi PM, Foroutan T, Javeri A, Taha MF. Extract of mouse embryonic stem cells induces the expression of pluripotency genes in human adipose tissue-derived stem cells. Iran J Basic Med Sci. 2017; 20(11): 1200-1206.
23. Soheilifar MH, Javeri A, Amini H, Taha MF. Generation of dopamine-secreting cells from human adipose tissue-derived stem cells in vitro. Rejuvenation Res. 2018; 21(4): 360-368.
24. Yuasa S, Fukuda K. Multiple roles for BMP signaling in cardiac development. Drug Discovery Today: Therapeutic Strategies. 2009; 5(4): 209-214.
25. Ladd AN, Yatskievych TA, Antin PB. Regulation of avian cardiac myogenesis by activin/TGFbeta and bone morphogenetic proteins. Dev Biol. 1998; 204(2): 407-419.
26. Yuasa S, Itabashi Y, Koshimizu U, Tanaka T, Sugimura K, Kinoshita M, et al. Transient inhibition of BMP signaling by Noggin induces cardiomyocyte differentiation of mouse embryonic stem cells. Nat Biotechnol. 2005; 23(5): 607-611.
27. Taha MF, Valojerdi MR, Mowla SJ. Effect of bone morphogenetic protein-4 (BMP-4) on cardiomyocyte differentiation from mouse embryonic stem cell. Int J Cardiol. 2007; 120(1): 92-101.
28. Taha MF, Valojerdi MR. Effect of bone morphogenetic protein-4 on cardiac differentiation from mouse embryonic stem cells in serum-free and low-serum media. Int J Cardiol. 2008; 127(1): 78-87.
29. Takei S, Ichikawa H, Johkura K, Mogi A, No H, Yoshie S, et al. Bone morphogenetic protein-4 promotes induction of cardiomyocytes from human embryonic stem cells in serum-based embryoid body development. Am J Physiol Heart Circ Physiol. 2009; 296(6): H1793-H1803.
30. Grajales L, García J, Geenen DL. Induction of cardiac myogenic lineage development differs between mesenchymal and satellite cells and is accelerated by bone morphogenetic protein-4. J Mol Cell Cardiol. 2012; 53(3): 382-391.
31. Hatcher CJ, Goldstein MM, Mah CS, Delia CS, Basson CT. Identification and localization of TBX5 transcription factor during human cardiac morphogenesis. Dev Dyn. 2000; 219(1): 90-95.
32. Misra C, Chang SW, Basu M, Huang N, Garg V. Disruption of myocardial Gata4 and Tbx5 results in defects in cardiomyocyte proliferation and atrioventricular septation. Hum Mol Genet. 2014; 23(19): 5025-5035.
33. Bruneau BG, Nemer G, Schmitt JP, Charron F, Robitaille L, Ca-

ron S, et al. A murine model of Holt-Oram syndrome defines roles of the T-box transcription factor Tbx5 in cardiogenesis and disease. Cell. 2001; 106(6): 709-721.
34. Joo HJ, Kim JH, Hong SJ. Adipose tissue-derived stem cells for myocardial regeneration. Korean Circ J. 2017; 47(2): 151-159.
35. Yu H, Lu K, Zhu J, Wang J. Stem cell therapy for ischemic heart diseases. Br Med Bull. 2017; 121(1): 135-154.
36. Choudhery MS, Badowski M, Muise A, Pierce J, Harris DT. Donor age negatively impacts adipose tissue-derived mesenchymal stem cell expansion and differentiation. J Transl Med. 2014; 12: 8.
37. Huangfu D, Osafune K, Maehr R, Guo W, Eijkelenboom A, Chen S, et al. Induction of pluripotent stem cells from primary human fibroblasts with only Oct4 and Sox2. Nat Biotechnol. 2008; 26(11): 1269-1275.
38. Chen J, Zhong Q, Wang J, Cameron RS, Borke JL, Isales CM, et al. Microarray analysis of Tbx2-directed gene expression: a possible role in osteogenesis. Mol Cell Endocrinol. 2001; 177(1-2): 43-54.
39. Jones GN, Moschidou D, Lay K, Abdulrazzak H, Vanleene M, Shefelbine SJ, et al. Upregulating CXCR4 in human fetal mesenchymal stem cells enhances engraftment and bone mechanics in a mouse model of osteogenesis imperfecta. Stem Cells Transl Med. 2012; 1(1): 70-78.
40. Gul H, Marquez-Curtis LA, Jahroudi N, Lo J, Turner AR, Janowska-Wieczorek A. Valproic acid increases CXCR4 expression in hematopoietic stem/progenitor cells by chromatin remodeling. Stem Cells Dev. 2009; 18(6): 831-838.

Original Article

Kinetics of Oncolytic Reovirus T3D Replication and Growth Pattern in Mesenchymal Stem Cells

Razieh Sadat Banijamali, M.Sc.[1], Hoorieh Soleimanjahi, Ph.D.[1]*, Sara Soudi, Ph.D.[2], Hesam Karimi, M.Sc.[1], Asghar Abdoli, Ph.D.[3], Seyed Mahmood Seyed Khorrami, M.Sc.[1], Keivan Zandi, Ph.D.[4]

1. Department of Virology, Faculty of Medical Sciences, Tarbiat Modares University, Tehran, Iran
2. Department of Immunology, Faculty of Medical Sciences, Tarbiat Modares University, Tehran, Iran
3. Department of Hepatitis and AIDS, Pasteur Institute of Iran, Tehran, Iran
4. Center for AIDS Research, Laboratory of Biochemical Pharmacology, Department of Pediatrics, Emory University School of Medicine, Atlanta, Georgia, USA

Corresponding Address: Department of Virology, Faculty of Medical Sciences, Tarbiat Modares University, Tehran, Iran
Email: soleim_h@modares.ac.ir

Received: 30/January/2019, Accepted: 20/April/2019

Abstract

Objective: Currently, application of oncolytic-virus in cancer treatment of clinical trials are growing. Oncolytic-reovirus is an attractive anti-cancer therapeutic agent for clinical testing. Many studies used mesenchymal stem cells (MSCs) as a carrier cell to enhance the delivery and quality of treatment with oncolytic-virotherapy. But, biosynthetic capacity and behavior of cells in response to viral infections are different. The infecting process of reoviruses takes from two-hours to one-week, depends on host cell and the duration of different stages of virus replication cycle. The latter includes the binding of virus particle, entry, uncoating, assembly and release of progeny-viruses. We evaluated the timing and infection cycle of reovirus type-3 strain Dearing (T3D), using one-step replication experiment by molecular and conventional methods in MSCs and L929 cell as control.

Materials and Methods: In this experimental study, L929 and adipose-derived MSCs were infected with different multiplicities of infection (MOI) of reovirus T3D. At different time points, the quantity of progeny viruses has been measured using virus titration assay and quantitative real-time polymerase chain reaction (qRT-PCR) to investigate the ability of these cells to support the reovirus replication. One-step growth cycle were examined by 50% cell culture infectious dose (CCID50) and qRT-PCR.

Results: The growth curve of reovirus in cells shows that MOI: 1 might be optimal for virus production compared to higher and lower MOIs. The maximum quantity of virus production using MOI: 1 was achieved at 48-hours post-infection. The infectious virus titer became stationary at 72-hours post-infection and then gradually decreased. The virus cytopathic effect was obvious in MSCs and this cells were susceptible to reovirus infection and support the virus replication.

Conclusion: Our data highlights the timing schedule for reovirus replication, kinetics models and burst size. Further investigation is recommended to better understanding of the challenges and opportunities, for using MSCs loaded with reovirus in cancer-therapy.

Keywords: Cancer, Mesenchymal Stem Cells, Oncolytic Viruses, Quantitative Real-Time Polymerase Chain Reaction, Reovirus Type 3

Cell Journal(Yakhteh), Vol 22, No 3, October-December (Autumn) 2020, Pages: 283-292

Citation: **Banijamali RS, Soleimanjahi H, Soudi S, Karimi H, Abdoli A, Seyed Khorrami SM, Zandi K. Kinetics of oncolytic reovirus T3D replication and growth pattern in mesenchymal stem cells. Cell J. 2020; 22(3): 283-292. doi: 10.22074/cellj.2020.6686.**

Introduction

Oncolytic viruses (OVs) have emerged as an efficient and promising new class of therapeutic agents to combat cancers and started a new era in cancer therapy (1). Recently, the clinical trials showed the effectiveness of OVs in human cancers. The US Food and Drug Administration (FDA) approved herpes virus based-OV for the treatment of progressive metastatic melanoma (2). Currently, there are a large number of other OVs under investigation in clinical trials (1).

Reovirus is a naturally occurring OV that has been used in therapy for a broad spectrum of human cancers (3). Many clinical trials evaluated the potential application of an oncolytic reovirus developed by Reolysin®, (pelareorep; wild-type reovirus; Serotype 3 Dearing; Oncolytics Biotech Inc.), for the treatment of different tumor cells (4). In 2015, the FDA has approved Reolysin®, as a first-in-class systemically administered an attractive anti-cancer agent for malignant glioma, ovarian and pancreatic cancers (2). The reovirus ability to selective replication in cancer cells is due to cancer cells mutations on a growth pathway known as the RAS signaling pathway (5). Reovirus considered relatively benign, but targets the gastrointestinal and upper respiratory tracts in newborns and immunocompromised individuals. Reovirus effectively infect and kill many types of transformed cells. Several studies have revealed that the reovirus T3D has oncolytic potential (6, 7). Due to extensive pre-clinical and clinical efficacy, replication competency, and low toxicity profile in humans, reovirus have considered as an attractive anti-cancer therapy in oncolytic virotherapy (8).

Despite the benefits of OVs, the therapeutic efficacy of OVs have been limited due to numerous biological, immunological, physiological and intra tumoral barriers (9). Delivery of the OVs to target sites is one of the major

obstacles due to virus elimination by the host antibodies and other immune cells before they reach destination. Several methods have been proposed to evade this particular problem (10). Early experiments showed the enhanced antitumor activity of virus-producing cells compared with naked viruses (11). Recent approaches tried to combine OVs with other methods like "smarter" carrier to improve delivery of the OVs (12). This finding led to the hypothesis that carrier cells could be used to hide the therapeutic virus from the host immune system and guarantee the biologically active virus transferring toward the target site (11). Several preclinical studies have extensively evaluated many different cell as carriers for oncolytic virotherapy (10). The viruses can be loaded onto cells without losing the biological activity of either virus or cell carrier (13).

In recent years, mesenchymal stem cells (MSCs) have received significant attention as efficient vehicle to transfer OVs towards the cancer cells (10, 14). MSCs known as fibroblast-like non-hematopoietic stem cells have been isolated from bone marrow (BM), adipose, fetal liver, placenta and umbilical cord blood. These cells are positive for surface markers CD105, CD73, and CD90 and lack expression of endothelial and hematopoietic lineage markers including CD45, CD34, CD14 or CD11b, CD79a or CD19, and HLA-DR (15, 16).

Since the cell and virus biology is affected by each other, the study of these changes are necessary to improve their consequences. The aim of the current study was to compare the reovirus growth life cycles and intracellular kinetic models in adipose-derived MSCs (AD-MSCs) as carrier for wild-type oncolytic activity of virus with L929 cell as control cell. For this purpose, monitoring of growth kinetics in one-step growth assays in both cells was investigated. A detailed growth kinetic models and virus production profile was optimized to the best-fit *in vitro* parameters. It could provide a starting point toward understanding of the virus growth dynamics, propagation and release. Here, we demonstrate a molecular and conventional methods to measure the kinetics of reovirus production in different cells.

Material and Methods

Isolation and culture of adipose-derived-mesenchymal stem cells

In this experimental study, adipose tissue was obtained from six-weeks-old female C57BL/6 mice (Pasteur Institute, Iran). Prior to the collection of the adipose tissue, mice were killed by cervical dislocation based an approval of the animal Ethics Committee (TMU.REC.1395.415) in Tarbiat Modares University (Tehran, Iran). During this study, we used standard protocols for the isolation of AD-MSCs using collagenase enzymatic digestion. Briefly, the adipose tissue were minced and incubated with 0.1% Type-I collagenase (Invitrogen, USA) for 30 minutes at 37˚C. Collagenase activity was neutralized by addition of Dulbecco's Modified Eagle's Medium (DMEM, Gibco, USA) containing 20% heat inactivated fetal bovine serum (FBS, Gibco, USA). It was centrifuged at 1,700 rpm for 7 minutes. The supernatant was discarded and the pellet re-suspended in 1 ml of cell culture medium, consisting of DMEM, 20% FBS, and 1% penicillin/streptomycin (Gibco, USA). The cells were counted and seeded in a 75 cm^2 flask with complete medium and incubated at 37˚C with 5% CO_2 in humidified atmosphere. The medium was changed twice a week until 70-80% confluence as determined by microscope observation. Then they were harvested and expanded. All the experiments were performed using AD-MSCs at passages three.

Adipose-derived-mesenchymal stem cells phenotyping

To analyze cell surface markers, AD-MSCs at passages 3 were harvested, washed with phosphate buffered saline (PBS), counted and 100 µl of the suspension incubated with monoclonal antibodies against defined markers CD29, CD34, CD45, CD90 and CD105 (all were purchased from BioLegend, USA) for 1 hour at 4˚C in the dark. The cells were fixed with 1% paraformaldehyde (Sigma-Aldrich, Germany) and analyzed using a FACSCanto II flowcytometer (BD Biosciences, USA) and FlowJo software.

Adipogenic and osteogenic differentiation assay

Differentiation potential of AD-MSCs into adipogenic and osteogenic were assessed. Briefly, AD-MSCs were treated with osteogenic medium [10 mM beta-glycerophosphate (Merck, UK), 50 mg/ml ascorbic acid-2-phosphate (Sigma-Aldrich, Germany), and 100 nM dexamethasone (Sigma-Aldrich, Germany)] or adipogenic medium [250 nM dexamethasone (Sigma-Aldrich, Germany), 0.5 mM 3-isobutyl-1-methylxanthine (Sigma-Aldrich, Germany), 5 mM insulin (Sigma-Aldrich, Germany), and 100 mM indomethacin (Sigma-Aldrich, Germany)] for 3 weeks, with medium changes every 3-4 days. After 21 days, lipid droplets were visualized using Oil red O staining (ORO, Sigma-Aldrich, Germany) and to measure mineralization, osteogenic culture stained with Alizarin red S (ARS, Sigma-Aldrich, Germany).

Culture of L929 cell and virus seed preparation

Murine L929 fibroblasts cells were a gift from Dr. Soudi (Tarbiat Modares University, Iran), propagated in DMEM containing 10% FBS, and 1% penicillin/streptomycin at 37˚C in a humidified 5% CO_2 incubator. The cells were passaged at 80% confluency, and incubated at 37˚C with 5% CO_2, 95% humidity.

The monolayers of L929 cells prepared in a 75 cm^2 flask and infected with wild-type reovirus T3D [a generous gift from Dr. Shamsi-Shahrabadi (Iran University of Medical Sciences, Iran)] at multiplicities of infection (MOI) of 0.1 for virus seed preparation. The infected cells were incubated at 37˚C for 1 hour. Cells were washed twice with PBS and incubated in fresh medium at 37˚C. Virus stock was harvested when the virus cytopathic effects

(CPE) become visible in more than 75% of the cells.

Characterization of reovirus T3D

The plaque assay is one of the most efficient biological assays used for the quantification of reovirus T3D. This assay is based on the CPE, which was caused by active and replicable forms of reovirus in cell culture and introduced to plaque-forming units per milliliter of virus (PFU/ml). For this purpose, L929 cell in six-well culture plates overlaid with serial dilutions (10^{-1}-10^{-5}) of the reovirus T3D. After 1 hour, unabsorbed viruses were removed by washing twice with PBS. The cell monolayers were covered with a layer that contained 1% cell grade agar (Sigma, USA) in DMEM, 1% penicillin/streptomycin without serum. Plates were incubated at 37˚C for 4-5 days. The cells fixed using 3.7% formaldehyde for at least 2 h and plaques were then visualized by 1% crystal violet (CV) in 20% ethanol and dH_2O.

For polyacrylamide gel electrophoresis (PAGE) and silver staining, double-stranded RNA of reovirus T3D was purified from the cells by RNA extraction solution (RiboEx, GeneAll, Korea). The genome of reovirus T3D was analyzed by electrophoresis on 12% polyacrylamide gels, and RNA segmented pattern confirmed by silver staining based on Laemmli protocol (17).

Inoculation of adipose-derived-mesenchymal stem cells and L929 cell with different multiplicities of infection by reovirus T3D

AD-MSCs and L929 cell were cultured in DMEM that contained 10% FBS, 1% penicillin-streptomycin in 6 well plates for 24 hours. Subsequently, cells were washed twice with PBS, inoculated with a MOI of 10, 1, 0.1, 0.01 and 0.001 of reovirus T3D stock. After 1 hour of adsorption at 37˚C, the cells were washed twice with PBS and incubated at 37˚C in 1 ml FBS free DMEM supplemented with 1% penicillin-streptomycin.

Then, culture supernatants of cells harvested and analyzed for 50% cell culture infectious dose ($CCID_{50}$) and quantitative real-time polymerase chain reaction (qRT-PCR) at the following time points: 1, 2, 3, 4, 5, 6, 7, 8, 12, 24, 48, 72 and 96 hours post-infection.

Reovirus titration in adipose-derived-mesenchymal stem cells and L929 cell by $CCID_{50}$ assay

AD-MSCs and L929 cell monolayer were prepared in a 48-well plate. Logarithmic dilutions (10^{-1}-10^{-10}) of each time point culture supernatants made in serum-free DMEM. The cells infected with each dilution, and the infected cells were examined for CPE presentation 72 hours post-infection. CPE results considered by comparing with positive (undiluted virus stock) and negative cell controls. Virus titers were calculated according to the method of Reed & Muench.

Primer designing, amplification and sequencing of polymerase chain reaction product

The primer for reovirus T3D genomic *L3* gene segment (major capsid protein lambda 1) was designed by Lasergene. The primers for amplification of *L3* gene are

F: 5′-CGCGTCCTCAATTTTGGGTAAAC-3′
R: 5′-CCGCCGTCTTTTGGATATGAACTA-3′.

To confirm the specificity of the designed primers, a PCR reaction was performed with the following conditions: The final PCR reaction volume was 25 µl with forward and reverse primers concentration at 10 pmol/µL. The first round PCR starts at 95˚C for 2 minutes, followed by 35 cycles of 95˚C for 20 seconds, 61˚C for 40 seconds, 72˚C for 1 minute, with a final extension of 72˚C for 5 minutes with Applied Biosystems PCR platforms.

The 135 bp PCR product was subsequently evaluated and visualized by electrophoresis on 2% agarose gel alongside the 100 bp DNA ladder (DM2300 ExcelBand, Taiwan). PCR products were isolated with the QIAquick Gel Extraction Kit (Qiagen, Germany) and directly sequenced with an Applied Biosystems (ABI) 3130 genetic analyzer (Tehran University of Medical Sciences, Iran). The sequence was compared to the Gene Bank database using the BLAST databases available on National Center for Biotechnology Information (NCBI).

Time point measurement of reovirus infectivity titers in adipose-derived-mesenchymal stem cells and L929 cell by real time quantitative polymerase chain reaction

A real-time PCR was developed to quantify reovirus T3D genomic RNA using the *L3* gene segment with indicated primer sets in previous section. Absolute viral RNA load quantitation within culture supernatants of infected mouse AD-MSCs and L929 fibroblasts were used for the construction of a standard curve. Viral RNA was extracted from each time point culture supernatants using the High Pure Viral Nucleic Acid Kit (Roche, Germany) according to the manufacturer's instructions. Extracted RNA was reverse transcribed into complementary DNA (cDNA) using cDNA synthesis kit (GeneAll, Korea), which included hexamer primers.

This assay was carried out on a serial logarithmic dilutions of virus positive control for each sample in order to construct the standard curves. Copy numbers for the standards were calculated based on Qiagen protocol (18). The reaction was carried out with EvaGreen/ Fluorescein master mix using Step One Plus Real-Time PCR System (Applied Biosystems, USA). A total volume of 20 µl amplification mixtures contained: 5X HOT FIREPol® EvaGreen® qPCR Mix Plus (ROX) 4 µl, forward and reverse primer (10 pmol/µL) 0.8µl, cDNA template 1 µl (225 ng/µl), nuclease-free water 14.2 µl. Reactions were run on a Step One Plus Real-Time PCR System. The cycle conditions were "holding stage 95˚C for 15 minutes; cycling stage 95˚C for 15 seconds and 61˚C for 20 seconds, 72˚C for 30 seconds for 40 cycles and a melt curve stage of 95˚C for 15 seconds, 70˚C for 1 minute and 95˚C for 15 seconds".

Comparison the rate of adsorption and penetration in adipose-derived-mesenchymal stem cells and L929 cell

We demonstrated the penetration and adsorption rates in AD-MSCs and L929 cell with oncolytic reovirus. In order to obtain this ambition, cells were infected with MOI: 1 of reovirus. Extra unabsorbed virus was removed 1-1.5 hour post-infection. Then, infected cells were collected and the viral genome was extracted by High Pure Viral Nucleic Acid Kit (Roche, Germany) according to the manufacturer's instructions. Synthesis of cDNA and Real-time PCR amplification was done similar to the previous section.

Statistical analysis

Data analysis was done by REST program using Real Time PCR outputs. Standard curves for each sample were constructed by plotting Ct values versus the viral RNA copy number using the StepOne Software (Applied Biosystems).

All experiments were performed in triplicate and repeated three times. All data were analyzed by Excel 2016 and GraphPad Prism 7.04 (GraphPad Software, USA) and reported as mean ± standard deviation (SD).

Results

Characterization of adipose-derived-mesenchymal stem cells

Cell surface markers of AD-MSCs isolated from C57BL/6 mice at passage three were examined by flow cytometry. AD-MSCs showed low expression of CD34 and CD45 markers, but CD29, CD90 and CD105 markers were expressed at mean percentages of 96.4, 85.2 and 65.9%, respectively (Fig.1A). Fibroblast-like morphology of AD-MSCs at passage three are presented in Figure 1B. Adipogenic and osteogenic differentiation potential of AD-MSCs was confirmed by ORO and ARS staining as indicated in Figure 1C and 1D, respectively.

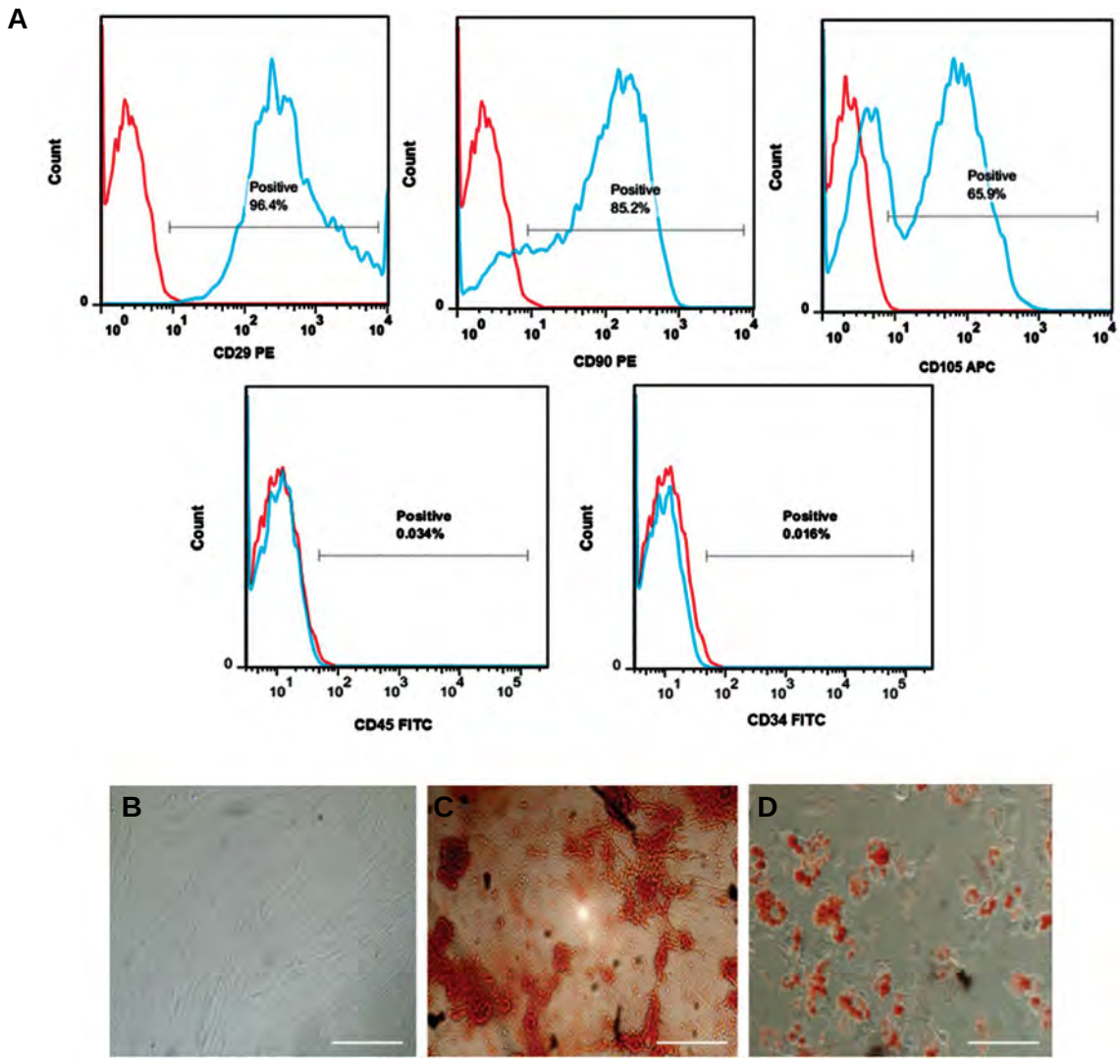

Fig.1: Characterization of adipose-derived-mesenchymal stem cells (AD-MSCs). **A.** Flow cytometry of AD-MSCs performed with monoclonal antibodies to detect cell surface markers. The expression of isotype controls is shown as red histograms, **B.** Fibroblast-like morphology of AD-MSCs at passage 3 in culture (scale bar: 100 µm), **C.** Matrix mineralization during osteogenesis of AD-MSCs was detected by Alizarin red S after 21 days of culture (scale bar: 20 µm), and **D.** Lipid droplets produced in AD-MSCs cultures after 21 days of adipogenesis, were stained by Oil red O (scale bar: 100 µm). The figure shows one representative results from three independent experiments.

Propagation of reovirus in L929 cell

We optimized the propagation conditions of reovirus by the sequential passage at MOI: 0.1 to reduce the rate of mutations. CPE has progressed to fully disrupt, three days after infection with reovirus T3D. Reovirus was released by the lysis of L929 infected cell and total cell lysate and medium was collected.

Characterization of reovirus T3D

The visible plaques were formed within four to five days after reovirus inoculation (Fig.2A). The nominal titers of virus stocks were calculated according to the current microbiology protocol (19).

The viral dsRNA was purified and separated by electrophoresis on 12% polyacrylamide gel and RNA segmented pattern confirmed by silver staining as shown in Figure 2B. The result showed normal RNA migration pattern of reovirus T3D in polyacrylamide gel electrophoresis.

Inoculation of reovirus in adipose-derived-mesenchymal stem cells and L929 cell

CPE in MOI: 1 of reovirus was obvious in both cells as shown in Figure 3 at deferent time points. At 24 hours post-infection, CPE was observed and completed at 72 hours post-infection.

Determining the highest dilution of virus suspension in cell infectious dose using the 50% cell culture infectious dose assay

L929 cell and AD-MSCs were infected with different MOIs. Supernatants were collected in different time intervals [1, 2, 3, 4, 5, 6, 7, 8, 12, 24, 48, 72 and 96 hours post-infection] and then virus infection was determined by $CCID_{50}$. As shown in Figure 4A, when AD-MSCs were infected with MOI: 10, the virus infectivity assay was positive 6 h post-infection. At MOI: 1, virus progeny production was observed 7 hours post-infection, reaching to its maximum level at 48 hours post-infection. In the current study, virus progeny production was initiated at the following MOI: 0.1 (t8), 0.01 (t12) and 0.001 (t48) and at 72 hours post-infection, the virus titer was reached a peak.

Infection of L929 cells with a higher MOI (MOI of 10 and 1) contain more residual infectious virus during adsorption and penetration and resulted in a productive infection earlier compared to the lower infectious virus titers as seen in Figure 4B. At MOI of 10 and 1 a regular rise in infectious virus titers were observed at 4 and 6 hours post-infection, reaching to its maximum level at 24 and 48 hours post-infection, respectively.

At MOI: 0.1 a rise in infectious virus titers was observed at 7 hours post-infection, reaching to its maximum level at 48 hours post-infection. Whereas for MOI of 0.01 and 0.001 progeny viruses was verified at 8-12 hours post-infection, reaching to its maximum level at 72 hours post-infection.

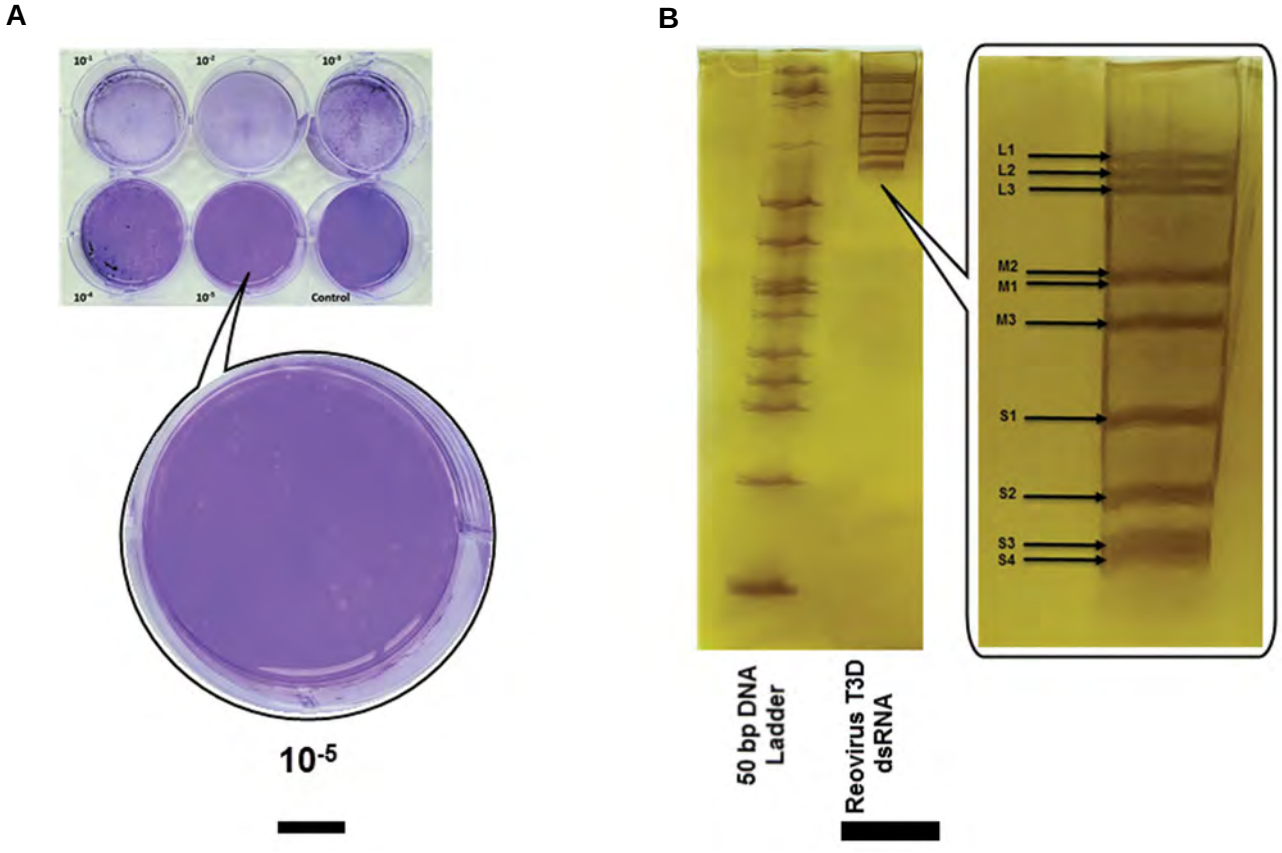

Fig.2: Characterization of reovirus T3D. **A.** Plaques formation by reovirus on monolayer L929 cell. About 50 plaques were counted for replicates of the 1×10^{-5} dilution, and the virus titer was 0.7×10^{7} PFU/ml. **B.** Electrophoretic migration pattern of dsRNA of reovirus T3D (3-3-2-2). RNA samples were analyzed by electrophoresis in a 12% PAGE gel and visualized by silver staining.

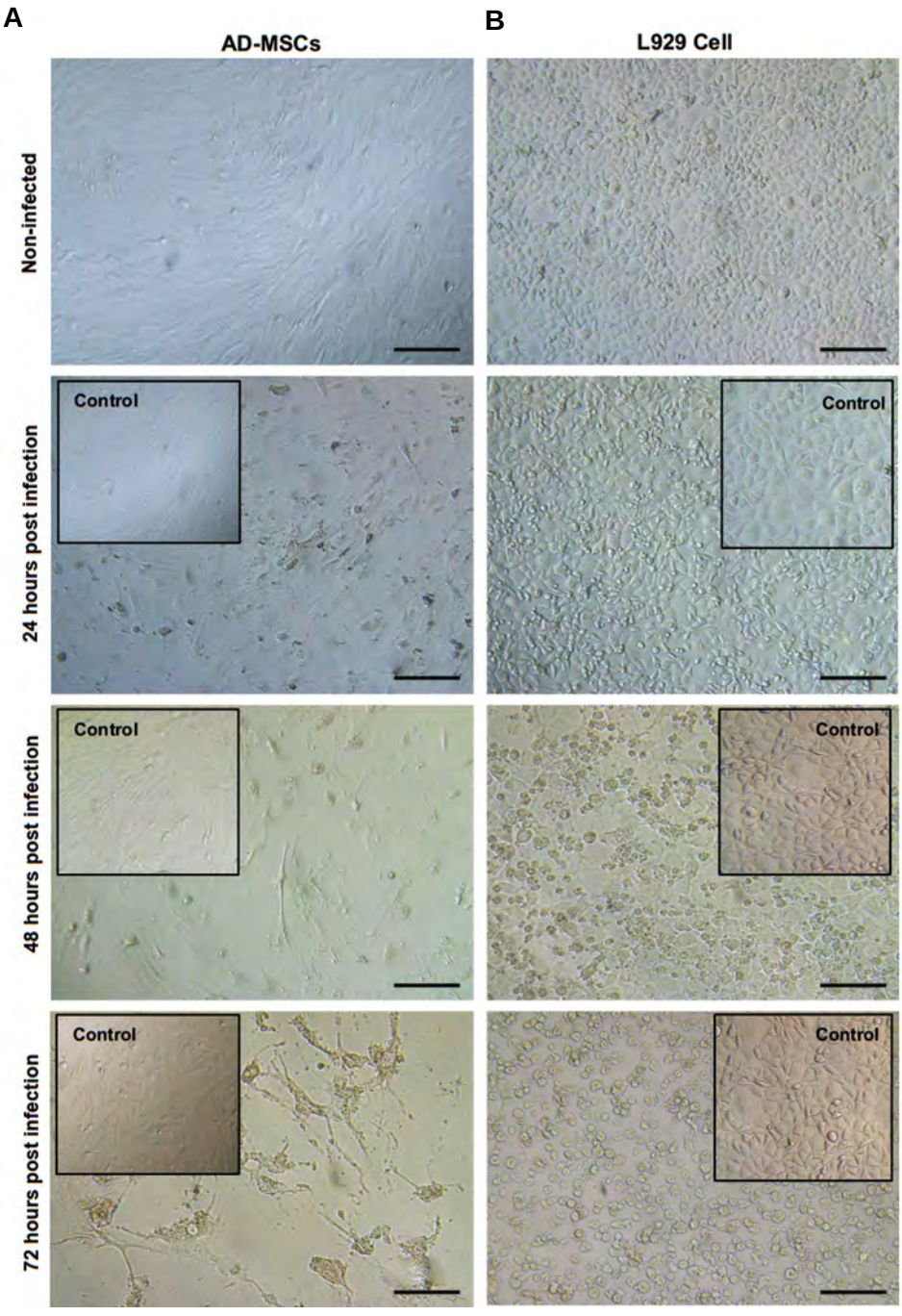

Fig.3: Phase contrast microscopy of confluent monolayer non-infected and infected AD-MSCs, L929 cell with MOI: 1, considering reovirus CPE in different time points. **A.** In AD-MSCs and **B.** In L929 cell (scale bars: 100 µm). AD-MSCs; Adipose-derived mesenchymal stem cells, MOI; Multiplicities of infection, and CPE; Cytopathic effect.

Absolute viral RNA load quantitation

Agarose gel electrophoresis was used for separating of PCR product with detectable size of 135 bp (data not shown). The cDNA sequence analysis confirmed that the PCR products corresponded to the reovirus *L3* gene segment (data not shown).

Amplification graph and melt curve analysis for each samples confirmed the specificity of the virus shedding. The viral RNA load (RNA logarithm of copies/ml), in each time point of AD-MSCs and L929 cell supernatants were calculated in comparison with standard curve (serial logarithmic dilutions of positive control) as illustrated in Figure 4C, D, and E, respectively. According to the result, Infection of both cells with different MOIs contain more residual infectious virus during adsorption and penetration and resulted in a productive infection earlier. In L929 cell, at MOI: 1 a regular rise in infectious viral load was observed at 5 hours post-infection, reaching to its maximum level at 48 hours post-infection; but in AD-MSCs, at MOI: 1, a regular rise in infectious viral load was observed 6 hours post-infection, reaching to its maximum level at 48 hours post-infection.

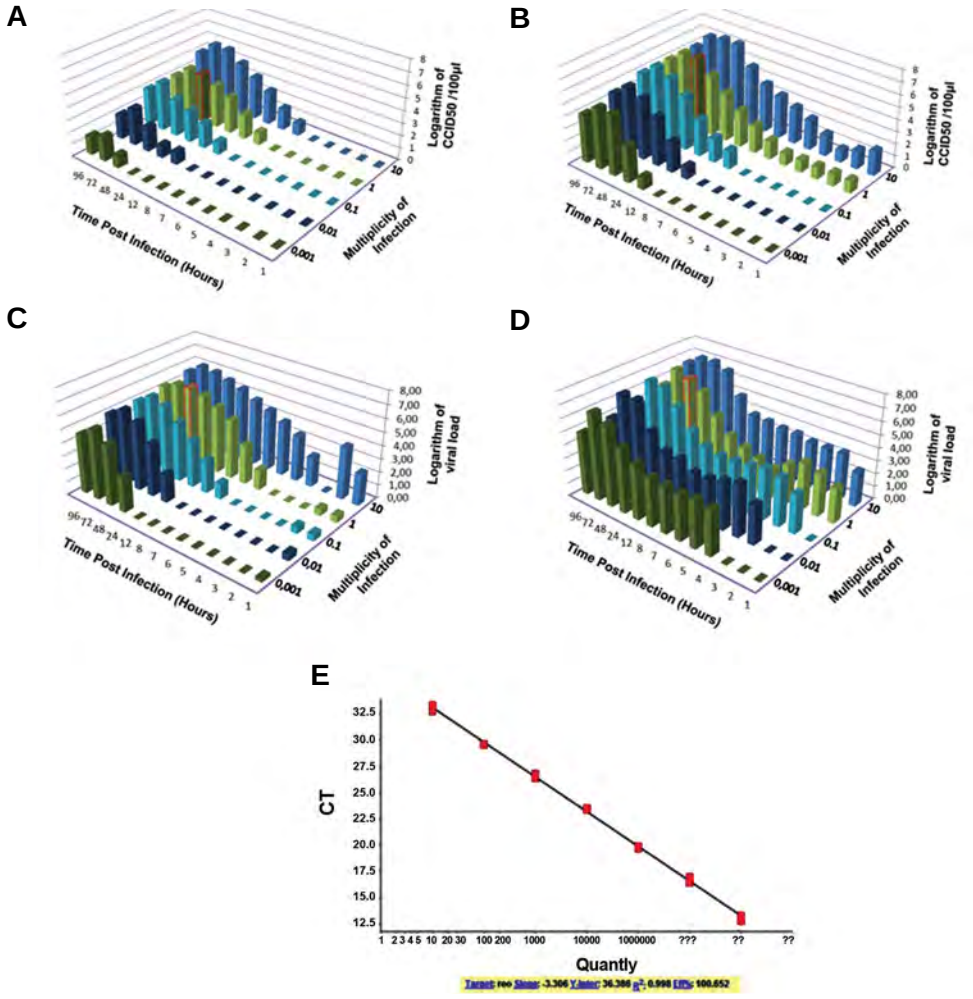

Fig.4: Kinetics of reovirus replication measured by $CCID_{50}$ and qRT-PCR assay. **A.** Based on $CCID_{50}$ results in mouse AD-MSCs, **B.** Based on $CCID_{50}$ results in murine L929 fibroblasts cell. The results were expressed as logarithm of $CCID_{50}$/100 µl. The growth curve of reovirus in AD-MSCs and L929 cell shown that, MOI: 1 might be optimal for virus production. In L929 cell, at MOI: 1 a regular rise in infectious virus titers was observed at 6 hours post-infection, reaching to its maximum level at 48 hours post-infection; but in AD-MSCs, at MOI: 1, virus progeny production was observed 7 hours post-infection, reaching to its maximum level at 48 hours post-infection. Data are expressed as the mean of three independent experiments, **C.** Based on qRT-PCR results in mouse AD-MSCs, **D.** Based on q RT-PCR results in murine L929 fibroblasts cell. The results were expressed as logarithm of copies/ml, and **E.** Ten-fold serial dilutions (10^1-10^7 copies/ml) of synthetic viral RNA standard were used to generate a standard curve. The growth curve of reovirus in AD-MSCs and L929 cell shown that, MOI: 1 might be optimal for virus production. In L929 cell, at MOI: 1 a regular rise in infectious viral load was observed at 5 hours post-infection, reaching to its maximum level at 48 hours post-infection; but in AD-MSCs, at MOI: 1, a regular rise in infectious viral load was observed 6 hours post-infection, reaching to its maximum level at 48 hours post-infection. Data are expressed as the mean of three independent experiments. $CCID_{50}$; Cell culture infectious dose 50%, qRT-PCR; Quantitative real-time polymerase chain reaction, AD-MSCs; Adipose-derived mesenchymal stem cells, and MOI; Multiplicities of infection.

The result of viral adsorption and penetration in adipose-derived-mesenchymal stem cells and L929 cell

Based on real-time quantitative PCR result, no significant differences were observed in the rates of adsorption and penetration between different MOI (data not shown), but as demonstrated in Figure 5, the virus adsorption and penetration of MOI: 1 in L929 cell is much more efficient than AD-MSCs.

Single cell cycle experiment using 50% cell culture infectious dose

The results of a one-step growth experiment establish a number of important features about viral replication. According to Figure 6A, the result of reovirus one-step growth on AD-MSCs showed, at time points 5 (MOI: 10), 6 (MOI: 1), 7 (MOI: 0.1), 8 (MOI: 0.01) and 12 (MOI: 0.001) hours post-infection constitutes the eclipse period. Exponential growth of virus was started at 6, 7, 8, 12, 24 hours post-adsorption, in different MOI of 10, 1, 0.1, 0.01, 0.001 respectively. The quantity of infectious virus begins to increase and CPE was detected, marking the onset of the synthetic phase, and continued by assembly of new virus particles. Ultimately, viruses are released and the growth cycle enter the stationary and decline phases and further not supported to additional replication round.

According to Figure 6B, the result of reovirus one-step growth in L929 cell showed, at time points 3 (MOI: 10), 5 (MOI: 1), 6 (MOI: 0.1), 7 (MOI: 0.01) and 8 (MOI: 0.001) hours post-infection, constitutes the eclipse phase and viral nucleic acid uncoating from its protective shells. The exponential phase of reovirus infection in L929 cell

was initiated at time points 4, 6, 7, 8 and 12 hours after adsorption with different MOIs of 10, 1, 0.1, 0.01 and 0.001, respectively; and the quantity of infectious virus begins to increase and CPE were detected.

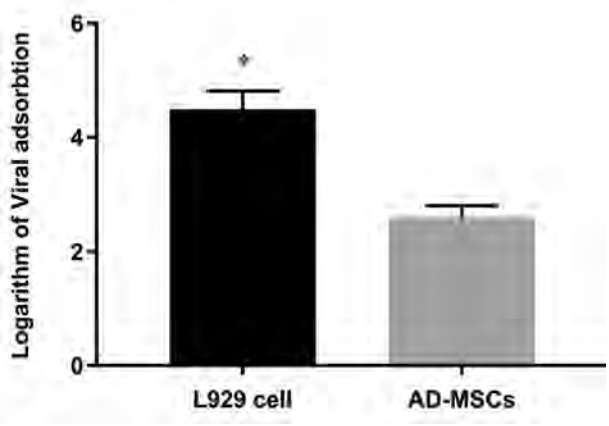

Fig.5: The rates of reovirus adsorption and penetration to AD-MSCs in comparison with L929 cell in MOI: 1. The results were expressed as logarithm of copies/ml. At this MOI, the virus adsorption and penetration in L929 cell is much more efficient than AD-MSCs. Data are expressed as the mean ± SD of three independent experiments. *; Indicated groups are significantly different from each other (P<0.05), AD-MSCs; Adipose-derived mesenchymal stem cells, and MOI; Multiplicities of infection.

Single cell cycle experiment using real time polymerase chain reaction

The result of reovirus one-step growth in AD-MSCs based on qRT-PCR showed in Figure 6C, at the time points 3 (MOI: 10), 5 (MOI: 1), 6 (MOI: 0.1), 8 (MOI: 0.01) and 12 (MOI: 0.001) hours post-infection, constitutes the eclipse phase and viral nucleic acid uncoating. The small number of infectious particles detected during this period probably results from adsorbed virus that was not uncoated. At time points 4 (MOI: 10), 6 (MOI: 1), 7 (MOI: 0.1), 12 (MOI: 0.01) and 24 (MOI: 0.001) hours after adsorption, the quantity of infectious virus begins to increase, corresponded to the onset of the synthetic phase, and during of new virus particles assembly and virions release from cells into the extracellular medium. Although, the result of one-step growth on L929 cell showed in Figure 6D, constitutes the eclipse period start at time points 1 (MOI: 10), 4 (MOI: 1), 8 (MOI: 0.1, 0.01, 0.001) hours post-infection and at time points 2 (MOI: 10), 5 (MOI: 1), 12 (MOI: 0.1, 0.01, 0.001) hours after adsorption, the quantity of infectious virus begins to increase and new progeny particles were assembled and released from cells into the extracellular medium. In both cells, ultimately after 72 hours, virus production plateaus as the cells become metabolically and structurally incapable of supporting additional virus replication.

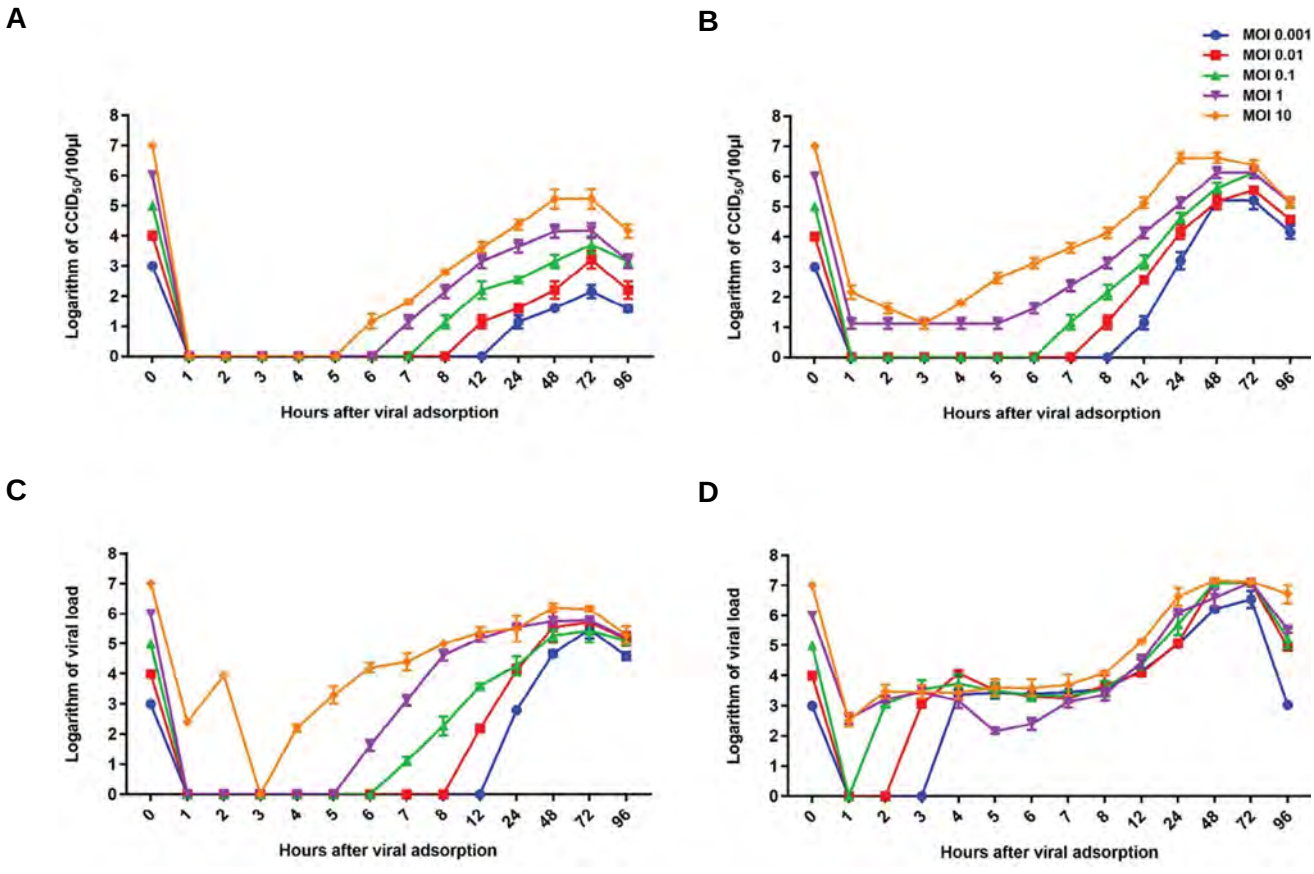

Fig.6: One-step growth curves of reovirus at different MOIs. **A.** Based on $CCID_{50}$ results in AD-MSCs, **B.** Based on $CCID_{50}$ results in L929 cell. The results were expressed as logarithm of $CCID_{50}$/100 µl, **C.** Based on viral load results in AD-MSCs, **D.** Based on viral load results in L929 cell. The results were expressed as logarithm of copies/ml. The growth curve of reovirus by $CCID_{50}$ and qRT-PCR in both cells showed that MOI: 1 might be optimal for virus production compared to higher and lower MOIs. Data are expressed as the mean ± SD of three independent experiments. MOI; Multiplicities of infection, $CCID_{50}$; Cell culture infectious dose 50%, AD-MSCs; Adipose-derived mesenchymal stem cells, and qRT-PCR; Quantitative real-time polymerase chain reaction.

Discussion

OVs are able to infect different kinds of host cells (20). The progression process occurs at 2-4 hours or more than 1-2 days depending on MOI of virus and cell type. Wild-type oncolytic reovirus is an attractive anti-cancer agent for clinical testing (21). The OV therapy is not successful alone, because circulating antiviral antibodies in the blood neutralize the OVs before reaching to the target site; or perhaps macrophages recognize infected cells with OVs and kill them (22). The main problem in oncolytic virotherapy is delivery and interaction of OVs with the immune system (23). To resolve this issue, a novel approach has been suggested which is focused on the using of cell carriers (10). In the present study, in order to enhance the quantity and capabilities of the AD-MSCs for delivery of OVs, biosynthetic capacity of the AD-MSCs was assessed. The behavior of L929 cells as susceptible host cell line was studied in response to reovirus infection.

The behavior of the cells is different in response to viral infection. This variability among different infected cells can be attributed to cell properties, stages of the cell cycle (24), genetic severe heterogeneity of the virus population (25), or host cells resource differences (20). The replicability of an oncolytic reovirus is measured by its burst size, for further use in near future.

The quantitative description of the crucial steps in reovirus infection cycle has been presented in this study. We evaluated the preferential cytotoxicity and shedding of reovirus in AD-MSCs and compared them, with L929 cells as susceptible host cell line. For this purpose, MOI optimization and monitoring of reovirus shedding were done in the two mentioned target cells. The appropriate titer of virus for one step growth cycle was obtained by $CCID_{50}$ and qRT-PCR.

According to the $CCID_{50}$ data, the viral shedding was started from the early hours in infected L929 cells with the MOI of 10 and 1. This can be considered as false positive, because a lot of viral particles might have not been internalized or re-entered into the supernatant without infecting the cells and progeny production. As data represents, AD-MSCs at 48 hours post-infection with MOI: 1 had the highest titer of the virus shedding. The viruses entering stationary phase at the 72 hours post-infection. Then, the virus shedding decreased. In the higher MOI (MOI: 10), lysis of the cells occurred early after infection, and increased by the high titer of viruses. In this situation, the optimal rate of virus replication was low. According to Igase et al. (26), more than 50% of hang-up of cell growth was evidenced at MOI: 10 in the MGT cell lines. In the MOI lower than 1, the reproduction rate was low compared with MOI: 1, due to the lower titer of the virus. From a higher level of MOI to lower level, the production of progeny and approaching the pick value were delayed. Comparing the two cell lines, one log reduction in virus titer has been observed in AD-MSCs in comparison with the L929 cell line. Jung et al. (27) reported that the final virus titer was closely linked to the input MOI and the host cell confluency at the time of infection. They reached a maximum virus titer when an MOI: 0.1 and the final host cell density of 1.0×10^6 cells/ml were used.

Based on qRT-PCR results, the viral shedding was started from the early hours in both infected cells with different MOIs. These can be considered as false positive, because a lot of viral particles might have not been internalized or re-entered into the supernatant without infecting the cells and progeny production. In MOI: 1, the ratio of virus to infected cells was optimum resulting in the highest level of virus replication similar to the results of $CCID_{50}$ at 48 hours post-infection.

According to the one-step growth curve of reovirus, at MOI: 1 the viruses in both cells has the most regular replication cycle. The eclipse period of reovirus in L929 cell and AD-MSCs occurred 4-5 hours post infection. The growth curve of reovirus in AD-MSCs and L929 cell has demonstrated that the lower MOI might be ideal for high virus production compared to higher MOI as seen in the literature. Parallel finding was reported by Grande and Benavente (28) in chicken embryo fibroblast cells infected with avian reovirus S1133.

In both cells the maximum virus titer in MOI: 1 was reached at 48 hours post-infection, then stabilized and gradually decreased. The adsorption time, rise time and the time interval over which the cell produces virus are different in cell types. These are affected by the number of infected cells. This finding illustrates that the optimum titer depends on the virus-cell ratio rather than the concentration of virus and cells for progeny production.

The evaluation of the penetration and adsorption rates have shown no obvious difference between different MOIs. These rates absolutely depends on cell type and other environmental elements. The importance of cell source, MOI and the distribution of virus yields could reflect different numbers of adsorbed virus particles to distinct cells when they are treated with different MOIs. The average yield from the single cells does not change significantly, but intact virus production remains to be determined.

Taken together, the comprehensive range of virus yields from different cells, potentially reflects different factors such as genetic variation, and the cell type in the replication kinetics during the early stages of growth cycle.

Conclusion

Based on the observed results, the cytopathic effect was seen in both cells, but one log reduction in virus titer and shedding in AD-MSCs was seen compared to L929 cell. According to their innate proliferation properties, AD-MSCs can be susceptible but are less permissive to viral infection. The suitability of AD-MSCs as efficient carriers for wild-type oncolytic reovirus to target the cancer cells

will be considered for further investigation.

These interpretations arise several questions about factors that influence virus–host interactions. We illustrated that the host cell resources capacity, virus MOI variation and burst size can affect strength of virus progeny production. A delay in adsorption and release of reoviruses in AD-MSCs could lead to the delivery of effective virus progeny at the right time per infected host as a carrier cell. This phenomenon needs further investigation for using infected AD-MSCs by oncolytic activity of reovirus in cancer therapy.

Acknowledgements

We wish to thank deputy of research, Tarbiat Modares University for their financial support and providing assistance. The results described in this manuscript were part of student thesis, which was supported by the grant number 52/7400 from the Research Deputy of Tarbiat Modares University, Faculty of Medical Sciences, and partially supported by NIMAD (National Institute for Medical Research Development) the grant number of 957970. The authors declare that they have no competing interests.

Authors' Contributions

H.S.; Contributed to study conception and design. H.S., R.S.B.; Conceptualized and designed the experiments. R.S.B., H.K.; Carried out experiments and acquired the data. R.S.B., H.S., S.S., H.K., A.A.; Interpreted the data and carried out data analysis and statistical analysis. R.S.B., H.K., S.M.S.K.; Drafted the manuscript. R.S.B., H.S., S.S., H.K., A.A., K.Z.; Wrote the manuscript. All authors read and approved the final manuscript.

Reference

1. Fukuhara H, Ino Y, Todo T. Oncolytic virus therapy: a new era of cancer treatment at dawn. Cancer Sci. 2016; 107(10): 1373-1379.
2. Ferhat M. Oncolytic viruses: the next major breakthrough in cancer treatment. J Hum Virol Retrovirol. 2017; 5(1): 00141.
3. Hall K, Scott KJ, Rose A, Desborough M, Harrington K, Pandha H, et al. Reovirus-mediated cytotoxicity and enhancement of innate immune responses against acute myeloid leukemia. Biores Open Access. 2012; 1(1): 3-15.
4. Chakrabarty R, Tran H, Selvaggi G, Hagerman A, Thompson B, Coffey M. The oncolytic virus, pelareorep, as a novel anticancer agent: a review. Invest New Drugs. 2015; 33(3): 761-774.
5. Gong J, Mita MM. Activated ras signaling pathways and reovirus oncolysis: an update on the mechanism of preferential reovirus replication in cancer cells. Front Oncol. 2014; 4: 167.
6. Gong J, Sachdev E, Mita AC, Mita MM. Clinical development of reovirus for cancer therapy: an oncolytic virus with immune-mediated antitumor activity. World J Methodol. 2016; 6(1): 25-42.
7. Kim M, Garant KA, zur Nieden NI, Alain T, Loken SD, Urbanski SJ, et al. Attenuated reovirus displays oncolysis with reduced host toxicity. Br J Cancer. 2011; 104(2): 290-299.
8. Thirukkumaran C, Morris DG. Oncolytic viral therapy using reovirus. Methods Mol Biol. 2015; 1317: 187-223.
9. Martinez-Quintanilla J, He D, Wakimoto H, Alemany R, Shah K. Encapsulated stem cells loaded with hyaluronidase-expressing oncolytic virus for brain tumor therapy. Mol Ther. 2015; 23(1): 108-118.
10. Kim J, Hall RR, Lesniak MS, Ahmed AU. Stem cell-based cell carrier for targeted oncolytic virotherapy: translational opportunity and open questions. Viruses. 2015; 7(12): 6200-6217.
11. Ahmed AU, Alexiades NG, Lesniak MS. The use of neural stem cells in cancer gene therapy: predicting the path to the clinic. Curr Opin Mol Ther. 2010; 12(5): 546-552.
12. Eisenstein S, Chen SH, Pan PY. Immune cells: More than simple carriers for systemic delivery of oncolytic viruses. Oncolytic Virother. 2014; 3: 83-91.
13. Willmon C, Harrington K, Kottke T, Prestwich R, Melcher A, Vile R. Cell carriers for oncolytic viruses: Fed Ex for cancer therapy. Mol Ther. 2009; 17(10): 1667-1676.
14. Duebgen M, Martinez-Quintanilla J, Tamura K, Hingtgen S, Redjal N, Wakimoto H, et al. Stem cells loaded with multimechanistic oncolytic herpes simplex virus variants for brain tumor therapy. J Natl Cancer Inst. 2014; 106(6): dju090.
15. Thanunchai M, Hongeng S, Thitithanyanont A. Mesenchymal stromal cells and viral infection. Stem Cells Int. 2015; 2015: 860950.
16. Busser H, Najar M, Raicevic G, Pieters K, Velez Pombo R, Philippart P, et al. Isolation and characterization of human mesenchymal stromal cell subpopulations: comparison of bone marrow and adipose tissue. Stem Cells Dev. 2015; 24(18): 2142-2157.
17. Laemmli UK. Cleavage of structural proteins during the assembly of the head of bacteriophage T4. Nature. 1970; 227(5259): 680-685.
18. Khansarinejad B, Soleimanjahi H, Mirab Samiee S, Hamidieh AA, Paryan M, Sanahmadi Y. Quantitation of human cytomegalovirus DNA in plasma using an affordable in-house qPCR assay. J Virol Methods. 2012; 183(2): 170-175.
19. Balish AL, Katz JM, Klimov AI. Influenza: propagation, quantification, and storage. Curr Protoc Microbiol. 2013; Chapter 15: Unit 15G.1.
20. Yin J, Redovich J. Kinetic modeling of virus growth in cells. Microbiol Mol Biol Rev. 2018; 82(2). pii: e00066-17.
21. Sahin E, Egger ME, McMasters KM, Zhou HS. Development of oncolytic reovirus for cancer therapy. Journal of Cancer Therapy. 2013; 4(6): 1100-1115.
22. Friedman A, Lai X. Combination therapy for cancer with oncolytic virus and checkpoint inhibitor: a mathematical model. PLoS One. 2018; 13(2): e0192449.
23. Ramírez M, García-Castro J, Melen GJ, González-Murillo Á, Franco-Luzón L. Patient-derived mesenchymal stem cells as delivery vehicles for oncolytic virotherapy: novel state-of-the-art technology. Oncolytic Virother. 2015; 4: 149-155.
24. Zhu Y, Yongky A, Yin J. Growth of an RNA virus in single cells reveals a broad fitness distribution. Virology. 2009; 385(1): 39-46.
25. Steinhauer DA, de la Torre JC, Meier E, Holland JJ. Extreme heterogeneity in populations of vesicular stomatitis virus. J Virol. 1989; 63(5): 2072-2080.
26. Igase M, Hwang CC, Coffey M, Okuda M, Noguchi S, Mizuno T. The oncolytic effects of reovirus in canine solid tumor cell lines. J Vet Med Sci. 2015; 77(5): 541-548.
27. Jung S, Behie LA, Lee PW, Farrell PJ. Optimization of reovirus production from mouse L-929 cells in suspension culture. Biotechnol Bioeng. 2004; 85(7): 750-760.
28. Grande A, Benavente J. Optimal conditions for the growth, purification and storage of the avian reovirus S1133. J Virol Methods. 2000; 85(1-2): 43-54.

Original Article

Short Pretreatment with Calcitriol Is Far Superior to Continuous Treatment in Stimulating Proliferation and Osteogenic Differentiation of Human Adipose Stem Cells

Fatemeh Mokhtari-Jafari, M.Sc.[1, 2], Ghassem Amoabediny, Ph.D.[1, 2, 3*], Mohammad Mehdi Dehghan, Ph.D.[4, 5], Marco N. Helder, Ph.D.[3], Behrouz Zandieh-Doulabi, Ph.D.[6#], Jenneke Klein-Nulend, Ph.D.[6#]

1. School of Chemical Engineering, College of Engineering, University of Tehran, Tehran, Iran
2. Department of Biomedical Engineering, Research Center for New Technologies in Life Science Engineering, University of Tehran, Tehran, Iran
3. Amsterdam UMC-location VUMC and Academic Centre for Dentistry Amsterdam (ACTA), Vrije Universiteit Amsterdam, Department of Oral and Maxillofacial Surgery/Oral Pathology, Amsterdam Movement Sciences, Amsterdam, The Netherlands
4. Department of Surgery and Radiology, Faculty of Veterinary Medicine, University of Tehran, Tehran, Iran
5. Institute of Biomedical Research, University of Tehran, Tehran, Iran
6. Department of Oral Cell Biology, Academic Centre for Dentistry Amsterdam (ACTA), University of Amsterdam and Vrije Universiteit Amsterdam, Amsterdam Movement Sciences, Amsterdam, The Netherlands

#The last two authors equally contributed to this work.

Corresponding Address: P.O.Box: 11365-4563, School of Chemical Engineering, College of Engineering, University of Tehran, Tehran, Iran
Email: amoabediny@ut.ac.ir

Received: 18/January/2019, Accepted: 20/April/2019

Abstract

Objective: This study investigated whether short stimulation (30 minutes) of human adipose stem cells (hASCs) with 1,25-dihydroxyvitamin D_3 (calcitriol or 1,25-$(OH)_2VitD_3$), fitting within the surgical procedure time frame, suffices to induce osteogenic differentiation, and compared this with continuous treatment with 1,25-$(OH)_2VitD_3$.

Materials and Methods: In this experimental study, hASCs were pretreated with/without 10 nM calcitriol for 30 minutes, seeded on biphasic calcium phosphate (BCP), and cultured for 3 weeks with/without 1,25-$(OH)_2VitD_3$. Cell attachment was determined 30 minutes after cell seeding. AlamarBlue assay, alkaline phosphatase (ALP) assay, ALP staining, real-time polymerase chain reaction (PCR), and protein assay were used to evaluate the effect of short calcitriol pretreatment on proliferation and osteogenic differentiation of hASCs up to 3 weeks.

Results: Pretreatment with 1,25-$(OH)_2VitD_3$ enhanced the attachment of hASCs to BCP by 1.5-fold compared to non-treated cells and increased the proliferation by 3.5-fold at day 14, and 2.6-fold at day 21. In contrast, continuous treatment increased the proliferation by 1.7-fold only at day 14. After 2 weeks, ALP activity was increased by 18.5-fold when hASCs were pretreated with 1,25-$(OH)_2VitD_3$ for 30 minutes but increased only 2.6-fold when compared with its continuous counterpart. Moreover, after 14 days, pretreatment resulted in significant upregulation of the osteogenic markers *RUNX2* and *SPARC* by 3.6-fold and 2.2-fold, respectively, while this was not observed upon continuous treatment. Finally, 30 minutes pretreatment of hASCs with 1,25-$(OH)_2VitD_3$ increased $VEGF_{189}$ expression, which may contribute to the process of angiogenesis.

Conclusion: This study is the first research showing that 30 minutes pretreatment of hASCs with 1,25-$(OH)_2VitD_3$, not only enhanced cell attachment to the scaffold at seeding time, but also promoted the proliferation and osteogenic differentiation of hASCs more strongly than continuous treatment, suggesting that short pre-treatment with 1,25-$(OH)_2VitD_3$ is a promising approach for the regeneration of bones in a one-step surgical procedure.

Keywords: 1,25-dihydroxy Vitamin D_3, Adipose-Derived Stem Cells, Bone, Osteogenesis, Proliferation

Cell Journal(Yakhteh), Vol 22, No 3, October-December (Autumn) 2020, Pages: 293-301

Citation: **Mokhtari-Jafari F, Amoabediny G, Dehghan MM, Helder MN, Zandieh-Doulabi B, Klein-Nulend J. Short pretreatment with calcitriol Is far superior to continuous treatment in stimulating proliferation and osteogenic differentiation of human adipose stem cells. Cell J. 2020; 22(3): 293-301. doi: 10.22074/cellj.2020.6773.**

Introduction

Bone regeneration is a process required for various bone diseases, including degenerative diseases, orthopedic surgeries, osteonecrosis, or non-union fractures, in which reconstruction of injured bone is needed (1). Engineered bone tissue is considered a potential alternative to the customary use of bone grafts due to the boundless supply and lack of disease transmission (2). Engineering the functional bone using a combination of (stem) cells, scaffolds, and osteostimulative factors is a promising strategy for the future development of bone regeneration.

Human adipose stem cells (hASCs) are the favoured cell source for the rehabilitation of massive bone defects due to its potential to trigger osteogenic and angiogenic differentiation (3, 4). Adipose tissue can be harvested with the least discomfort to patients and easily upscaled as needed. Moreover, it contains a high number of stem cell in comparison with its volume, which allows obtaining highly enriched ASC [residing in the stromal vascular fraction (SVF)] within a short time frame. Taken together, this implies that clinically relevant stem cell quantities can be achieved instantly after adipose tissue processing in a one-step surgical procedure (5). This novel concept is not only cost-effective but also beneficial to the

patients, mainly because a second surgical intervention can be avoided. Moreover, clinical results showed the efficiency, feasibility, and safety of applying autologous ASCs in the human maxillary sinus floor elevation, and high angiogenic power of SVF. The potential of ASCs to stimulate osteogenesis and angiogenesis offers a promising solution for the field of bone tissue engineering (3).

Previously, we found that within the short time frame of the one-step surgical procedure, *ex vivo* exposure to a physiological concentration (10 ng/ml) of recombinant human bone morphogenetic protein-2 (rhBMP2) for 10-30 minutes caused a pronounced increase in proliferation and acceleration of osteogenic differentiation (6). However, rhBMP2 is rather expensive and associated with some adverse effects when not properly used (7). Since 1,25-$(OH)_2VitD_3$ is a well-known accelerator of osteoblast differentiation and mineralization (8, 9) as well as a potent osteogenic inducer of ASC differentiation and mechano-responsiveness (10), we tested whether 1,25-$(OH)_2VitD_3$ could be a cheaper while equally effective alternative to rhBMP2.

Since 1,25-$(OH)_2VitD_3$ plays an active role in bone regeneration, many studies have investigated the effect of different types of calcitriol administration on osteogenic differentiation and bone formation. For instance, the intraperitoneal administration of 1,25-$(OH)_2VitD_3$ after implantation of beta-tricalcium phosphate (β-TCP) loaded with ASCs contributed to the increase of bone volume (11). Similarly, local administration of 1,25-$(OH)_2VitD_3$ into rat mandibular bone defects revealed significantly higher bone volume after 1 and 2 weeks and more mineralized bone and uniform collagen structure after 4 and 8 weeks (12). Although, the osteogenic markers, including alkaline phosphatase, osteopontin and osteocalcin were enhanced by 25-hydroxyvitamin D_3 and 1,25-$(OH)_2VitD_3$ in a dose-dependent manner. Also, 10 nM 1,25-$(OH)_2D_3$ promoted ALP activity and osteogenic differentiation more than 0.05, 0.1, and 1 nM (8).

Earlier, we found that biphasic calcium phosphate scaffolds (BCP) can be used as bone substitute material for dental and orthopedic applications (13), and clinical results have shown that BCP, containing 20% HA and 80% β-TCP (BCP20/80) (Institut Straumann AG, Switzerland), might give a superior performance as a scaffold for bone augmentation in maxillary sinus floor elevation compared to BCP that composed of 40% HA and 60% β-TCP (BCP40/60), owing to more bone formation and osteoid deposition (13).

Therefore, the aim of this study was to indicate the osteogenic and angiogenic response of hASCs to short (30 minutes) pre-treatment with 1,25-$(OH)_2VitD_3$, to reveal whether this approach could promote bone regeneration. Moreover, we compared the potency of 1,25-$(OH)_2VitD_3$ for osteogenic induction in this short-term stimulation protocol, to continuous stimulation with the factor.

Materials and Methods

Biphasic calcium phosphate scaffolds

In this experimental study, Straumann Bone Ceramic 20/80 (Institut Straumann AG, Switzerland), a custom-made porous BCP scaffold that composed of 20% HA and 80% β-TCP (BCP20/80) was used as a scaffold. The particle properties include the size range between 500 and 1000 µm, micro-porosity 2%, interconnected pores between 100 and 500 µm, and porosity 90%. The crystal size of BCP 20/80 was 1.0-6.0 µm, and the granules had a specific surface area of 9.5×10^{-3} m^2/g. Surface morphology and characteristics have been previously reported (14).

Donors

Subcutaneous adipose tissue was obtained from residues of abdominal wall resections belonging to 3 healthy female donors (age: 33, 40, 47), who underwent elective surgery for abdominal wall correction at the Tergooi Hospital Hilversum and a clinic in Bilthoven, The Netherlands. The Ethical Review Board of the Vrije Universiteit (VU) Amsterdam University Medical Center, The Netherlands, confirmed the study protocols. All patients signed informed consent. Phenotypical and functional characterizations of freshly isolated adipose tissue-derived stem cells have been reported previously by our group (11).

1,25-$(OH)_2VitD_3$ treatment and human adipose stem cells attachment to biphasic calcium phosphate scaffolds

The isolation of hASCs has been described earlier (6). Pooled hASCs from 3 donors at passage 3 were used. hASCs were either or not incubated with 10^{-8} M 1,25-$(OH)_2VitD_3$ at room temperature for 30 minutes. Then, the cells were washed twice with PBS to remove 1,25-$(OH)_2VitD_3$, centrifuged, and resuspended in Dulbecco's Minimum Essential Medium (DMEM, Gibco, Life Technologies, USA) without any supplements. Cells were seeded at the density of 5.5×10^4 cells per 25-35 mg of BCP20/80 scaffold in 2 mL tubes (Eppendorf Biopur®, Germany), and allowed to adhere for 30 minutes to the scaffolds. After washing twice with PBS, scaffolds with attached cells were transferred into 12-well plates with Costar® Transwell® containers (Corning Life Sciences, Lowell, MA, USA) containing expansion medium (DMEM) supplemented with 10% fetal clone I (FCI, ThermoFisher Scientific, USA) as an alternative to fetal bovine serum (FBS), antibiotics [1% penicillin/streptomycin/fungizone (PSF)), 50 µM ascorbic acid (Merck, Germany), and 10 mM β-glycerol phosphate (Merck, Germany). The hASCs-seeded scaffolds were incubated at 5% CO_2 in a humidified incubator at 37˚C for 3 weeks.

DNA quantification

hASCs were treated for 30 minutes with 10^{-8} M 1,25-$(OH)_2VitD_3$, seeded on BCP20/80, and following the initial attachment for 30 minutes, BCP20/80 was washed with PBS, and the number of detached cells was

measured. Unattached hASC from the washing steps were centrifuged and lysed in cOmplete™ Lysis-M buffer (Roche Laboratories, IN, USA) for DNA quantification using the Cyquant Cell Proliferation Assay Kit (Molecular Probes/Invitrogen, Carlsbad, CA, USA) according to the manufacturer's protocols. Absorption was read at 480 nm excitation and 520 nm emission in a Synergy HT spectrophotometer (BioTek Laboratories, PA, USA).

Human adipose stem cell proliferation on biphasic calcium phosphate scaffolds

Proliferation was assessed using AlamarBlue® fluorescent assay (Invitrogen, Frederick, MD, USA), at day 4, 14, and 21, according to the manufacturer's instructions. We observed a linear relationship between AlamarBlue fluorescence and the cell number (data not shown). Fluorescence was measured in medium samples at 530 nm excitation and 590 nm emission using a Synergy HT spectrophotometer.

Colony-forming unit assay

Colony-forming unit assay (CFU) was performed to assess the colony forming capacity of hASCs in hASC culture at passage 3. Cells were seeded in 6-well plates (Greiner Bio-One™, Alphen a/d Rijn, The Netherlands) at concentrations of 1, 5, 10, 50, and 100 cells/well. After 14 days of culture, 4% formaldehyde was prepared to fix the cells, and then 0.2% toluidine blue in the borax buffer (PH=12) was used for 1 minute to stain the cells. A colony was specified as a visible mass of the cells which composed of more than 10 clustered cells. Colony counting was performed under a light microscope at 100x magnifications. The percentage of CFU per total number of hASCs was reported.

Alkaline phosphatase activity

Alkaline phosphatase (ALP) activity can signify the initiation of osteogenic differentiation of hASC seeded on BCP20/80 scaffolds. After 4, 14, and 21 days of culture, scaffolds were transferred into 24-well culture plates (Cellstar, Germany) and washed with PBS. The cells were lysed with cOmplete™ Lysis-M buffer to assess ALP activity and protein contents. P-nitrophenyl-phosphate (Fluka, Poole, UK) at pH=10.3 was designated as the substrate for ALP. The absorbance was read at 405 nm. ALP activity was normalized to cellular protein and expressed as µmoles of p-nitrophenol formed per hour per milligram of cellular protein. After 4, 7, and 14 days of culture, ALP activity was also visualized using nitro blue tetrazolium chloride/5-bromo-4-chloro-3-indolyl phosphate (NBT/BCIP; Roche, Germany) following the standard protocols. Assessment of protein content was carried out by a BCA Protein Assay Reagent Kit (Pierce™, Rockford, III, USA), and the absorbance was measured at 540 nm with a Synergy HT spectrophotometer.

Analysis of gene expression

Total RNA was isolated from hASCs (from 3 donors) cultured on BCP20/80 scaffolds for 4, 14, and 21 days, using TRIzol® reagent (Life Technologies™) according to the manufacturer's instructions, and stored at -80˚C until further use. cDNA was synthesized using a thermocycler GeneAmp® PCR System9700 PE (Applied Biosystems, Foster City, CA, USA), using SuperScript® VILO™ cDNA Synthesis Kit (Life Technologies™, USA) with 0.1 µg total RNA in a 20 µL reaction mix containing VILO™ Reaction Mix and SuperScript® Enzyme Mix. cDNA was stored at -20˚C before the real-time PCR analysis.

Real-time PCR reactions were run in a LightCycler® (Roche Diagnostics) using 1 µL of 5x diluted cDNA and SYBR® Green Mastermix (Roche Laboratories, IN, USA), according to the manufacturer's protocols, for the following cycles: 10 minutes pre-incubation at 95˚C, followed by 45 cycles of amplification at 95˚C for 2 seconds, 56˚C for 8 seconds, 72˚C for 10 seconds, and 82˚C for 5 seconds, after which melting curve analysis was performed. In each run, the reaction mixture without cDNA was used as the negative control. All primers used for real-time PCR were procured from Life Technologies™ (Table 1). The relative gene expression was normalized against the relative human 14-3-3 protein zeta/delta (*YWHAZ*) and hypoxanthine-guanine phosphoribosyltransferase (*HPRT*) as housekeeping genes. Real-time polymerase chain reaction (PCR) was used to determine the expression of Runt-related transcription factor 2 (*RUNX2*), *ALP*, osteonectin (*SPARC*), osteopontin (*OPN*), dentin matrix acidic phosphoprotein 1 (*DMP1*), proliferation marker *ki-67*, vitamin D nuclear receptor *VDR*, cytochrome p450-enzyme (*CYP24*), and vascular endothelial growth factor (*VEGF*). In each assay, for osteogenic markers, cDNA from osteoblasts or human reference (Agilent Technologies, Stratagene Products Division, La Jolla, CA, USA) was used as the reference DNA. Crossing points were plotted versus the serial dilutions of the known concentrations of the reference DNA (2.5-0.004 ng/µL) using the Light Cycler® software (version 1.2). The gene expression analysis was studied between the cells treated with or without 1,25-$(OH)_2VitD_3$ treatment.

Statistical analysis

The obtained data were analyzed by the GraphPad software version 5 (GraphPad Software, USA) and expressed as the means and standard error of the mean (mean ± SEM). To assess the statistical significance between the experimental groups, Student's t test, and two-way analysis of variance (ANOVA) were conducted where appropriate. The level of significance was set at $P<0.05$. All experiments were performed in triplicate.

Results

Human adipose stem cell attachment to biphasic calcium phosphate scaffold

The number of CFU was counted 14 days after the cell culture of non-treated hASCs on tissue culture plastic. CFU-f frequency of non-treated hASCs was

around 53%, representing the number of viable hASCs in adipose tissue (Fig.1A). Pretreatment of hASCs with 1,25-$(OH)_2VitD_3$ for 30 minutes increased the attachment of cells to BCP20/80 scaffolds by 1.5-fold (from 54 to 83%) at seeding time compared to non-treated cells (Fig.1B).

Table 1: Primer sequences for the evaluation of angiogenesis and osteogenesis through real-time polymerase chain reaction

Target gene (human)	**Primer sequence (5′-3′)**
YWHAZ	F: GATGAAGCCATTGCTGAACTTG
	R: CTATTTGTGGGACAGCATGGA
HPRT	F: GCTGACCTGCTGGATTACAT
	R: CTTGCGACCTTGACCATCT
RUNX2	F: ATGCTTCATTCGCCTCAC
	R: ACTGCTTGCAGCCTTAAAT
ALP	F: AGGGACATTGACGTGATCAT
	R: CCTGGCTCGAAGAGACC
SPARC	F: CTGTCCAGGTGGAAGTAGG
	R: GTGGCAGGAAGAGTCGAAG
Ki-67	F: CCCTCAGCAAGCCTGAGAA
	R: AGAGGCGTATTAGGAGGCAAG
OPN	F: TTCCAAGTAAGTCCAACGAAAG
	R: GTGACCAGTTCATCAGATTCAT
DMP1	F: TAGGCTAGCTGGTGGCTTCT
	R: AACTCGGAGCCGTCTCCAT
VDR	F: GACACAGCCTGGAGCTGAT
	R: CAGGTCGGCTAGCTTCTGGA
CYP24a1	F: AGCCTGCTGGAAGCTCTGTACC
	R: TGTTCAGCTCGCTGTACAAGTC
$VEGF_{189}$	F: ATCTTCAAGCCATCCTGTGTGC
	R: CACAGGGAACGCTCCAGGAC

Effect of 30 minutes pre-treatment with calcitriol on human adipose stem cell proliferation

Thirty minutes pre-treatment with calcitriol significantly increased the cell number after 2 and 3 weeks compared to continuous treatment. Thirty minutes pre-treatment with 1,25-$(OH)_2VitD_3$ increased the cell number at day 14 by 3.5-fold, and at day 21 by 2.6-fold. Continuous treatment with 1,25-$(OH)_2VitD_3$ for 3 weeks increased the cell number only at day 14 by 1.7-fold, but not at day 21 compared to non-treated controls (Fig.1C).

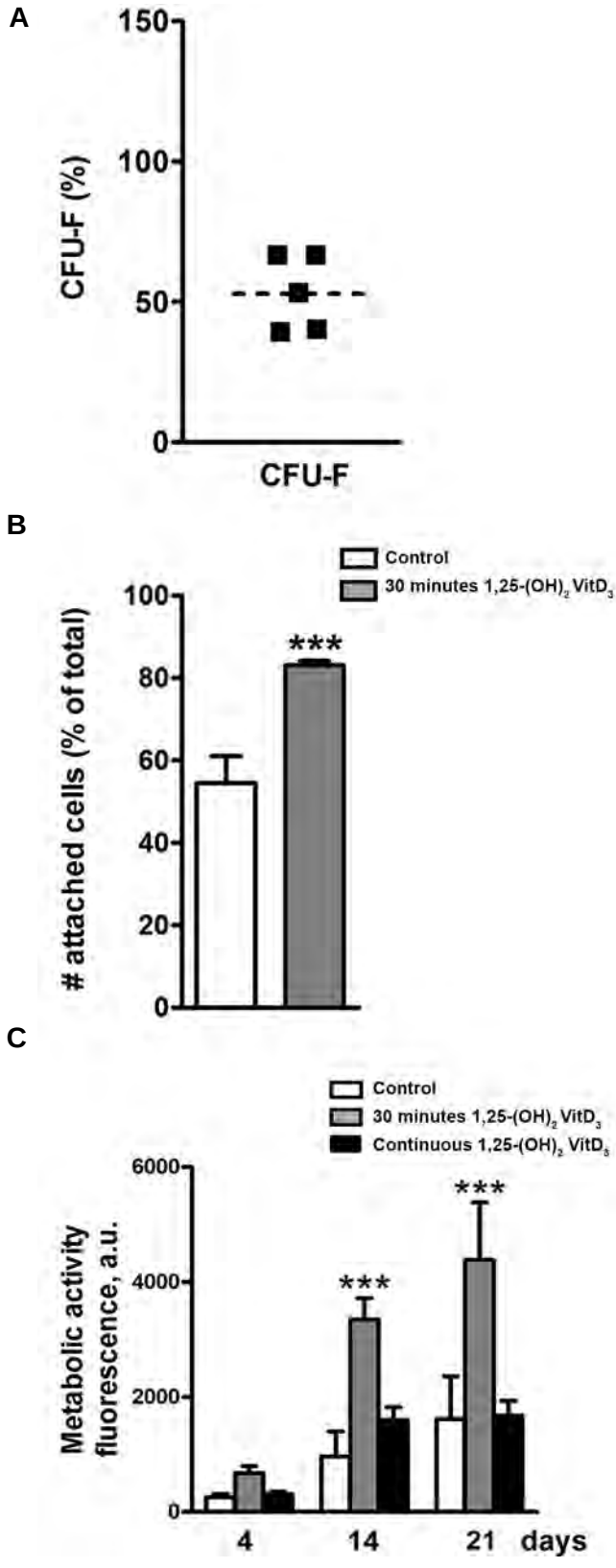

Fig.1: hASC attachment to BCP20/80 scaffold with or without 1,25-$(OH)_2VitD_3$ at day 0 and the effect of 1,25-$(OH)_2VitD_3$ treatment on the metabolic activity of hASCs. **A.** The average of CFU of non-treated hASCs cultured on tissue culture plastic for 2 weeks was nearly 53% (dotted line), **B.** Cell attachment to BCP after 30 minutes pre-treatment with 10^{-8} M 1,25-$(OH)_2VitD_3$ was significantly increased compared to controls, and **C.** Thirty minutes incubation with 1,25-$(OH)_2VitD_3$ significantly increased the proliferation after 14 and 21 days compared to continuous treatment with 1,25-$(OH)_2VitD_3$. Values are expressed as mean ± SEM (n=3). hASCs; Human adipose stem cells, BCP; Biphasic calcium phosphate, CFU; Colony forming unit, and ***; Significantly different from control, P<0.001.

Effect of 30 minutes pre-treatment with 1,25-$(OH)_2VitD_3$ on alkaline phosphatase activity in human adipose stem cells

Thirty minutes pre-treatment of hASCs with 1,25-$(OH)_2VitD_3$ significantly increased ALP activity in hASCs after 2 and 3 weeks of the cell culture compared to continuous treatment with 1,25-$(OH)_2VitD_3$ and non-treated hASCs. ALP activity in hASCs after 30 minutes pre-treatment with 1,25-$(OH)_2VitD_3$ was increased by 18.5-fold compared to non-treated cells after 2 weeks, while ALP activity of continuous treatment with 1,25-$(OH)_2VitD_3$ was increased 2.6-fold compared to non-treated cells after 2 weeks (Fig.2). This was confirmed by ALP staining after 14 days of the cells culture (Fig.3).

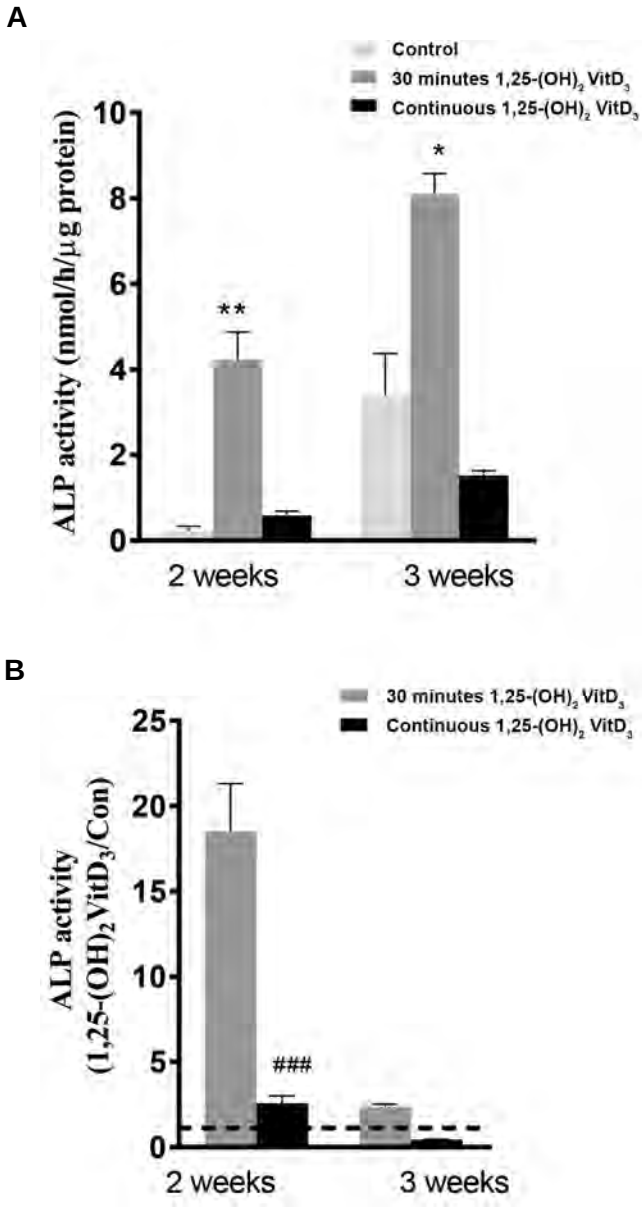

Fig.2: Short (30 minutes) versus long (3 weeks) 1,25-$(OH)_2VitD_3$ treatment effects on ALP activity in hASCs. Thirty minutes incubation with 1,25-$(OH)_2VitD_3$ increased ALP activity after 2 weeks (18.5-fold) and 3 weeks (2.4-fold). Continuous treatment with 10^{-8} M 1,25-$(OH)_2VitD_3$ increased ALP activity after 2 weeks (2.6-fold), but not at 3 weeks (0.4-fold). Values are presented as mean ± SEM (n=3). ALP; Alkaline phosphatase, hASCs; Human adipose stem cells, *; Significantly different from control, P<0.05, **; P<0.01, and ###; Significantly different from 30 minutes 1,25-$(OH)_2VitD_3$, P<0.001.

Effect of 30 minutes pre-treatment with 1,25-$(OH)_2VitD_3$ on osteogenic gene expression in human adipose stem cells

The stimulatory effect of 30 minutes pretreatment with 1,25-$(OH)_2VitD_3$ on osteogenic gene expression in hASCs seeded on BCP20/80 at day 21 was more pronounced than that of continuous treatment with 1,25-$(OH)_2VitD_3$. The expression of the *Runx2* gene, which is well-known as master transcriptional regulator of skeletogenesis (15), was analyzed and found that thirty minutes pretreatment of hASCs with 1,25-$(OH)_2VitD_3$ increased the expression of this gene (early osteogenic marker) by 3.6-fold after 2 weeks, and 5.7-fold after 3 weeks compared to non-treated hASCs. However, continuous treatment with 1,25-$(OH)_2VitD_3$ decreased *RUNX2* expression by 0.81-fold after 2 weeks and increased 2.4-fold after 3 weeks (Fig.4A). Thirty minutes pretreatment with 1,25-$(OH)_2VitD_3$ upregulated *ALP* expression, as an early marker of osteoblastic differentiation, in hASCs seeded on BCP20/80 (Fig.4B). Thirty minutes pre-treatment with 1,25-$(OH)_2VitD_3$ increased *SPARC* expression by 2.1-fold at day 14, while continuous treatment decreased the expression of *SPARC* by 0.8-fold (Fig.4C). *SPARC* regulates the activity of osteoblasts and osteoclasts, and it is expressed in osteoblasts undergoing active matrix deposition (16).

The expression of a proliferation marker *Ki-67* was decreased in cells pre-treated with 1,25-$(OH)_2VitD_3$ for 30 minutes but did not change when treated with 1,25-$(OH)_2VitD_3$ in continuous mode during 3 weeks of the cell culture (Fig.4D). The gene expression of *OPN*, which is considered crucial for bone remodeling and bio-mineralization (17), was upregulated in continuous treatment at day 4, whereas 30 minutes pretreatment of hASCs with 1,25-$(OH)_2VitD_3$ increased *OPN* expression at day 21 (Fig.4E). A gradual; however, no significant increase in *DMP1* gene expression, was observed over time (Fig.4F). *DMP1* is a highly-expressed bone extracellular matrix protein that regulates both bone development and phosphate metabolism (18).

1,25-$(OH)_2D_3$ exerts its actions via a nuclear vitamin D receptor (*VDR*), and it is regarded as the most active form of vitamin D (8). Thirty minutes pre-treatment with 1,25-$(OH)_2VitD_3$ increased *VDR* gene expression in hASCs compared to continuous treatment, with maximal stimulation at day 14 (Fig.4G). Continuous treatment with 1,25-$(OH)_2VitD_3$ increased, interestingly, the *CYP24* gene, associated with inactivation of vitamin D_3. *CYP24*, as one of the most vitamin D-responsive genes (8), was not expressed in non-treated controls and cells pretreated with 1,25-$(OH)_2VitD_3$ for 30 minutes, but significantly increased in cells treated with 1,25-$(OH)_2VitD_3$ in a continuous mode for 3 weeks (Fig.4H). The expression of the $VEGF_{189}$ gene was increased in hASCs pre-treated cells with 1,25-$(OH)_2VitD_3$ for 30 minutes but reached almost at baseline in cells in a continuous treatment mode. The expression of $VEGF_{189}$ in cells pretreated with 1,25-$(OH)_2VitD_3$ for 30 minutes was increased by 1.5-fold at day 21, but decreased in the continuous treatment method by 0.6-fold compared to non-treated hASCs (Fig.4I).

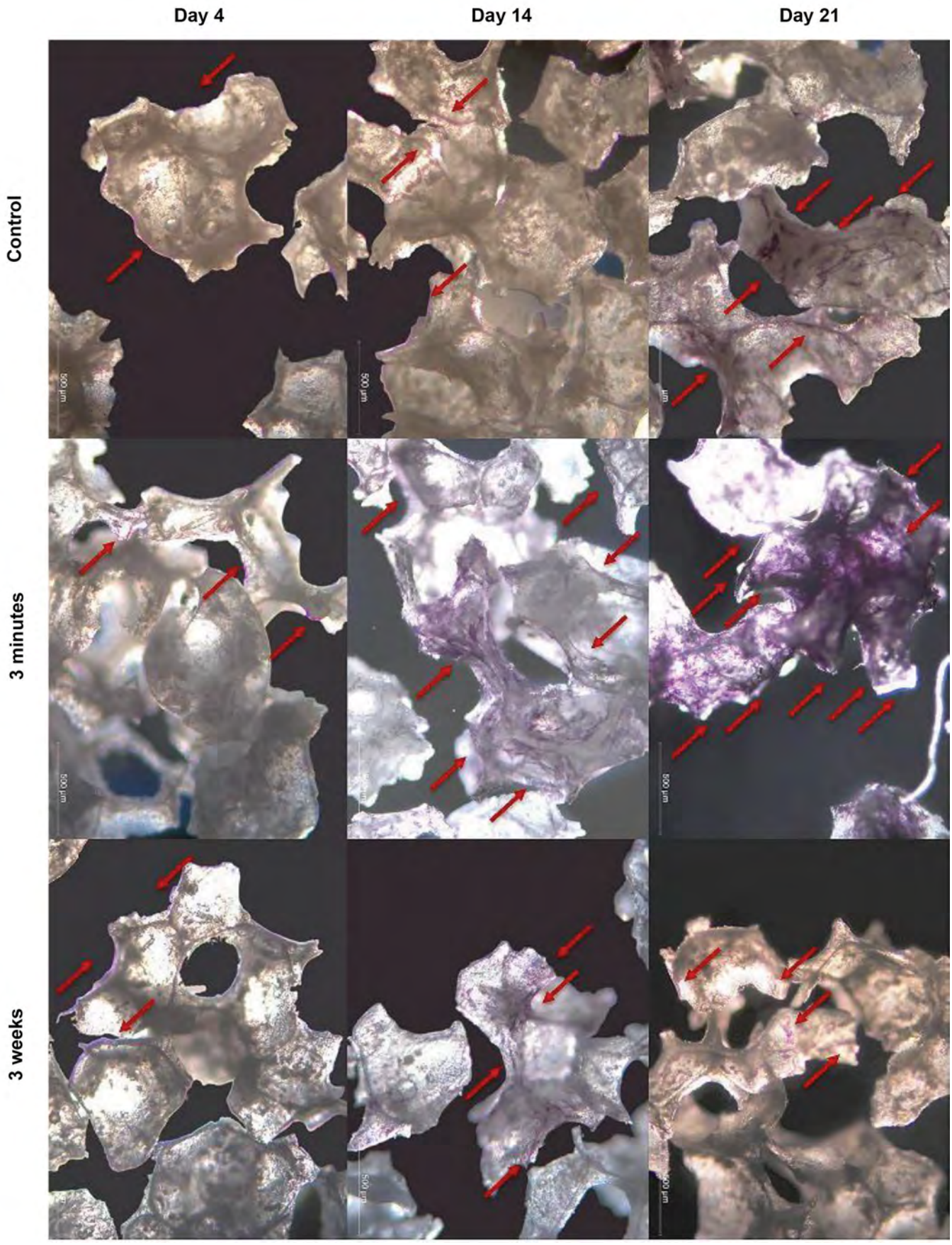

Fig.3: The effects of short (30 minutes) versus long (3 weeks) treatment with 1,25-$(OH)_2VitD_3$ on ALP activity. hASCs were stained to detect ALP activity using NBT/BCIP. Pretreatment with 1,25-$(OH)_2VitD_3$ for 30 minutes notably increased ALP activity after 2 and 3 weeks compared to the continuous treatment. Red arrows show ALP activity of hASCs. ALP; Alkaline phosphatase, hASCs; Human adipose stem cells, and NBT/BCIP; Nitro blue tetrazolium chloride/5-bromo-4-chloro-3-indolyl phosphate (scale bar: 500 µm).

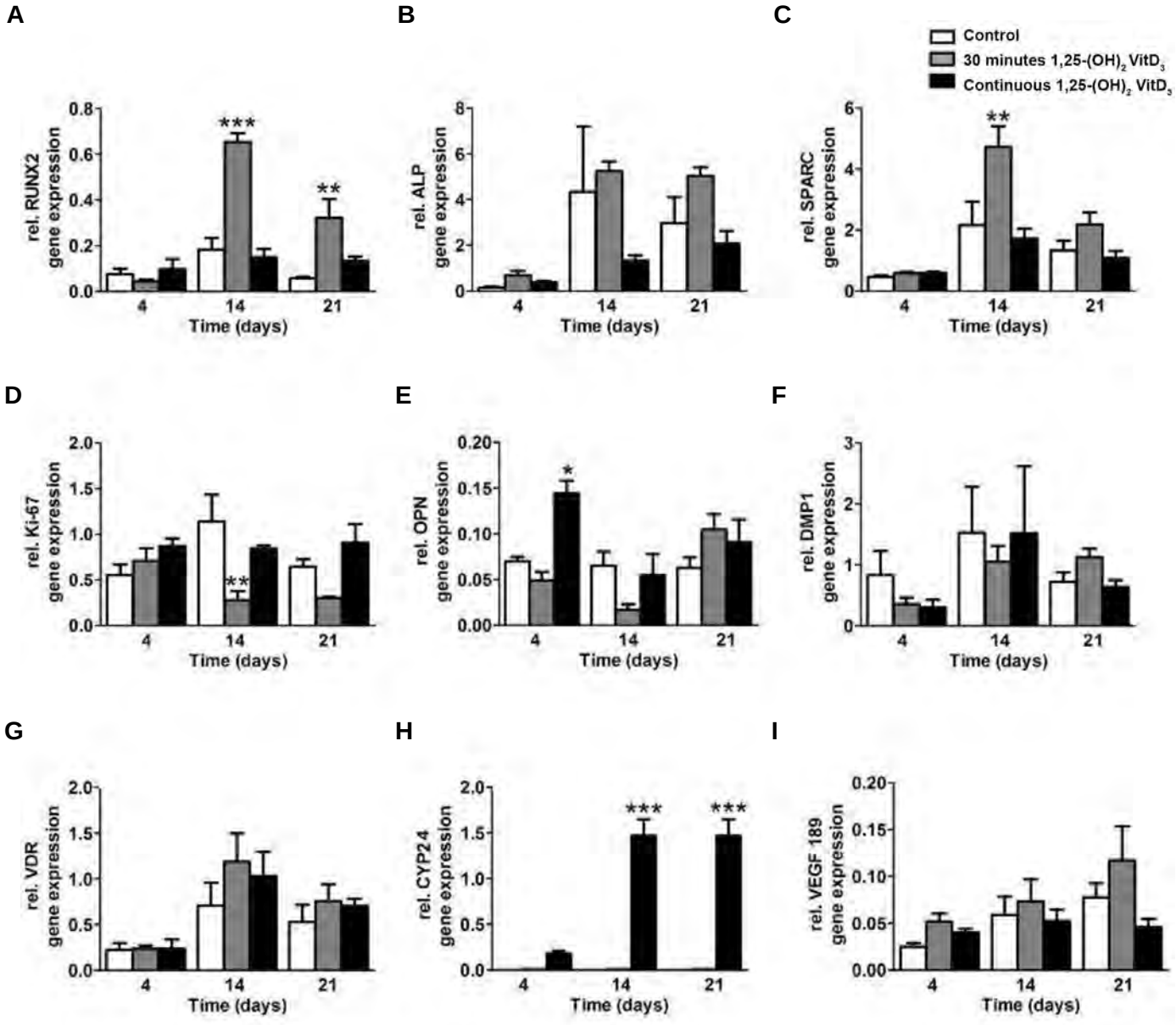

Fig.4: The impact of short (30 minutes) versus long (3 weeks) treatment of hASCs with 1,25-$(OH)_2VitD_3$ on osteogenic gene expression in hASCs. **A.** 30 minutes incubation with 1,25-$(OH)_2VitD_3$ increased *RUNX2* (early osteogenic marker), **B.** *ALP* (intermediate osteogenic marker) expression in hASCs after 2 and 3 weeks compared to continuous treatment with 1,25-$(OH)_2VitD_3$, **C.** 30 minutes pretreatment with 1,25-$(OH)_2VitD_3$ upregulated *SPARC* (late osteogenic marker) expression at day 14. The treatment with 1,25-$(OH)_2VitD_3$ also affected the expression of **D.** *ki-67* (proliferative marker), **E.** *OPN* (intermediate osteogenic marker), **F.** *DMP1* (late osteogenic marker), **G.** *VDR*, **H.** *CYP24*, and **I.** $VEGF_{189}$ in hASCs. Values are expressed as mean ± SEM (n=3). ALP; Alkaline phosphatase, hASCs; Human adipose stem cells, BCP; Biphasic calcium phosphate, *; Significantly different from control, P<0.05, **; P<0.01, and ***; P<0.001.

Discussion

In the current study, we evaluated whether a short pre-treatment of hASCs with 1,25-$(OH)_2VitD_3$ would result in a prolonged stimulatory effect on osteogenic differentiation *in vitro*. The ultimate goal was to move one step closer to the one-step surgical procedure, as described earlier (13). We found that hASCs showed differential responses after pre-treatment of hASCs with 10^{-8} M 1,25-$(OH)_2VitD_3$ for 30 minutes More specifically, we observed that i. Pre-treated hASCs with 1,25-$(OH)_2VitD_3$ adhered better to BCP20/80 scaffolds compared to non-treated hASCs, ii. Proliferation and several osteogenic differentiation markers (ALP activity, *RUNX2*, and *SPARC* gene expression) were significantly enhanced when pretreated with1,25-$(OH)_2VitD_3$ for 30 minutes compared to control treatment, iii. The effect of short (30 minutes) pre-treatment of hASCs with 1,25-$(OH)_2VitD_3$ on osteogenic differentiation was more pronounced compared to continuous treatment with 1,25-$(OH)_2VitD_3$, and (iv) 30 minutes pre-treatment with 1,25-$(OH)_2VitD_3$ may contribute to the promotion of angiogenesis.

We found the rapid attachment of hASCs to BCP scaffolds, which was in agreement with previous findings by our group for other types of scaffolds consisting of polymeric, collagenous (19), β-TCP, and BCP20/80 biomaterials (slightly a higher attachment rate compared

to β-TCP) (6). Interestingly, our data indicated a significantly higher attachment rate for the pre-treated hASCs on BCP scaffolds (1.5-fold) when compared with non-treated hASCs, which is in contrast to findings by Overman and colleagues, who found no effect of bone morphogenetic protein-2 (BMP-2), a member of the transforming growth factor-b superfamily, on attachment in an identical setting (6). Hence, 30 minutes pre-treatment with 1,25-$(OH)_2VitD_3$ appears superior to BMP2 in this regard, which may benefit the one-step surgical procedure.

Calcitriol plays an autocrine or a paracrine role in the local regulation of cell proliferation and differentiation (8). The increase in cell proliferation of hASCs pre-treated with1,25-$(OH)_2VitD_3$ for 30 minutes was noticeable after 2 and 3 weeks of the incubation period. On the other hand, Three-week continuous treatment significantly decreased the proliferation rate, which is in line with the findings by others using ASCs (20) and primary rat osteoblasts (10). Therefore, enhancement of cell proliferation through 30 minutes pre-treatment with 1,25-$(OH)_2VitD_3$ seems promising for implantation *in vivo* due to the enhanced extracellular matrix formation and consequently, bone formation.

We found that the impact of 30 minutes pre-treatment with 1,25-$(OH)_2VitD_3$ on osteogenic differentiation and ALP activity was more pronounced after 14 days of the cell culture compared to the culture period at day 4 and 21, indicating a time-dependency of the stimulation of hASCs by 1,25-$(OH)_2VitD_3$. The results of continuous treatment with 1,25-$(OH)_2VitD_3$ have also been reported in other studies performed on MC3T3-E1 cells (18), Primary rat osteoblasts (10), mesenchymal stem cells derived from human alveolar periosteum (21), hASCs (22), human dental pulp, and dental follicle cells (23), which are in agreement with our current data. Nevertheless, our findings showed, for the first time, that following 14 days of incubation, ALP activity was significantly increased in hASCs pre-treated with 1,25-$(OH)_2VitD_3$ for 30 minutes compared to cells treated with 1,25-$(OH)_2VitD_3$ in a continuous treatment mode.

Most of the biological activities of 1,25-$(OH)_2VitD_3$, including cell proliferation and differentiation, are considered to be exerted through the *VDR*-mediated control of target genes (24). Moreover, silencing VDR caused a significant decrease in mineralized bone volume after the treatment with 1,25-$(OH)_2VitD_3$ (25). *VDR* gene expression was slightly higher in hASCs pretreated with 1,25-$(OH)_2VitD_3$ for 30 minutes, but had no significant differences when compared between the groups. However, the upregulation of *CYP24* gene expression was observed in hASCs continuously treated with 1,25-$(OH)_2VitD_3$, but not in hASCs in pretreatment method as well as control cells, suggesting an alternative explanation. We speculate that the upregulation of the *CYP24* gene may have resulted in the inactivation of 1,25-$(OH)_2VitD_3$ as a consequence of the long-term treatment with 1,25-$(OH)_2VitD_3$, a mechanism that has also been reported earlier (24, 26). Also, the upregulation of *CYP24* by continuous treatment with 1,25-$(OH)_2VitD_3$ may also explain the findings in the study of De Kok et al. (21), who found that continuous treatment failed to induce bone formation in mesenchymal stem cells pretreated with 1,25-$(OH)_2VitD_3$.

Thirty minutes pre-treatment with 1,25-$(OH)_2VitD_3$ enhanced the expression of $VEGF_{189}$. $VEGF_{189}$ stimulates the endothelial cell proliferation and migration *in vitro* and contributes to the promotion of angiogenesis. Interestingly, *VEGF* participates in the coupling of osteogenesis to angiogenesis and bone healing during different phases of bone repair (16). The expression of *VEGF* is correlated with osteoblastic differentiation, and it is downregulated at the initiation of osteoblastogenesis, while during mineralization, its expression reaches at the highest levels (27). Continuous treatment (21 days) adversely influenced the gene expression of $VEGF_{189}$ in hASCs to a level even below that of non-treated hASCs.

Conclusion

This study demonstrated that 30 minutes stimulation with a low physiological dose of 1,25-$(OH)_2VitD_3$ (10^{-8} M) is sufficient to promote cell attachment to BCP20/80 scaffolds compared to non-treated cells. Moreover, short pre-treatment with calcitriol showed higher proliferation and osteogenic responses than other treatment protocols, including continuous treatment or non-treatment methods. Furthermore, short pre-treatment (30 minutes) with 1,25-$(OH)_2VitD_3$ is expected to promote angiogenesis in bone tissue-engineered constructs. Our findings indicate that a short pre-treatment with 1,25-$(OH)_2VitD_3$ could be a promising solution for a one-step surgical procedure. These results will be extrapolated and implemented in the future development of treatment strategies for large bone defects.

Acknowledgements

The current work belonging to F. Mokhtari-Jafari was financially sponsored by a grant from the University of Tehran for encouraging academically talented students in Iran. There is no conflict of interest in this study.

Authors' Contributions

F.M.-J.; Collection and assembly of data, data analysis and interpretation and manuscript writing. G.A.; Conception and design and manuscript editing. M.M.D.; Data analysis and interpretation and manuscript editing. M.N.H., J.K.-N.; Conception and design, data analysis and interpretation and manuscript editing. B.Z.-D.; Conception and design, collection and assembly of data, data analysis and interpretation. All authors read and approved the final manuscript.

References

1. Diaz-Tocados JM, Herencia C, Martinez-Moreno JM, Montes de Oca A, Rodriguez-Ortiz ME, Vergara N, et al. Magnesium chloride promotes osteogenesis through notch signaling activation and expansion of mesenchymal stem cells. Sci Rep. 2017; 7(1): 7839.
2. Amini AR, Laurencin CT, Nukavarapu SP. Bone tissue engineering: recent advances and challenges. Crit Rev Biomed Eng. 2012;

40(5): 363-408.
3. Farré-Guasch E, Bravenboer N, Helder MN, Schulten EAJM, Ten Bruggenkate CM, Klein-Nulend J. Blood vessel formation and bone regeneration potential of the stromal vascular fraction seeded on a calcium phosphate scaffold in the human maxillary sinus floor elevation model. Materials (Basel). 2018; 11(1). pii: E161.
4. Du J, Xie P, Lin S, Wu Y, Zeng D, Li Y, et al. Time-phase sequential utilization of adipose-derived mesenchymal stem cells on mesoporous bioactive glass for restoration of critical size bone defects. ACS Appl Mater Interfaces. 2018; 10(34): 28340-28350.
5. Prins HJ, Schulten EA, Ten Bruggenkate CM, Klein-Nulend J, Helder MN. Bone regeneration using the freshly isolated autologous stromal vascular fraction of adipose tissue in combination with calcium phosphate ceramics. Stem Cells Transl Med. 2016; 5(10): 1362-1374.
6. Overman JR, Farré-Guasch E, Helder MN, ten Bruggenkate CM, Schulten EA, Klein-Nulend J. Short (15 minutes) bone morphogenetic protein-2 treatment stimulates osteogenic differentiation of human adipose stem cells seeded on calcium phosphate scaffolds in vitro. Tissue Eng Part A. 2013; 19(3-4): 571-581.
7. James AW, LaChaud G, Shen J, Asatrian G, Nguyen V, Zhang X, et al. A review of the clinical side effects of bone morphogenetic protein-2. Tissue Eng Part B Rev. 2016; 22(4): 284-297.
8. Lou YR, Toh TC, Tee YH, Yu H. 25-Hydroxyvitamin D3 induces osteogenic differentiation of human mesenchymal stem cells. Sci Rep. 2017; 7: 42816.
9. van der Meijden K, Bakker AD, van Essen HW, Heijboer AC, Schulten EA, Lips P, et al. Mechanical loading and the synthesis of 1,25(OH)2D in primary human osteoblasts. J Steroid Biochem Mol Biol. 2016; 156: 32-39.
10. Knippenberg M, Helder MN, Doulabi BZ, Semeins CM, Wuisman PI, Klein-Nulend J. Adipose tissue-derived mesenchymal stem cells acquire bone cell-like responsiveness to fluid shear stress on osteogenic stimulation. Tissue Eng. 2005; 11(11-12): 1780-1788.
11. Varma MJ, Breuls RG, Schouten TE, Jurgens WJ, Bontkes HJ, Schuurhuis GJ, et al. Phenotypical and functional characterization of freshly isolated adipose tissue-derived stem cells. Stem Cells Dev. 2007; 16(1): 91-104.
12. Xie X, Zhu J, Hu X, Dai L, Fu X, Zhang J, et al. A co-culture system of rat synovial stem cells and meniscus cells promotes cell proliferation and differentiation as compared to mono-culture. Sci Rep. 2018; 8(1): 7693.
13. Helder MN, van Esterik FAS, Kwehandjaja MD, Ten Bruggenkate CM, Klein-Nulend J, Schulten E. Evaluation of a new biphasic calcium phosphate for maxillary sinus floor elevation: Micro-CT and histomorphometrical analyses. Clin Oral Implants Res. 2018; 29(5): 488-498.
14. van Esterik FA, Zandieh-Doulabi B, Kleverlaan CJ, Klein-Nulend J. Enhanced osteogenic and vasculogenic differentiation potential of human adipose stem cells on biphasic calcium phosphate scaffolds in fibrin gels. Stem Cells Int. 2016; 2016: 1934270.
15. Chan CKF, Gulati GS, Sinha R, Tompkins JV, Lopez M, Carter AC, et al. Identification of the Human Skeletal Stem Cell. Cell. 2018; 175(1):43-56. e21.
16. Hu K, Olsen BR. Vascular endothelial growth factor control mechanisms in skeletal growth and repair. Dev Dyn. 2017; 246(4): 227-234.
17. Singh A, Gill G, Kaur H, Amhmed M, Jakhu H. Role of osteopontin in bone remodeling and orthodontic tooth movement: a review. Prog Orthod. 2018; 19(1): 18.
18. Sun Y, Weng Y, Zhang C, Liu Y, Kang C, Liu Z, et al. Glycosylation of dentin matrix protein 1 is critical for osteogenesis. Sci Rep. 2015; 5: 17518.
19. Jurgens WJ, Kroeze RJ, Bank RA, Ritt MJ, Helder MN. Rapid attachment of adipose stromal cells on resorbable polymeric scaffolds facilitates the one-step surgical procedure for cartilage and bone tissue engineering purposes. J Orthop Res. 2011; 29(6): 853-860.
20. Malladi P, Xu Y, Yang GP, Longaker MT. Functions of vitamin D, retinoic acid, and dexamethasone in mouse adipose-derived mesenchymal cells. Tissue Eng. 2006; 12(7): 2031-2040.
21. De Kok IJ, Hicok KC, Padilla RJ, Young RG, Cooper LF. Effect of vitamin D pretreatment of human mesenchymal stem cells on ectopic bone formation. J Oral Implantol. 2006; 32(3): 103-109.
22. Song I, Kim BS, Kim CS, Im GI. Effects of BMP-2 and vitamin D3 on the osteogenic differentiation of adipose stem cells. Biochem Biophys Res Commun. 2011; 408(1): 126-131.
23. Khanna-Jain R, Vuorinen A, Sándor GKB, Suuronen R, Miettinen S. Vitamin D(3) metabolites induce osteogenic differentiation in human dental pulp and human dental follicle cells. J Steroid Biochem Mol Biol. 2010; 122(4): 133-141.
24. Lin Z, Chen H, Belorusova AY, Bollinger JC, Tang EKY, Janjetovic Z, et al. 1α,20S-dihydroxyvitamin D3 interacts with vitamin d receptor: crystal structureand route of chemical synthesis. Sci Rep. 2017; 7(1): 10193.
25. O'Brien J, Wilson I, Orton T, Pognan F. Investigation of the Alamar Blue (resazurin) fluorescent dye for the assessment of mammalian cell cytotoxicity. Eur J Biochem. 2000; 267(17): 5421-5426.
26. Bikle DD, Patzek S, Wang Y. Physiologic and pathophysiologic roles of extra renal CYP27b1: Case report and review. Bone Rep. 2018; 8: 255-267.
27. Chen J, Deng L, Porter C, Alexander G, Patel D, Vines J, et al. Angiogenic and osteogenic synergy of human mesenchymal stem cells and human umbilical vein endothelial cells cocultured on a nanomatrix. Sci Rep. 2018; 8(1): 15749.

Original Article

Protective Effect of Royal Jelly against Cyclophosphamide-Induced Thrombocytopenia and Spleen and Bone Marrow Damages in Rats

Fatemeh Khazaei, B.Sc.[1], Elham Ghanbari, M.Sc.[2], Mozafar Khazaei, Ph.D.[2]*

1. Student Research Committee, Kermanshah University of Medical Sciences, Kermanshah, Iran
2. Fertility and Infertility Research Center, Health Technology Institute, Kermanshah University of Medical Sciences, Kermanshah, Iran

Corresponding Address: P.O.Box: 6714869914, Fertility and Infertility Research Center, Health Technology Institute, Kermanshah University of Medical Sciences, Kermanshah, Iran
Email: mkhazaei1345@yahoo.com

Received: 15/January/2019, Accepted: 17/April/2019

Abstract

Objective: Despite the effective role of chemotherapy in cancer treatment, several side effects have been reported to date. For instance, Cyclophosphamide (CP) induces deleterious effects on both cancer and normal cells. Royal jelly (RJ) has a lot of beneficial properties, such as anti-oxidant and anti-inflammatory activities. The aim of the present study was to examine the protective effect of RJ against CP-induced thrombocytopenia, as well as bone marrow, spleen, and testicular damages in rats.

Material and Methods: In this experimental study, 48 male Wistar rats were divided into six groups (n=8/group); control, CP, RJ (100 mg/kg), RJ (200 mg/kg), RJ (100 mg/kg)+CP, and RJ (200 mg/kg)+CP groups. RJ was administered orally for 14 days. Then, CP at concentrations of 100, 50, and 50 mg/kg was intraperitoneally injected at day 15, 16, 17, respectively. The animals were sacrificed three days after the last injection of CP. Hematological parameters, serum levels of platelet factor 4 (PF4), nitric oxide (NO), and ferric reducing antioxidant power (FRAP) were measured. Also, the pathological analysis of bone marrow, spleen, and testicles was assessed.

Results: CP caused a significant decrease in the number of platelets, white and red blood cells ($P<0.001$), as well as the levels of FRAP ($P<0.01$), whereas the serum levels of PF4 and NO were significantly increased. These detrimental alterations were significantly reversed to the baseline upon pretreatment of rats with RJ in the RJ100+CP and RJ200+CP groups ($P<0.05$). CP caused histological changes in bone marrow, spleen, and testes. Pretreatment with RJ showed noticeable protection against these harmful effects.

Conclusion: RJ prevented CP-induced biochemical and histological damages.

Keywords: Bone Marrow, Cyclophosphamide, Platelet, Spleen, Thrombocytopenia

Cell Journal(Yakhteh), Vol 22, No 3, October-December (Autumn) 2020, Pages: 302-309

Citation: **Khazaei F, Ghanbari E, Khazaei M. Protective effect of royal jelly against cyclophosphamide-induced thrombocytopenia and spleen and bone marrow damages in rats. Cell J. 2020; 22(3): 302-309. doi: 10.22074/cellj.2020.6703.**

Introduction

Cyclophosphamide (CP) is a chemotherapeutic alkylating agent widely used against a variety of malignant tumors and some immune diseases. Also, it also been used as an immunosuppressive agent for organ transplantation, multiple sclerosis, and systemic lupus erythematosus (1). Like other chemotherapeutic drugs, CP has a broad range of side effects such as the reduction in the number of platelets (PLTs), white and red blood cells (WBCs, RBCs). It can cause severe thrombocytopenia, as well (2).

Thrombocytopenia, defined as a decrease in the number of PLTs to less than 150,000/mL, is a common side effect of chemotherapy and one of the lethal hematological disorders (3). Its occurrence is either due to inhibited/insufficient production of PLT in bone marrow or increased destruction of the cells (in malaria and dengue fever). In this context, most of the chemotherapeutic agents can result in the development of thrombocytopenia (4). PLT factor 4 (PF4) is an important mediator in blood coagulation, released from alpha-granules of the activated PLTs. It plays a significant role in blood coagulation, wound healing (5), and inflammation (6). The blood usually contains very low amounts of PF4, and only in pathological conditions, such as sepsis and acute tissue injury, high levels of PF4 release from the activated PLTs into blood (7).

Histological evaluation of the bone marrow in thrombocytopenic patients indicated a marked rise in the number of megakaryocytes, implying that the disorder is mainly caused by the destruction of peripheral PLT without a suitable bone marrow compensation (8). Also, morphological alterations are usually detected in the spleen of patients after the injection of CP, which include the depletion of white and red cells. Also, the bone marrow showed hematopoietic cells reduction (9). As shown in previous studies, the counts of splenic and bone marrow cells are decreased in cyclophosphamide-treated mice due to oxidative stress (OS) caused by the metabolite compounds of CP (10). It is well-known that chemotherapeutic drugs induce thrombocytopenia by two primary mechanisms: an increase in PLT destruction or a decrease in PLT production by apoptosis of megakaryocytes (11).

Also, CP has cytotoxic effects on rapidly proliferating tissues such as testicles which are more sensitive to its

toxic impacts. Following therapy of cancer with CP, oligo- and azoospermia lead to male infertility (12, 13). Moreover, experimental studies have also shown that treatment of mice or rats with CP resulted in decreased sperm counts and sperm motility, as well as the reduced testosterone concentrations (14, 15). On the other hand, CP not only influences cancer cells but also affects normal cells, and it can increase the formation of reactive oxygen species (ROS) and nitric oxide (NO), leading to peroxynitrite generation which damages the cellular proteins, DNA, and lipids (16). It seems that antioxidant compounds should be able to inhibit the harmful effects of ROS during the use of chemotherapy drugs (17).

Royal jelly (RJ) has different medicinal properties, including antioxidant and anti-inflammatory potential, as well as enhancement of immune activity and infertility improvement (18, 19). The antioxidant activity and scavenging potency of RJ were reported against free radicals such as superoxide anions, hydroxyl, and DPPH (1, 1 diphenyl-2-picrylhydrazyl) radicals in several studies. Also, the beneficial effects of RJ supplementation on the reproductive system have been addressed in different animals (19).

Chemotherapy induced-thrombocytopenia is a major clinical problem in cancer therapy. However, no appropriate treatment and/or preventive strategy to resolve this problem. Hence, there is a need for new factors that would be enabled to protect normal cells and tissues against chemotherapy-induced toxicity with no protection against tumor cells. It seems that the combination of the drug with an antioxidant agent can be an appropriate approach to decrease the side effects of CP (20). The aim of this study was to investigate the protective effect of RJ pretreatment against thrombocytopenia, oxidative stress, as well as bone marrow, spleen, and testicular damages induced by CP in rats.

Material and Methods

In this experimental study, male Wistar rats (200 ± 20 g) were kept under standard laboratory conditions at the temperature of 24˚C, the relative humidity of 60-70%, and a 12/12-hour light/dark cycle. All animals had free access to standard chow and tap water. This experimental study was carried out in accordance with the guide for the care and use of laboratory animals and approved by the Local Ethics Committee of Kermanshah University of Medical Sciences with a code number IR.KUMS.REC.1397. 296.

The fresh RJ was provided from local beekeeping (Urmia, Iran), and was stored until the use in a freezer. Also, the quality of RJ was approved by an expert academic member of the Urmia University of Medical Sciences. The CP (Baxter Oncology, Germany Lot No.7E074A) was provided by national Co. (Iran).

Study protocol

Rats were divided into six groups (n=8/group): 1) Control group was orally administered 0.5 ml distilled water (RJ solvent) for 2 weeks. 2) CP group was orally received 0.5 ml distilled water for 14 days, and then CP was injected intraperitoneally (IP) at doses of 100, 50 and 50 mg/kg at days 15, 16, and 17, respectively (21). 3, 4) RJ groups orally received 100 or 200 mg/kg/day RJ for 14 days. 5, 6) RJ+CP groups were orally received 100 or 200 mg/kg/day RJ for 14 days. The doses of RJ were selected based on our pervious study conducted on rats (22). Afterward, CP at concentrations of 100, 50, and 50 mg/kg was administered at days 15, 16, and 17, respectively.

The body weight of rats was measured on day 1, and the day when the study was finished. After 72 hours of the last CP injection, rats were sacrificed after an overnight fast. Blood samples were collected from the heart and divided into two parts; the first part was collected in anticoagulant tubes for blood analysis. Then, sera were isolated from the second part of the blood samples and used for the measurement of PF4, NO, and FRAP levels. Conversely, spleen, femur-derived bone marrow tissue, and testes were removed immediately and fixed in formalin (10%). The weight of spleen were determined, and it ratios to body weight were calculated using the following formulas: [weight of the spleen (g)/body weight of the rat (g)] × 100 (23).

Blood analysis

The blood was collected into tubes containing EDTA as an anticoagulant agent to determine PLTs, WBCs, and RBCs counts using an automated hematology analyzer (Sysmex XW™-100, America).

PF4 measurement

Serum level of PF4 was analyzed using the PF4 ELISA kit according to the manufacturer's instructions. Ultimately, the absorbance was measured at 450 nm with an ELISA reader (Stat fax 100, USA).

FRAP assay

The reduction of Fe^{+3} to Fe^{+2} by antioxidant compounds was monitored (22). The working FRAP solution was prepared by mixing 1 ml of 2,4,6-tripyridyl-s-triazine (40 mM dissolved in 40 mM HCl) and 1 ml of $FeCl_3.6H_2O$ (20 mM in water) with 10 ml of acetate buffer (300 mM, pH=3.6). Next, the mixture was heated to 37˚C for 10 minutes before the use. For a manual FRAP assay, 200 µl of serum samples were added to 1.5 ml of working FRAP solution. The mixtures were incubated in the dark at 37˚C for 30 minutes, and then the absorbance of samples was recorded at 593 nm by a spectrophotometer device.

Nitric oxide assay

The serum levels of NO were determined according to the Griess method (24). Briefly, 400 µL of serum samples were deproteinized by adding 6 mg of zinc sulfate and then centrifuged (12 minutes, 12000 g/4˚C). Standard solutions

were prepared as 0, 6.25, 12.5, 25, 50, 100, and 200 µM nitrite. Afterward, 100 µL of deproteinized samples were poured into wells, and 100 µL of vanadium chloride was added to all wells, followed by rapid addition of 50 µL of sulfanilamide, and 50 µL of N-(1-naphthyl) ethylene diamine di-hydrochloride. The mixture was incubated for 30 minutes, and then the absorbance was measured at the wavelengths of 450 and 630 nm using an ELISA Reader (Statfax 100, USA).

Histopathological analysis

The spleen, femoral bone marrow, and testes were slowly rinsed with phosphate-buffered saline (PBS), dried, weighed, and consequently fixed in 10% formalin. The tissues were dehydrated using the ascending grades of ethanol, then cleared in xylene, and finally embedded in paraffin wax. The tissue sections (5 µm) were prepared and dried at 37˚C in an incubator. The sections were deparaffinized in xylene and rehydrated by the descending grades of ethanol and stained with hematoxylin and eosin. The slides were evaluated for histological analysis under a light microscope (×10 and ×40 magnification). The images were captured by a calibrated microscope connected to a computer equipped with the KECAM software.

For the spleen histological analysis, the following parameters were used: the diameter and count of white pulps per sections, hemosiderin deposition, as well as red and white pulp cellularity. Also, cellularity of femoral bone marrow, including the number of megakaryocytes, was determined. The histological changes in testicular tissues, including seminiferous tubule diameters (STD) and atrophy, were measured (25).

Statistical analysis

All data were expressed as the mean ± SE and analyzed using the SPSS software package version 18 (Inc. Chicago, IL, USA). The difference among the groups was also analyzed by one-way analysis of variance (ANOVA), followed by Duncan post hoc test. The $P<0.05$ were considered statistically significant.

Results

The administration of CP in rats led to a significant ($P<0.001$) decrease in the number of PLTs (48.11 ± 18.35×10³/µl) and caused severe thrombocytopenia. The pretreatment of rats with RJ (100 and 200 mg/kg) increased the number of PLTs in the RJ+CP groups in a dose-dependent manner (Fig.1A). Also, the administration of CP significantly ($P<0.001$) decreased the frequency of WBCs (0.45 ± 0.17×10³/µl), while RJ (100 and 200 mg/kg) increased the number of WBCs in the RJ+CP groups, and the highest increase was observed in the RJ100+CP group which was the same as the control group (Fig.1B). The administration of CP significantly ($P=0.001$) diminished the number of RBCs (5.528 ± 0.46×10⁶/µl), but the reduction was not as great as that of observed in PLTs and WBCs. The administration of RJ increased the number of RBCs in the RJ+CP groups; however, no significant difference was shown when compared with the control group (Fig.1C).

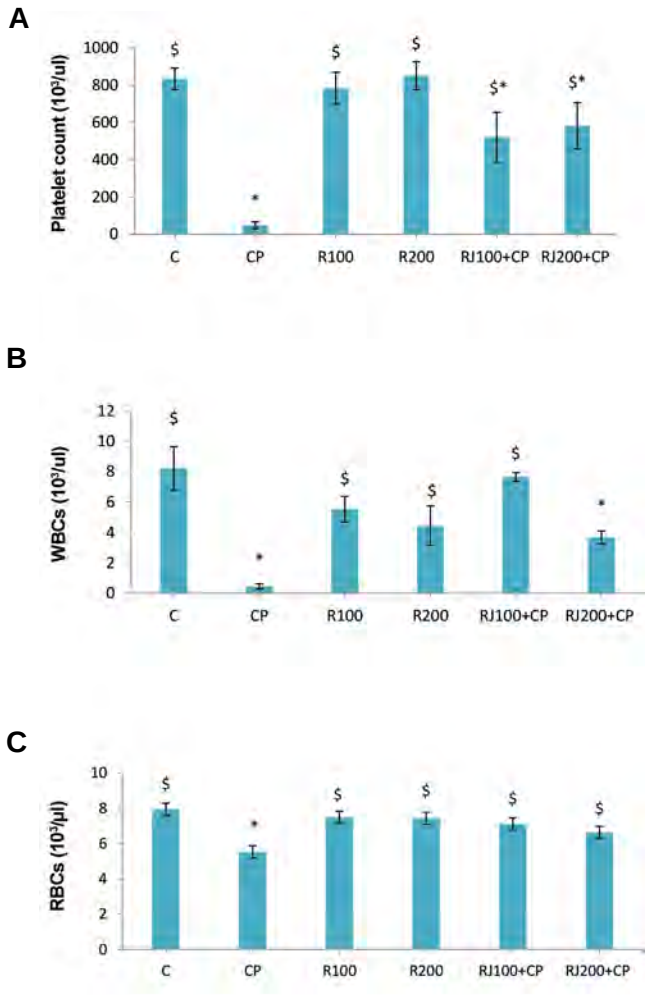

Fig.1: Changes of blood cells in different groups. RJ pretreatment and CP-induced changes in the number of **A.** PLT, **B.** WBCs, and **C.** RBCs. Data are represented as the mean ± SE (n=8). *; Significant ($P<0.05$) difference vs. the control group, $; Significant ($P<0.05$) difference versus the CP group, C; Control, CP; Cyclophosphamide, R; Royal Jelly, PLT; Platelets, WBC; White blood cell, and RBC; Red blood cell.

PF4 levels

CP significantly ($P<0.001$) increased the serum level of PF4 (28.10 ± 1.11 vs. 15.29 ± 4.91 ng/ml). RJ alone caused no change in the concentration of PF4, while it decreased PF4 levels in the RJ+CP groups in a dose-dependent manner and reached the level of PF4 to the normal level as observed in the RJ200+CP group (Fig.2A).

Nitric oxide, and FRAP levels

CP significantly ($P<0.001$) increased NO levels. The level of NO was decreased in the RJ+CP groups in a dose-dependent manner, but RJ alone did not change the concentration of NO (Fig.2B).

The serum levels of FRAP showed a significant decrease in the CP group ($P<0.01$, Fig.2C). There was a significant increase in FRAP levels in the RJ+CP groups compared

to the CP group. RJ (100 and 200) elevated the levels of FRAP when compared to the control group; however, the increase was not statistically significant.

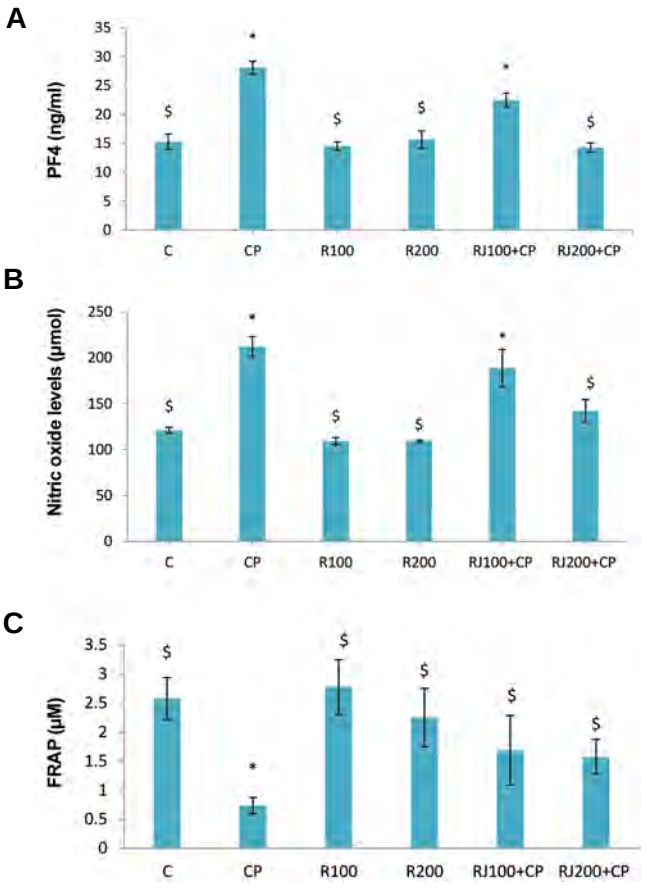

Fig.2: Changes of biochemical factors of serum. The effect of RJ on CP-induced changes of **A.** PF4 level, **B.** NO, and **C.** FRAP in serum samples of study groups. Values are expressed as the mean ± SE (n=8). *; Significant (P< 0.05) difference versus the control group, $; Significant (P<0.05) difference versus the CP group, C; Control, CP; Cyclophosphamide, R; Royal Jelly, PF4; Platelets Factor 4, FRAP; Ferric reducing antioxidant power, and NO; Nitric oxide.

Body weight

CP significantly (P=0.001) decreased BW (164.4 ± 14.5 vs. initial weight 201.9 ± 7.6). RJ treatment increas BW in all groups, and there was no significant difference between RJ groups compared with the control group. RJ protects BW loss in the RJ+CP groups. RJ alone did not change BW, but it increased BW in the RJ+CP groups; however, the increase was not statistically meaningful (Fig.3A). There was a significant increase (P<0.01) in the spleen/BW ratio in the CP group (0.59 ± 0.05 vs. control 0.35 ± 0.01), however, it was normalized in the RJ+CP groups (0.33 ± 0.01 and 0.45 ± 0.06), and no significant difference was found when compared with the RJ groups.

Histological changes

Some histological changes of bone marrow (number of megakaryocyte), spleen (white pulp), and testes (seminiferous tubules) were shown in (Fig.3B-D). In control groups, bone marrow showed normal histology (Fig.4A). CP decreased the number of hematopoietic cells in the bone marrow and showed severe hemorrhage and an increase in the frequency of adipose-like cells (Fig.4B). RJ alone showed no pathological changes in bone marrow (Fig.4C, D). RJ+CP-treated rats protected bone marrow against CP tissue injuries (Fig.4E, F).

The number of megakaryocytes was significantly lower in the CP group compared with other groups, while it was considerably higher in the RJ+CP groups in comparison with other experimental groups (P<0.01, Fig.3B).

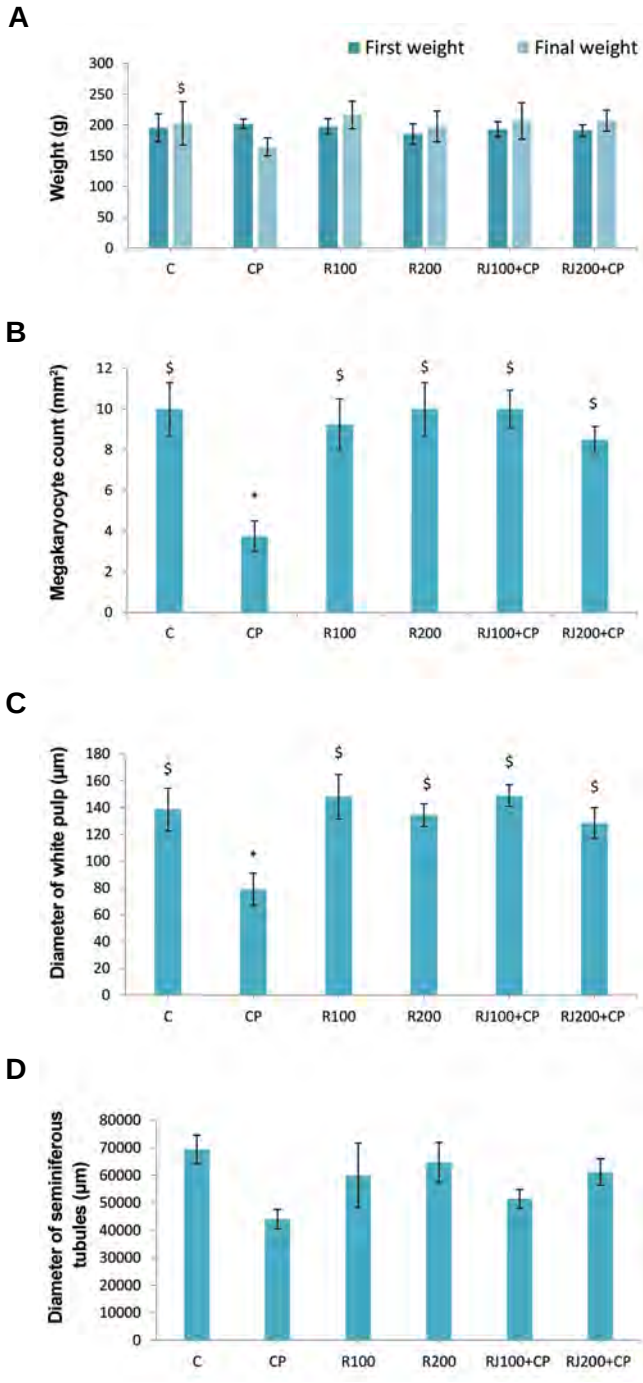

Fig.3: The impact of CP and RJ on the body weight, bone marrow, spleen, and testes in rats. **A.** Initial and final BW, **B.** Count of megakaryocytes, **C.** Diameter of white pulps, and **D.** Diameter of seminiferous tubules in the control and experimental groups. Data are presented as the mean ± SE (n=8). *; Significant (P< 0.05) difference versus the control group, $; Significant (P<0.05) difference versus the CP group, C; Control, CP; Cyclophosphamide, and R; Royal Jelly.

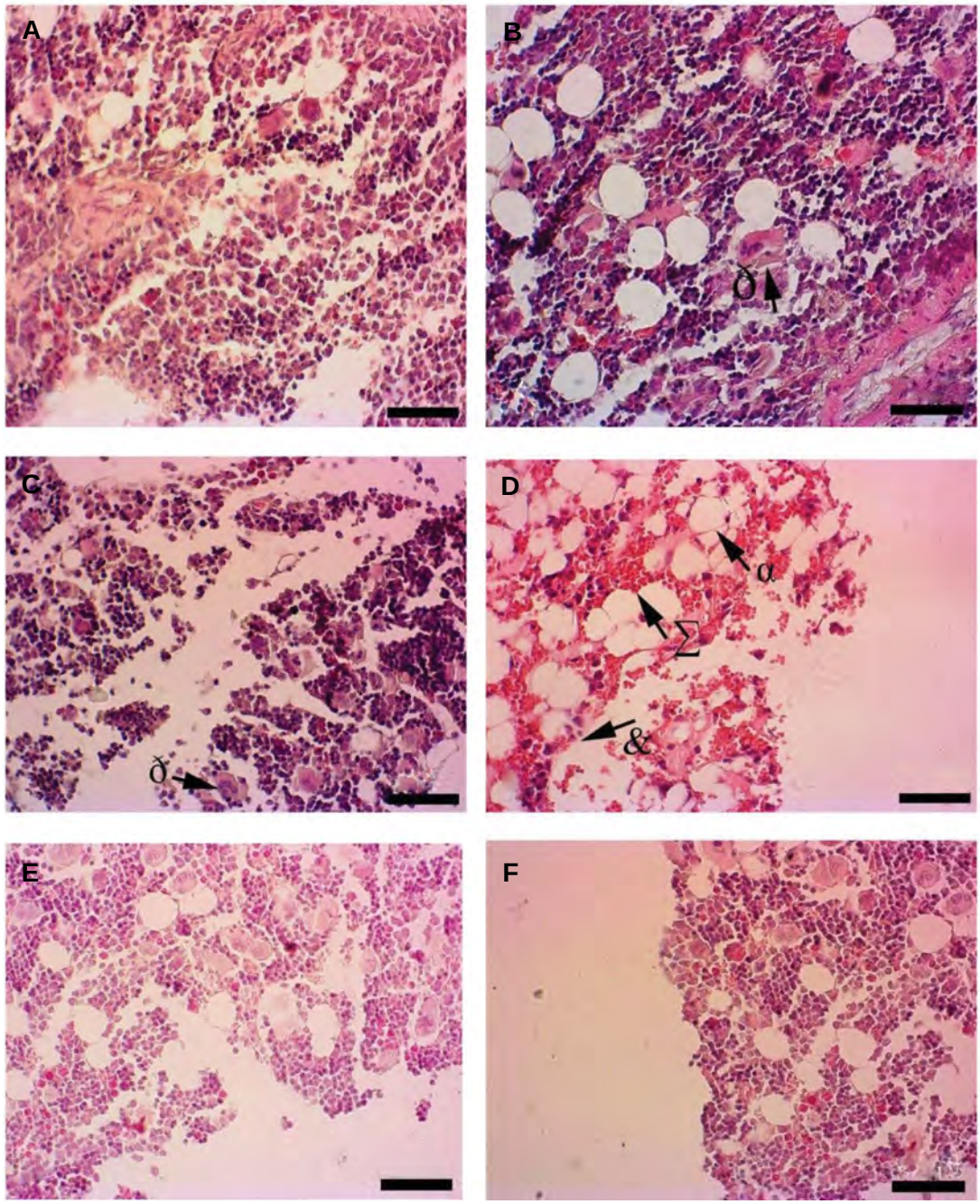

Fig.4: Hisopathological changes of femoral bone marrow in different groups. **A.** The Control, **B.** R100, **C.** R200 groups, showing no pathological changes, megakaryocytes (ð). **D.** The CP group with decreased cellularity in hematopoietic cells (&), severe hemorrhage (∑) and adipose-like cells (α), **E.** CP+100 group, and **F.** CP+200 group (H&E, ×40) (scale bar: 100 µm). CP; Cyclophosphamide and R; Royal Jelly.

Splenic histology didn't showed changes in control group (Fig.5A), CP led to disorganization in splenic structures such as hemosiderin deposition and reduction of the diameter of white pulp (Fig.5B). RJ alone did not affect the structure of spleen (Fig.5C, D) and it was similar to the control group. White pulp diameter in the CP group was significantly decreased; whereas, it was increased in the RJ+CP groups ($P<0.01$, Fig.3C). RJ+CP decreased hemosiderin deposition (Fig.5E, F).

Testicular histology of the control group didn't showed changes (Fig.6A). Severe degenerative alterations were found in the CP group, characterized by a decreased number of germ cells (seminal linage) with disorganized morphology in seminiferous tubules, as well as the presence of multinucleated giant cells (Fig.6B). Cellular arrangement in seminiferous tubules was the same as the RJ and control groups (Fig.6C, D). RJ protects testicular tissues against CP toxicity in the RJ+CP groups (Fig.6E, F). The diameter of seminiferous tubules in the CP group was decreased; however, it was not statistically significant. Also, there was no significant difference when compared with other groups (Fig.3D).

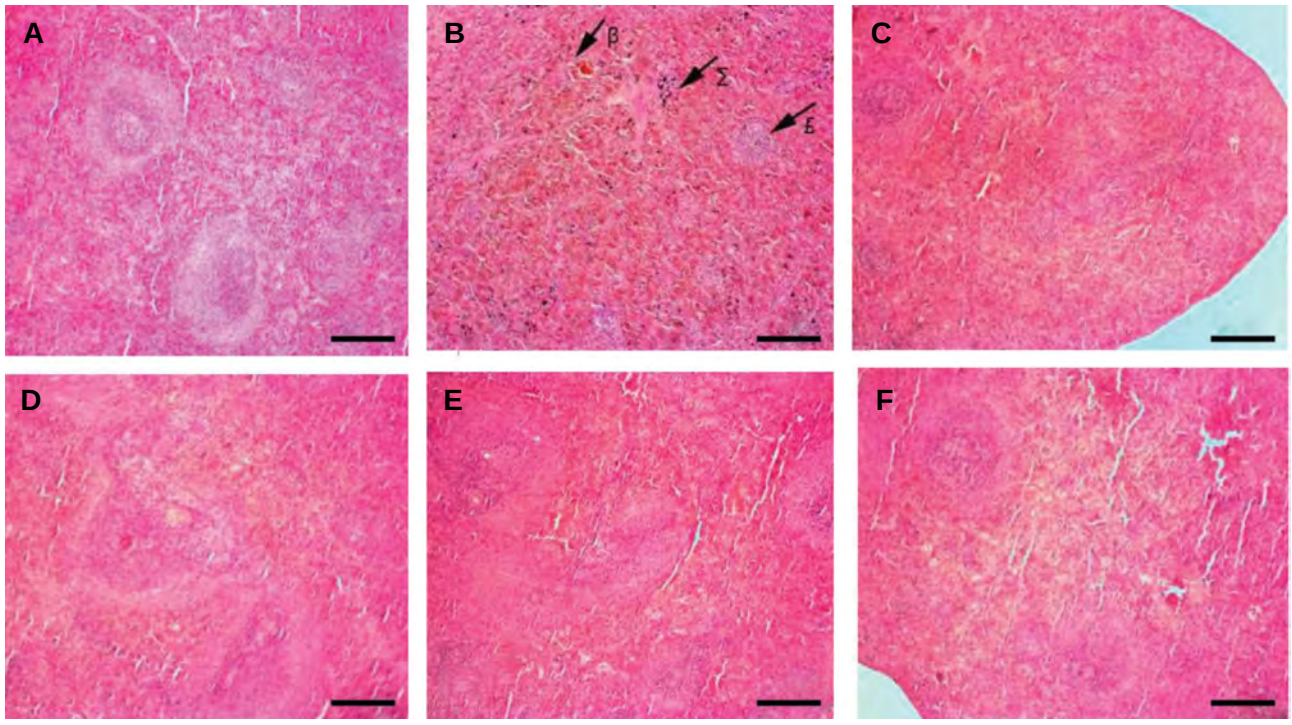

Fig.5: The spleen sections (H&E, ×10). **A.** The control group shows the normal architecture of spleen. **B.** The CP group indicates a decrease in the diameter of white pulps (£), the increase rate of hemorrhage (β), hemosiderin deposition (∑), as well as the red and white pulp cellularity. **C.** The R100, **D.** R200 groups demonstrate the normal structure, **E.** The CP+100, and **F.** CP+200 groups show the decreased hemosiderin deposition (scale bar: 50 µm). CP; Cyclophosphamide and R; Royal Jelly.

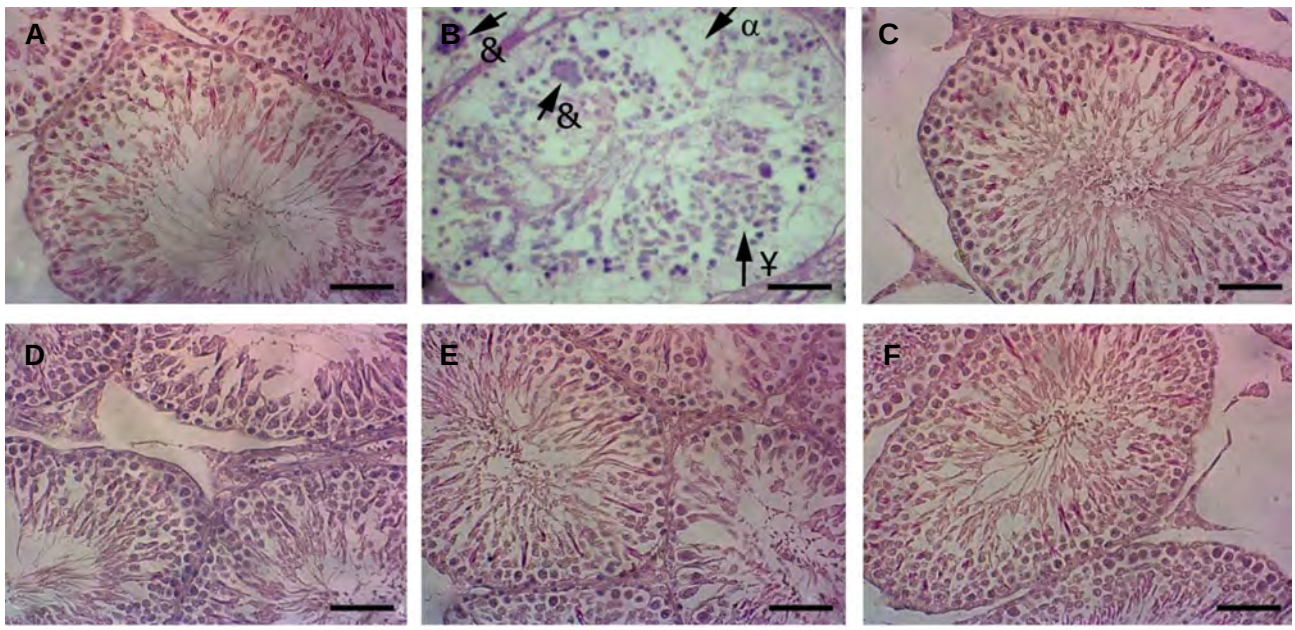

Fig.6: The testicular sections (H&E, ×40). **A.** The control group, **B.** The CP group indicates the severe degenerative changes in seminiferous tubules (¥), decreased number of germ cells (α) and presence of giant multinucleated cells (&). **C.** The R100, **D.** R200 groups were the same as the control group. **E.** The CP+100, and **F.** CP+200 groups show the morphological structure of the seminiferous tubules as the same as the control group (scale bar: 100 µm). CP; Cyclophosphamide and R; Royal Jelly.

Discussion

In this experimental study, RJ pretreatment protected the animals against the side effects of CP injection on the cell number of PLTs and WBCs, levels of serum biochemical factors, and histological structures of bone marrow, spleen, and testes. The main aim of this study was to find anti-thrombocytopenic properties of RJ. To our knowledge, this is the first report on the protective effect of RJ against CP-induced thrombocytopenia and some other side effects. Also, RJ normalizes serum levels of PF4, NO, and FRAP.

The adverse effects of CP in the therapy of solid tumors,

lymphomas, and leukemia are well characterized such as bone marrow suppression, leading to the reduction of PLTs and WBCs, the impairment of organ functions in patients, and the reduction of the quality of life in patients (1, 26). CP-induced thrombocytopenia and leucopenia (27) can increase the PLT destruction and/or reduce the PLTs production in bone marrow (28). It is mainly associated with bleeding and prolonged clotting due to the lowered number of PLTs (29).

The present model of animal thrombocytopenia in rats was introduced by our previous study (21). After CP injection, similar clinical symptoms of thrombocytopenia such as anorexia, diarrhea, weight loss, and alopecia were observed. RJ pretreatment protects thrombocytopenia and leucopenia. These data were in agreement with a previous study, which showed that CP-induced leucopenia in mice (30).

The antioxidant compounds had beneficial effects on the treatment course of patients with immune thrombocytopenia (31). On the other hand, it was documented that the use of antioxidant supplementation protects CP-induced toxicity (32). The protective role of RJ against CP-induced OS could be attributed to its antioxidant properties. It should be noted that the animals in the RJ+CP groups received RJ (14 days) before CP that was injected at days 15, 16, and 17, and no direct interference was evident when RJ and CP were applied. RJ has many components, such as growth factors and immune modulator compounds (19), which can protect bone marrow and other organs against CP toxicity.

PF4 decreased the production of PLTs through the inhibition of colony growth *in vivo* (33). We showed that CP increased the serum levels of PF4 in thrombocytopenic rats. Pretreatment of rats with RJ (100 and 200 mg/kg) dramatically reversed the detrimental effects caused by the administration of CP. RJ has been shown to have strong antioxidant properties, protecting organs, tissues, and cells against oxidative injuries caused by free radicals (19).

CP treatment increased the serum level of NO (one of the indices of oxidative stress) in rats, suggesting that CP can cause oxidative damage. Also, the serum levels of FRAP were lower in the CP group compared with treatment groups. RJ pretreatment increased FRAP levels and decreased the serum levels of NO, indicating that RJ prevented CP-induced elevation of NO and reduction of FRAP.

The count of nucleated cells in the bone marrow is a direct index of the process of hematopoiesis. A reduction in the number of these cells in the CP group showed the acute injuries in bone marrow and apoptosis of these cells, although this damage was not apparent in rats treated with RJ+CP. The spleen can perform compensatory hematopoiesis and restore this hematological process when the bone marrow function is disrupted (34). Consistent with previous studies, we showed that the injection of CP decreased the number of megakaryocytes in the bone marrow (11). However, RJ pretreatment exhibited that megakaryocyte was significantly increased in rats. So, we concluded that RJ pretreatment might mitigate thrombocytopenia through the alleviation of the loss of bone marrow cells in CP-induced cytotoxicity.

The splenic histology changed due to oxidative stress, following the administration of CP. These alterations were significantly improved in the RJ+CP groups, which can be attributed to RJ pretreatment, abrogating CP-induced spleen atrophy. Also, the increase of the diameter of white pulps indicates that RJ pretreatment can promote the recovery of this damage after CP administration.

Patients with cancer have low-antioxidant capacity before initiating therapy; therefore, chemotherapeutic compounds exacerbate OS as indicated by lipid peroxidation and DNA oxidation after and/or during cancer treatment. Natural antioxidants before or after the administration of these agents protect normal cells from additional OS and treatment-induced toxicity (35).

In this study, disorganization in the seminiferous tubules and presence of giant multinucleated cells, and decreased diameter of seminiferous tubules were observed in rats after CP treatment that the results were in agreement with the findings of the previous study (36). RJ pretreatment in the RJ+CP groups reversed these alterations. In line with this finding, our previous study showed that RJ ameliorated diabetes-induced impairment in the testicular tissue, probably caused by its antioxidant activity (25).

Conclusion

The current evidence increases the possibility of RJ potential to normalize the number of PLTs in thrombocytopenic rats caused by chemotherapy. We showed that RJ protected CP-induced thrombocytopenia, as well as the changes in other hematological parameters, probably as a result of its antioxidant and anti-cancer properties. CP-induced histopathological changes in organs were prevented by RJ pretreatment. Thus, RJ can be suggested as a food supplement to ameliorate the adverse effects of chemotherapeutic drugs.

Acknowledgements

This study was funded by vice chancellor for Research, KUMS with No: 97320. The authors declare no conflict of interest.

Authors' Contributions

F.K.; Carried out the experiment, data collection, and wrote and corrected the manuscript. E.G.; Did the data collection and participated in experiments. M.K.; Designed the study, carried out the statistical analysis, and drafted the final version of the manuscript. All authors read and approved the final manuscript.

Reference

1. Feng L, Huang Q, Huang Z, Li H, Qi X, Wang Y, et al. Optimized

animal model of cyclophosphamide-induced bone marrow suppression. Basic Clin Pharmacol Toxicol. 2016; 119(5): 428-435.
2. Cao Y, Wang X, Li S, Wang H, Yu L, Wang P. The effects of l-carnitine against cyclophosphamide-induced injuries in mouse testis. Basic Clin Pharmacol Toxicol. 2017; 120(2): 152-158.
3. Brass L. Understanding and evaluating platelet function. Hematology Am Soc Hematol Educ Program. 2010; 2010: 387-396.
4. Gauer RL, Braun MM. Thrombocytopenia. Am Fam Physician. 2012; 85(6): 612-622.
5. Anitua E, Andia I, Ardanza B, Nurden P, Nurden AT. Autologous platelets as a source of proteins for healing and tissue regeneration. Thromb Haemost. 2004; 91(1): 4-15.
6. Eisman R, Surrey S, Ramachandran B, Schwartz E, Poncz M. Structural and functional comparison of the genes for human platelet factor 4 and PF4alt. Blood. 1990; 76(2): 336-344.
7. Maurer AM, Zhou B, Han ZC. Roles of platelet factor 4 in hematopoiesis and angiogenesis. Growth Factors. 2006; 24(4): 242-252.
8. Mahabir VK, Ross C, Popovic S, Sur ML, Bourgeois J, Lim W, et al. A blinded study of bone marrow examinations in patients with primary immune thrombocytopenia. Eur J Haematol. 2013; 90(2): 121-126.
9. Lapointe JM, Valdez RA, Ryan AM, Haley PJ. Evaluation of the utility of popliteal lymph node examination in a cyclophosphamide model of immunotoxicity in the rat. J Immunotoxicol. 2016; 13(4): 449-452.
10. Patra K, Bose S, Sarkar S, Rakshit J, Jana S, Mukherjee A, et al. Amelioration of cyclophosphamide induced myelosuppression and oxidative stress by cinnamic acid. Chem Biol Interact. 2012; 195(3): 231-239.
11. Lee H-R, Yoo N, Jeong J, Sohn K-Y, Yoon SY, Kim JW. PLAG alleviates chemotherapy-induced thrombocytopenia via promotion of megakaryocyte/erythrocyte progenitor differentiation in mice. Thromb Res. 2018; 161: 84-90.
12. Jalali AS, Hasanzadeh S, Malekinejad H. Crataegus monogyna aqueous extract ameliorates cyclophosphamide-induced toxicity in rat testis: stereological evidences. Acta Med Iran. 2012; 50(1): 1-8.
13. Bakhtiary Z, Shahrooz R, Ahmadi A, Zarei L. Evaluation of antioxidant effects of crocin on sperm quality in cyclophosphamide treated adult mice. Veterinary Research Forum. 2014; 5(3): 231-218.
14. Arena AC, Jorge BC, Silva MC, de Barros AL, Fernandes AAH, Nóbrega RH, et al. Acrocomia aculeata oil: Beneficial effects on cyclophosphamide-induced reproductive toxicity in male rats. Andrologia. 2018; 50(6): e13028.
15. Onaolapo AY, Oladipo BP, Onaolapo OJ. Cyclophosphamide-induced male subfertility in mice: An assessment of the potential benefits of Maca supplement. Andrologia. 2018; 50(3).
16. Abdel-Hafez SMN, Rifaai RA, Abdelzaher WY. Possible protective effect of royal jelly against cyclophosphamide induced prostatic damage in male albino rats; a biochemical, histological and immuno-histo-chemical study. Biomed Pharmacother. 2017; 90: 15-23.
17. Tang MS, Wang HT, Hu Y, Chen WS, Akao M, Feng Z, et al. Acrolein induced DNA damage, mutagenicity and effect on DNA repair. Mol Nutr Food Res. 2011; 55(9): 1291-1300.
18. Ramadan MF, Al-Ghamdi A. Bioactive compounds and health-promoting properties of royal jelly: a review. J Funct Foods. 2012; 4(1): 39-52.
19. Khazaei M, Ansarian A, Ghanbari E. New findings on biological actions and clinical applications of royal jelly: a review. J Diet Suppl. 2018; 15(5): 757-775.
20. Selvakumar E, Prahalathan C, Sudharsan PT, Varalakshmi P. Chemoprotective effect of lipoic acid against cyclophosphamide-induced changes in the rat sperm. Toxicology. 2006; 217(1): 71-78.
21. Kamali H, Khazaei MR, Shobeiri E, Khazaei M. Experimental models of thrombocytopenia in laboratory animals and their application in identifying the complications of chemotherapy drugs. JBUMS. 2018; 20(4): 48-58.
22. Ghanbari E, Khazaei MR, Khazaei M, Nejati V. Royal Jelly promotes ovarian follicles growth and increases steroid hormones in immature rats. Int J Fertil Steril. 2018; 11(4): 263-269.
23. Senin MiM, Al-Ani IM, Mahmud MIA, Muhammad N, Kasmuri HM. Protective effect of virgin coconut oil on cyclophosphamide-induced histological changes in lymphoid tissues. IMJM. 2018;17(3): 65-74.
24. Khazaei MR, Rashidi Z, Chobsaz F, Khazaei M. Apoptosis induction of human endometriotic epithelial and stromal cells by noscapine. Iran J Basic Med Sci. 2016; 19(9): 940-945.
25. Ghanbari E, Nejati V, Khazaei M. Antioxidant and protective effects of Royal jelly on histopathological changes in testis of diabetic rats. Int J Reprod Biomed (Yazd). 2016; 14(8): 519-526.
26. Nielsen LK, Klausen TW, Jarden M, Frederiksen H, Vangsted AJ, Do T, et al. Clarithromycin added to bortezomib-cyclophosphamide-dexamethasone impairs health-related quality of life in multiple myeloma patients. Eur J Haematol. 2019; 102(1): 70-78.
27. Hassan B. Role of cancer and chemotherapy in the incidence of thrombocytopenia. Pharmaceut Anal Acta. 2013; 4: 10.
28. Visentin GP, Liu CY. Drug-induced thrombocytopenia. Hematol Oncol Clin North Am. 2007; 21(4): 685-696.
29. Kim EJ, Lim KM, Kim KY, Bae ON, Noh JY, Chung SM, et al. Doxorubicin-induced platelet cytotoxicity: a new contributory factor for doxorubicin-mediated thrombocytopenia. J Thromb Haemost. 2009; 7(7): 1172-1183.
30. Anisimova NY, Ustyuzhanina NE, Bilan MI, Donenko FV, Ushakova NA, Usov AI, et al. Influence of Modified fucoidan and related sulfated oligosaccharides on hematopoiesis in cyclophosphamide-induced mice. Mar Drugs. 2018; 16(9). pii: E333.
31. Gaman A, Gaman M. The antioxidant treatment in patients with immune thrombocytopenia. Haematologica. 2014; 99: 773-774.
32. Sherif IO. The effect of natural antioxidants in cyclophosphamide-induced hepatotoxicity: Role of Nrf2/HO-1 pathway. Int Immunopharmacol. 2018; 61: 29-36.
33. Lu W, Jia D, An S, Mu M, Qiao X, Liu Y, et al. Calf spleen extractive injection protects mice against cyclophosphamide-induced hematopoietic injury through G-CSF-mediated JAK2/STAT3 signaling. Sci Rep. 2017; 7(1): 8402.
34. Han J, Xia J, Zhang L, Cai E, Zhao Y, Fei X, et al. Studies of the effects and mechanisms of ginsenoside Re and Rk3 on myelosuppression induced by cyclophosphamide. J Ginseng Res. 2018; (In Press).
35. Block KI, Koch AC, Mead MN, Tothy PK, Newman RA, Gyllenhaal C. Impact of antioxidant supplementation on chemotherapeutic efficacy: a systematic review of the evidence from randomized controlled trials. Cancer Treat Rev. 2007; 33(5): 407-418.
36. Ghobadi E, Moloudizargari M, Asghari MH, Abdollahi M. The mechanisms of cyclophosphamide-induced testicular toxicity and the protective agents. Expert Opin Drug Metab Toxicol. 2017; 13(5): 525-536.

Original Article

Cytotoxicity Evaluation of The Bioresorbable and Titanium Plates/Screws Used in Maxillofacial Surgery on Gingival Fibroblasts and Human Mesenchymal Bone Marrow Stem Cells

Masoud Vatani, Ph.D.[1], Mohammad Hossein Beigi, M.Sc.[2], Fatemeh Ejeian, M.Sc.[2], Ahmad Mottaghi, Ph.D.[1]*, Afshin Yadegari-Naeini, Ph.D.[1], Mohammad Hossein Nasr-Esfahani, Ph.D.[2]*

1. Department of Oral and Maxillofacial Surgery, School of Dentistry, Islamic Azad University, Khorasgan Branch, Isfahan, Iran
2. Department of Cellular Biotechnology, Cell Science Research Center, Royan Institute for Biotechnology, ACECR, Isfahan, Iran

Corresponding Addresses: P.O.Box: 81595158, Department of Oral and Maxillofacial Surgery, School of Dentistry, Islamic Azad University, Khorasgan Branch, Isfahan, Iran
P.O.Box: 8159358686, Department of Cellular Biotechnology, Cell Science Research Center, Royan Institute for Biotechnology, ACECR, Isfahan, Iran
Emails: Dr.motaghi@yahoo.com, mh.nasr-esfahani@royaninstitute.org

Received: 17/October/2018, Accepted: 8/June/2019

Abstract

Objective: Bioresorbable and titanium plates/screws are considered as a standard treatment for fixation of the bone segments of craniofacial area and paying attention to their biocompatibility is an important issue along with other aspects of application. The purpose of the study was to evaluate the cell viability of two types of plate and screw used in maxillofacial surgeries in contact with gingival fibroblasts and bone marrow stem cells.

Materials and Methods: In this experimental study after extraction and cultivation of cells from healthy human gingival tissue and alveolar bone of jaw, cytotoxicity of device was evaluated. In direct contact method, samples had near vicinity contact with the both cell lines and in indirect contact method, by-products released, like ions, from samples after 8 weeks were used to assess cytotoxicity. Then cytotoxicity was evaluated on the 2nd, 4th and 6th day with MTS tests and microscopy. The data were analyzed by one-way ANOVA and independent t tests.

Results: There was a statistically significant difference between the German plate and screw and all the samples studied on day 6 ($P<0.05$). Furthermore, a statistically significant difference was observed between both metal samples and both bio-absorbable samples on day 6 and both cell lines ($P<0.05$). Comparisons between the two groups with each other for both cell lines on the 6th day were statistically significant ($P<0.05$).

Conclusion: Our results suggest that that cytotoxicity of biomaterial, from different brands, were not similar and some of the biomaterial showed lower degree of toxicity compared to others and specialist using these products showed be aware of this differences. Our investigation indicates more biocompatibility of bioresorbable plates and screws compared to titanium. In addition our results suggest that biomaterials were not completely neutral.

Keywords: Bone Marrow Stem Cell, Cytotoxicity Test, Dental Implant Materials, Fibroblast Cells

Cell Journal(Yakhteh), Vol 22, No 3, October-December (Autumn) 2020, Pages: 310-318

Citation: **Vatani M, Beigi MH, Ejeian F, Mottaghi A, Yadegari-Naeini A, Nasr-Esfahani MH. Cytotoxicity evaluation of the bioresorbable and titanium plates/screws used in maxillofacial surgery on gingival fibroblasts and human mesenchymal bone marrow stem cells. Cell J. 2020; 22(3): 310-318. doi: 10.22074/cellj.2020.6409.**

Introduction

Primary stability and appropriate contact between fractured bone segments are essential for bone remodeling, maturity and reconstruction following maxillofacial trauma, orthognathic surgery and Healing of pathologic defects. Therefore, over centuries, clinicians have paid particular attention to these issues and developed various types of plates and screws, splints, arch bars and inter-maxillary wires in different sizes, shapes, and thicknesses. The introduction of new materials such as polymers, composites, and compound alloys during the recent decades have led to a great revolution in production and application of wide range of innovative devices in this field (1).

Different metals from stainless steel and commercial titanium alloys to nickel-chromium-cobalt and titanium-aluminum-vanadium alloys have long been used in the reconstruction of dental structures and bone tissues. Titanium alloys have been widely used in implantology for over seven decades. In maxillofacial surgery, titanium alloys are largely utilized in production of plates and screws, reconstruction meshes, and even jaw distraction devices (2). Moreover, development and progress of material engineering and clearer understanding of atomic and molecular structures of materials have resulted in production of novel biomaterials and absorbable polymers such as poly-lactic acid, poly-glycolic acid and their copolymers. Based on the unique molecular structures of these materials and their interactions with living tissues, several types of absorbable sutures and plates and screws have been produced and applied in craniofacial and orthopedic surgeries (1), specially . for the stabilization of fracture segments and osteotomy sites and internal fixation (3).

Following the development of any biomaterial,

its stability, aesthetic and functional aspects, and biocompatibility should be regularly assessed by both the manufacturers and clinicians (4). Considering the improvement of international health and safety standards, governments and organizations pay utmost attention to safety of medical equipments and implantable devices. Hence, before clinical application in humans, biocompatibility of all materials is widely evaluated through standardized tests (5). In addition to technological advancements in production of instruments and biomaterials, an increasing diversity of commercial products are produced by different companies. In fact, various brands and novel products are distributed in the global market in response to the emerging global medical demands. Considering these products are in short-term or long-term contact with biological environments and their byproducts will be released after their usage and become in contact with surrounding tissue, therefore development of biocompatible materials which yield appropriate biological responses and minimize possible health risks for the patients is of paramount importance. Despite the importance of this issue, biocompatibility of some implantable devices has not been thoroughly investigated. According to available research, corrosion of implanted metallic devices and chronic exposure to their derivatives, cause acute or chronic toxicity. The consequent oxidative changes taking place in vicinity of metallic bonds of these materials can induce changes in biological molecules such as DNA and could subsequently lead to a wide range of diseases including cancers (6).

Analysis of the ions released form implanted metals indicates the potential of these ions for localized accumulation in patients' blood, serum, or different organs (7). Researchers have long agreed on the release of titanium ions from implanted titanium alloys and monitored accumulation of these ions in patients' lymph nodes and various organs (e.g. liver, gallbladder, and lungs), and even serum and urine (8, 9). Even the lower concentrations of metal ions can inhibit half of cellular activities and titanium and cobalt inhibit cell-specific functions including alkaline phosphatase activity, extracellular calcification, and bone-specific gene expression (10). Based on available evidence, long-term release of aluminum and vanadium from titanium alloys would cause peripheral neuropathy, osteomalacia and Alzheimer's disease (11). Bio-absorbable implants are recognized as foreign body by the organism. Furthermore, degradation of these materials leads to release and accumulation of acidic byproducts and cause aseptic inflammation in the host's responses, cytotoxicity, and changes in cell behaviors (12). Additionally, the complexity of healing and regeneration processes of both soft and hard tissues at surgical site also depends on the type of biomaterial used and this has become for global market. Considering these facts, this study was designed to evaluate the biocompatibility and cytotoxicity of four well-known brands applied in maxillofacial treatments through both direct and indirect contact with two cell types, including human gingival fibroblasts and human bone marrow stem cells.

Materials and Methods

Ethical consideration

The experiments were approved by the Ethical Committee of Isfahan Medical University (IR.MUI.REC.1395.4.040). Before surgery to obtain human gingival tissues and alveolar bone marrow stem cells patients were informed regarding the aim of the study and informed consent form was signed with each individual. Healthy human gingival tissue was obtained from 5 patients undergoing crown lengthening surgery at the Department of Oral and maxillofacial Surgery, Faculty of Dentistry, Isfahan Azad University, Iran and alveolar bone marrow stem cells were obtained from 7 patients undergoing orthognathic surgeries in Amin Hospital (Isfahan, Iran).

Isolation and cell culture of gingival fibroblast cell

In this experimental study, after surgery all human samples were transferred to the lab Royan Institute in phosphate- buffered saline (PBS) containing 100 U/ml penicillin, 50 µg/ml streptomycin and 0.25 µg/ml amphotericin B. The gingival tissue were thoroughly washed and cut into small pieces (0.5×0.5 mm) and placed in high glucose Dulbecco's modified Eagle's medium (DMEM) containing 15% fetal bovine serum (FBS), 1% L-glutamine, 100 U/ml penicillin, 50 µg/ml streptomycin and 0.25 µg/ml amphotericin B. The culture plates were incubated at 37˚C in a humidified atmosphere of 95% air and 5% CO_2 and daily monitored for any infection. As the hallmark of *in vitro* fibroblast isolation, primary cell outgrowth was observed after 10 days, which were labeled as passage zero (Fig.S1) (See Supplementary Online Information at www.celljournal.org). During this period the medium was replaced twice a week. Upon confluence, cells were passaged and cells from passage 3 were used for the study. Passaging will remove other cell contaminate and help to obtain uniform gingival fibroblasts with spindle shaped morphology (Fig.1). All chemicals and reagents, unless otherwise stated, were purchased from Sigma® (St. Louis, MO). Media were purchase from Gibco (USA), unless otherwise stated.

Isolation and cell culture of alveolar bone marrow cells

On the other hand, alveolar bone fragments obtained during orthognathic surgeries were placed over mesh covered with 4-(2-hydroxyethyl)-1-piperazineethanesulfonic acid (HEPS) medium and centrifuged at 2500 rpm to with force out alveolar bone marrow cells from the bone fragments. The cells were seeded on 25 cm^2 flasks containing DMEM medium supplemented with 15% FBS, antibiotics (penicillin 0.1 g/L; streptomycin 0.1 g/L) at 37˚C in a humidified air atmosphere containing 5% CO_2. Upon confluence these cells were considered as passage zero. In order to evaluate the stem cell properties of harvested cells, expression of

common MSC markers (CD73, CD90, and CD105) were examined after 5 passages. In addition, the multilineage potential of cells were assesses after 3 weeks induction in specific adipo and osteogenic medium (Fig.S1) (See supplementary Online Information at www.celljournal.org).

Direct and indirect cytotoxicity assessment

In this study, four brands of plates and screws composition were used as shown with more details in Table 1. Accordingly, M1, M2, B1 and B2 products are made in Iran, Germany, Finland and Taiwan, respectively.

Initially, all titanium plates and screws were placed in double-distilled water and then immersed in ethanol for 20 minutes and washed abundantly with double-distilled water and then sterilized at 121˚C (15 minutes). On the other way, all bio-absorbable plates and screws were sterilized using ultraviolet light. Finally, all samples were washed twice with PBS prior to use. All experiments (direct and indirect cytotoxicity assessment) were carried out according to ISO 10993-5 standardized procedures and recommendations (13).

For direct cytotoxicity, the plates and screws were placed on the surface of culture plates of 12 well dishes and the results were compared with the dish with absence of these materials. Subsequently, 3×10^4 cells/well were added to each well (3 well/per group) and MTS assay was carried out at 2, 4 and 6 days post exposure. According to part 4.2.3.3 of ISO 10993-5, in the indirect method, pH was adjusted after incubation period, prior to cellular treatment.

Also, indirect assay was carried out according to part 8.4 of ISO 10993-5 standardized procedures (13). Preparation of condition medium performed in sterile, chemically inert, closed containers by using aseptic techniques, in accordance with ISO 10993-12. Briefly, plates and screws were added to 15 ml tubes containing DMEM for 8 weeks (14). Subsequently, this medium was supplemented with 15% FBS, antibiotics (penicillin 0.1 g/L; streptomycin 0.1 g/L). Then, the cells were seeded at density of 3×10^4 cells/well in 12 well plate using the medium which was exposed to plates and screws. The cells were cultured at 37˚C in a humidified air atmosphere containing 5% CO_2. MTS assay was carried out at 2, 4 and 6 days post culture. DMEM not exposed to plates and screws was considered as control group for all the experiments (ISO 10993-5).

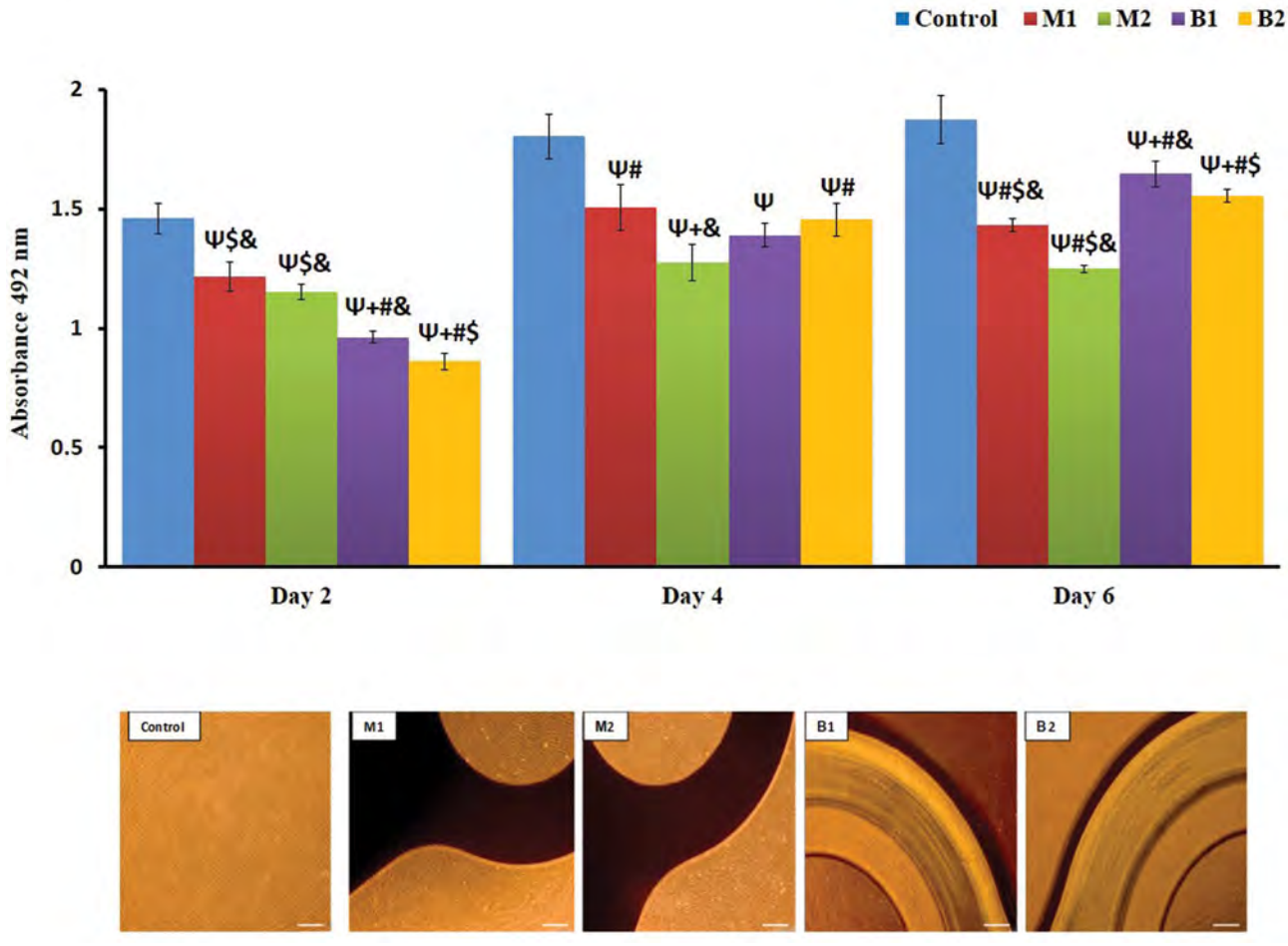

Fig.1: Effect of direct contact with HGFs in MTS assay and phase-contrast microscopy images (scale bar: 200). Ψ; Indicates statistically significant difference compared with control group at P<0.05, +; Indicates statistically significant difference compared with M1 group at P<0.05, #; Indicates statistically significant difference compared with M2 group at P<0.05, $; Indicates statistically significant difference compared with B1 group at P<0.05, &; Indicates statistically significant difference compared with B2 group at P<0.05, M1; Iran, M2; Germany, B1; Finland, B2; Taiwan, and HGF; Human gingival fibroblasts.

Table 1: Profile screws and plates used

	Type of materials	Form/Diameter	Ingredients	Manufacturers	Application
M1	Titanium alloy plate and screw	Plate: 4 holes straight 2 mm Screw: 7×2 mm	Ti-6Al-4V	Persian tohid medical, Iran	Craniofacial osteosynthesis
M2	Titanium alloy plate and screw	Plate: 4 holes straight 2 mm Screw: 7×2 mm	Ti-6Al-4V	Mondeal, Germany	Craniofacial osteosynthesis
B1	Plate and screw bioabsorbable	Plate: 4 holes straight 2 mm Screw: 7×2 mm	17% L-lactic acid copolymer, 78.5% D,L-lactic acid copolymer, 4.5% trimethylene carbonate monomers	Inion CPS, Tampere Finland	Craniofacial osteosynthesis
B2	Plate and screw bioabsorbable	Plate: 4 holes straight 2.5 mm Screw: 7×2 mm	90% L-lactide acid copolymer 10% D,L lactide acid copolymer	Biotech one inc. Bonamates series, Taiwan	Craniofacial osteosynthesis

MTS assay

MTS assay was a colorimetric assay for assessing cell metabolic activity. Micro plate Reader (Fluostar Optima, BMG Lab Technologies, Germany) at 492 nm was used to analyze the absorbance. Results were normalized as the ratio of main medium without cells and cell viability was calculated. It should be noted that on the 6^{th} day and in both methods, the phase contrast microscopy was used to assess the quality of cells.

Statistical methods

Statistical analysis was performed using SPSS software version 18 (IBM, USA). One-way ANOVA test was adopted to quantitatively compare among each sample and control group (more than two groups) in terms of cytotoxicity. Pairwise comparisons of the groups (Titanium alloy and bio-absorbable plates and screws) in terms of cytotoxicity were performed using independent t test. Significance was accepted at a level of $P<0.05$.

Results

Direct contact of plates and screws with human gingival fibroblast

The results showed a significant difference between the control group and all plate and screw samples ($P<0.05$) on the second, fourth and sixth days. All plate and screw samples revealed significant differences with each other except between M1 and M2. Moreover, independent t tests, showed a significant difference in cytotoxicity between the two groups of metallic and bio-absorbable plates and screws ($P<0.05$). While, the M2 sample just showed significant differences with the M1, B2 sample showed no significant differences between the bio-absorbable and metallic plates and screws in terms of cytotoxicity on fourth days of cell culture ($P<0.05$). Furthermore, all samples were showed significantly difference with each other ($P<0.05$) and no significant difference in cytotoxicity was observed between the bio-absorbable and metallic samples on the day 6 ($P<0.05$). Microscopic evaluation of direct contact of plates and screws with HGFs revealed that the control group contained a high density (viability) of fibroblasts cells which might be similar to B1 bio-absorbable plate and screw samples which also showed to contain cells on their surface. Unlike the control group, lowest cell density was observed in M2 group. The differences between groups and their significance, are shown in Figures 1 and 2.

Indirect contact of plates and screws with human gingival fibroblast

Results indicated that there were significant differences between the control group and all plate and screw samples except with M1 on day six. However, no statistical differences were found in pairwise comparisons of all four plate and screw groups ($P<0.05$). On the fourth day, pairwise comparisons of the samples indicated that the M2 group was significantly different from all other plate and screw samples and there were no significant differences between the B1 with B2 and M1 groups. However, a significant difference was observed between M1 with B2. On the other hand, significant differences were found between all samples on the day six ($P<0.05$). Also, the results of independent t-test revealed that the bio-absorbable and metallic plates and screws had significant differences in terms of cytotoxicity on day four and six ($P<0.05$).The microscopic evaluation also confirmed the MTS test results which means that M2 group contained the lowest cell density with a higher number of dead cells than the other groups.

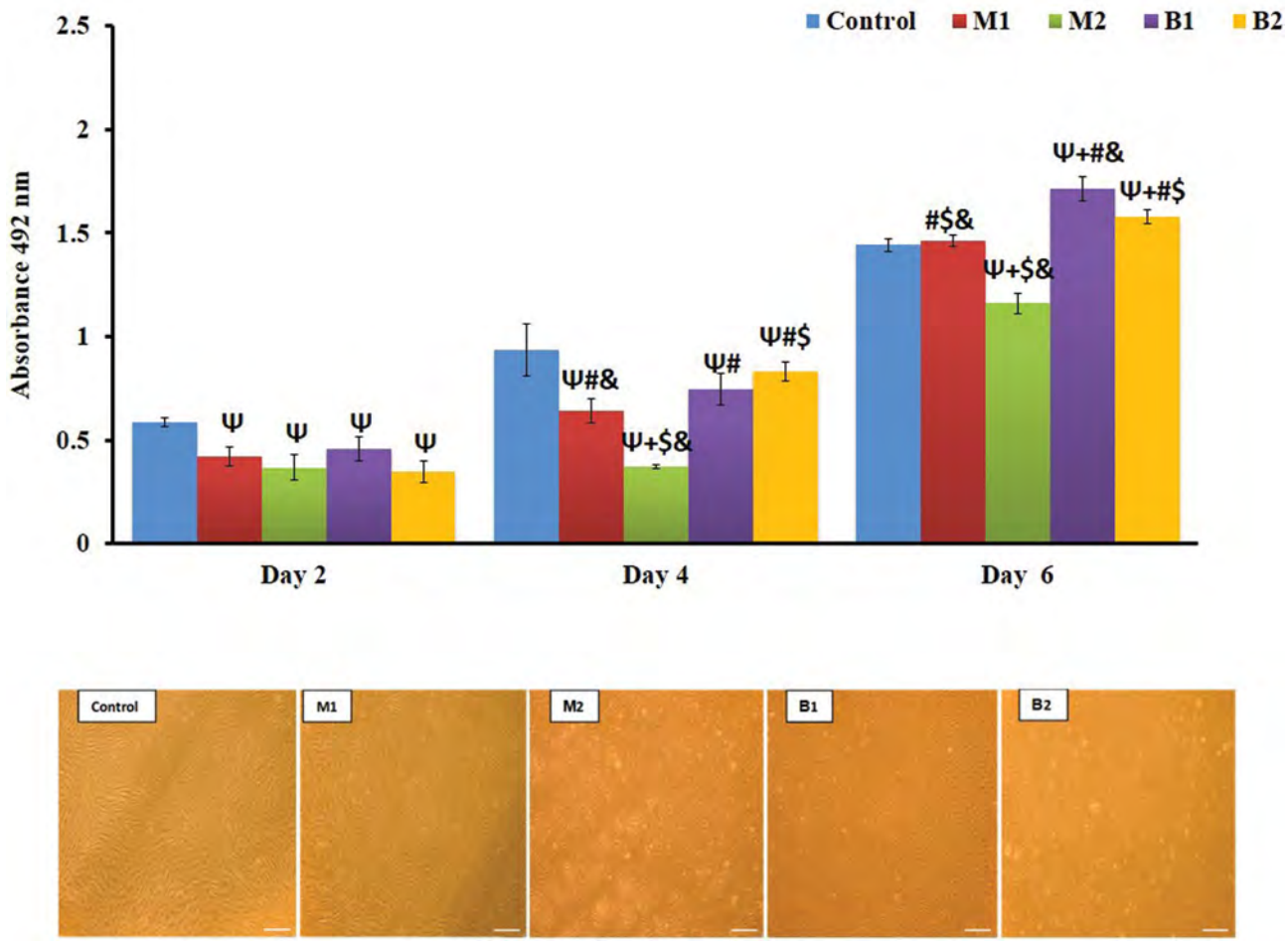

Fig.2: Effect of indirect contact with HGFs in MTS assay and Phase-contrast microscopy images (scale bar: 200 µm). Ψ; Indicates statistically significant difference compared with control group at P<0.05, +; Indicates statistically significant difference compared with M1 group at P<0.05, #; Indicates statistically significant difference compared with M2 group at P<0.05, $; Indicates statistically significant difference compared with B1 group at P<0.05, &; Indicates statistically significant difference compared with B2 group at P<0.05, M1; Iran, M2; Germany, B1; Finland, B2; Taiwan, and HGF; Human gingival fibroblast.

Direct contact of plates and screws with alveolar bone marrow cells

The results of direct contact with bone marrow stem cells (BMSCs) showed a significant statistical difference between control group and all the other groups except with M1 and B1 groups on the fourth day and B1 on the second day (Fig.3). Pairwise comparisons of the samples did not show significant differences between the M2 with M1 and M2 with B2 plate and screw samples. However B1 bio-absorbable samples were significantly different from all other samples on second day (P<0.05). The results of the fourth day showed that there were no significant differences between M1 with B1 groups and in contrast, significant differences were observed between the other groups (P<0.05). The results of ANOVA, revealed that there was significant deference between the control group and all samples (P<0.05). In addition, M1 and B2 samples were almost similar (P<0.05) and other samples had significant differences with each other on sixth day (P<0.05). The results of independent t-tests showed that there were significant differences between the metallic and bio-absorbable samples the fourth and sixth days (P<0.05). Microscopic evaluation demonstrated that the density of BMSCs around and even on the B2 bio-absorbable plates and screws was higher than the other groups. In addition, the M2 and control groups were relatively similar in the density of cells and the M2 had the lowest cell density (Fig.3).

Indirect contact of plates and screws with alveolar bone marrow stem cells

The results indicated significant differences between the control group and all other groups, except for absorbable samples with control on second day, M1, B1 and B2 on the fourth day and M1 in sixth day (P<0.05, Fig.4). Pairwise comparisons of other samples displayed no significant differences between the M1with M2, as well as between the B1 with B2 groups (P<0.05). On the fourth day, there were no statistically significant differences between the M1, B1 and B2 with each other, but the M2 group was significantly different from all other samples (P<0.05).

Likewise**,** on day 4, the results showed significant differences between the M1, M2, B1, and B2 groups (P<0.05). Independent t test revealed a significant difference between the metallic and bio-absorbable groups for the all days (P<0.05). The microscopic evaluation also confirmed the MTS test results (Fig.4).

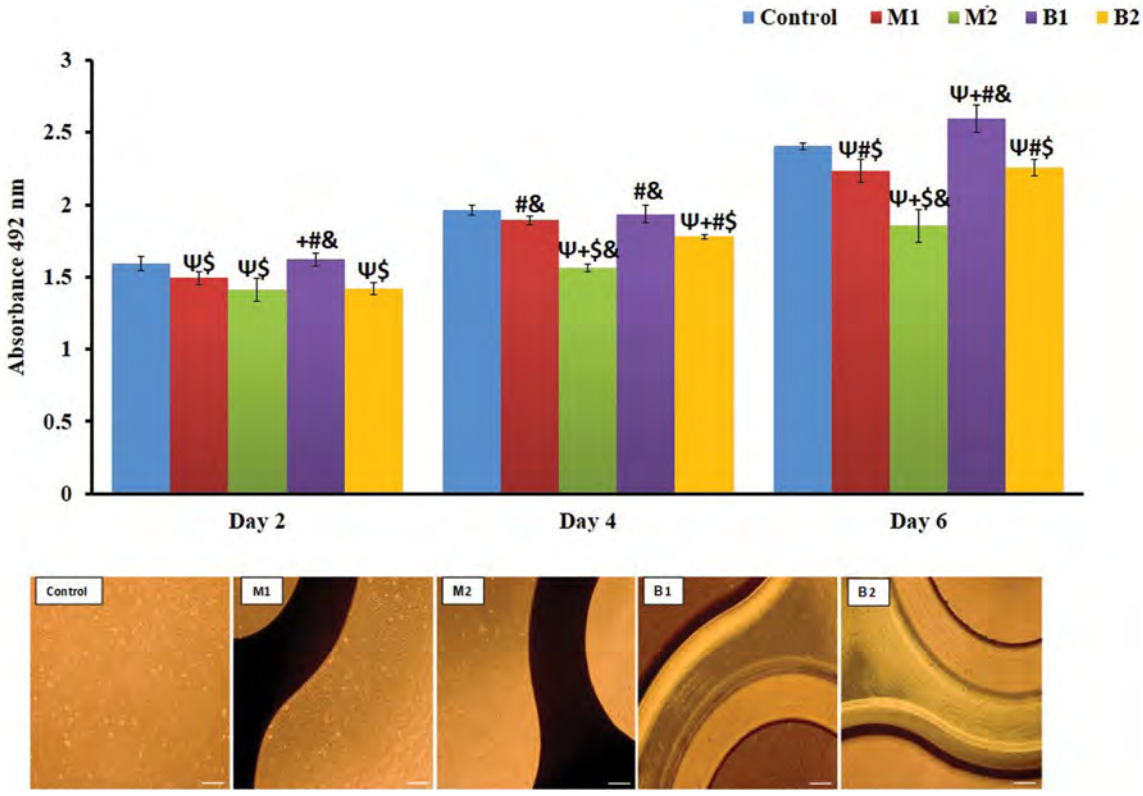

Fig.3: Effect of direct contact with bone marrow stem cells (BMSc) in MTS assay and Phase-contrast microscopy images. Ψ; Indicates statistically significant difference compared with control group at P<0.05, +; Indicates statistically significant difference compared with M1 group at P<0.05, #; Indicates statistically significant difference compared with M2 group at P<0.05, $; Indicates statistically significant difference compared with B1 group at P<0.05, &; Indicates statistically significant difference compared with B2 group at P<0.05, M1; Iran, M2; Germany, B1; Finland, and B2; Taiwan.

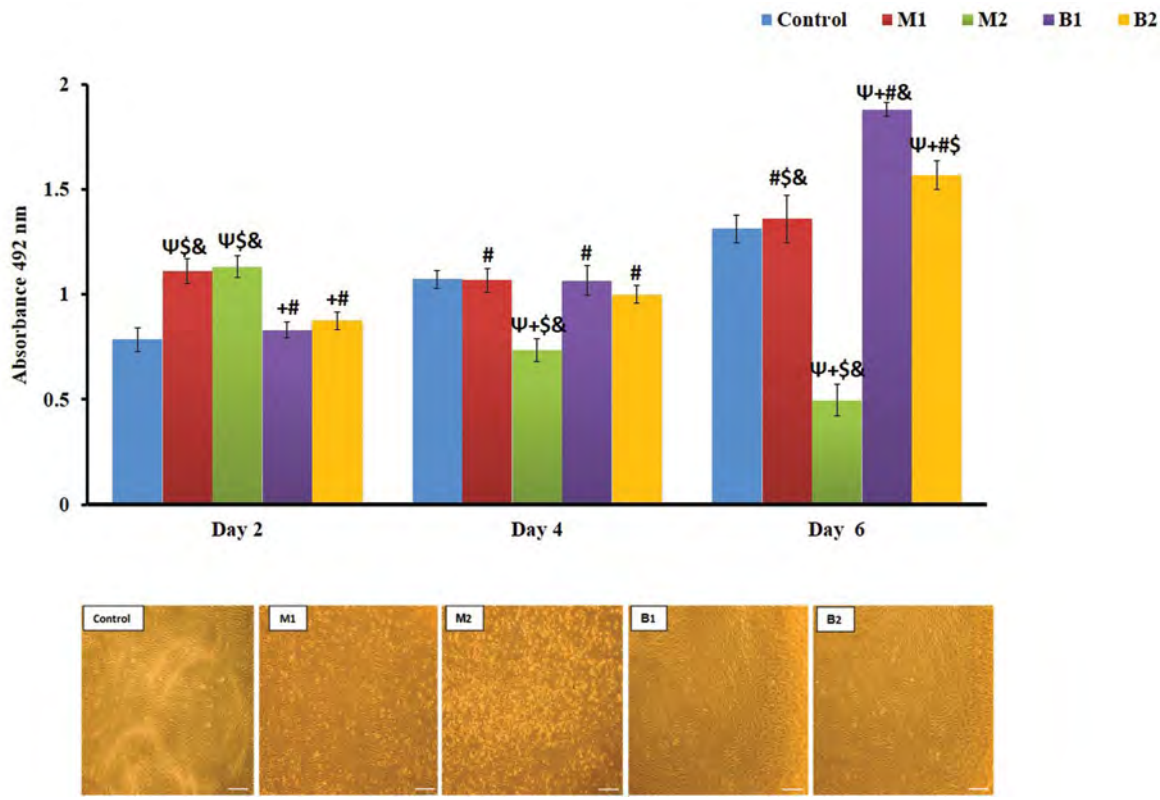

Fig.4: Effect of indirect contact with bone marrow stem cells (BMSc) in MTS assay and phase-contrast microscopy images. Ψ; Indicates statistically significant difference compared with control group at P<0.05, +; Indicates statistically significant difference compared with M1 group at P<0.05, #; Indicates statistically significant difference compared with M2 group at P<0.05, $; Indicates statistically significant difference compared with B1 group at P<0.05, &; Indicates statistically significant difference compared with B2 group at P<0.05, M1; Iran, M2; Germany, B1; Finland, and B2; Taiwan.

Discussion

Nowadays, the use of bio-absorbable and titanium plates and screws in various types and forms are proposed as a gold standard to integrate and stabilize a fracture or osteotomy sites. In addition, rigid internal fixation plays a crucial role in management of reconstruction of traumatic injuries, rehabilitation of pathological defects and congenital anomalies in craniofacial area and orthognathic surgeries.

As with increased advancements in technology and biomaterials development in terms of reconstruction, replacement or repair of tissue functions in living systems, manufacturing companies and clinicians are required to consider and evaluate biocompatibility as a functional ability of a material under special conditions in the presence of an appropriate host response, in addition to considering the strength, abrasion and corrosion resistance, beauty and other practical aspects (4). Despite many studies on physical and mechanical properties and features of absorbable and titanium plates and screws used in maxillofacial region, less attention is paid to biocompatibility of these devices.

In this study, cytotoxicity of two kinds of plate and screw made of titanium alloys (Ti-6A1-4V) and bio-absorbable polymers with main structure of Poly (L-lactic acid) and Poly (D, L Lactic acid) were evaluated. Ideally, if possible, cytotoxicity tests should be selected by similar cell and tissue samples with maximum efforts to stimulate implanting and using inside of the body. The use of cell culture media is regarded as an important part of tests recommended for evaluation of biologic behaviors of materials in contact with human tissues; and primary cells have high priority in comparison with prepared cell banks in order to obtain real results and evaluate biologic behaviors and features (15, 16). So, in this study, because of close vicinity of plates and screws to bone tissues and covering mucosa, bone marrow stem cells of alveolar jaw and oral gingival fibroblast cells of human were used.

It is noteworthy that in this study, culture media with these two cell lines have been used as control group to compare cytotoxicity of plate and screw samples. Here, toxicity of plates and screws were evaluated using direct and indirect contact methods. Direct contact method has high sensitivity, and observed changes regarding cell density and morphology are representative of material's special features during a short interval in close contact with cells. In indirect method, the effects of byproducts and materials released from samples on cells are investigated in terms of quantity and even morphology during a similar period with clinical application conditions in the body. In this study, the materials released from plate and screw samples were placed in contact with cells after an interval about 8 weeks and similar to required conditions and time in order to heal and integrate in bone segments (14).

On the other hand, MTS laboratory test was used for quantitative evaluating the survival cells in vicinity of plate and screw samples or by-products and for reducing possible errors caused by qualitative evaluation methods.

The results of direct contact of plate and screw samples with titanium alloy in two cell lines of gingival fibroblast cells and bone marrow stem cells of jaw showed a significant statistical difference compared to control group except for M1 and B1 groups with control on day 4 and B1 on day 2 in BMCs. Overall reduction in cell number compared to control group is expected as there is less area for these cells to attach unless the cells can attached to the plates and screws. This proposition is in line with cell attachment observed on B group. However, to prove that this observation or reduction in cell proliferation is not due to cellular toxicity but rather than the reduced area, the indirect culture was carried out. The results indicate that cellular proliferation was even higher or at least similar for the explants except for M2 which appear to be cytotoxic at both MTS and microscopic level in indirect method, the reduced cellular proliferation appears to be more pronounce on early days of culture (0 to day 2) compared to day 4 to 6 in HGFs a detailed explanation of which is given below.

Comparison of MTS assay between B1 and B2 with M1 and M2 in indirect method on day 6 revealed significant increase in cell proliferation in the former group (B1 and B2). Partially the same pattern existed for the direct method. Increased attachment area may also account for this observation in B compared to M group. This is in line with reports in literature that cells cannot attach to metal surfaces like titanium (17). The second reason for reduced cell proliferation in M groups is stated in the section below.

Corrosion, ionization, and abrasion of alloy samples, existence of proteins, amino acids, low concentration of insoluble oxygen, ambient temperature changes, and even higher concentration of chloride ion play an important role in ion release in adjacent tissues (18). These ionic compounds in biologic environments and plasma proteins lead to induction of thermodynamic forces for oxidation-reduction reactions (19). The pH changes during the first two weeks after surgery which causes surface changes of alloys, ion release and by-products (18). Galeotti et al. (20) investigated the pH effects on biocompatibility of orthodontic mini screws in keratinocyte, human osteosarcoma, and human gingival fibroblast cultures. They found that all mini screws had tissue compatibility at pH=7 and cytotoxicity responses appeared clearly after reduced pH. Therefore, to prevent the effect of pH changes in the media which can affect cell survival and proliferation, the pH of culture medium was adjusted before exposure to cells. However, it is important to note that after contact to culture media with metal plates and screws gradual release of metallic compounds and metal ions present in these alloys and this may account for cytotoxicity observed in M group, especially M2 group. The difference between M1 and M2 is related to differences between the compositions of these two alloys, especially for vanadium. M2 probably contain a

higher degree of vanadium in composition. Nevertheless the reason for higher composition of vanadium is that it improves the strength and hardness of titanium alloys to counteract the deformation of plates and screws against biting force and muscle tension on both sides of the fracture line (21). It is also important to note that vanadium is an essential micro element and plays an important physiological and pharmaceutical properties, such as insulin-like effects (22, 23). However, vanadium released faster than aforementioned alloys and at doses higher than physiological level is considered to have a high toxicity effect in comparison with other essential elements and also titanium, aluminum, nickel and cobalt (7, 18, 22, 24). On the other hand, cells with different origin are characterized by specific and sometimes different inherent features and responses in dealing with ionic metal compounds or other foreign body, and therefore the results of a cell line may not be fully consistent or comparable to another cell line, this is the reason that we used primary cell lines obtained from maxillofacial region (15, 16). In this study, based on absorbance difference one might conclude that more cellular changes were observed in bone marrow stem cells as compared to gingival fibroblast cells, which may be due to different behaviors and responses of different cell lines in direct proximity to the study materials. Nevertheless this conclusion should be taken with caution, as direct comparison between two cell lines are not possible unless cellular doubling time should also be taken into account (25) but if overlook this assumption, pre-osteoblast appear to be more sensitive than fibroblast.

The data from both direct contact and indirect methods revealed significant difference between B1 and B2 for both cell lines. The rate of proliferation was slower in B2. This is likely due to the higher biodegradation rate of B2 compared to B1 which resulted in higher rate of hydrolysis and further release of the by-products and changes in pH of the environment. These results and propositions are in agreement with microscopic observation of two cell line between the two groups.

As stated above, pH in vicinity of implanted devices may have a profound effect on cellular behavior. It is important to note that the pH in the medium, may be slightly different from the pH on surface of the implanted devices as the concentration of by-products release and therefore changes are higher in the vicinity of these medical devises (10, 26, 27). To counteract the pH shift near these medical implants, some companies have included tri-methylene carbonate in their chemical composition. According, Wake et al. (10), showed that this compound in the polymer structure has a strong buffering capacity and can neutralize the acidity shift and may protect cells from this side effect. In addition they reported that presence of inflammatory cells in the vicinity of polymers containing tri-methylene carbonate was lower than that of poly l lactic acid (PLLA) polymers. In this regard other carbonates like calcium alkaline carbonate, sodium bicarbonate and calcium bicarbonate has been added to polymers to improve buffering capacity (28).

One of the shortcoming of *in vitro* studies is that a healthy immune system along with a blood circulatory system and a healthy lymphatic drainage in the human body or every living creature is missing in this system and our study is no exemption from this shortcoming. However, it might be beneficial to investigate the effects of these plates and screws in future animal models. In this regard, selecting the most appropriate *in vivo* model is essential during the biomaterials development process to enable accurate modelling of therapeutic efficacy.

Conclusion

Cytotoxicity testing is a mandatory part of devices in contact with living tissues. Considering the important role played by titanium and absorbable plates and screws in medicine and dentistry, especially in craniofacial surgery, therefore, it should be important for the specialist to have an insight on differential toxicity of any type of medical implant available in the market. Our results revealed different toxicity levels between different products with two primary cell lines derived from oral and maxillofacial region. Therefore, our recommendation to specialist is working with common products in their field to periodically check their cytotoxicity in order to improve the health care of their patients.

Acknowledgements

This study was financially supported by Khorasgan Islamic Azad University and Royan Institute. The authors declare no conflict of interest.

Authors' Contributions

A.M., A.Y.-N., M.H.N.-E.; Perceived and designed the study. M.V., M.H.B., F.E.; Performed the experiments. M.V., M.H.B., M.H.N.-E.; Wrote the manuscript. M.H.B., F.E.; Analyzed the data. All authors participated in the finalization of the manuscript and approved the final draft.

References

1. Neumann A, Kevenhoerster K. Biomaterials for craniofacial reconstruction. GMS Curr Top Otorhinolaryngol Head Neck Surg. 2009; 8.
2. Zaffe D, Bertoldi C, Consolo U. Element release from titanium devices used in oral and maxillofacial surgery. Biomaterials. 2003; 24(6): 1093-1099.
3. Yoruc ABH, Gülay O, Sener BC. Examination of the properties of Ti-6Al-4V based plates after oral and maxillofacial application. J Optoelectron Adv M. 2007; 9(11): 3389-3395.
4. Sakaguchi R, Ferrance J, Rowers J, editors. Craig's restorative dental materials. Restorative dental materials. St. Louis, Missouri: Elsevier; 2012: 109-133.
5. Li W, Zhou J, Xu Y. Study of the in vitro cytotoxicity testing of medical devices. Biomed Rep. 2015; 3(5): 617-620.
6. Valko M, Rhodes CJ, Moncol J, Izakovic M, Mazur M. Free radicals, metals and antioxidants in oxidative stress-induced cancer. Chem Biol Interact. 2006; 160(1): 1-40.
7. Sun ZL, Wataha JC, Hanks CT. Effects of metal ions on osteoblast-like cell metabolism and differentiation. J Biomed Mater Res. 1997; 34(1): 29-37.
8. Bessho K, Iizuka T. Clinical and animal experiments on stress corrosion of titanium miniplates. Clinical Materials. 1993; 14(3): 223-227.
9. Jacobs JJ, Skipor AK, Patterson LM, Hallab NJ, Paprosky WG, Black J, et al. Metal release in patients who have had a primary

total hip arthroplasty. A prospective, controlled, longitudinal study. J Bone Joint Surg Am. 1998; 80(10): 1447-1458.
10. Wake MC, Gerecht PD, Lu L, Mikos AG. Effects of biodegradable polymer particles on rat marrow-derived stromal osteoblasts in vitro. Biomaterials. 1998; 19(14): 1255-1268.
11. Gomes CC, Moreira LM, Santos VJ, Ramos AS, Lyon JP, Soares CP, et al. Assessment of the genetic risks of a metallic alloy used in medical implants. Genet Mol Biol. 2011; 34(1): 116-121.
12. He Y, Wang W, Ding J. Effects of L-lactic acid and D, L-lactic acid on viability and osteogenic differentiation of mesenchymal stem cells. Chinese Science Bulletin. 2013; 58(20): 2404-2411.
13. ISO/DIS 10993-12. Biological evaluation of medical devices-Part 12: Sample preparation and reference materials. ISO Geneva; 1996.
14. Razukevicius D, Sabalys G, Kubilius R. Comparative analysis of the effectiveness of the mandibular angle fracture treatment methods. Stomatologija. 2005; 7(2): 35-39.
15. Pan C, Kumar C, Bohl S, Klingmueller U, Mann M. Comparative proteomic phenotyping of cell lines and primary cells to assess preservation of cell type-specific functions. Mol Cell Proteomics. 2009; 8(3): 443-450.
16. Lorsch JR, Collins FS, Lippincott-Schwartz J. Cell Biology. Fixing problems with cell lines. Science. 2014; 346(6216): 1452-1453.
17. Feller L, Jadwat Y, Khammissa RA, Meyerov R, Schechter I, Lemmer J. Cellular responses evoked by different surface characteristics of intraosseous titanium implants. Biomed Res Int. 2015; 2015: 171945.
18. Hanawa T. Metal ion release from metal implants. Materials Science and Engineering C. 2004; 12(6): 745-752.
19. Langley A, Dameron CT. Modern metal implant toxicity and anaesthesia. Australasian Anaesthesia. 2015(2015): 57-65.
20. Galeotti A, Uomo R, Spagnuolo G, Paduano S, Cimino R, Valletta R, et al. Effect of pH on in vitro biocompatibility of orthodontic miniscrew implants. Prog Orthod. 2013; 14: 15.
21. Niinomi M. Mechanical properties of biomedical titanium alloys. Materials Science and Engineering: A. 1998; 243(1-2): 231-236.
22. Woodman JL, Jacobs JJ, Galante JO, Urban RM. Metal ion release from titanium-based prosthetic segmental replacements of long bones in baboons: a long-term study. J Orthop Res. 1984; 1(4): 421-430.
23. Heinemann G, Fichtl B, Vogt W. Pharmacokinetics of vanadium in humans after intravenous administration of a vanadium containing albumin solution. Br J Clin Pharmacol. 2003; 55(3): 241-245.
24. Harle F, Champy M, Terry B. Atlas of craniomaxillofacial osteosynthesis: microplates, miniplates and screws. 2nd ed. 2009.
25. Egusa H, Sonoyama W, Nishimura M, Atsuta I, Akiyama K. Stem cells in dentistry-part I: stem cell sources. J Prosthodont Res. 2012; 56(3): 151-165.
26. Eglin D, Alini M. Degradable polymeric materials for osteosynthesis: tutorial. Eur Cell Mater. 2008; 16: 80-91.
27. Ignatius AA, Claes LE. In vitro biocompatibility of bioresorbable polymers: poly (L, DL-lactide) and poly (L-lactide-co-glycolide). Biomaterials. 1996; 17(8): 831-839.
28. Chen D, Su Z, Weng L, Cao L, Chen C, Zeng S, et al. Effect of inflammation on endothelial cells induced by poly-L-lactic acid degradation in vitro and in vivo. J Biomater Sci Polym Ed. 2018; 29(15): 1909-1919.

Original Article

Adverse Drug Reaction Detection in Social Media by Deep Learning Methods

Zahra Rezaei, Ph.D.[1*], Hossein Ebrahimpour-Komleh, Ph.D.[1*], Behnaz Eslami, M.Sc.[2], Ramyar Chavoshinejad, D.V.M.[3], Mehdi Totonchi, Ph.D.[4, 5]

1. Department of Computer and Electrical Engineering, University of Kashan, Kashan, Iran
2. Department of Computer Engineering, Science and Research Branch, Islamic Azad University, Tehran, Iran
3. Mabna Veterinary Lab, Karaj, Alborz, Iran
4. Department of Genetics, Reproductive Biomedicine Research Center, Royan Institute for Reproductive Biomedicine, ACECR, Tehran, Iran
5. Department of Stem Cells and Developmental Biology, Cell Science Research Center, Royan Institute for Stem Cell Biology and Technology, Tehran, Tehran, Iran

**Corresponding Address: P.O.Box: 8731753153, Department of Computer and Electrical Engineering, University of Kashan, Kashan, Iran*
Emails: z.rezaei2010@gmail.com, ebrahimpour@kashanu.ac.ir

Received: 25/December/2018, Accepted: 14/April/2019

Abstract

Objective: Health-related studies have been recently at the heart attention of the media. Social media, such as Twitter, has become a valuable online tool to describe the early detection of various adverse drug reactions (ADRs). Different medications have adverse effects on various cells and tissues, sometimes more than one cell population would be adversely affected. These types of side effect are occasionally associated with the direct or indirect influence of prescribed drugs but do not have general unfavorable mutagenic consequences on patients. This study aimed to demonstrate a quick and accurate method to collect and classify information based on the distribution of approved data on Twitter.

Materials and Methods: In this classification method, we selected "ask a patient" dataset and combination of Twitter "Ask a Patient" datasets that comprised of 6,623, 26,934, and 11,623 reviews. We used deep learning methods with the word2vec to classify ADR comments posted by the users and present an architecture by HAN, FastText, and CNN.

Results: Natural language processing (NLP) deep learning is able to address more advanced peculiarity in learning information compared to other types of machine learning. Moreover, the current study highlighted the advantage of incorporating various semantic features, including topics and concepts.

Conclusion: Our approach predicts drug safety with the accuracy of 93% (the combination of Twitter and "Ask a Patient" datasets) in a binary manner. Despite the apparent benefit of various conventional classifiers, deep learning-based text classification methods seem to be precise and influential tools to detect ADR.

Keywords: Adverse Drug Reaction, Classification, Deep Learning, Natural Language Processing, Social Network

Cell Journal(Yakhteh), Vol 22, No 3, October-December (Autumn) 2020, Pages: 319-324

Citation: Rezaei Z, Ebrahimpour-Komleh H, Eslami B, Chavoshinejad R, Totonchi M. Adverse drug reaction detection in social media by deep learning methods. Cell J. 2020; 22(3): 319-324. doi: 10.22074/cellj.2020.6615.

Introduction

Adverse drug reactions (ADRs) are defined as the side effect of medications on health care. A systematic review of 25 prospective observational studies demonstrated that 5.3% of patients have been dealing with ADRs (1). Thus, early detection of these events probably would have an incredible impact on human health. According to the Agency for Healthcare Research and Quality report, annually, over 770,000 of people have been hurt and/or even passed away in hospitals due to the consequence of ADRs (2). Hence, societies require an alternative approach to detect ADRs related to clinical medications. Economically, ADRs noticeably increases the expenses of hospitalization (3, 4).

In this context, social media provide a considerable amount of information to detect ADRs, using the NLP technique. One of these social media is Twitter, which is a good source of data for broad-spectrum issues, particularly ADR-related discussions and posts. Currently, Twitter has the record of daily 342,000,000 active and 135,000 registered users. It has been revealed that the majority of patients positively shared the data about their health status in different medical, public webpages or open forum such as "Ask a Patient" website (5), Twitter, etc., provided a powerful tool for ADR monitoring. However, the extraction of useful information from social media is difficult due to its writing style and language, used to transfer this type of information. While the creation of a proper model, as a monitoring tool typically requires massive data and health experts, they significantly improve ADR identification through social media, led to the reduction in manually data labeling. Deep learning currently achieved impressive results in addressing the numerous NLP-related problems in this study. In this study, we collected quite various comments and automatically processed them using a deep learning method.

Related work

Sarker and Gonzalez (6) highlighted the importance of generating advanced NLP-based information for accurate ADR sentence detection and data classification through a traditional approach like Naïve Bayes, Maximum Entropy, and Support Vector Machine.

These methods presented an annotated Twitter corpus detection based on ADR as a general keyword. Sarker and Gonzalez applied two supervised machine learning approaches (NB and SVM) on a broad range of annotated medications with regard to ADR tweets (7). Although the classifier shows moderate performance, it was considered a fundamental method for further development of advanced techniques. In line with this approach, Akhtyamova et al. (8) applied convolutional neural networks (CNN) model, built in word2vec for classification of Twitter comments.

Also, Lee et al. (9) suggested a partially supervised CNN framework to classify the report of the inauspicious incidence of medication on Twitter. A Twitter dataset is not only used for the task associated with public service broadcasting (PSB) 2016 social medium but also applied to evaluate the model, which induces a high-performance classification of adverse drug event (ADE) with +9.9% F1-Score. Notably, the ADE detection surveillance systems require a small number of labeled instances. Moreover, the introduced model by Tiftikci et al. (10) consisted of CNN, conditional random fields (CRF), bi-directional long- and short-term memory (Bi-LSTM), and the alternative part which has the function of ADR detection. In other words, the ML-based approach first detects the ADRs and then normalizes them to MedDRA Preferred Terms through a rule-based method and dictionary. The F1 scores their introduced model to detect and normalize tasks, and they were 76.97% and 82.58%. The increased spectrum to precisely identify more items in the text was also considered in their model.

Akhtyamova et al. (11) presented a CNN-based architecture, consisting of numerous parameters to predict ADRs based on the number of votes. With regard to the evaluation of the performance of the model, they utilized a broad-spectrum medical dataset derived from medical websites. In contrast to previous reports of networks, the proposed end-to-end model does not need artificial attribute and information pre-processing, which ends up with an enormous improvement in standard CNN-based methods.

Finally, Devlin et al. (12) pointed out Bidirectional Encoder Representations from Transformers (BERT) method, whose function is associated with both left and right context in all layers. Also, pre-trained BERT does only need to be adapted with one additional output layer to become capable of various tasks, which indicates the simplicity and flexibility of BERT.

Taken together, due to the imbalanced Twitter data in this suggested approach, we combined datasets which improved the accuracy of classification. We analyzed the accuracy of three different deep learning classifiers and found that the accuracy of each model strictly depends on the type of data. In these three models, various hyper-parameters were analyzed by applying different batches in epoch 100. We discovered that the exact identification of the learning rate is impossible to be determined because of variations in learning rate among different batch numbers and the way that datasets are distributed. Therefore, these models are unable to identify ADR-related comments in social media such as Twitter, and we analyzed recognition speeds in all three models, which has not been conducted in previous studies.

Materials and Methods

Study design

The classification methods research consists of five steps (Fig.1), starting with data input from three different databases, followed by pre-processing of the data to improve quality of texts, cross-validation tests (grouping input data into train and test category), and classification by deep learning algorithms at the final stage.

Data sources

As shown in Table 1, in order to find input datasets, 6623 comments out of 10822 ones were extracted (14), resulting in an imbalanced data between ADR and non-ADR, and generation of poor Kappa coefficient. In order to overcome this challenge, we combined ADR comments on Twitter with "Ask a patient" datasets (5). According to the importance of special side effects in posted comments, we compared these two datasets to evaluate the method. Regarding the registration of special side effects posted in comments, we used these datasets to compare comments with Twitter whose range of perspectives is quite broad, and then evaluated the method.

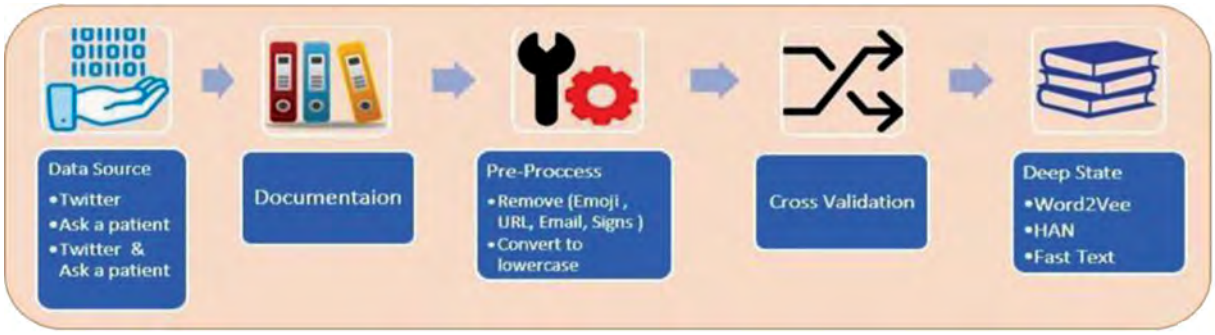

Fig.1: The workflow of the proposed model-based strategy.

Table 1: Input datasets (Twitter, "Ask a Patient" and "Twitter/ Ask a Patient")

Dataset	ADR category	Non-ADR category	Total
Twitter	727	5896	6623
Twitter and ask a patient (ADR)	5727	5896	11623
Ask a patient	12538	14396	26934

ADR; Adverse drug reaction.

Pre-processing

The pre-processing of comments in both datasets was performed as follows:
1. Data shuffling
2. Converting all uppercase words into lowercase
3. Elimination of special characters such as @, !, /, *, $, etc.
4. Remove stop word: at, of, the, …
5. Correction of words with repeated characters including pleaseeeeeeeeee and/or yessss
6. Convert acronym or abbreviation to complete form like: "I'm" →"I am"
7. Lemmatization: for example, "I started taking almost two months ago," → "I started to take almost two months ago."

Error handling

It is required to deal with several challenges to work with Twitter data. The purpose suggested a deep learning approach to use the model for ADR detection automatically; therefore, the following errors were resolved in the pre-processing phase.

In this section, we considered the leading causes of classification errors in these two datasets and discussed potential approaches to solve these challenges. The common causes of misclassifications are:

Non-standard terms of English: The broad-spectrum ADR description is explained by non-medical related terms, which are very rare and unrepeated in posts. Hence, the majority of classifiers are unable to capture these posts.

Short posts: A large number of posts are small sentences and composed of very few medical terms. These types of posts increase the rate of misclassification.

A large proportion of spelling errors: The majority of posts consists of a series of grammatical errors and typos. Thus, these posts not only negatively contribute to lexicon/topic scores, but also are mistaken with non-ADR groups.

Cross-validation

In the majority of the category of models, the complication of the network would be managed by many factors.

In this study, we figured out an appropriate value of the complexity parameters to achieve the highest prediction of performance. Also, we classified all information based on the evaluation, validation, and training sub-database. However, the actual data resources are restricted in the case of testing and training; this result would end-up with the growth of generalized mistakes. The strategy of cross-validation benefit decline of the generalized mistakes and prevent data overlapping. Data distribution for each group is shown in Table 2.

Table 2: Distribution of data in cross-validation phase

Dataset	All content	Train	Test	Validation
Twitter (ADR/Non-ADR)	6623	5962	661	1100
Twitter (ADR/Non-ADR) & Ask a Patient (ADR)	11623	10462	1161	2000
Ask a patient (ADR/Non-ADR)	26934	24242	2692	5000

ADR; Adverse drug reaction.

Deep classification

The methods of data classification include CNN (13), HNN (15), and FastText (16) with similar word2vec section. Then word2vec is generated to proceed into further steps.

Convolutional neural network method

The CNN architecture for sentence classification is composed of three different filter region size; 2, 3 and 4, and each region contains two sub-filters. Filters fold the sentence matrix and generate (variable- length) features maps. One-maximum pooling generates over each map, resulting in six univariate feature vectors. Finally, these six features are connected to each other to form a feature vector for the penultimate layer. Once the feature vector develops, it will be used as input data in the final softmax to classify sentences into two possible output states (13).

Hierarchical Attention Network method

Hierarchical Attention Network (HAN) has two distinctive characteristics: i. A hierarchical structure and ii. Two levels of the word and sentence sensitivity, enabling the network to differentially participate in somewhat valuable content at the time of representing any designed document. Also, the HAN network is made of quite a few parts, including word/sentences-level attention layers and sequence encoder. HAN works based on this thought that sentence and documents structure in modeling plays a decisive role in better proper representation of document structure. In fact, the directional models read the text input sequentially (left-to-right or right-to-left). Conversely, the transformer encoder reads the entire sequence of words, once. Therefore, it is considered bidirectional. Actually, it would be more accurate to say that it is non-directional. This characteristic allows the model to learn the context

of a word-based on all of its surroundings (left and right of the word).

FastText method

This method proposes a simple and efficient approach for classification of the texts and its expression. A large amount of research shows that the rapid classification of text with this method is faster than deep learning in terms of accuracy and using commands for training and evaluation. Basically, two major and influential differences are considered in this regard:

Softmax: is a hierarchy, based on the Huffman encoded tree structure that reduces Time Complexity O (Kd) to O (d log k) in which K is the number of targets, D is the hidden layer dimension.

N-gram attributes: the pool of words have a fixed number of words; however, occasionally, putting this order clearly into consideration costs a lot in terms of computer work. Instead, we used n-gram pool as an extra attribute to obtain data with regard to the sequence of words, locally.

Evaluation metrics

Precision (positive predictive value) and recall (sensitivity): These metrics are an appropriate fraction of retrieved samples from all and relevant instances. The application of these metrics depends on understanding and measuring relevance.

Accuracy: This criterion is the accuracy of the x-group classification against all items where the x-tag is suggested by means of classification for recorded investigation. This criterion indicates how much the output of classification would be reliable.

F-measure: This criterion is a combination of call metrics and accuracy, and it is used to find out if it is possible to consider special importance of each of the two other criteria (precision and accuracy).

Kappa: This criterion is often employed to test the reliability of the viewer and to compare the accuracy of the system in terms of how much the generated output is coincident.

Result

Usage model

In this study, we benefited from user's comments posted on Twitter and "Ask a Patient" to extract side effects of drugs. In the field of deep learning, the following issues are considered in the training phase. Generally, the size of a window that moves on texts in both FastText and HAN methods is called Pad_Seq_Len, and usually, the maximum size of tweets and comments is 150 where the length of sentences and semantic conjugation are essential. The Embedding_dim value of 100 was considered for the creation of Word2Vec. We evaluated several optimizations, such as Stochastic Gradient Descent (SGD), RMS prob, etc. Among them, Adam showed better results.

Implementation method

We used NVIDIA GEFORCE GTX 1050 and CPU Intel Core i7 hardware in our study. Three methods of classification were applied against three different data groups, listed in Table 3. In each method, the learning rate and batch size were evaluated, and different criteria have been tested for each type of model according to the type of data. For example, FastText method covered 64 samples in each batch, and the rate of learning was 0.1 on Twitter datasets, resulting in the highest accuracy (0.927). As shown in Table 3, the best value for each dataset in different methods has been highlighted.

Table 3: Output of deep learning classification on three datasets

Dataset	Method	Batch size	Learning rate	Accuracy	Kappa	Recall	Precision	F1_Score	TP	TN	FP	FN
TW	CNN	64	0.1	0.913767	0.34377775	0.6163577	0.90453353	0.66366127	587	17	55	2
	HAN	128	0.001	0.903341	0.319789	0.620908	0.7547446	0.655598	576	19	53	13
	FastText	64	0. 1	0.927983	0.2949333	0.604319	0.78937729	0.6405655	581	16	56	8
TW+ASKA	CNN	128	0.001	0.927648	0.85516381	0.9272798	0.92888383	0.92753972	561	516	56	28
	HAN	128	0.001	0.930099	0.8535246	0.926708	0.92684784	0.9267609	549	572	45	40
	FastText	128	0.001	0.9173126	0.8346399	0.917446	0.91737198	0.9173111	535	530	42	54
ASKA	CNN	128	0.01	0.772421	0.54426175	0.7705728	0.77561211	0.77173868	1191	894	359	248
	HAN	128	0.001	0.759448	0.5187235	0.760284	0.75912463	0.7592033	1081	964	289	358
	FastText	64	0.01	0.753564	0.4990743	0.750270	0.74925432	0.7494246	1074	945	308	365

TP; True positive, TN; True negative, FP; False positive, FN; False negative, TW; Twitter, ASKA; Ask a patient, CNN; Convolutional neural network, and HAN; Hierarchical attention network.

Table 3 shows the results of 3 different dataset analyses, using 3 different methods of deep learning. At first glance, a significant difference between accuracy and Kappa ratio is observed. The results show the highest accuracy rate (0.927) versus learning rate and a batch with the size of 0.1 and 64. However, the Kappa value does not represent a satisfactory result, and the weak value of Kappa is mainly due to an imbalanced distribution of Twitter data.

In order to overcome this challenge, we pooled ADR-related data of both "Ask a patient" and Twitter. Compared to CNN and FastText, a significant precision degree in HAN was 0.930 T, the rate of learning and batch size were 0.001 and 128. We found a direct correlation between the balanced number of documents and the accuracy of classification in each category that presented in (Fig.2). We analyzed speed recognition features of three models based on the best result of Table 3 and Figure 3.

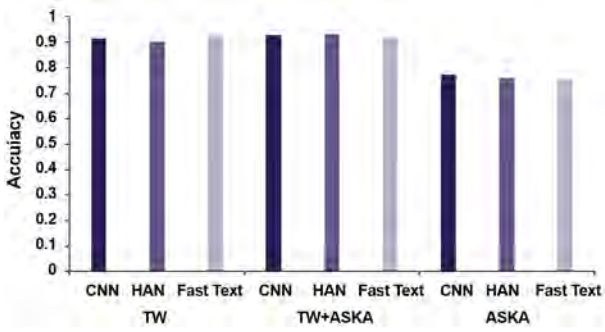

Fig.2: Accuracy of classification in three datasets.

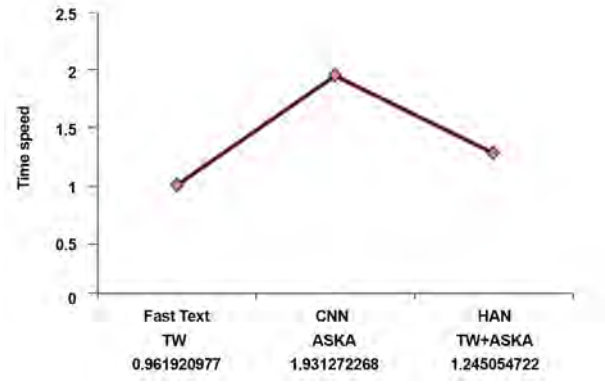

Fig.3: Time speed overview classification in three datasets.

In the following Table, we compared epochs and groups against various hyper-parameters of learning rate.

The best performance was highlighted in Table 3.

'Epoch': It means that how many times our model should be trained.

'Batch size': It refers to how many data records that one batch has.

'Learning rate': It is a kind of the hyper-parameter which regulates the level of adjusted weight in our network in association with gradient.

Large batch sizes in comparison with small ones produce more states of similarity, while latter meet lower training span; thus, the latter seems to have better efficacy, in terms of computational perspectives.

Discussion

The approach of this study was to group processing and challenges into adverse drug events into ADR and non-ADR classes and analyze them using deep learning as a tool.

In this model, we suggested three methods for pre-processing of data analyses, i.e., cleaning/removing URLs, emoji, and hashtags, which are recommended based on data shuffling. The ADR recognition was accomplished through various features extraction networks such as HAN, FastText, and CNN. Finally, the obtained preliminary results of drug classifications were applicable for confusion matrices and consequently interpreted by means of measuring accuracy and false positive ratio. We used numerous deep learning methods for text classification. Compared to current deep learning-based networks, our results showed that the FastText, CNN, and HAN were much faster and more accurate.

Furthermore, in comparison with unsupervised trained word vectors, the word vector, developed in our models, would be incorporated to generate an appropriate sentence representation (6). According to deep learning models, we suggested the approach of end-to-end, in which artificial attribute and preprocessed information are not necessary. The obtained results demonstrated that the proposed models would significantly improve the performance of baseline methods for different datasets.

We noticed that increasing batch size during training steps considerably reduced the learning rate in the network. Conversely, we tested various optimizers including SGD, RMS, and Adam in datasets, "Ask a patient" dataset, and found that Adam shows better results compared to RMS and SGD.

Conclusion

All in all, the main focus of this study was on Twitter data. However, we added some data from other public databases for scientific comparisons. The obtained results highlighted that the combination of "Ask a patient," and Twitter datasets significantly improved the accuracy of classification. Furthermore, pooling ADR training data for "Ask a patient", and Twitter datasets showed a slight improvement in classification.

These results suggest that normalized datasets in terms of type and structure of sentences are able to be merged as a training dataset. "Ask a patient", and

Twitter datasets represent different characteristics. The former present valuable information related to the cause of side effects which leads to a better orientation of user comments, the latter does not have this feature, which mainly ends up with more general points of view over a specific drug.

In order to measure the compatibility of text, several features have been considered, including the indication of topics, ADRs, and concepts. We used two categories of data to detect medication side effects and to generate and analyze combined dataset by deep learning. The findings pointed out that using large batch size not only significantly improves efficacy and accuracy of classification, but also reduces the number of required parameters, updated for model training, which consequently decrease training time.

We categorize the public opinions on Twitter towards the side effect of medications. This study would make the possibility of further investigations into their adverse effects on the various cell through text mining and summarization techniques for evaluation of the scientific publications related to ADR in PubMed.

Acknowledgements

The authors have no proprietary, financial, professional, or other personal interest of any nature in any product, service, or company. There is no conflict of interest in this study.

Authors' Contributions

H.E.-K.; Scientific supervisor of the project, finalized manuscript and was in charge of overall directions and planning. Z.R., B.E.; Analyzed and implemented the raw idea and did the literature review to develop the idea, concept, design, analyzed and implement the results statistically and scientifically, participated in drafting the manuscript as well as data collection and contributed to figures preparation and visualization. M.T., R.Ch.; Did editing and participated in proofreading the manuscript, approved the final draft, provided scientific advice throughout the project and also performed cell and medical culture. All authors read and approved the final draft of the manuscript.

References

1. Kongkaew C, Noyce PR, Ashcroft DM. Hospital admissions associated with adverse drug reactions: a systematic review of prospective observational studies. Ann Pharmacother. 2008; 42(7): 1017-1025.
2. Classen DC, Pestotnik SL, Evans RS, Lloyd JF, Burke JP. Adverse drug events in hospitalized patients. Excess length of stay, extra costs, and attributable mortality. JAMA. 1997; 277(4): 301-306.
3. Harpaz R, Callahan A, Tamang S, Low Y, Odgers D, Finlayson S, et al. Text mining for adverse drug events: the promise, challenges, and state of the art. Drug Saf. 2014; 37(10): 777-790.
4. Sultana J, Cutroneo P, Trifir G. Clinical and economic burden of adverse drug reactions. J Pharmacol Pharmacother. 2013; 4(Suppl1): S73-S77.
5. A website for research drugs and health care topics. Available from: https://www.AskaPatient.com/ (10 Nov 2018).
6. Sarker A, Gonzalez G. Portable automatic text classification for adverse drug reaction detection via multi-corpus training. J Biomed Inform. 2015; 53: 196-207.
7. Ginn R, Pimpalkhute P, Nikfarjam A, Patki A, O'Connor K, Sarker A, et al. Mining twitter for adverse drug reaction mentions: a corpus and classification benchmark. Fourth workshop on Building and Evaluating Resources for Health and Biomedical Text Processing (BioTxtM). Reykjavik, Iceland: 2014.
8. Akhtyamova L, Alexandrov M, Cardiff J, editors. Adverse drug extraction in twitter data using convolutional neural network; 2017; Lyon, France: IEEE; 28th International Workshop on Database and Expert Systems Applications (DEXA); 2017.
9. Lee K, Qadir A, Hasan SA, Datla V, Prakash A, Liu J, et al. Adverse drug event detection in tweets with semi-supervised convolutional neural networks. 26th International Conference on World Wide Web; 2017; 705-714.
10. Tiftikci M, Özgür A, He Y, Hur J. Extracting adverse drug reactions using deep learning and dictionary based approaches. Text Analysis Conference (TAC); 2017.
11. Akhtyamova L, Ignatov A, Cardiff J. A Large-Scale CNN Ensemble for Medication Safety Analysis. Springer; International Conference on Applications of Natural Language to Information Systems; 2017; 247-253.
12. Devlin J, Chang MW, Lee K, Toutanova K. BERT: pre-training of deep bidirectional transformers for language understanding; 2018.
13. Kim Y. Convolutional neural networks for sentence classification; 2014.
14. Biomedical Informatics Lab at ASU, Diego Lab. Available from: http://diego.asu.edu/downloads/adr_classify_ twitter_data.txt (10 Nov 2018).
15. Yang Z, Yang D, Dyer C, He X, Smola A, Hovy E. Hierarchical attention networks for document classification. Conference of the North American Chapter of the Association for Computational Linguistics: human language technologies (NAACL); 2016; 1480-1489.
16. Joulin A, Grave E, Bojanowski P, Mikolov T. Bag of tricks for efficient text classification; 2016.

Original Article

PolyI:C Upregulated *CCR5* and Promoted THP-1-Derived Macrophage Chemotaxis via TLR3/JMJD1A Signalling

Xiaoxiao Yu, Ph.D.[1], Huayang Wang, M.D.[2], Hongjia Shao, M.M.[1], Cuijuan Zhang, Ph.D.[3], Xiuli Ju, Ph.D.[1], Jie Yang, Ph.D.[1]*

1. Department of Paediatrics, Qilu Hospital of Shandong University, Jinan, Shandong, China
2. Department of Clinical Laboratory, Qilu Hospital of Shandong University, Jinan, Shandong, China
3. Department of Pathology, Qilu Hospital of Shandong University, Jinan, Shandong, China

***Corresponding Address: Department of Paediatrics, Qilu Hospital of Shandong University, Jinan, Shandong, China**
Email: yangj6466@163.com*

Received: 21/January/2019, Accepted: 15/May/2019

Abstract

Objective: This study aimed to evaluate the specific roles of polyinosinic:polycytidylic acid (polyI:C) in macrophage chemotaxis and reveal the potential regulatory mechanisms related to chemokine receptor 5 (*CCR5*).

Materials and Methods: In this experimental study, THP-1-derived macrophages (THP1-Mφs) induced from THP-1 monocytes were treated with 25 μg/mL polyI:C. Toll-like receptor 3 (*TLR3*), Jumonji domain-containing protein (JMJD)1A, and *JMJD1C* small interfering RNA (siRNAs) were transfected into THP1-Mφs. Quantitative real-time reverse transcriptase polymerase chain reaction (qRT-PCR) was used to detect the expression levels of *TLR3, CCR5*, 23 Jumonji C domain-containing histone demethylase family members, *JMJD1A*, and *JMJD1C* in THP1-Mφs with different siRNAs transfections. Western blot was performed to detect *JMJD1A*, JMJD1C, H3K9me2, and H3K9me3 expressions. A transwell migration assay was conducted to detect THP1-Mφ chemotaxis toward chemokine ligand 3 (CCL3). A chromatin immunoprecipitation (ChIP) assay was performed to detect H3K9me2-CCR5 complexes in THP1-Mφs.

Results: PolyI:C significantly upregulated *CCR5* in THP1-Mφs and promoted chemotaxis toward *CCL3* ($P<0.05$); these effects were significantly inhibited by *TLR3* siRNA ($P<0.01$). *JMJD1A* and *JMJD1C* expression was significantly upregulated in polyI:C-stimulated THP1-Mφs, while only *JMJD1A* siRNA decreased *CCR5* expression ($P<0.05$). *JMJD1A* siRNA significantly increased H3K9me2 expression in THP1-Mφs but not in polyI:C-stimulated THP1-Mφs. The ChIP result revealed that polyI:C significantly downregulated H3K9me2 in the promoter region of *CCR5* in THP1-Mφs.

Conclusion: PolyI:C can enhance THP1-Mφ chemotaxis toward *CCL3* regulated by *TLR3/JMJD1A* signalling and activate *CCR5* expression by reducing H3K9me2 in the promoter region of *CCR5*.

Keywords: Chemokine Receptor 5, Chemotaxis, Macrophages, Polyinosinic:polycytidylic Acid

Cell Journal(Yakhteh), Vol 22, No 3, October-December (Autumn) 2020, Pages: 325-333

Citation: Yu X, Wang H, Shao H, Zhang C, Ju X, Yang J. PolyI:C upregulated CCR5 and promoted THP-1-Derived macrophage chemotaxis via TLR3/JMJD1A signalling. Cell J. 2020; 22(3): 325-333. doi: 10.22074/cellj.2020.6713.

Introduction

Acute lung injury (ALI) is an inflammation characterized by the breakdown of the endothelial and epithelial lung barrier (1). Monocyte-derived macrophages are important in the pathogenesis of ALI. Under the pathological conditions of ALI, activated circulating monocytes infiltrate the alveolar space to form alveolar macrophages. Subsequently, alveolar macrophages may secrete several inflammatory mediators, such as cytokines and chemokines, to induce the migration of mature neutrophils and $CD4^+$T cells into the alveolar space, thereby prompting an inflammation response that may kill pathogenic microbes (2, 3). A previous study showed that the depletion of circulating monocytes and subsequently recruited alveolar macrophages significantly suppressed ALI in mice (4). Therefore, the function and activity of macrophages are extremely important in the development and prognosis of ALI.

Toll-like receptors (TLRs) are categorized as innate immune sensors, which play an important role in the process of antigen recognition for innate immune cells such as macrophages (5). It has been reported that *TLR3* is upregulated in alveolar macrophages throughout the ALI pathogenesis (6). Chemokines comprise a class of cytokines that act as signalling molecules in the regulation of inflammatory response (7). Chemokine receptors (CCRs) are specific receptors for chemokines that are integral to the recruitment of alveolar macrophages (8). *TLR3* and CCRs participate in ALI-induced inflammatory response through the recognition of pathogen-related molecular processes or the recruitment of macrophages; however, whether a direct regulating mechanism between CCRs and *TLR3* exists in macrophages has not been thoroughly researched.

Histone demethylation is an important form of epigenetic modification that is regulated by Jumonji C domain-containing histone demethylases (JHDMs) (9). Histone demethylation is involved in the transcriptional repression and activation of target genes, and is closely associated with the inflammatory response of macrophages. It has been reported that Jumonji domain-containing protein 3 (*JMJD3*) influences transcriptional gene expression in lipopolysaccharide (LPS)-activated macrophages, and the regulatory role of *JMJD3* is dependent upon H3K4me3

(10). An H3K27me3 inhibitor reduces LPS-induced proinflammatory cytokine production by macrophages, and this process is regulated by *UTX* and *JMJD3* (11). Moreover, a pervious study reported that high glucose upregulates diverse inflammatory cytokines in macrophages, including *IL-6, IL-12p40,* and *MIP-1α/β*; this process is closely associated with H3K9 methylation (12). However, the specific role of H3K9 methylation in *TLR3* signalling for macrophage-involved inflammatory responses remains unknown.

Polyinosinic:polycytidylic acid (PolyI:C) is a viral mimetic that mimics inflammatory responses to systemic viral infection (13). In this study, the effects of polyI:C on THP-1-derived macrophage (THP1-Mφ) chemotaxis, as well as potential regulatory mechanisms related to *TLR3* and CCRs, are explored. The aim of this study is to provide new insight into the underlying regulatory mechanisms for macrophage participation in ALI.

Materials and Methods

Cell culture and induction of THP-1-derived macrophages (THP1-Mφs)

In this experimental study, human THP-1 monocytes were purchased from the American Type Culture Collection (Manassas, VA, USA) and cultured in RPMI-1640 medium that contained 10% heat-inactivated foetal bovine serum (FBS, Gibco, USA) and 100 U/mL penicillin-streptomycin. Cells were maintained in an atmosphere of 5% CO_2 at 37˚C. Exponential-phase cells were used in the following assays.

THP-1 monocytes were induced to differentiate into macrophages *in vitro*. Simply, THP-1 monocytes suspended in RPMI-1640 medium were seeded in 6-well plates at a density of 2×10^5 cells/mL. Then, 100 ng/mL phorbol-12-myristate acetate (PMA) (Sigma, St. Louis, MO, USA) was added to the THP-1 monocytes. After a 48-hour incubation period, the adherent macrophages were used in the following assays (THP1-Mφs). For polyI:C treatment, THP-1 monocytes were incubated with 100 ng/mL PMA for 6 hours, and then treated with 25 μg/mL polyI:C (R&D Systems, Minneapolis, MN, USA). After 42 hours of incubation, the adherent macrophages were used in the following assays (polyI:C-stimulated THP1-Mφs).

Quantitative real-time reverse transcriptase polymerase chain reaction

Total RNA was extracted from cells of different groups using TRIzol (Fermentas, Burlington, Ontario, Canada) and reverse-transcribed by RevertAid M-MuLV Reverse Transcriptase (Fermentas, Canada) in accordance with the manufacturer's instructions. Quantitative real-time reverse transcriptase polymerase chain reaction (qRT-PCR) was performed on a LightCycler 2.0 Instrument (Roche, Germany) using the SYBR Green PCR Kit (TaKaRa, Japan). The relative expression levels of target genes were calculated by $2^{-\Delta\Delta Ct}$, using *GAPDH* as an internal control. The primer sequences are shown in Table 1.

Flow cytometry

Flow cytometry was performed to detect chemokine receptor 5 (*CCR5*) expression in THP1-Mφs. Simply, cells were suspended in fresh RPMI-1640 medium and incubated with CCR5-PE antibody (R&D Systems, USA) in the dark for 30 minutes at room temperature. Data were collected using the FACSCalibur flow cytometer (BD Biosciences, San Jose, CA, USA) and analysed with CellQuest software (BD Biosciences).

siRNA transfection

siRNAs targeting *TLR3*, Jumonji domain-containing protein 1A (*JMJD1A*), and *JMJD1C* were obtained from Shanghai GeneChem Company (Shanghai, China), as follows:

TLR3 siRNA:
5′-CCUGAGCUGUCAAGCCACUACCUUU-3′

JMJD1A siRNA:
5′-GCAAUUGGCUUGUGGUUACUU-3′

JMJD1C siRNA:
5′-GCAAUUGGCUUGUGGUUACUU-3′.

After 6 hours of incubation with 100 ng/mL PMA, THP1-Mφs were incubated with specific siRNAs and Lipofectamine 2000 reagent (ThermoFisher, Waltham, MA, USA) for 6 hours. Transfected cells were treated with 25 μg/mL polyI:C for an additional 42 hours. The efficacy of the *TLR3* transfection was detected using qRT-PCR and flow cytometry as described above, while the efficacy of *JMJD1A* and *JMJD1C* siRNA-mediated gene silencing was monitored using Western blotting.

Transwell migration assay

THP1-Mφ chemotaxis toward chemokine ligand 3 (*CCL3*) was detected using transwell inserts. Transwell inserts with a pore size of 8 μm were placed into 24-well plates. Cells were suspended in serum-free RPMI-1640 medium and inoculated into the upper chamber at a density of 1×10^5 cells/mL. RPMI-1640 medium that contained 100 ng/mL recombinant human CC chemokine ligand 3 (rhCCL3;#270-LD, R&D Systems, USA) and 10% FBS was added into the lower chamber. Following 12 hours of incubation at 37˚C, the non-migrated cells were removed from the upper chamber, and migrated cells in the lower chamber were fixed with methanol and stained with eosin. Five random fields of each well were observed using light microscopy, and the number of migrated cells was counted.

Chromatin immunoprecipitation assay

The chromatin immunoprecipitation (ChIP) assay was performed to detect H3K9 methylation in THP1-Mφs. After being fixed in 1% formaldehyde, the chromatin was extracted from THP1-Mφs using sonication. Then, the chromatin was immunoprecipitated with H3K9me2 (Abcam, Cambridge, MA, USA) or H3K9me3 antibody (Abcam, USA) pre-bound Protein G-plus Agarose beads, overnight at 4˚C. Precipitated protein-DNA complexes were eluted in Tris-EDTA buffer that contained 2% sodium dodecyl sulfonate (SDS), and the crosslink was reversed through a 16 hour incubation period at 65˚C. The precipitated DNA fragments were analysed by qRT-PCR as described above. The primer sequences of *CCR5*-ChIP are shown in Table 1. qRT-PCR was performed

on a LightCycler 2.0 Instrument (Roche, Germany) using TB Green Fast qPCR Mix (Code No. RR430S/A/B, TaKaRa, Japan).

Table 1: Sequences of specific primers used in quantitative real-time reverse transcriptase polymerase chain reaction (qRT-PCR)

Gene	Primer sequence (5´-3´)
CCR1	F: CGAAAGCCTACGAGAGTGGAA
	R: CGGACAGCTTTGGATTTCTTCT
CCR2	F: GAGCCATACCTGTAAATGCC
	R: GAGCCCAGAATGGTAATGTG
CCR4	F: CATGAACCCCACGGATATAGCA
	R: CTACTCCCCAAATGCCTTGATG
CCR5	F: TGTCCCCTTCTGGGCTCACTAT
	R: TGGACGACAGCCAGGTACCTA
CCR6	F: TCGCCATTGTACAGGCGACTA
	R: CGCTGCCTTGGGTGTTGTAT
CCR7	F: CCTGGGGAAACCAATGAAAAGC
	R: GAGCATGCCCACTGAAGAAGC
CXCR4	F: TTCCTGCCCACCATGTAGTC
	R: TCGATGCTGATCCCAATGTA
FBXL10	F: CAGTGGGTGGAGGGACTAAA
	R: ACTGAGGTGGAGCTTGGAGA
FBXL11	F: ATAACCAACCGTTCCCACCT
	R: TGCCCAGTCCATCATAATCC
JMJD1A	F: ATGCCCACACAGATCATTCC
	R: CTGCACCAAGAGTCGATTTT
JMJD1B	F: AACTTCCTCAAACCCCCTTG
	R: CCCATCACCATCTCCTTCAC
JMJD1C	F: TCCAGAATCCCAGTCACCAC
	R: CAGCAAATCCCGTAAGGTTG
JMJD2A	F: CAGAGGACCAAGCCATTGAT
	R: ATTGGCTGAACACCGAGAAC
JMJD2B	F: GGGGAGGAAGATGTGAGTGA
	R: CTATGGGTGCCTCCTTCTCA
JMJD2C	F: TGCCTGAGGTTCTGTCCATT
	R: GCTGCTATCTGGCTTGTGGT
JMJD2D	F: AAATATGTACGGGGCAACCA
	R: TACTCAGACCTGGGGGTACG
JMJD3	F: CTGATGCTAAGCGGTGGAAG
	R: TGTTGATGTTGACGGAGCAG
JMJD4	F: ACTGGGTCAATGGCTTCAAC
	R: AGGACCAGGAGCCTCTTCTC
JMJD5	F: ACATCAGCATCCCCGACTAC
	R: AGGGTACAGAGCCCCTGACT
JARID1A	F: TGAACGATGGGAAGAAAAGG
	R: AGCGTAATTGCTGCCACTCT
JARID1B	F: TTGGGATTGAAAAGGAAGCA
	R: CAGCAATTTCCCTTCATTGG
JARID1C	F: CAGGGCTTACTGGAGAATGG
	R: TTCTCATCCAGGGTCACCTC
JARID1D	F: ACTGAACTCCGGGTCCTTCT
	R: GCTTCAGGCACCTCTACACC
JARID2	F: CTGTCTGGAGTGTGCTCTGC
	R: ACGTCCACTGTCGCTCTCTT
UTX	F: CGTGTCGTATCAGCAGGAAA
	R: CACCCCAGTAACCTTCAGGA
HR	F: CAGTCAGCGTCACTCAGCA
	R: CGATCCCAGACACCTAGCA
HSPBAP1	F: AAGCTCAAAGACATGCGGTTA
	R: CAGGCTCTGGTATTTTGTGGA
HIFAN	F: ACAATCCCGACTACGAGAGGT
	R: GCCACTTTCTGATGAGCTTTG
MINA	F: ACTTTGGCTCCTTGGTTGG
	R: CCCGGCTTCAGCATAAAC
PHF2	F: ATCTTTAAGTCCCGGTCGAAG
	R: TTCCTCTTGGCACTCTTTT
PHF8	F: CTGATGATGATGACCCTGCTT
	R: TTCTTCTTTTGGGCCTTCTGT
PHF20	F: ACCCGGCTCCCCAAAGGTGA
	R: CTGCCACTGGTGCTGGGAGC
CCR5-ChIP	F: TGTGGGCTTTTGACTAGATGA
	R: TAGGGGAACGGATGTCTCAG
GAPDH	F: CAACTGGTCGTGGACAACCAT
	R: GCACGGACACTCACAATGTTC

Western blot

THP1-Mφs were lysed in RIPA buffer. Total proteins were separated by SDS-polyacrylamide gel electrophoresis on 10% polyacrylamide gels and transferred to nitrocellulose membranes (Bio-Rad, Hercules, CA, USA). The membrane was blocked with 5% skim milk in TBST for 2 hours and incubated with special primary antibody (anti-H3K9me2, anti-H3K9me3, Abcam, USA) at 4˚C for 12 hours. After there were washed three times with TBST, the membrane was incubated with horseradish peroxidase-conjugated secondary antibody (Abcam, USA) at 25˚C for 2 hours. Protein bands were visualized with the Image Station IS2000 (Kodak, Rochester, NY, USA).

Statistical analysis

All experiments were performed in triplicate, and all data are presented as means ± standard deviation. The statistical analysis conducted in this study was performed using SPSS 13.0 (SPSS Inc., Chicago, IL, USA). The Shapiro-Wilk was used to test the normality of the distribution. For the data presenting a normal distribution, the mann-withney (two groups) and kruskal-wallis (more than two groups) were used to compare results among different groups. The Wilcoxon rank-sum test was used for non-normally distributed data. P<0.05 denoted statistically significant results.

Results

Polyinosinic:polycytidylic acid upregulated chemokine receptor 5 expression in THP-1-derived macrophages through toll-like receptor 3 signalling

The expression levels of diverse CCRs in THP-1 monocytes and THP1-Mφs were detected. As shown in Figure 1A, *CCR1*, *CCR4*, *CCR5*, and *CCR6* were expressed in both THP-1 monocytes and THP1-Mφs. *CCR1* expression was significantly higher in THP1-Mφs than in THP-1 monocytes (P=0.031). *CCR2*, *CCR7*, and *CXCR4* expressions at the mRNA level were not detected in THP-1 monocytes and THP1-Mφs (Fig.1A). Then, the effects of polyI:C on *CCR1*, *CCR4*, *CCR5*, and *CCR6* expressions were evaluated in THP-1 monocytes and THP1-Mφs. qRT-PCR demonstrated that *CCR5* expression was significantly elevated by polyI:C treatment in THP1-Mφs, while *CCR5* expression was not significantly changed by polyI:C treatment in THP-1 monocytes (Fig.1B). The remarkably increased *CCR5* expression in polyI:C-stimulated THP1-Mφs was also confirmed by flow cytometry (45.9% vs. 20.8%, P=0.017, Fig.1D).

Since macrophages can recognize polyI:C stimulation through *TLR3* signalling. The effects of *TLR3* silencing on *CCR5* expression were detected in polyI:C-stimulated THP1-Mφs. Flow cytometry and qRT-PCR showed that *TLR3* siRNA transfection significantly inhibited *TLR3* expression in polyI:C-stimulated THP1-Mφs (80.2% vs. 48.8%, P=0.011, Fig.1C, E). *CCR5* expression was significantly inhibited by *TLR3* siRNA transfection in polyI:C-stimulated THP1-Mφs (P=0.044, Fig.1F).

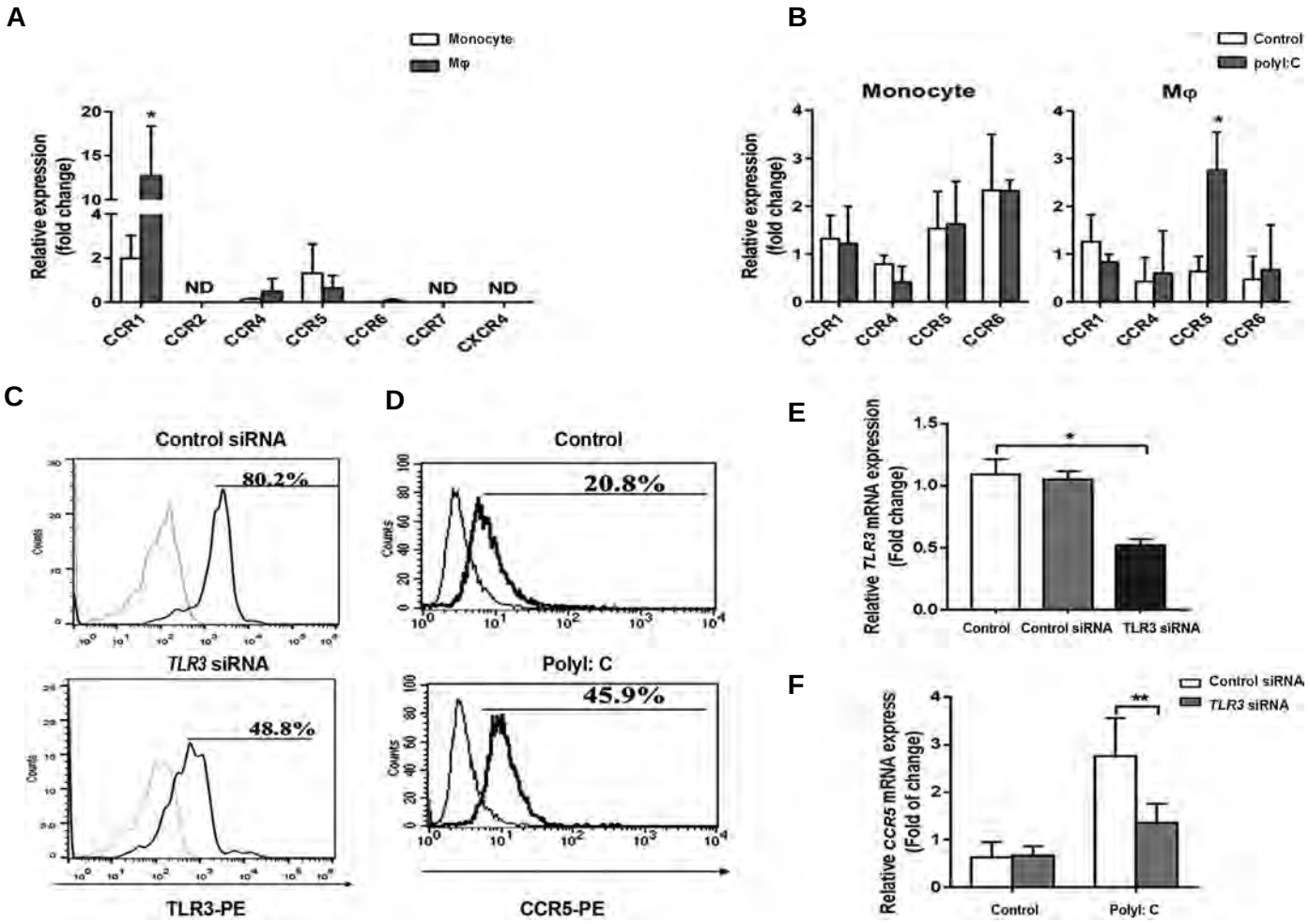

Fig.1: Polyinosinic:polycytidylic acid (PolyI:C) upregulated chemokine receptor 5 (*CCR5*) expression in THP-1-derived macrophages (THP1-Mφs) through toll-like receptor 3 (*TLR3*) signalling. **A.** Expression profile of chemokine receptors in THP-1 monocytes and THP1-Mφs (Mφ) by quantitative real-time reverse transcriptase polymerase chain reaction (qRT-PCR) (fold change at the mRNA level), **B.** *CCR1, CCR4, CCR5*, and *CCR6* expressions in polyI:C-stimulated THP-1 monocytes and THP1-Mφs by qRT-PCR, **C.** CCR5 expression in polyI:C-stimulated THP1-Mφs by flow cytometry, **D.** TLR3 expression in THP1-Mφs with *TLR3* siRNA by flow cytometry, **E.** Knockdown efficiency of *TLR3* siRNA by qRT-PCR, and **F.** *CCR5* expression in polyI:C-stimulated THP1-Mφs transfected with *TLR3* siRNA. *; P<0.05 and **; P<0.01

Polyinosinic:polycytidylic acid promoted THP-1-derived macrophage chemotaxis toward chemokine ligand 3 through toll-like receptor 3 signalling

Since *CCR5* can be activated by *CCL3*, THP1-Mφ chemotaxis toward *CCL3* was analysed. As shown in Figure 2A, THP1-Mφs easily migrated to rhCCL3 (P=0.0005). PolyI:C significantly increased THP1-Mφ chemotaxis toward rhCCL3 (P=0.0006, Fig.2A). In addition, *TLR3* siRNA transfection significantly inhibited polyI:C-stimulated THP1-Mφ chemotaxis toward rhCCL3 (P=0.0029, Fig.2B).

Polyinosinic:polycytidylic acid upregulated Jumonji domain-containing protein 1A and JMJD1C in THP-1-derived macrophages

Since histone methylation is involved in the inflammatory response of macrophages, the expression levels of 23 JHDM family members were observed in polyI:C-stimulated THP1-Mφs by qRT-PCR. As shown in Figure 3A, polyI:C significantly increased *JMJD1A*, *JMJD1C*, *JMJD2A*, *JARID1A*, and *HSPBAP1* expressions in THP1-Mφs (all P<0.01, Fig.3A). Notably, two JHDM2 subgroup members, *JMJD1A* and *JMJD1C*, were highly expressed and abundant in polyI:C-stimulated THP1-Mφs. In addition, *TLR3* siRNA transfection significantly reversed the upregulatory effect of polyI:C on *JMJD1A* and *JMJD1C* on THP1-Mφs (*JMJD1A*, P=0.002; *JMJD1C*, P=0.018, Fig.3B). Therefore, *JMJD1A* and *JMJD1C* were chosen as the targets for the following investigative processes.

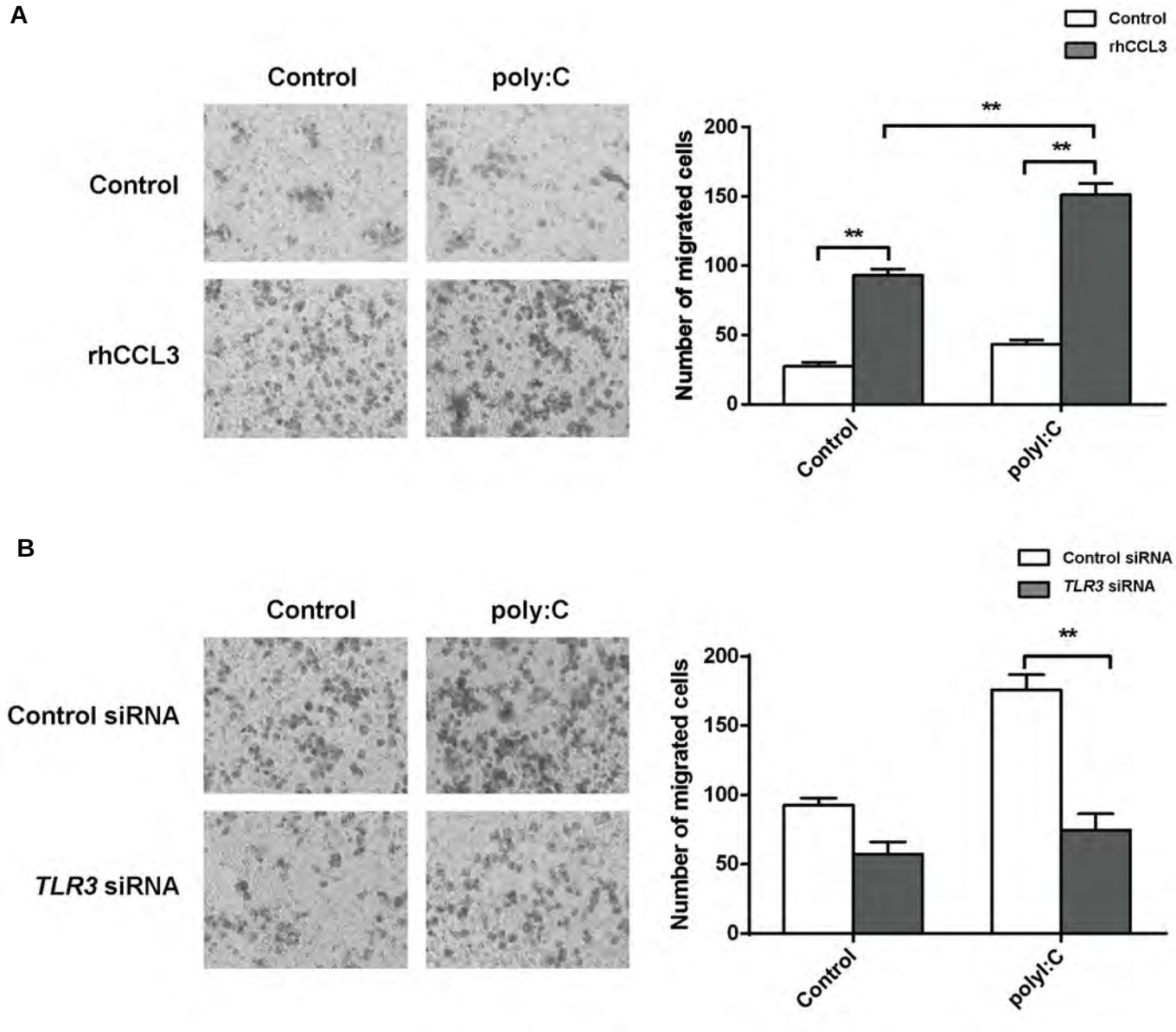

Fig.2: Polyinosinic:polycytidylic acid (PolyI:C) promoted THP-1-derived macrophage (THP1-Mϕ) chemotaxis to chemokine ligand 3 (*CCL3*) via toll-like receptor 3 (*TLR3*) signalling. **A.** THP1-Mϕs migration toward *CCL3* by polyI:C treatment and **B.** PolyI:C-stimulated THP1-Mϕ migration toward *CCL3* by *TLR3* siRNA transfection. **; P<0.01.

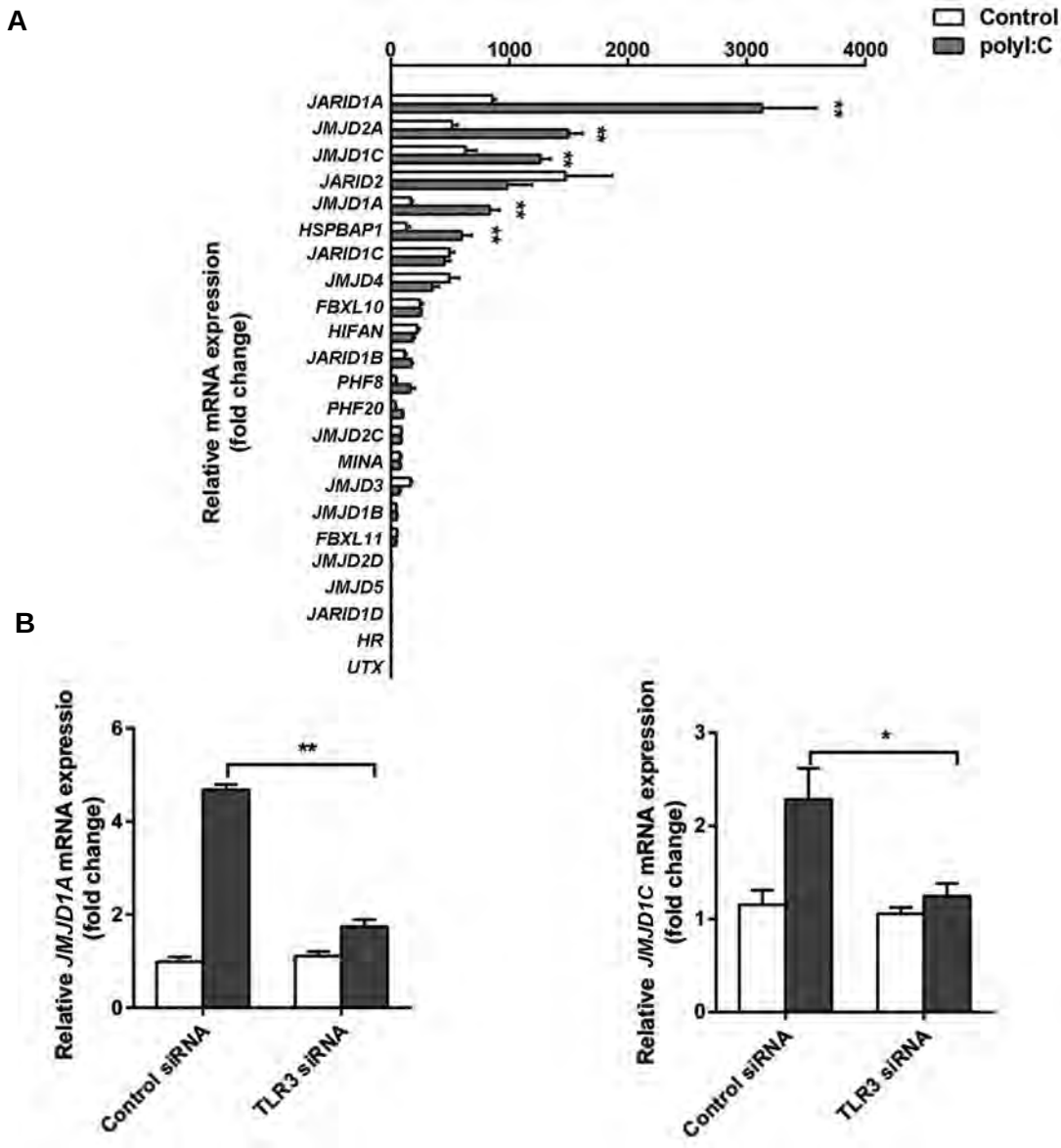

Fig.3: Jumonji C domain-containing histone demethylase (JHDM) family members expression in polyinosinic:polycytidylic acid (polyI:C)-stimulated THP-1-derived macrophages (THP1-Mφs). **A.** The expression levels of 23 JHDM family members in polyI:C-stimulated THP1-Mφs by quantitative real-time reverse transcriptase polymerase chain reaction (qRT-PCR,fold change at mRNA level) and **B.** Jumonji domain-containing protein (*JMJD)1A* and *JMJD1C* expression in polyI:C-stimulated THP1-Mφs transfected with toll-like receptor 3 (*TLR3*) siRNA. *; P<0.05 and **; P<0.01.

Polyinosinic:polycytidylic acid-mediated Jumonji domain-containing protein 1A upregulated chemokine receptor 5 by inhibiting H3K9me2

In order to investigate whether the promoted expression of *JMJD1A* and *JMJD1C* is involved in the regulation of *CCR5* expression, *JMJD1A* and *JMJD1C* were silenced in THP1-Mφs. As shown in Figure 4A, the protein expressions of JMJD1A and JMJD1C were significantly reduced in THP1-Mφs with JMJD1A or JMJD1C siRNA transfection. In addition, JMJD1A siRNA transfection significantly decreased CCR5 expression in both THP1-Mφs (P=0.007, Fig.4B) and polyI:C-stimulated THP1-Mφs (P=0.013, Fig.4B). However, CCR5 expression was not significantly influenced by JMJD1C siRNA transfection (Fig.4B). The downregulation of CCR5 expression induced by JMJD1A siRNA was also confirmed in polyI:C-stimulated THP1-Mφs by flow cytometry (43.8 vs. 32.6%, P<0.05, Fig.4C).

Since H3K9 is known to be the substrate of JMJD1A, we sought to determine if the regulatory role of JMJD1A in *CCR5* expression was dependent on H3K9 methylation. As shown in Figure 4D, H3K9me2 expression was decreased in polyI:C-treated THP1-Mφs, while H3K9me3 expression was not significantly changed. In addition, H3K9me2 was significantly upregulated by *JMJD1A* siRNA transfection in THP1-Mφs. However, H3K9me3 expression was not influenced by *JMJD1A* siRNA transfection in polyI:C-stimulated THP1-Mφs (Fig.4E). In addition, polyI:C treatment downregulated H3K9me2 expression in the promoter region of *CCR5* in THP1-Mφs (Fig.4F).

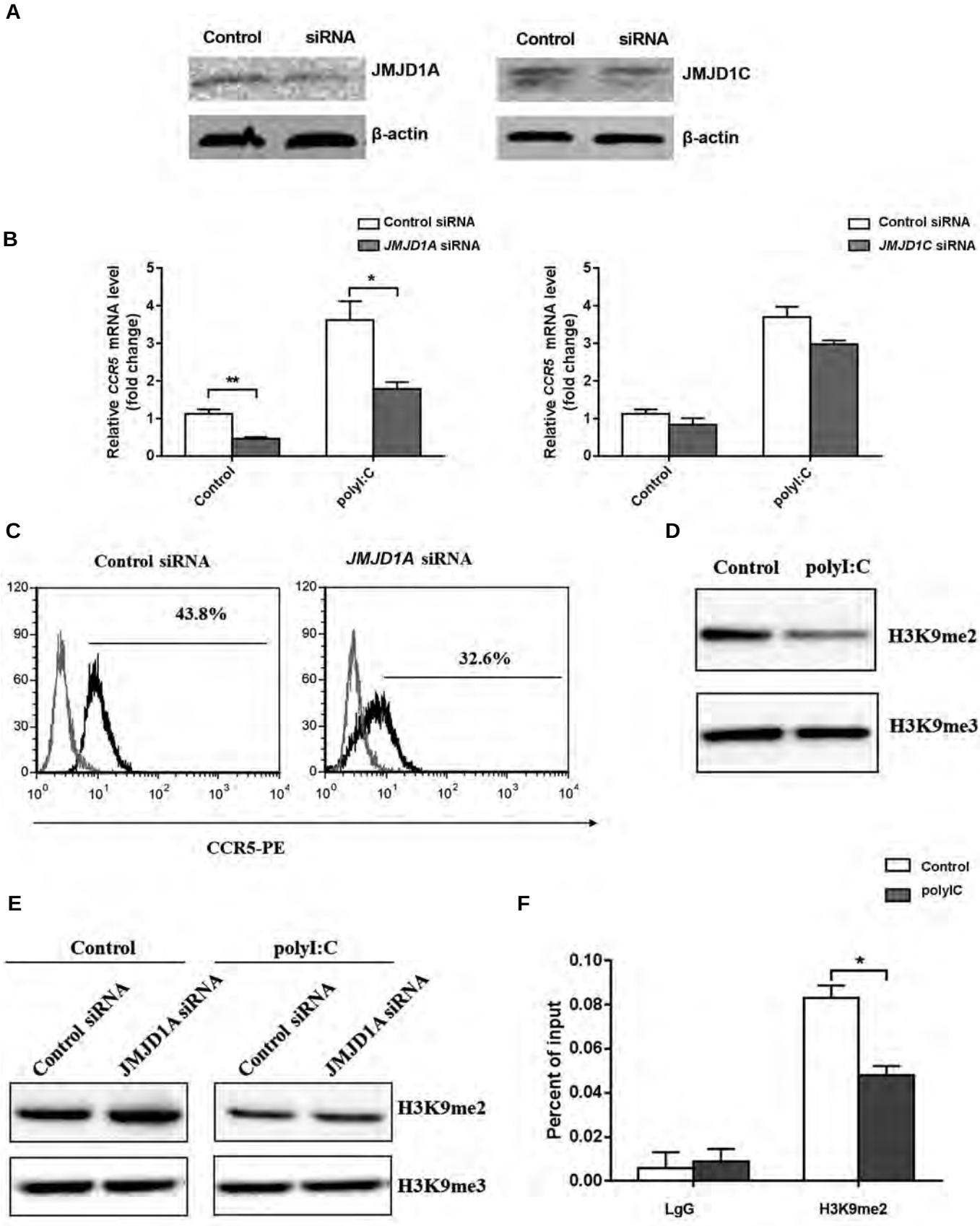

Fig.4: Polyinosinic:polycytidylic acid (PolyI:C)-mediated Jumonji domain-containing protein 1A (*JMJD1A*) upregulated chemokine receptor 5 (*CCR5*) by reducing H3K9me2. **A.** JMJD1A and JMJD1C expression in THP-1-derived macrophages (THP1-Mϕs) treated with *JMJD1A* or *JMJD1C* siRNA by Western blot, **B.** *CCR5* expression in polyI:C-stimulated THP1-Mϕs transfected with *JMJD1A* siRNA and *JMJD1C* siRNA by quantitative real-time reverse transcriptase polymerase chain reaction (qRT-PCR) (fold change at the mRNA level), **C.** CCR5 expression in polyI:C-stimulated THP1-Mϕs transfected with *JMJD1A* siRNA by flow cytometry, **D.** H3K9me2 and H3K9me3 expression in polyI:C-stimulated THP1-Mϕs by Western blot (protein level), **E.** H3K9me2 and H3K9me3 expressions in polyI:C-stimulated THP1-Mϕs transfected with *JMJD1A* siRNA by Western blot (protein level), and **F.** H3K9me2 expression in the promoter region of *CCR5* in THP1-Mϕs by chromatin immunoprecipitation (ChIP) analysis. *; P<0.05 and **; P<0.01.

Discussion

Macrophage chemotaxis is an important component of ALI pathogenesis. It is known that viral infections can induce alveolar macrophage recruitment, but the regulatory mechanisms of viral infection (polyI:C) on monocyte-derived macrophages are still unclear. Thus, in this study, we have explored the regulatory mechanisms of polyI:C on THP1-Mφs. The results showed that polyI:C significantly upregulated *CCR5* in THP1-Mφs and promoted THP1-Mφ chemotaxis toward *CCL3* via *TLR3* signalling. In addition, polyI:C-upregulated *CCR5* was mediated by *JMJD1A*, and H3K9me2 was downregulated in the promoter region of *CCR5* in THP1-Mφs.

Since CCRs are important in macrophage chemotaxis, the expression levels of diverse CCRs were examined in THP1-Mφs after polyI:C treatment. Our results demonstrated that only *CCR5* was significantly upregulated by polyI:C treatment in THP1-Mφs. *CCR5* is a cell surface G protein-coupled receptor that is involved in inflammatory response via interaction with specific chemokine ligands, including *CCL3*, *CCL4*, and *CCL5* (14-16). The activation of *CCR5* and *CCL5* is required to prevent the apoptosis of virus-infected macrophages (17). In addition, *CCR5* is involved in obesity-induced adipose tissue inflammation via regulation of macrophage recruitment (18, 19). Moreover, it has been reported that polyI:C-treated macrophages can promote *CCR5* expression (20), which is consistent with the findings of our study. It was supposed that *CCR5* is involved in polyI:C-induced inflammation in THP1-Mφs. Subsequently, THP1-Mφ chemotaxis toward *CCL3* (a ligand of CCR5) was investigated. The results suggest that polyI:C significantly increased THP1-Mφ chemotaxis toward *CCL3*. A previous study reported that *CCL3* expression was significantly elevated in the lung of a murine model of LPS-induced ALI and mediated an enhanced inflammatory injury-possibly by recruiting macrophages (21). Therefore, polyI:C-upregulated *CCR5* contributes to the promotion of macrophage chemotaxis by interacting with *CCL3*.

Moreover, our results also suggest that *TLR3* siRNA transfection significantly suppressed *CCR5* expression in polyI:C-stimulated THP1-Mφs and inhibited chemotaxis toward *CCL3*. *TLR-3* is responsible for anti-viral immunity against several virus infections via double-stranded RNA recognition and the activation of multiple antiviral factors in macrophages (20). Similarly, *TLR-3* is activated in macrophages in response to encephalomyocarditis infection via type 1 IFN production. It has been reported that *CCR5* may participate in virus replication and acts as the primary receptor for regulating encephalomyocarditis infection in mediating inflammatory response–related genes in macrophages (22). These results indicate that macrophages may recognize polyI:C stimulation through TLR3 signalling. PolyI:C may upregulate *CCR5* expression and promote THP1-Mφ chemotaxis toward *CCL3* through *TLR3* signalling.

Histone demethylation, dynamically regulated by JHDMs, is implicated in the regulation of inflammatory response of macrophages (23). Previous studies have reported that *JMJD3* is over-expressed in LPS-activated macrophages, which regulates diverse genes involved in LPS-induced immune and inflammatory responses (10, 24). However, few studies have focused on the regulatory mechanisms of polyI:C in histone demethylation in macrophages. In this study, the expression levels of 23 JHDM family members were detected in polyI:C-stimulated THP1-Mφs. The expression levels of *JMJD1A*, *JMJD1C*, *JMJD2A*, *JARID1A*, and *HSPBAP1* were significantly increased by polyI:C in THP1-Mφs, while that of *JMJD3* was not significantly changed. These results indicated that the effects of polyI:C on inflammatory responses of macrophages might differ from LPS. Since *JMJD1A* and *JMJD1C* could be regulated by *TLR3* in polyI:C-stimulated THP1-Mφs, the regulatory roles of *JMJD1A* and *JMJD1C* on *CCR5* were further analysed in this study. It was revealed that *CCR5* was significantly downregulated by *JMJD1A* siRNA transfection in polyI:C-stimulated THP1-Mφs, while *CCR5* expression was not significantly influenced by *JMJD1C* siRNA transfection. The regulatory role of *JMJD1A* has been found to affect the proliferation, migration, and invasion of cancer cells in various cancer types (25-27). It has been reported that *JMJD1A* inhibition suppresses tumour growth by downregulating angiogenesis and macrophage infiltration (28). Our findings indicate that polyI:C treatment may induce a similar macrophage inflammatory response with cancer; PolyI:C may enhance *CCR5* expression by upregulating *JMJD1A* in THP1-Mφs.

Since *JMJD1A* is a H3K9 demethylase, the H3K9 methylation state of *CCR5* was analysed in polyI:C-stimulated THP1-Mφs. Our results showed that H3K9me2 expression was significantly decreased by polyI:C treatment in THP1-Mφs. H3K9me2 downregulation might have attributed to the upregulation of *JMJD1A*. However, H3K9me3 expression was not significantly influenced by polyI:C treatment. Our findings indicate that the regulatory role of *JMJD1A* on *CCR5* was dependent on H3K9me2. In addition, H3K9me2 was upregulated by *JMJD1A* siRNA transfection in THP1-Mφs, while H3K9me2 expression was not significantly influenced by *JMJD1A* siRNA in polyI:C-stimulated THP1-Mφs. This may be explained by the fact that some other upregulated JHDMs induced by polyI:C, such as *JMJD1C*, and *JMJD2A* may share a target with *JMJD1A*. *JMJD1C* and *JMJD2A* exhibit redundant effects on H3K9me2 expression. The presence of H3K9me2 in the promoter region of target genes typically results in reduced expressions of its targets. A previous study has reported that H3K9 exhibits a low methylation level in response to the activation of dendritic cells and is erased from the promoters of some activated inflammatory genes (29). Consistent with the results of that study, our results reveal that H3K9me2 expression was significantly reduced by polyI:C treatment in the promoter region of *CCR5* in THP1-Mφs. We suspected that polyI:C-mediated *JMJD1A* upregulation may

upregulate *CCR5* by reducing H3K9me2 in the promoter region of *CCR5*. Interestingly, *JMJD1A* is also a hypoxia-inducible gene that has been found to be upregulated in hypoxia-stimulated macrophages. However, hypoxia treatment decreases *CCR5* expression via H3K9me2 upregulation in the promoter region of *CCR5* (30). This may be explained by the effects of hypoxia-induced repressive JMJDs, which can overwhelm the effects of *JMJD1A*.

Conclusion

The present study revealed that polyI:C upregulated *JMJD1A* expression in THP1-Mφs, thereby elevating the *CCR5* expression by reducing H3K9me2 in the promoter region of *CCR5* via *TLR3* signalling. However, this study is still limited to the cellular level, and the validation of these results in animal models is required in future research.

Acknowledgements

This study was financially supported by Key Research and Development Plan of Shandong Province (2016GSF201031). The authors declare that they have no conflict of interest.

Authors' Contributions

X.Y., H.W.; Participated in study design, data collection and evaluation, drafting, and statistical analysis. H.S., C.Z., X.J.; Performed the study and contributed extensively in interpreting data and developing conclusions. J.Y.; Participated in study design, data analysis and responsible for overall supervision. All authors participated in the editing and finalization of the manuscript and approved the final draft for submission.

Reference

1. Butt Y, Kurdowska A, Allen TC. Acute Lung Injury: A clinical and molecular Review. Arch Pathol Lab Med. 2016; 140(4): 345-350.
2. Bhatia M, Zemans RL, Jeyaseelan S. Role of chemokines in the pathogenesis of acute lung injury. Am J Respir Cell Mol Biol. 2012; 46(5): 566-572.
3. Niesler U, Palmer A, Radermacher P, Huber-Lang MS. Role of alveolar macrophages in the inflammatory response after trauma. Shock. 2014; 42(1): 3-10.
4. Jiang Z, Zhou Q, Gu C, Li D, Zhu L. Depletion of circulating monocytes suppresses IL-17 and HMGB1 expression in mice with LPS-induced acute lung injury. Am J Physiol Lung Cell Mol Physiol. 2017; 312(2): L231-L242.
5. Fukata M, Vamadevan AS, Abreu MT. Toll-like receptors (TLRs) and Nod-like receptors (NLRs) in inflammatory disorders. Semin Immunol. 2009; 21(4): 242-253.
6. Ding X, Jin S, Tong Y, Jiang X, Chen Z, Mei S, et al. TLR4 signaling induces TLR3 up-regulation in alveolar macrophages during acute lung injury. Sci Rep. 2017; 7: 34278.
7. Xuan W, Qu Q, Zheng B, Xiong S, Fan GH. The chemotaxis of M1 and M2 macrophages is regulated by different chemokines. J Leukoc Biol. 2015; 97(1): 61-69.
8. Stone MJ, Hayward JA, Huang C, E Huma Z, Sanchez J. Mechanisms of regulation of the chemokine-receptor network. Int J Mol Sci. 2017; 18(2). pii: E342.
9. Phan AT, Goldrath AW, Glass CK. Metabolic and epigenetic coordination of T cell and macrophage immunity. Immunity. 2017; 46(5): 714-729.
10. De Santa F, Narang V, Yap ZH, Tusi BK, Burgold T, Austenaa L, et al. Jmjd3 contributes to the control of gene expression in LPS-activated macrophages. EMBO J. 2009; 28(21): 3341-3352.
11. Kruidenier L, Chung CW, Cheng Z, Liddle J, Che K, Joberty G, et al. A selective jumonji H3K27 demethylase inhibitor modulates the proinflammatory macrophage response. Nature. 2012; 488(7411): 404-408.
12. Li MF, Zhang R, Li TT, Chen MY, Li LX, Lu JX, et al. High glucose increases the expression of inflammatory cytokine genes in macrophages through H3K9 methyltransferase mechanism. J Interferon Cytokine Res. 2016; 36(1): 48-61.
13. Fortier ME, Kent S, Ashdown H, Poole S, Boksa P, Luheshi GN. The viral mimic, polyinosinic:polycytidylic acid, induces fever in rats via an interleukin-1-dependent mechanism. Am J Physiol Regul Integr Comp Physiol. 2004; 287(4): R759-R766.
14. Lederman MM, Penn-Nicholson A, Cho M, Mosier D. Biology of CCR5 and its role in HIV infection and treatment. JAMA. 2006; 296(7): 815-826.
15. Oppermann M. Chemokine receptor CCR5: insights into structure, function, and regulation. Cell Signal. 2004; 16(11): 1201-1210.
16. Raghu H, Lepus CM, Wang Q, Wong HH, Lingampalli N, Oliviero F, et al. CCL2/CCR2, but not CCL5/CCR5, mediates monocyte recruitment, inflammation and cartilage destruction in osteoarthritis. Ann Rheum Dis. 2017; 76(5): 914-922.
17. Tyner JW, Uchida O, Kajiwara N, Kim EY, Patel AC, O'sullivan MP, et al. CCL5-CCR5 interaction provides antiapoptotic signals for macrophage survival during viral infection. Nat Med. 2005; 11(11): 1180-1187.
18. Kitade H, Sawamoto K, Nagashimada M, Inoue H, Yamamoto Y, Sai Y, et al. CCR5 plays a critical role in obesity-induced adipose tissue inflammation and insulin resistance by regulating both macrophage recruitment and M1/M2 status. Diabetes. 2012; 61(7): 1680-1690.
19. O'Brien PD, Hinder LM, Parlee SD, Hayes JM, Backus C, Zhang H, et al. Dual CCR2/CCR5 antagonist treatment attenuates adipose inflammation, but not microvascular complications in ob/ob mice. Diabetes Obes Metab. 2017; 19(10): 1468-1472.
20. Zhou Y, Wang X, Liu M, Hu Q, Song L, Ye L, et al. A critical function of toll-like receptor-3 in the induction of anti-human immunodeficiency virus activities in macrophages. Immunology. 2010; 131(1): 40-49.
21. Quintero PA, Knolle MD, Cala LF, Zhuang Y, Owen CA. Matrix metalloproteinase-8 inactivates macrophage inflammatory protein-1 alpha to reduce acute lung inflammation and injury in mice. J Immunol. 2010; 184(3): 1575-1588.
22. Christmann BS, Moran JM, McGraw JA, Buller RM, Corbett JA. Ccr5 regulates inflammatory gene expression in response to encephalomyocarditis virus infection. Am J Pathol. 2011; 179(6): 2941-2951.
23. Poralla L, Stroh T, Erben U, Sittig M, Liebig S, Siegmund B, et al. Histone deacetylase 5 regulates the inflammatory response of macrophages. J Cell Mol Med. 2015; 19(9): 2162-2171.
24. De Santa F, Totaro MG, Prosperini E, Notarbartolo S, Testa G, Natoli G. The histone H3 lysine-27 demethylase Jmjd3 links inflammation to inhibition of polycomb-mediated gene silencing. Cell. 2007; 130(6): 1083-1094.
25. Zhan M, Wen F, Liu L, Chen Z, Wei H, Zhou H. JMJD1A promotes tumorigenesis and forms a feedback loop with EZH2/let-7c in NSCLC cells. Tumour Biol. 2016; 37(8): 11237-11247.
26. Agarwal S, Chen Z, Tomolonis JA, Vasudevan SA, Shohet JM. Abstract 4781: Epigenetic regulation of neuroblastoma tumorigenicity through MLL1 and JMJD3 modulation in cancer stem cells. Cancer Research. 2017; 77(13 Supplement): 4781.
27. Kaukonen R, Mai A, Georgiadou M, Saari M, De Franceschi N, Betz T, et al. Normal stroma suppresses cancer cell proliferation via mechanosensitive regulation of JMJD1a-mediated transcription. Nat Commun. 2016; 7: 12237.
28. Osawa T, Tsuchida R, Muramatsu M, Shimamura T, Wang F, Suehiro J, et al. Inhibition of histone demethylase JMJD1A improves anti-angiogenic therapy and reduces tumor-associated macrophages. Cancer Res. 2013; 73(10): 3019-3028.
29. Saccani S, Natoli G. Dynamic changes in histone H3 Lys 9 methylation occurring at tightly regulated inducible inflammatory genes. Genes Dev. 2002; 16(17): 2219-2224.
30. Sar A, Ponjevic D, Nguyen M, Box AH, Demetrick DJ. Identification and characterization of demethylase JMJD1A as a gene upregulated in the human cellular response to hypoxia. Cell Tissue Res. 2009; 337(2): 223-234.

Original Article

Allograft of Sertoli Cell Transplantation in Combination with Memantine Alleviates Ischemia-Induced Tissue Damages in An Animal Model of Rat

Zeinab SafialHosseini, M.Sc.[1], Mohammadreza Bigdeli, Ph.D.[1, 2]*, Sepideh Khaksar, Ph.D.[3], Abbas Aliaghaei, Ph.D.[4]

1. Department of Physiology, Faculty of Life Sciences and Biotechnology, Shahid Beheshti University, Tehran, Iran
2. Institute for Cognitive and Brain Science, Shahid Beheshti University, Tehran, Iran
3. Department of Herbal Science, Faculty of Biological Sciences, Alzahra University, Tehran, Iran
4. Department of Anatomy and Cell Biology, School of Medicine, Shahid Beheshti University of Medical Science, Tehran, Iran

Corresponding Address: Department of Physiology, Faculty of Life Sciences and Biotechnology, Shahid Beheshti University, Tehran, Iran
Email: bigdelimohammadreza@yahoo.com

Received: 3/January/2019, Accepted: 8/June/2019

Abstract

Objective: Brain ischemia is the most common disease in the world caused by the disruption of the blood supply of brain tissue. Cell therapy is one of the new and effective strategies used for the prevention of brain damages. Sertoli cells (SCs) can hide from the host immune system and secrete trophic factors. So, these cells have attracted the attention of researchers as a therapeutic option for the treatment of neurodegenerative diseases. Also, memantine, as a reducer of glutamate and intracellular calcium, is a suitable candidate for the treatment of cerebral ischemia. The principal target of this research was to examine the effect of SC transplantation along with memantine on ischemic injuries.

Materials and Methods: In this experimental research, male rats were classified into five groups: sham, control, SC transplant recipient, memantine-treated, and SCs- and memantine-treated groups. SCs were taken from another rat tissue and injected into the right striatum region. A week after stereotaxic surgery and SCs transplantation, memantine was injected. Administered doses were 1 mg/kg and 20 mg/kg at a 12-hour interval. One hour after the final injection, the surgical procedures for the induction of cerebral ischemia were performed. After 24 hours, some regions of the brain including the cortex, striatum, and Piriform cortex-amygdala (Pir-Amy) were isolated for the evaluation of neurological deficits, infarction volume, blood-brain barrier (BBB) permeability, and cerebral edema.

Results: This study shows that a combination of SCs and memantine caused a significant decrease in neurological defects, infarction volume, the permeability of the blood-brain barrier, and edema in comparison with the control group.

Conclusion: Probably, memantine and SCs transplantation reduce the damage of cerebral ischemia, through the secretion of growth factors, anti-inflammatory cytokines, and antioxidant factors.

Keywords: Brain Ischemia, Cell Transplantation, Memantine, Sertoli Cell

Cell Journal(Yakhteh), Vol 22, No 3, October-December (Autumn) 2020, Pages: 334-343

Citation: **SafialHosseini Z, Bigdeli MR, Khaksar S, Aliaghaei A . Allograft of sertoli cell transplantation in combination with memantine alleviates ischemia-induced tissue damages in an animal model of rat. Cell J. 2020; 22(3): 334-343. doi: 10.22074/cellj.2020.6689.**

Introduction

Cerebral ischemia is the third reason of death and physical impairment in the world caused by the blood vessel blockage, through a blood clot or rupture of a vessel, responsible for the supply of a part of brain tissue (1). About 85% of stroke cases are caused by ischemia and 15% by a brain hemorrhage. The best way for controlling the stroke is the early prevention of ischemic damage expansion and thrombotic therapy (2). During cerebral ischemia, due to lack of oxygen and ATP, the ion pumps that are dependent on ATP, such as sodium-potassium and calcium pumps suffer from functional impairment (3). So, the excessive release of glutamate into the synaptic space leads to excitotoxicity.

Consequently, the extreme influx of extracellular calcium causes an imbalance in cellular homeostasis. An increase in the concentration of calcium inside the cell can activate the caspase enzymes that are in charge of inducing cell death and damages to ischemic cells. Moreover, intracellular calcium can increase the production of free radicals and cause more damages to ischemic cells (4). It should also be emphasized that the main reason for ischemic tissue damage is excitotoxicity. Therefore, a decrease in the concentration of glutamate in the synaptic space can significantly reduce ischemic damages (5).

One of the reasonable choice for reducing glutamate effects in synaptic space is blockage of the N-methyl-D aspartate (NMDA) receptor. NMDA is a receptor for stimulant neurotransmitters, called glutamate, which is a mediator of stimulant neural transmissions in the central nervous system. The excessive activity of this receptor leads to an increase in calcium intake, which provokes excitotoxicity and ultimately death of cells (6). In physiological conditions, the coupling of Mg^{2+} ion with the NMDA receptor prevents over-depolarization of the nerves, and in pathological conditions, lack of binding of Mg^{2+} ion to the NMDA receptor stimulates the nerve extremely (7). Memantine, as a non-competitive antagonist of the NMDA receptor, has a significant role in decreasing the destructive cytotoxicity of the stroke. Memantine is prescribed for the treatment of dementia, Alzheimer's

disease, and Parkinson's disease. The advantage of this drug in comparison with other glutamate receptor antagonists is that it blocks the NMDA receptor without affecting on the natural activity of the receptor, leading to the reduction in neuronal function and excitotoxicity (8). This drug prevents the toxic interactions of free radicals, such as nitric oxide (NO) and reactivity oxygen groups (ROS) with vital macromolecules and also prevents the stimulation and activation of apoptosis-stimulating proteins, such as caspases, neural NO synthase (nNOS), and cytochrome C (9). In another report, it was proved that memantine alone and in combination with melatonin reduced brain damages due to the reduction of P38, ERK-1/2, and inducible NO synthase (iNOS) (10). Also, memantine ameliorated the pathogenesis of Alzheimer's disease in animal models via blockage of the NMDA receptor and reduction of glutamate excitability (11).

In the brain, non-fatal ischemia can induce protective responses against subsequent intensive ischemic injury, called ischemic tolerance (12). The cerebral ischemia is common in people who are susceptible to cerebral ischemia, including patients with a history of heart attack and aneurysm. Accordingly, our purpose is the induction of ischemic tolerance by pretreatment of rats with Sertoli cells (SCs) and memantine.

Along with drug treatment, new strategies, such as cell-based therapy is used for the treatment of stroke. The most of cell resources, including fetal neural cells, stem cells, and SCs (as somatic cells) are suggested as an effective way for the management of some neurodegenerative diseases such as Alzheimer's disease, amyotrophic lateral sclerosis, Huntington's disease, and stroke. These cells are viable and can be replaced with the cells that reside in damaged tissues. They are also capable of reconstructing neural circuits and reducing functional impairment in the brain of patients with the above disorders (13). In the current research, transplanted SCs, as a pretreatment option, for brain ischemia were used. These cells are found in testicular tissues, possessing a high antigenic property, and providing a proper environment for the development of germ cells (14). Also, SCs express neurotrophic and growth factors, such as glial cell-derived neurotrophic factor (GDNF), insulin-like growth factor (IGF), transforming growth factor (TGF), vascular endothelial growth factor (VEGF), and fibroblast growth factor (FGF) (15). The reason for choosing the SCs for this research is the dominant properties of SCs compared with other somatic cells, including the inhibition of the immune system by SCs preventing the rejection of organ in a recipient.

Furthermore, SCs suppress the immune system by forming the tight connections around the nerve cells, thereby the production of interleukin-2 (IL-2) inhibitory factor, and inhibition of expression of major histocompatibility complex (MHC) (16). In another study, it was found that the co-culture of embryonic stem cells with SCs led to the differentiation of embryonic stem cells into dopaminergic neurons as a result of the presence of GDNF factor that is secreted from SCs and acts as a dopaminergic inducer in stem cells (17). Moreover, it was indicated that transplantation of SCs reduced the ischemic damages, such as infarction, brain edema, and the breakdown of the blood-brain barrier (BBB) (18). Concerning the characteristics mentioned about SCs, they could be applied as competent candidates for the amelioration of ischemic injuries.

In the current research, we focused on the effect of transplanted SCs in combination with the use of memantine in an animal model of cerebral ischemia.

Materials and Methods

Animal assignment and experimental protocol

In this experimental study, 98 adult male rats (with the weight range between 250 and 350 g, age range between 5 to 7 weeks) were procured from the Pasteur Institute. The water and food were given to all rats without restriction, and they were kept in standard conditions at the temperature of 22 ± 2˚C and 12:12 light-dark (LD) cycle. Rats were randomly divided into five groups: sham, control, allograft SC transplant recipient, memantine-treated group, and SC- and memantine-treated groups. The control group (n=21) consisted of rats that underwent ischemia following MCAO surgery. The control group was classified into three sub-groups to evaluate infarction (n=7), the BBB permeability (n=7), and brain edema (n=7). The sham group (n=14) consisted of rats that were suffered from the same surgery procedure of MCAO without importing suture and subdivided to assess the BBB permeability (n=7) and cerebral edema (n=7). The animals belonging to the allograft SC transplantation group received SCs from another rat tissue and were induced by MCAO surgery. The allograft SC transplantation group (n=21), the memantine-treated group (n=21), and the SC and memantine-treated group (n=21), divided into subgroups, as well as the control group. All rats were examined for the neurological deficit.

In this research, the two groups were selected for receiving SC culture medium and SCs without ischemic surgery. The comparison between these two groups and allograft SC transplantation did not indicate any significant difference. Also, the experimental methods were accomplished on vehicle (solvent of memantine) group. There was no remarkable difference between the vehicle group and other groups. So, the data of these groups are not shown.

Ethical statement

This study was designed according to the rules of the National Institutes of Health and Care Guidance, the use of the Animal Laboratory (NIH Publications) revised in 2011, and the Ethics Committee of Shahid Beheshti University (No. 1012.667). Our whole effort was to use the lowest number of animals in this research.

Pharmaceutical compound

Memantine, as a NMDA receptor blocker was used in

this study was injected with different doses (1 mg/kg and 20 mg/kg; intraperitoneally). A week after stereotaxic surgery and SC transplantation, the injection of the drug was performed. Memantine was solved in saline. First, the high dose of 20 mg/kg and 12 hours later a low dose (1 mg/kg) was injected. One hour after the final injection, middle cerebral artery occlusion (MCAO) surgery was started. The minimum dose of memantine for each rat was 1 mg/kg, and the minimum toxic dose was 25 mg/kg; so, the most appropriate dose used as the therapeutic dose was 20 mg/kg (19, 20). According to the previous studies, the dose of 20 mg/kg was selected in this research. By injecting this dose, the concentration of the drug in the brain tissue reaches 1-10 micromolar that this concentration is suitable for blocking a large number of NMDA receptors.

Moreover, the half-life of the drug is 12 hours. Therefore, for keeping the levels of the drug at 1-10 micromolar in the brain, 12 hours after the first injection, the preservative dose of 1 mg/kg was administered (19, 20).

Isolation and culture of sertoli cell

At first, rats were sacrificed, and their testis removed and transferred into a falcon containing the culture medium and antibiotics. Under sterile conditions, the small pieces were separated from testicular tissue. Tissues were transmitted to tubes containing trypsin (0.25%, Gibco, USA) and were incubated at 37˚C for 15 minutes. First, the nephrotic tubes were separated; then, trypsin was aspirated, and 1% collagenase was added to the tubes consisting of tissues, and the samples were incubated at 37˚C for 15 minutes. After pipetting the samples and addition of the serum, the samples were centrifuged, and the resultant pellet was transferred into the culture flasks containing Dulbecco's Modified Eagle's Medium (DMEM/F12, Gibco, USA) culture medium supplemented with 10% fetal bovine serum (FBS, Gibco, USA) and antibiotics. After 48 hours of the culture period, the culture medium was replaced by the new one. When the cells reached to appropriate density, they were passaged with trypsin (18).

Immunocytochemistry of Sertoli cells

SCs were transferred into the plates for 24 hours, and after the cells reached appropriate density, the whole culture medium was removed. Then, it was washed with phosphate buffered saline (PBS), and the cells were fixed by 4% paraformaldehyde solution. The cells were permeabilized by 0.3% Triton X-100 solution (Sigma Aldrich, USA), and then incubated in blocking solution. Afterward, the cells were incubated with the primary antibody (anti-GATA4, Abcam, USA) overnight. Subsequently, the cells were washed with PBS and incubated with the second antibody (goat conjugated-FITC anti-mouse antibody). The nuclei of the cells were stained by Hoechst and were observed under a fluorescent microscope. The presence of SCs was performed by the immunocytochemistry technique, as GATA4 was defined as a marker.

Stereotaxic surgery and injecting Sertoli cells

After SCs reached to appropriate density, the cells were located in a suspension of a 2 µl DMEM aliquot. Then, they were separated with a trypsin solution. After centrifuging, the cells were counted with trypan blue staining method, and 500,000 cells were selected for the injection. Rats were anesthetized, and their heads were fixed in a stereotaxic device. After cleaning the skull surface, the distance between the Lambda and Bregma was found, and injection of the cells into the right striatum was carried out by a Hamilton micro-syringe, according to the coordinates of the brain atlas specified for rats: Bregma: +0.5 mm AP; ± 2.6 mm ML; -5 mm DV (21).

The injected cells were labeled with DiI (5 µg/ml for 20 minutes before the injection) (Sigma Aldrich, USA) and Hoechst staining. After 7 days, rats were sacrificed, and the brain was prepared for the determination of the survival and distribution of transplanted cells. The cells were detected by fluorescing microscopy.

Induction of focal ischemic stroke

Anesthesia of rats was performed with chloral hydrate (400 mg/kg). According to the method explained by Lange et al. (22), MCAO surgery was performed. In this surgery, a 0-3 nylon suture was inserted to the internal artery through the trunk of the common carotid artery and to the anterior cerebral artery. It continued through the internal carotid artery. Due to the insertion of the suture and blockage of arterial blood flow, the blood flow was not able to reach MCA. After 60 minutes, the suture was withdrawn and the right hemisphere blood flow restored through the Willis Ring.

Neurobehavioral evaluation

Behavioral evaluation of neurological defects was conducted 24 hours after the reperfusion process. The neurological finding was categorized into 5 parts, including motor function, sensory function, beam test, raise the Tail, and reflex activity. The maximum score for each animal was 18 (23).

Infarction volume assessment

After 24 hours of the reperfusion process, rats were sacrificed with a high dose of an anesthetic drug, their brains were isolated, and kept at 4˚C for 10 minutes. Then, brains were coronally sectioned at a thickness of 2 µm. After that, 2% triphenyl tetrazolium chloride solution was poured on the slides, and incubated at 37˚C for 15 minutes. The summed infarct volume from all brain sections was calculated as the total infarct volume. The contribution of the edema to the infarct volume was modified with the formula mentioned below. The evaluation of infarct volume in the cortex, striatum, and the Piriform cortex-amygdala regions was also accomplished separately (24). The corrected volume of damaged area=left hemisphere volume - (left hemisphere volume - damaged area volume).

Assessment of brain edema

After removing the brains from the skulls, the weights of various areas including the striatum, cortex, and cortex Piriform-amygdala as the wet weight were measured and after incubation at 120˚C for 24 hours, the dry weight (DW) was also measured. Finally, the content of brain water was estimated according to the following formula (24). [(WW-DW)/WW]×100

Measuring the permeability of the blood-brain barrier

After 30 minutes of the induction of ischemia, the injection of 2% Evans Blue solution (in the amount of 4 ml/kg) was carried out through the blood vein. Perfusion was performed using 250 ml saline, 24 hours after the withdrawal of suture. The different parts of the brain, including the striatum, cortex, and the Piriform cortex-amygdala were separated from each other, and each of them was weighed, separately. Then, it was homogenized with phosphate buffered solution, and after mixing with 60% acid trichloroacetic acid, it was agitated by a vortex for 3 minutes. Then, micro-tubes were kept at 4˚C for 30 minutes. In the next step, the samples were centrifuged at 1000 rpm for 30 minutes. Therefore, the light absorbance of brain solution was measured at the wavelength of 610 nm and compared with the standard concentration curve, and concentration of Evans Blue dry was calculated as µg/g of the brain tissue (24).

Statistical analysis

All of the statistical analyses were conducted by the SPSS software version 22 (SPSS Inc, Chicago, IL, USA). The data from NDS were quantified by the non-parametric test (Kruskal-Wallis), followed by the Dunn test. The volume of tissue damage (infarction) was determined by the ImageJ software (Version 1.50), and the obtained findings were analyzed by one-way ANOVA. The comparison of the BBB integrity and brain edema were calculated by one-way ANOVA, followed by the Bonferroni post hoc test. The results were expressed as mean ± SEM. The level of significance was set at $P<0.05$.

Results

Confirming the presence of Sertoli cells in testicle-derived cells

The immunocytochemistry analysis of SCs against anti-GATA4 antibody showed that the cultured cells expressed the GATA4 marker. GATA4 is expressed in SCs (green color). The nuclear staining conducted by Hoechst confirmed that the blue nuclei belonged to SCs (Fig.1A).

Survival of injected cells in the striatum after 7 days

Staining injected SCs with DiI (a fluorescent lipophilic cationic indocarbocyanine dye) confirmed the survival of injected cells in the striatum after 7 days (Fig.1B).

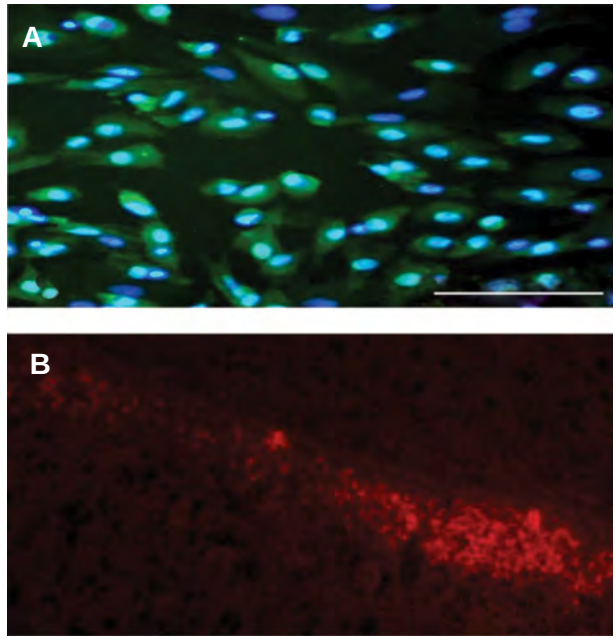

Fig.1: The identification and presence of Sertoli cells in testicle-derived cells. **A.** Sertoli cells expressed GATA4 marker that is shown in green. Staining the cultured cells with Hoechst showed that the Sertoli cells with blue nuclei (scale bar: 200 µm, ×20). The immunocytochemistry proves that the cultured cells are Sertoli cells. **B.** Staining the injected Sertoli cells with DiI. By using fluorescent microscopy, it was illustrated that the injected cells are alive after 7 days (scale bar: 200 µm, ×20).

The effect of Sertoli cell transplantation and injection of memantine on neurological deficits

The analysis of the total score of the behavioral assessment showed that in the allograft SC transplantation, memantine, and allograft SC transplantation+memantine a significant decrease groups was observed in neurological deficits compared with the control group. Moreover, the total score obtained from the neurological examinations in the sham group had a significant decrease compared with the MCAO surgery or control group (Fig.2). The partial tests were statistically analyzed separately in the experimental groups. The results revealed that SCs, memantine, and the simultaneous administration SCs with memantine exerted a reduction in neurological tests such as reflex activity, sensory functions, and motor functions (Table 1).

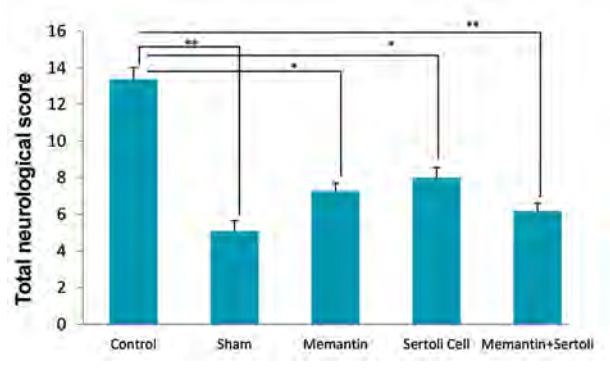

Fig.2: The effect of the Sertoli cell transplantation, memantine, and allograft transplantation of Sertoli cells plus memantine on total neurological deficit scores. Values are expressed as the mean ± SEM (n=10). $P<0.05$ compared with the control group (Nonparametric Kruskal-Wallis analysis). *; $P<0.05$ and **; $P<0.01$.

Table 1: The partial neurologic deficit scores in each experimental group (n=10)

		Neurological deficits scores							
Experimental groups	**Rats**	**Raise the tail**	**Motor function**	**Sensory function**	**Beam test**	**Reflex activity**	**Sum**	**Average**	**Survey result**
Control (MCAO)	1	2	4	2	2	1	11	13.2	Meaningful to the sham group (P<0.001)
	2	2	4	2	2	2	12		RT: 1-2 (P=0.002)
	3	1	5	2	3	2	13		MF: 1-2 (P=0.001)
	4	3	5	2	3	2	15		SF: 1-2 (P=0.002)
	5	3	4	2	2	3	14		BT: 1-2 (P=0.003)
	6	3	6	2	2	2	15		RA: 1-2 (P=0.001)
	7	2	5	2	2	2	13		
	8	2	4	2	3	3	14		
	9	2	5	2	2	2	13		
	10	2	5	2	2	1	12		
Sham	1	1	1	2	1	1	6	5	
	2	0	2	1	0	1	4		
	3	0	2	0	2	2	6		
	4	0	2	1	1	0	4		
	5	1	3	1	0	1	6		
	6	0	1	1	2	0	4		
	7	0	1	2	1	1	5		
	8	0	1	1	1	1	4		
	9	1	2	1	1	0	5		
	10	0	1	1	2	2	6		
Sertoli cells	1	0	3	2	1	1	7	8	Meaningful to the control group (P=0.04)
(SCs cells)	2	1	5	2	1	1	10		RT: 3-1 (P=0.01)
	3	1	3	1	1	1	7		MF: 3-1 (P=0.03)
	4	2	5	1	1	2	11		SF: 3-1 (P=0.03)
	5	0	4	2	2	2	10		BT: 3-1 (P=0.05)
	6	1	4	0	1	1	7		RA : 3-1 (P=0.03)
	7	1	2	1	1	1	6		
	8	1	5	1	1	1	9		
	9	1	3	2	0	2	8		
	10	0	2	1	1	1	5		

Table 1: Continued

Neurological deficits scores									
Experimental groups	**Rats**	**Raise the tail**	**Motor function**	**Sensory function**	**Beam test**	**Reflex activity**	**Sum**	**Average**	**Survey result**
Memantine	1	1	3	1	1	1	7	7.1	Meaningful to the control group (P=0.01)
	2	2	2	1	1	2	8		RT: 4-1 (P=0.03)
	3	1	3	2	0	1	7		MF: 4-1 (P=0.01)
	4	0	5	1	1	1	8		SF: 4-1 (P=0.03)
	5	1	4	1	0	1	7		BT: 4-1 (P=0.02)
	6	1	3	2	0	0	6		RA: 4-1 (P=0.001)
	7	1	3	1	1	1	7		
	8	1	4	1	1	1	8		
	9	0	3	1	2	1	7		
	10	1	2	2	0	1	6		
SCs+Memantine	1	2	2	1	2	2	9	6.1	Meaningful to the control group (P<0.001)
	2	2	1	1	2	2	8		RT: 5-1 (P=0.01)
	3	2	3	0	0	1	6		MF: 5-1 (P=0.001)
	4	1	2	1	1	2	7		SF: 5-1 (P=0.003)
	5	1	1	1	1	0	4		BT: 5-1 (P=0.04)
	6	0	3	1	0	1	5		RA: 5-1 (P=0.02)
	7	0	2	1	1	2	6		
	8	1	2	1	1	2	7		
	9	1	1	1	1	1	5		
	10	1	1	0	1	1	4		

MCAO; Middle Cerebral Artery Occlusion, SCs; Sertoli cells, RT; Raise the tail, MF; Motor function, SF; Sensory function, BT; Beam test, RA; Reflex action, 1: Control group, 2; Sham group, 3, Sertoli cell group, 4; Memantine group, and 5; The Sertoli cell transplantation+memantine (Nonparametric Kruskal-Wallis analysis).

The effect of Sertoli cell transplantation and injection of memantine on infarct volume

The effect of SCs and memantine on infarction volume was evaluated 24 hours after reperfusion. The results showed that pretreatment of allograft SCs, memantine, and allograft transplantation of SCs plus memantine caused a reduction in infarct volume in the total, the striatum, the cortex, and the Pir-Amy regions compared with the control group (Fig.3). Analysis of the total infarct volume in the experimental groups revealed that the memantine (95.48 ± 7.70 mm^3, P=0.001), allograft SC transplantation (142.69 ± 5.74 mm^3, P=0.03), SC transplantation plus memantine (59.24 ± 9.59 mm^3, P=0.001) groups indicated a significant reduction in comparison with the control group (213.86 ± 13.42 mm^3). The administration of memantine (51.11 ± 6.31 mm^3, P=0.003), allograft SCs (86.38 ± 9.80 mm^3, P=0.03), and SC transplantation plus memantine (25.09 ± 7.40 mm^3, P=0.001) caused a decrease in the cortex infarct volume in comparison with the control group (116.98 ± 9.26 mm^3). The Pir-Amy infarct volume in the memantine (17.32 ± 2.69 mm^3, P=0.01), the allograft SC transplantation (21.05 ± 3.32 mm^3, P=0.04), and SC transplantation plus memantine (12.21 ± 2.03 mm^3, P=0.001) groups was diminished compared with the control group (37.34 ± 3.63 mm^3). Furthermore, the infarct volume of the striatum in the memantine (26.07

± 3.52 mm^3, P=0.02), the allograft SC transplantation (33.64 ± 3.80 mm^3, P=0.04), and SC transplantation plus memantine (17.75 ± 4.04 mm^3, P=0.006) groups showed a remarkable decrease in comparison with the control group (61.37 ± 6.95 mm^3).

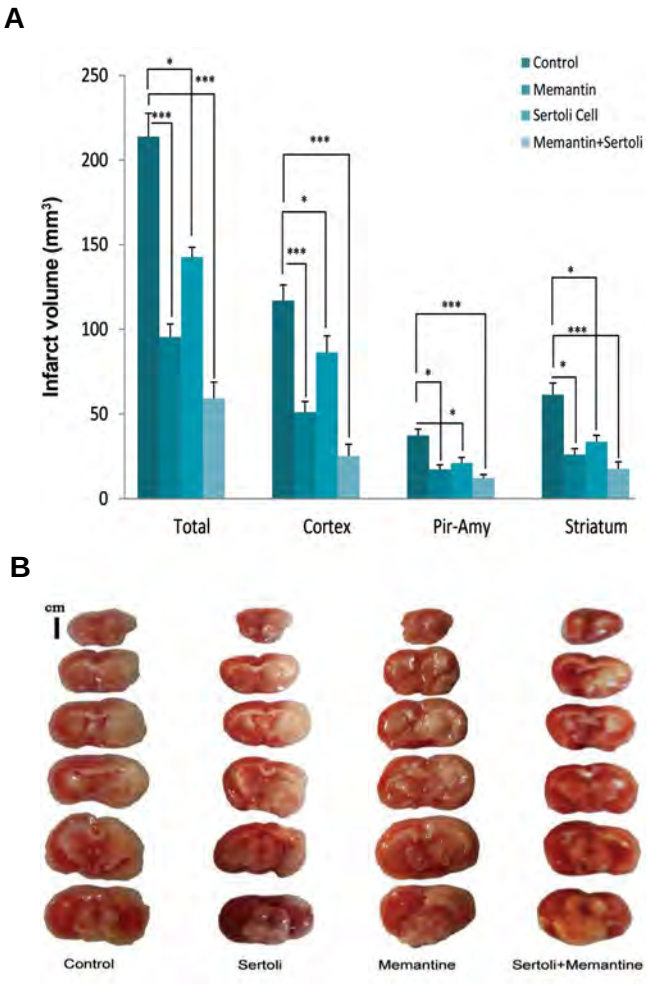

Fig.3: The effect of the Sertoli cell transplantation on infarction volume. **A.** The graph shows the effect of Sertoli cell transplantation, memantine, and allograft transplantation of Sertoli cells plus memantine on infarction volume in the total, cortex, striatum, and Piriform cortex-amygdala (Pir-Amy). Each column illustrates the mean ± SEM of the infarct volume (n=7). P<0.05 compared with the control group (One-way ANOVA test). *; P<0.05 and ***; P<0.001. **B.** The Sertoli cell transplantation and injection of memantine reduced infarct volume in comparison with the control. Each column displays coronal sections of the control, Sertoli cell transplantation, memantine, and the Sertoli cells+memantine groups. Strained or red parts, as well as unstained or white parts of the brain tissue, are considered as normal and damaged areas, respectively.

The effect of Sertoli cell transplantation and injection of memantine in brain water content

The results of brain edema also revealed the reduction of brain edema in the right striatum, cortex, and Pir-Amy regions of the brain compared with the control group (Fig.4). The beneficial effect of SC transplantation and the injection of memantine on brain edema in the cortex of the memantine- (77.99 ± 0.75%, P=0.005), allograft SC transplantation (78.14 ± 0.52%, P=0.03), and SC transplantation plus memantine (76.64 ± 0.65%, P=0.003) groups was demonstrated in comparison with the control group (82.45 ± % 0.79). Brain edema in the Pir-Amy of the memantine (76.58 ± 0.66%, P=0.01), allograft SC transplantation (77.10 ± 0.9%, P=0.01), and SC transplantation plus memantine (76.33 ± 0.53%, P=0.004) groups were minimized compared with the control group (80 ± 0.93%). The memantine (79.92 ± 0.67%, P=0.004), allograft SC transplantation (80.31 ± 1.02%, P=0.04), and SC transplantation plus memantine (77.96 ± 0.75%, P=0.001) groups showed the protective role of our therapeutic strategy (memantine and SC) on the brain water in comparison with the control group (84.18 ± 1.02%). Moreover, the brain edema was enhanced in the control group compared with the sham group in three areas of the brain, as expected (data not shown).

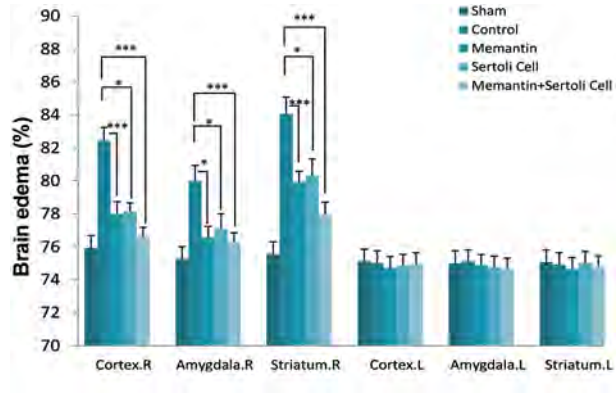

Fig.4: Brain edema in experimental groups, including ischemic hemisphere (Total. R), non-ischemic hemisphere (Total. L), striatum (right and left), cortex (right and left), and Piriform cortex-amygdala (Pir-Amy) (right and left) areas of the control, sham, Sertoli cells transplant, memantine, and allograft Sertoli cell transplantation plus memantine groups. Values are expressed as the mean ± SEM (n=7). P<0.05 (One-way ANOVA test). *; P<0.05 and ***; P<0.001.

The effect of Sertoli cell transplantation and injection of memantine on blood-brain barrier permeability

These results showed a reduction in the BBB breakdown in the right striatum, cortex, and Pir-Amy areas in comparison with the control group (Fig.5). The BBB breakdown in the right cortex of the memantine (3.11 ± 0.06, P=0.02), allograft SC transplantation (3.42 ± 0.21, P=0.03), and SC transplantation plus memantine (3.01 ± 0.09, P=0.01) groups was decreased in comparison with the control group (4.31 ± 0.12). The reduction of BBB permeability in the Pir-Amy of memantine (2.76 ± 0.16, P=0.002), the allograft SC transplantation (2.81 ± 0.18, P=0.04), and transplantation of SCs plus memantine (2.54 ± 0.10, P=0.003) was observed compared with the control group (3.33 ± 0.28). Analysis of Evans blue concentration in the striatum of the memantine (3.44 ± 0.12, P=0.001), allograft SC transplantation (4.21 ± 0.08, P=0.02), and SC transplantation plus memantine (3.04 ± 0.20, P=0.001) groups illustrated the reduction of BBB permeability in comparison with the control group (5.01 ± 0.11). Furthermore, the increase in the BBB permeability was observed in the control group compared with the

sham group in three areas of the brain, as expected (data not shown).

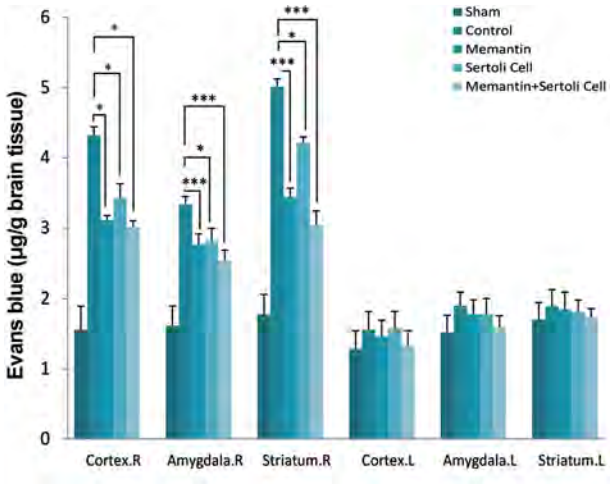

Fig.5: The Evans Blue extravasations in ischemic hemisphere (Total. R), non-ischemic hemisphere (Total. L), cortex (right and left), striatum (right and left), Piriform cortex-amygdala (Pir-Amy) (right and left) areas of the control, shame, Sertoli cell transplantation, memantine, and allograft Sertoli cell transplantation plus memantine groups. Values are expressed as the mean ± SEM (n=7). P<0.05 compared with the control group (One-way ANOVA test). *; P<0.05 and ***; P<0.001.

Discussion

As a pioneer, we focused on investigating the effect of the combination of SC and memantine on ischemic damages. The result of the study demonstrated that allograft transplantation of SC, the injection of memantine, and simultaneous administration of SCs plus memantine reduced ischemic damages in ischemic rats. Ischemic injuries occur in forms of neurological deficits, infarction, cerebral edema, and increased permeability of the blood-brain barrier. Transplanted SCs, along with memantine injection, significantly ameliorated these injuries in the striatum (transplantation area), cortex, and Piriform cortex-amygdala.

Evaluating sensory and motor behaviors in stroke-related research are conventional methods to identify the severity of the injury or the recovery process after treatment. The present result shows that memantine could decrease neurological deficits. According to the previous studies, the significant effect of memantine on the improvement of the neurological deficits in experimental and clinical observations was reported (11, 25, 26). With reference to the reported findings, transplantation of SCs reduced the severity of neurological function (18). For the first time, the notable reduction was also observed in the neurological deficits scores in the SCs+memantine recipient group. Probably, improvement of the neurological function is associated with attenuation of damages in related brain areas.

The other considerable result of this work is the decrease of infarction volume in both memantine-treated and SC-transplanted groups compared with the control group. Based on the preliminary reports, the positive effect of memantine on infarction volume was confirmed (11, 25, 27). In the past investigation, the SC transplantation could result in a significant reduction in infarction (18). Subsequently, the simultaneous use of transplanted SCs and memantine exerted more neuroprotective effect than the other two groups. In line with this finding, there is no report. A direct relationship was proved between infarction and cellular death (28). One of the pathophysiological processes in neurodegenerative diseases, such as cerebral ischemia, is excitotoxicity that causes severe and destructive damages.

Excitotoxicity is also defined by increased NMDA activity, glutamate level, and intracellular calcium. The extracellular glutamate levels have a direct effect on cellular death. Memantine, as a NMDA receptor antagonist, exclusively protects neurons against glutamate-induced neurotoxicity and reduces calcium intake. Consequently, it is expectable that memantine prevents excitotoxicity-related cellular loss (8). With regard to the mentioned properties of memantine, the previous report showed that the reduction of glutamate levels in the cortex, hippocampus, and striatum could be exerted following the pre-ischemic use of memantine (29). Cell therapy has attracted much attention since it could be used for the compensation of damages caused by cerebral ischemia. Transplanted SCs induce their efficacy via the improvement in ischemic damages, through various mechanisms. SCs can also be able to secrete factors that protect the brain against the injuries induced by ischemia, including GDNF and VEGF (15). It should also be stated that the increased expression of GNDF and VEGF attenuated the infarction in cerebral ischemia (30, 31).

On the other hand, the elevation of GDNF and VEGF was demonstrated by the injection of memantine in the striatum and cortex. Moreover, memantine stimulated capillary formation around the infarct area (11). Eventually, the neuroprotective effect of the combination of SCs and memantine probably was enhanced through the secretion of GDNF and VEGF.

It is worth noting that memantine and transplanted SCs could induce a remarkable effect on reducing BBB breakdown and brain edema. Similarly, other investigations confirmed the protective effect of memantine on these ischemic injuries (27, 32). Only Milanizadeh and colleagues studied the protective effect of SCs on the brain water content and permeability of the BBB in cerebral ischemia (18). On the other hand, memantine, by blocking the NMDA receptor, reduces the expression of matrix metalloproteinases (MMPs), triggering the breakdown of the BBB (33). During ischemia, the NOS enzyme increases the production of oxygen free radicals (such as ROS), impairs the cellular energy system, and finally induces DNA damage (34). Considering the antioxidant properties of memantine, as inhibitory agent against NOS activity, it can be useful in maintaining BBB integrity, as well as reducing the cerebral edema (35). The distinguished neuroprotective mechanisms of memantine are the attenuation of inflammation through decreasing activated microglia and inhibition of

MAPK p38 (and NF-kB) activity (32, 36). Referring to the detrimental role of inflammation in BBB breakdown and induction of edema, memantine can prevent these damages following stroke. Oxidative stress is a pathophysiological process that happens by an imbalance in the amount of free radicals and antioxidants. So, when oxidative stress is inhibited, free radicals are reduced, and eventually, cell death is oppressed. In this respect, it was reported that oxidative stress increases the secretion of inflammatory factors, such as IL-6, IL-5, and TNF-α, triggering the breakdown of the BBB integrity and edema (37). SCs can protect the BBB through the secretion of antioxidant enzymes, including superoxide dismutase (SOD), glutathione transferase (GT), and glutathione reductase (GR). Hence, the ability of these cells in the inhibition of vasogenic edema by preventing permeability of BBB is expected (38). Furthermore, SCs can cause detrimental effects on inflammatory factors, including TNF-a, that could result in a decrease in permeability of the BBB and brain water content (39). Accordingly, the protective effect of the administration of SC plus memantine on the BBB permeability and edema is probably associated with the exclusive capabilities in the suppression of free radicals and inflammatory factors.

Referring to the previous study, the combination of the drug and cell therapy in cerebral ischemia treatment (40) can open up a new horizon for clinical research.

Conclusion

According to the observed results in this study, the administration of memantine or SCs caused a reduction in ischemic injuries. Furthermore, the neuroprotective findings were apparent in the transplanted SCs plus memantine group. The neuroprotective effects of SCs and memantine are probably mediated by the blockage of NMDA receptor, decreasing intracellular calcium, the release of antioxidant enzymes, secretion of growth and neurotrophic factors, reducing inflammatory factors, and inhibiting apoptosis.

Acknowledgements

This research is a part of the thesis belonging to Zeinab SafialHosseini, supervised by three professors. There is no financial support and conflicts of interest in this study.

Authors' Contributions

M.B.; Is the supervisor, the project designer, administrative coordinator, and the financial support of this project. Z.S.; Contributed to data acquisition or data analysis and interpretation. S.Kh.; Contributed to the performance of the project, analysis, and writing manuscript. A.A.; Is the advisor of the cell transplantation, performer and analyzer of the related data. All authors read and approved the final manuscript.

References

1. Jastrzebski K, Kacperska MJ, Majos A, Grodzka M, Glabinski A. Hemorrhagic stroke, cerebral amyloid angiopathy, Down syndrome and the Boston criteria. Neurol Neurochir Pol. 2015; 49(3): 193-196.
2. Nikkhah K, Avan A, Shoeibi A, Azarpazhooh A, Ghandehari K, Foerch C, et al. Gaps and hurdles deter against following stroke guidelines for thrombolytic therapy in Iran: exploring the problem. J Stroke Cerebrovasc Dis. 2015; 24(2): 408-415.
3. Masri A, Al-Ammouri I. Clinical presentation, etiology, and outcome of stroke in children: a hospital-based study. Brain Dev. 2016; 38(2): 204-208.
4. Bano D, Nicotera P. Ca2+ signals and neuronal death in brain ischemia. Stroke. 2007; 38(2 Suppl): 674-676.
5. George PM, Steinberg GK. Novel Stroke Therapeutics: Unraveling Stroke Pathophysiology and Its Impact on Clinical Treatments. Neuron. 2015; 87(2): 297-309.
6. Baxter PS, Bell KF, Hasel P, Kaindl AM, Fricker M, Thomson D, et al. Synaptic NMDA receptor activity is coupled to the transcriptional control of the glutathione system. Nat Commun. 2015; 6: 6761.
7. Hanson JE, Pare JF, Deng L, Smith Y, Zhou Q. Altered GluN2B NMDA receptor function and synaptic plasticity during early pathology in the PS2APP mouse model of Alzheimer's disease. Neurobiol Dis. 2015; 74: 254-262.
8. Amidfar M, Réus GZ, Quevedo J, Kim YK, Arbabi M. Effect of co-administration of memantine and sertraline on the antidepressant-like activity and brain-derived neurotrophic factor (BDNF) levels in the rat brain. Brain Res Bull. 2017; 128: 29-33.
9. Zhu G, Li J, He L, Wang X, Hong X. MPTP-induced changes in hippocampal synaptic plasticity and memory are prevented by memantine through the BDNF-TrkB pathway. Br J Pharmacol. 2015; 172(9): 2354-2368.
10. Kelestemur T, Yulug B, Caglayan AB, Beker MC, Kilic U, Caglayan B, et al. Targeting different pathophysiological events after traumatic brain injury in mice: Role of melatonin and memantine. Neurosci Lett. 2016; 612: 92-97.
11. Wang YC, Sanchez-Mendoza EH, Doeppner TR, Hermann DM. Post-acute delivery of memantine promotes post-ischemic neurological recovery, peri-infarct tissue remodeling, and contralesional brain plasticity. J Cereb Blood Flow Metab. 2017; 37(3): 980-993.
12. Ruscher K, Freyer D, Karsch M, Isaev N, Megow D, Sawitzki B, et al. Erythropoietin is a paracrine mediator of ischemic tolerance in the brain: evidence from an in vitro model. J Neurosci. 2002; 22(23): 10291-1301.
13. Hemendinger R, Wang J, Malik S, Persinski R, Copeland J, Emerich D, et al. Sertoli cells improve survival of motor neurons in SOD1 transgenic mice, a model of amyotrophic lateral sclerosis. Exp Neurol. 2005; 196(2): 235-243.
14. Zhao S, Zhu W, Xue S, Han D. Testicular defense systems: immune privilege and innate immunity. Cell Mol Immunol. 2014; 11(5): 428-437.
15. Chiappalupi S, Luca G, Mancuso F, Madaro L, Fallarino F, Nicoletti C, et al. Intraperitoneal injection of microencapsulated Sertoli cells restores muscle morphology and performance in dystrophic mice. Biomaterials. 2016; 75: 313-326.
16. Willing AE, Cameron DF, Sanberg PR. Sertoli cell transplants: their use in the treatment of neurodegenerative disease. Mol Med Today. 1998; 4(11): 471-477.
17. Yue F, Cui L, Johkura K, Ogiwara N, Sasaki K. Induction of midbrain dopaminergic neurons from primate embryonic stem cells by coculture with sertoli cells. Stem Cells. 2006; 24(7): 1695-1706.
18. Milanizadeh S, Zuwarali KNN, Aliaghaei A, Bigdeli MR. Therapeutic potential of pretreatment with allograft sertoli cells transplantation in brain ischemia by improving oxidative defenses. J Mol Neurosci. 2018; 64(4): 533-542.
19. Wesemann W, Schollmeyer JD, Sturm G. Distribution of memantine in brain, liver, and blood of the rat. Arzneimittelforschung. 1982; 32(10): 1243-1245.
20. Chen HS, Pellegrini JW, Aggarwal SK, Lei SZ, Warach S, Jensen FE, et al. Open-channel block of N-methyl-D-aspartate (NMDA) responses by memantine: therapeutic advantage against NMDA receptor-mediated neurotoxicity. J Neurosci. 1992; 12(11): 4427-4436.
21. Paxinos G, Watson CR, Emson PC. AChE-stained horizontal sections of the rat brain in stereotaxic coordinates. J Neurosci Methods. 1980; 3(2): 129-149.
22. Longa EZ, Weinstein PR, Carlson S, Cummins R. Reversible middle cerebral artery occlusion without craniectomy in rats. Stroke. 1989; 20(1): 84-91.
23. Long J, Cai L, Li J, Zhang L, Yang H, Wang T. JNK3 involvement in

nerve cell apoptosis and neurofunctional recovery after traumatic brain injury. Neural Regen Res. 2013; 8(16): 1491-1499.
24. Khaksar S, Bigdeli MR. Anti-excitotoxic effects of cannabidiol are partly mediated by enhancement of NCX2 and NCX3 expression in animal model of cerebral ischemia. Eur J Pharmacol. 2017; 794: 270-279.
25. Görgülü A, Kinş T, Cobanoglu S, Unal F, Izgi NI, Yanik B, et al. Reduction of edema and infarction by Memantine and MK-801 after focal cerebral ischaemia and reperfusion in rat. Acta Neurochir (Wien). 2000; 142(11): 1287-1292.
26. Kafi H, Salamzadeh J, Beladimoghadam N, Sistanizad M, Kouchek M. Study of the neuroprotective effects of memantine in patients with mild to moderate ischemic stroke. Iran J Pharm Res. 2014; 13(2): 591-598.
27. Aluclu MU, Arslan S, Acar A, Guzel A, Bahceci S, Yaldiz M. Evaluation of effects of memantine on cerebral ischemia in rats. Neurosciences (Riyadh). 2008; 13(2): 113-116.
28. Fernández-López D, Martínez-Orgado J, Casanova I, Bonet B, Leza JC, Lorenzo P, et al. Immature rat brain slices exposed to oxygen-glucose deprivation as an in vitro model of neonatal hypoxic-ischemic encephalopathy. J Neurosci Methods. 2005; 145(1-2): 205-212.
29. Pandya RS, Mao L, Zhou H, Zhou S, Zeng J, Popp AJ, et al. Central nervous system agents for ischemic stroke: neuroprotection mechanisms. Cent Nerv Syst Agents Med Chem. 2011; 11(2): 81-97.
30. Wang Y, Lin SZ, Chiou AL, Williams LR, Hoffer BJ. Glial cell line-derived neurotrophic factor protects against ischemia-induced injury in the cerebral cortex. J Neurosci. 1997; 17(11): 4341-4348.
31. Wang Y, Kilic E, Kilic U, Weber B, Bassetti CL, Marti HH, et al. VEGF overexpression induces post-ischaemic neuroprotection, but facilitates haemodynamic steal phenomena. Brain. 2005; 128(Pt 1): 52-63.
32. Dogan A, Eras MA, Rao VL, Dempsey RJ. Protective effects of memantine against ischemia-reperfusion injury in spontaneously hypertensive rats. Acta Neurochir (Wien). 1999; 141(10): 1107-1113.
33. Chen HS, Wang YF, Rayudu PV, Edgecomb P, Neill JC, Segal MM, et al. Neuroprotective concentrations of the N-methyl-D-aspartate open-channel blocker memantine are effective without cytoplasmic vacuolation following post-ischemic administration and do not block maze learning or long-term potentiation. Neuroscience. 1998; 86(4): 1121-1132.
34. Hossmann KA. Pathophysiology and therapy of experimental stroke. Cell Mol Neurobiol. 2006; 26(7-8): 1057-1083
35. Lipton SA. Possible role for memantine in protecting retinal ganglion cells from glaucomatous damage. Surv Ophthalmol. 2003; 48 Suppl 1: S38-S46.
36. Rosi S, Vazdarjanova A, Ramirez-Amaya V, Worley PF, Barnes CA, Wenk GL. Memantine protects against LPS-induced neuroinflammation, restores behaviorally-induced gene expression and spatial learning in the rat. Neuroscience. 2006; 142(4): 1303-1315.
37. Bhat AH, Dar KB, Anees S, Zargar MA, Masood A, Sofi MA, et al. Oxidative stress, mitochondrial dysfunction and neurodegenerative diseases; a mechanistic insight. Biomed Pharmacother. 2015; 74: 101-110.
38. Mruk DD, Silvestrini B, Mo MY, Cheng CY. Antioxidant superoxide dismutase - a review: its function, regulation in the testis, and role in male fertility. Contraception. 2002; 65(4): 305-311.
39. Luca G, Bellezza I, Arato I, Di Pardo A, Mancuso F, Calvitti M, et al. Terapeutic potential of microencapsulated sertoli cells in huntington disease. CNS Neurosci Ther. 2016; 22(8): 686-690.
40. Kaengkan P, Kam KY, Do BR, Kang SG. Combination effect of memantine and mesenchymal stem cells on the recovery of brain damage in a rat model of brain ischemia. Animal Cells and Systems. 2015; 19(2): 110-118.

Original Article

Extraction and Evaluation of Outer Membrane Vesicles from Two Important Gut Microbiota Members, *Bacteroides fragilis* and *Bacteroides thetaiotaomicron*

Sara Ahmadi Badi, Ph.D.[1], Arfa Moshiri, Ph.D.[2, 3], Fatemeh Ettehad Marvasti, M.Sc.[1, 4], Mojtaba Mojtahedzadeh, Ph.D.[5], Vida Kazemi, Ph.D.[6]*, Seyed Davar Siadat, Ph.D.[4, 7]*

1. Department of Biology, Science and Research Branch, Islamic Azad University, Tehran, Iran
2. Cancer Department, Gastroenterology and Liver Diseases Research Center, Research Institute for Gastroenterology and Liver Diseases, Shahid Beheshti University of Medical Sciences, Tehran, Iran
3. Laboratory of Experimental Therapy in Oncology, G. Gaslini Children's Hospital, Genoa, Italy
4. Microbiology Research Centre, Pasteur Institute of Iran, Tehran, Iran
5. Department of Pharmacotherapy, Faculty of Pharmacy, Tehran University of Medical Sciences, Tehran, Iran
6. Medicinal Plants Research Centre, Faculty of Pharmacy, Tehran University of Medical Sciences, Tehran, Iran
7. Mycobacteriology and Pulmonary Research Department, Pasteur Institute of Iran, Tehran, Iran

Corresponding Addresses: P.O.Box: 14155-6451, Medicinal Plants Research Centre, Faculty of Pharmacy, Tehran University of Medical Sciences, Tehran, Iran
P.O.Box: 113169-43551, Mycobacteriology and Pulmonary Research Department, Pasteur Institute of Iran, Tehran, Iran
Emails: dv.kazemi@gmail.com, d.siadat@gmail.com

Received: 27/November/2018, Accepted: 28/April/2019

Abstract

Objective: The gastrointestinal tract (GI) is colonized by a complex microbial community of gut microbiota. Bacteroides spp. have significant roles in gut microbiota and they host interactions by various mechanisms, including outer membrane vesicle (OMVs) production. In the present study, we extracted and assessed *Bacteroides fragilis (B. fragilis)* and *Bacteroides thetaiotaomicron (B. thetaiotaomicron)* OMVs in order to evaluate their possible utility for *in vivo* studies.

Materials and Methods: In this experimental study, OMVs extraction was performed using multiple centrifugations and tris-ethylenediaminetetraacetic acid (EDTA)-sodium deoxycholate buffers. Morphology, diameter, protein content, profile, and lipopolysaccharide (LPS) concentrations of the OMVs were assessed by scanning electron microscopy (SEM), nanodrop, Bradford assay, sodium dodecyl sulphate-polyacrylamide gel electrophoresis (SDS-PAGE), and the Limulus Amoebocyte Lysate (LAL) test, respectively. Zeta potential (ζ-P) was also assessed. The viability effect of OMVs was assessed by the 3-(4,5-dimethylthiazol-2-yl)-2, 5-diphenyltetrazolium bromide (MTT) assay in Caco-2 cells.

Results: Spherical OMVs with diameters of 30-110 nm were produced. The OMVs had different protein profiles. The LPS concentrations of the *B. fragilis* and *B. thetaiotaomicron* OMVs were 1.80 and 1.68 EU/mL, respectively. ζ-P of the *B. fragilis* OMVs was -34.2 mV and, for *B. thetaiotaomicron*. it was -44.7 mV. The viability of Caco-2 cells treated with OMVs was more than 95%.

Conclusion: The endotoxin concentrations of the spherical OMVs from *B. fragilis* and *B. thetaiotaomicron* were within the safe limits. Both OMVs had suitable stability in sucrose solution and did not have any cytotoxic effects on human intestinal cells. Based on our results and previous studies, further molecular evaluations can be undertaken to design OMVs as possible agents that promote health properties.

Keywords: *Bacteroides fragilis, Bacteroides thetaiotaomicron*, Gut Microbiota

Cell Journal(Yakhteh), Vol 22, No 3, October-December (Autumn) 2020, Pages: 344-349

Citation: **Ahmadi Badi S, Moshiri A, Ettehad Marvasti F, Mojtahedzadeh M, Kazemi V, Siadat SD. Extraction and evaluation of outer membrane vesicles from two important gut microbiota members, bacteroides fragilis and bacteroides thetaiotaomicron. Cell J. 2020; 22(3): 344-349. doi: 10.22074/cellj.2020.6499.**

Introduction

Gut microbiota are a diverse and complicated microbial community that colonize the gastrointestinal tract (GI) (1). The gut microbiota have beneficial roles in the host that include colonization resistance, assist with digestion, harvest energy from the diet, metabolism of nutrients, and immune system regulation (2, 3). This microbial community consists of bacteria, archea, viruses, fungi, and protozoa (4). Bacteria are the dominant microbial population. Bacteroidetes and Firmicutes constitute two major bacterial phyla in gut microbiota (5). Bacteroidetes are gram-negative bacteria are abundant and diverse in gut microbiota (6). These bacteria are found at high frequencies (up to 10^{11} cells/g) in intestinal material (7). Bacteroidetes are important in host metabolism since they degrade proteins and complex carbohydrates (8). Moreover, the *Bacteroides spp.* affect function of the immune system, specifically, the tolerance for intestinal commensal bacteria (9). *Bacteroides fragilis (B. fragilis)* and

Bacteroides thetaiotaomicron (B. thetaietomicron) affect gut microbiota-host interactions as they contain broad metabolic and immune regulating potentials (10). Various strategies are employed by *Bacteroides spp.* in their interaction with the host, including production of metabolites (such as short chain fatty acids) and outer membrane vesicles (OMVs) (11, 12).

OMVs are nano-sized vesicles (20 to 250 nm) secreted by gram-negative bacteria under various conditions during all growth phases (13). The bacterial OMVs were first reported in the 1970s when *Escherichia coli (E. coli)* OMVs were identified in *E. coli* cultures grown under lysine-limiting conditions (14-17). Thereafter, it has been found that bacterial vesiculation occurs in planktonic cultures, biofilms, and *in vivo* (14). These spherical particles originate from the bacterial outer membrane and contain a wide range of compounds, such as lipopolysaccharide (LPS), outer membrane proteins (OMPs), phospholipids, periplasmic components, DNA, RNA, hydrolytic enzymes, and signaling molecules (18, 19). OMVs play a role in bacterial interactions with the environment. These particles are considered interesting bacterial components due to their participation in numerous processes, including pathogenesis, bacterial survival under stress, and regulation of prokaryote-prokaryote and prokaryote-eukaryote communications (11, 18-20).

In the normal state, the gut microbiota-host interactions are balanced due to desirable functions of the gut barrier. Many factors such as intestinal epithelial cell integrity, tight junction proteins, and the mucus layer maintain proper gut barrier functions that control gut microbiota-host interactions (8, 21). In recent studies, it was demonstrated that beneficial intestinal commensal bacteria might have adverse effects on the host, while their OMVs maintain beneficial effects on the host functions in leaky gut syndrome, which is characterized by disruption of gut barrier integrity and increased intestinal epithelial cell permeability (21, 22).

The roles of OMVs in gut microbiota homeostasis and host functions are under investigation. In this regard, the study of OMVs production from key gut microbiota members and their properties could contribute to an understanding of the gut microbiota-host interactions. Accordingly, in the present study, the OMVs from two important gut microbiota members, *B. fragilis* and *B. thetaiotaomicron,* were extracted and their physicochemical properties (size, morphology, protein concentration/bands, LPS concentration, and surface charge) were evaluated. Finally, the OMVs effect on the viability of the Caco-2 cell line, as a human gastrointestinal epithelial cell model, was assessed.

Materials and Methods

Bacterial strains and growth conditions

In this experimental study, *B. fragilis* ATCC 23745 and *B. thetaiotaomicron* CCUG 10774 were grown either on blood agar plates that contained 5% defibrinated horse blood or brain heart infusion (BHI) broth supplemented with hemin (5 µg/ml) and menadione (1 µg/ml), and incubated at 37˚C under anaerobic conditions (80% N_2, 10% Co_2, and 10% H_2) using an Anoxomat™ MARK II system (10).

Outer membrane vesicle purification

After an overnight incubation under anaerobic conditions, OMVs were isolated as described previously (23). Briefly, 500 mL of the bacterial cultures were centrifuged at 6000 g at 4˚C. The cell pellets were washed twice in phosphate-buffered solution (PBS). Then, the cell pellets were resuspended in a 9% sodium chloride solution. The cell suspensions were homogenized and concentrated by centrifugation at 2900 g for 1 hour at 4˚C. The total wet weight of cell pellets was calculated and resuspended in 7.5 times the wet weight of 0.1 M tris-10 mM ethylenediaminetetraacetic acid (EDTA) buffer (Sigma-Aldrich, USA). The vesicles were extracted by the addition of $1/20^{th}$ the volume of 0.1 M Tris, 10 mM EDTA, and sodium deoxycholate (100 g/L) buffer (Merck, Germany). OMVs were separated from cell debris at 20 000 g for 60 minutes at 4˚C. The supernatant that contained the vesicles was centrifuged at 20 000 g for 120 minutes at 4˚C in order to concentrate the vesicles. The pellet was re-suspended in 10 mM EDTA, 0.1 M Tris, and sodium deoxycholate (5 g/L) buffer, and the suspension was centrifuged again at 20000 g for 120 minutes at 4˚C. The concentrated OMVs were resuspended in a 3% sucrose solution. Finally, the suspension was filtered through a 0.22-µm polyvinylidene difluoride filter (Millipore, Billerica, MA, USA).

Scanning electron microscopy

The OMVs were fixed with 2.5% glutaraldehyde and 2% paraformaldehyde in PBS (Sigma-Aldrich, USA). After washing with PBS, dried samples were coated with gold by a sputter coater (SBC-12, KYKY, China) using a physical vapor deposition method. The prepared samples were examined by SEM (KYKY-EM3200, KYKY, China) (24).

Determination of the outer membrane vesicle protein content and pattern

To estimate the amount of total proteins, purified OMVs were analyzed using a NanoDrop spectrophotometer (Thermo Scientific, Wilmington,

DE, USA) and the Bradford assay with coomassie brilliant blue, at 590 nm. The protein contents of *B. fragilis* and *B. thetaiotaomicron* OMVs were separated by SDS-PAGE on 12% gels that were stained with coomassie brilliant blue (24).

Quantification of outer membrane vesicle endotoxins

The content and biological activity of the OMVs endotoxins was measured using the Pierce™ LAL Chromogenic Endotoxin Quantitation Kit (Thermo Scientific, USA) according to the manufacturer's instructions. Briefly, the microplate was incubated for 10 minutes at 37˚C. We dispensed 50 µL each of the samples and standards into the microplate wells and allowed them to incubate for 5 minutes at 37˚C. Then, 50 µL of LAL was added to each well. The plate was incubated at 37˚C for 10 minutes. We added 100 µL of substrate solution to the microplate and incubated it for 6 minutes at 37˚C. Finally, 50 µL of stop reagent (25% acetic acid) was added to each well and we measured the optical density (OD) the wells at 405-410 nm on a plate reader. The amount of endotoxin in the samples was calculated using the standard curve (25).

Zeta (ζ-P) potential measurement

The OMVs were prepared by sonication in 35 kHz for 3 minutes (Bandelin ultrasonic bath). The zeta (ζ-P) potential of the OMVs was assessed using a Malvern Zetasizer Nano ZEN3600 (Malvern Instruments, United Kingdom).

3-(4,5-dimethylthiazol-2-yl)-2, 5-diphenyltetrazolium bromide assay

The human epithelial cell line, IBRC C10094 Caco-2 (Iranian Biological Resource Centre) was cultured in Dulbecco's modified eagle medium (DMEM/high glucose, Gibco, USA), supplemented with 10% fetal bovine serum (FBS, Gibco USA), 1% non-essential amino acids (Gibco, USA), and 1% penicillin/streptomycin (Gibco USA) and incubated at 37˚C in a 5% CO_2 atmosphere. Caco-2 cells were seeded at a density of 2×10^4 cells/well in a 96-well culture plate and incubated overnight before the OMVs treatment. The cells were treated with OMVs (50 µg/ml) and incubated for 24 hours. The cell culture medium was discarded and replaced by fresh medium. After 4 hours of incubation, the cells were incubated with 100 µl medium with MTT for 4 hours. After incubation, the medium was removed and 100 µl dimethyl sulfoxide (DMSO) was added to each well to dissolve the formazan crystals that formed in the living cells. The absorbance was measured at 570 nm (26).

Results

B. fragilis and *B. thetaiotaomicron* produced spherical OMVs with diameters of 30-110 nm, as determined by SEM (Fig.1).

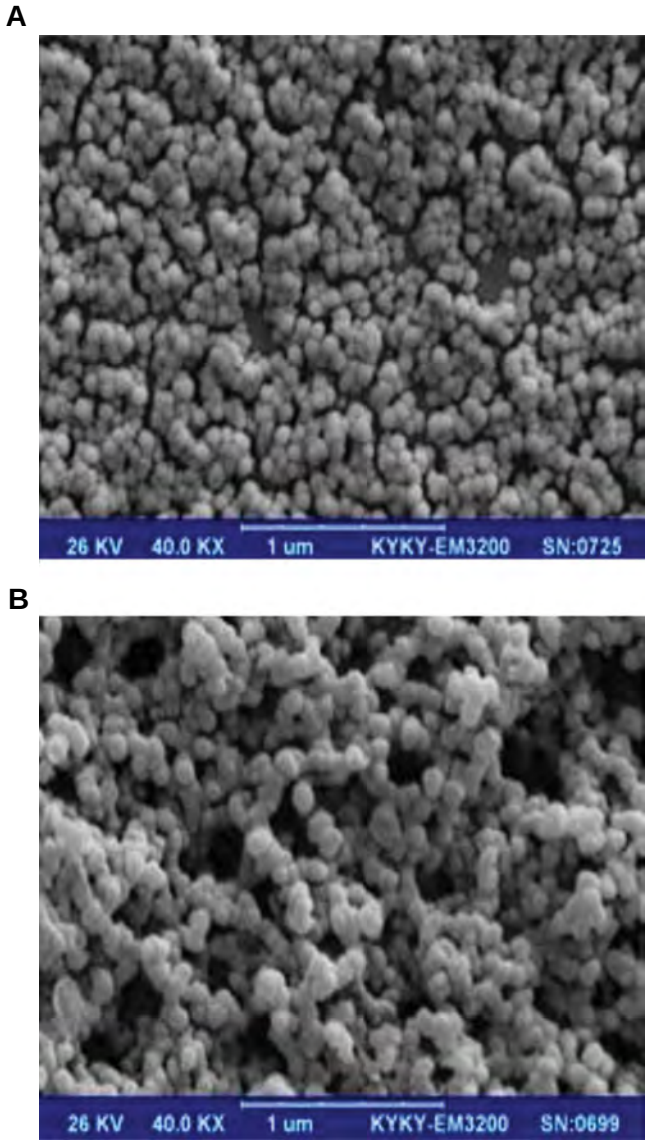

Fig.1: Scanning electron microscopy (SEM) of outer membrane vesicles (OMVs). **A.** *Bacteroides fragilis* (*B. fragilis*) and **B.** *Bacteroides thetaiotaomicron* (*B. thetaiotaomicron*) derived OMVs (SEM at magnification: ×40 KX).

Our results based on SDS-PAGE showed that OMVs derived from *B. fragilis* and *B. thetaiotaomicron* had different protein profiles. After OMV purification, we measured the protein content of these particles by using a NanoDrop and the Bradford assay. The protein content of the OMVs from *B. fragilis* was 0.35 mg/ml and it was 0.45 mg/ml for *B. thetaiotaomicron*. SDS-PAGE analysis showed different protein bands of OMVs, especially between 11-17 KDa, in *B. fragilis* and *B. thetaiotaomicron* (Fig.2).

The LAL test was performed to detect and quantify the amount of endotoxin from the OMVs. By using the standard curve (Fig.3), we determined that the LPS concentration of OMVs from *B. fragilis* was 1.80 EU/mL and it was 1.68 EU/mL for *B. thetaiotaomicron* derived-OMVs.

ζ-P of these vesicles was measured by electrophoretic light scattering (ELS). Both *B. fragilis* and *B. thetaiotaomicron* OMVs had negative surface charges of -34.2 and -44.7 mV, respectively (Figs.4, 5).

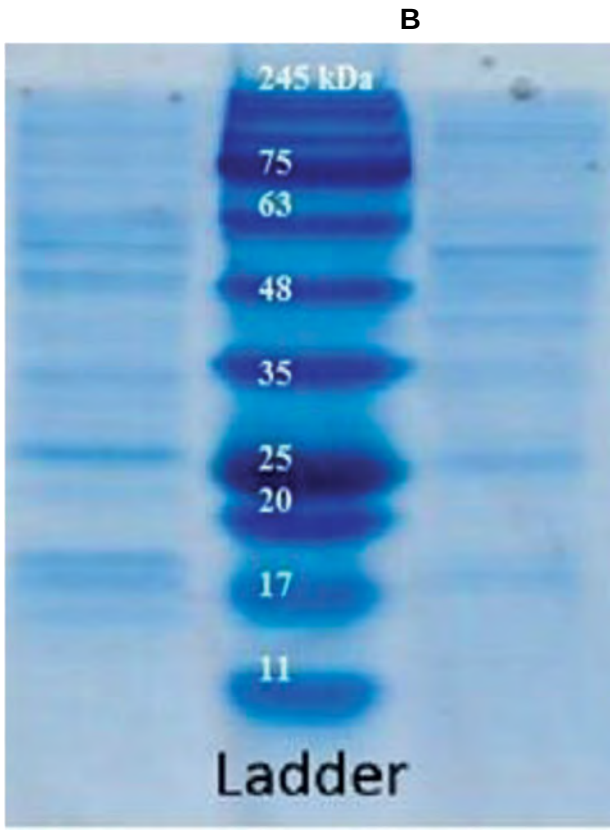

Fig.2: Sodium dodecyl sulfate polyacrylamide gel (SDS-PAGE) showing the protein profile of outer membrane vesicles. The protein bands of **A.** *Bacteroides fragilis* (*B. fragilis*) and **B.** *Bacteroides thetaiotaomicron* (*B. thetaiotaomicron*) derived- outer membrane vesicles (OMVs) at 0.35 mg/ml and 0.45 mg/ml protein concentrations, respectively.

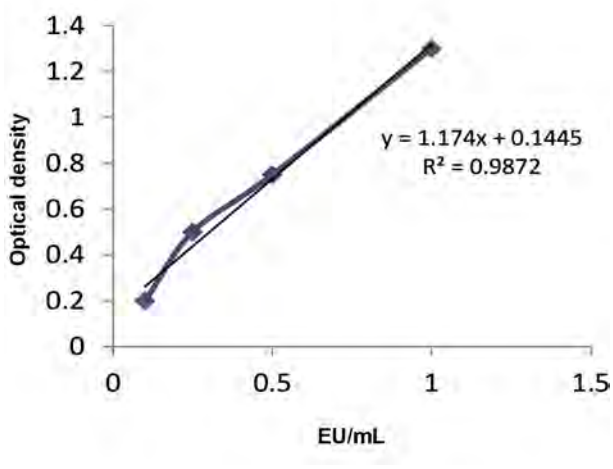

Fig.3: The standard curve of the limulus amoebocyte lysate (LAL) test to determine the endotoxin levels of *Bacteroides fragilis (B. fragilis)* and *Bacteroides thetaiotaomicron (B. thetaiotaomicron)* derived-outer membrane vesicles (OMVs).

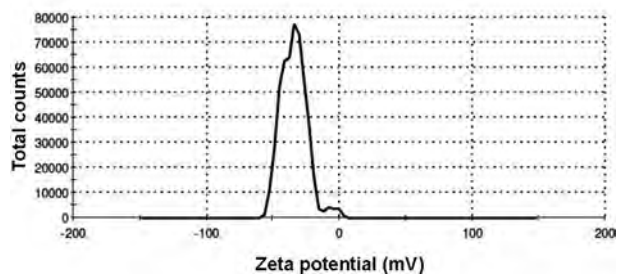

Fig.4: The zeta potential (ζ-P) distribution of *Bacteroides fragilis (B. fragilis)* derived-outer membrane vesicles (OMVs).

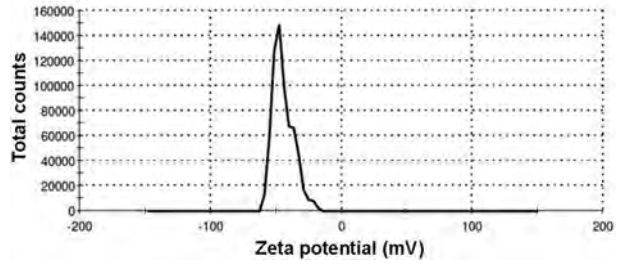

Fig.5: The zeta potential (ζ-P) distribution of *Bacteroides thetaiotaomicron (B. thetaiotaomicron)* derived-outer membrane vesicles (OMVs).

The human intestinal epithelial cell line, Caco-2, was used to study the effects of *B. fragilis* and *B. thetaiotaomicron* derived OMVs on epithelial cell viability. MTT assays showed more than 95% viability of Caco-2 cells treated with both OMVs at a specific concentration.

Discussion

It is well documented that gut microbiota has a profound effect on host health and diseases. The communication between gut microbiota and the host is mainly dependent on the microbial released factors, which could access intestinal epithelial cells (27). OMVs have considerable roles in putative communication since they interact with host cells through their various components, such as bacterial outer membrane determinants, hydrolytic enzymes, and signaling molecules (11). Among numerous microbial species that colonize the GI, the Bacteroidetes comprise the most gram-negative bacteria. Both *B. fragilis* and *B. thetaiotaomicron* have important roles in gut microbiota which produce OMVs that are delivered to distant targets of the host (6). In the present study, we aimed to extract and evaluate the characteristics of OMVs from *B. fragilis* and *B. thetaiotaomicron*.

OMVs originate from the outer membrane of gram-negative bacteria and are released to the extracellular milieu as small particles by bilayer spherical shaped vesicles. Several pathogenic and non-pathogenic bacteria are proposed to produce OMVs, such as *Mycobacterium tuberculosis* (28), *Neisseria meningitides* (29), and *E.coli* (30). *B. fragilis* and *B. thetaiotaomicron* are two predominant gut microbiota which produces OMVs to exert beneficial effects on the host, including mediation of anti-inflammatory responses, immune tolerance

to the gut microbiota, and homeostasis (31). Stentz et al. (32) and Elhenawy et al. (10) purified *B. fragilis* and *B. thetaiotaomicron* OMVs by ultrafiltration and ultracentrifugation, respectively. In the present study, *B. fragilis* and *B. thetaiotaomicron* derived-OMVs were extracted by sequential centrifugation and buffers that contained sodium deoxycholate based on the modified method of Claassen et al. (23).

The evaluation of the physicochemical properties of OMVs is a characteristic examination marker. Morphology, size, and protein content of *B. fragilis* and *B. thetaiotaomicron* OMVs were reported by transmission electron microscopy (TEM) and SDS-PAGE, respectively (10, 32). According to the current study, spherical shaped vesicles from *B. fragilis* and *B. thetaiotaomicron* were observed that ranged in diameter from 30 to 110 nm with SEM. These organisms produced OMVs with different protein bands by SDS-PAGE.

Recently, several studies have reported the potential applications of OMVs as novel vaccine adjuvants and cancer immunotherapeutic agents (33, 34). As mentioned, a previous work and our studies (unpublished data) have noted potent roles for *B. fragilis* and *B. thetaiotaomicron* derived-OMVs, which has made them promising agents to improve targeted pathways of hosts, including the immune and metabolic systems. For this propose, we performed this study to evaluate endotoxin level, surface charge, and cytotoxicity effect on human intestinal epithelial cells.

Bacteroidetes phylum is the major LPS-producing bacteria in gut microbiota. In this study, the LPS concentration of OMVs was assessed by the LAL test. This test, which is known as the bacterial endotoxin test (BET), is performed for over 90% of pyrogenic tests. This measurement is significant for OMVs application as therapeutic agents. To our knowledge, this is the first report of the LPS concentration of *B. fragilis* and *B. thetaiotaomicron* OMVs, which was identified as 1.80 and 1.68 EU/mL, respectively. These obtained values are less than the defined tolerable endotoxin amount according to the United States Pharmacopeia (35).

Surface charges of vesicles are measured and reported as ζ-P potentials. The particle charge has a determinative role in the physical stability of suspensions. Generally, particles which have ζ-P potentials more positive than +30 mV or more negative than -30 mV are stable (36). Measurement of ζ-P potential could provide information about the aggregation and stability of OMVs in sucrose solution. In this study, the ζ-P potentials of *B. fragilis* and *B. thetaiotaomicron* derived OMVs were measured for the first time. These values were found to be less aggregated and thus more stable in sucrose solution.

Intestinal epithelial cells are the interface between gut microbiota and host interactions. Therefore, the effects of *B. fragilis* and *B. thetaiotaomicron* derived OMVs on Caco-2 cell viability (a human intestinal epithelial cell model) were assessed. Our result showed that these particles did not have cytotoxic effects on Caco-2 cells at a specific concentration.

Conclusion

According to our results, *B. fragilis* and *B. thetaiotaomicron* spherical nanosized OMVs have different protein profiles, a safe endotoxin content, and no cytotoxic effect at a specific concentration on a human epithelial cell line. They could be new promising agents to suggest their utility in *in vivo* studies as the novel therapeutic candidates. However, further molecular investigations are needed to explore their roles in more details.

Acknowledgements

This research was funded by Iran Biotech Fund grant 94/10243 and Pasteur Institute of Iran. The authors would like to thank our colleagues at the Pasteur Institute of Iran. There is no conflict of interest in this study.

Authors' Contributions

S.A.B., A.M., F.E.M., V.K., M.M., S.D.S.; Contributed to conception and design of all experimental work, data and statistical analysis, and interpretation of data. S.D.S., V.K.; Were responsible for overall supervision. All authors read and approved the final manuscript.

References

1. Benson AK, Kelly SA, Legge R, Ma F, Low SJ, Kim J, et al. Individuality in gut microbiota composition is a complex polygenic trait shaped by multiple environmental and host genetic factors. Proc Natl Acad Sci USA. 2010; 107(44): 18933-18938.
2. Cho I, Blaser MJ. The human microbiome: at the interface of health and disease. Nat Rev Genet. 2012; 13(4): 260-270.
3. Wallace TC, Guarner F, Madsen K, Cabana MD, Gibson G, Hentges E, et al. Human gut microbiota and its relationship to health and disease. Nutr Rev. 2011; 69(7): 392-403.
4. Sánchez B, Delgado S, Blanco-Míguez A, Lourenço A, Gueimonde M, Margolles A. Probiotics, gut microbiota, and their influence on host health and disease. Mol Nutr Food Res. 2017; 61(1).
5. Turnbaugh PJ, Ley RE, Mahowald MA, Magrini V, Mardis ER, Gordon JI. An obesity-associated gut microbiome with increased capacity for energy harvest. Nature. 2006; 444(7122): 1027-1031.
6. Shen Y, Giardino Torchia ML, Lawson GW, Karp CL, Ashwell JD, Mazmanian SK. Outer membrane vesicles of a human commensal mediate immune regulation and disease protection. Cell Host Microbe. 2012; 12(4): 509-520.
7. Rajilić-Stojanović M, de Vos WM. The first 1000 cultured species of the human gastrointestinal microbiota. FEMS Microbiol Rev. 2014; 38(5): 996-1047.
8. Tremaroli V, Bäckhed F. Functional interactions between the gut microbiota and host metabolism. Nature. 2012; 489(7415): 242-249.
9. Troy EB, Kasper DL. Beneficial effects of Bacteroides fragilis polysaccharides on the immune system. Front Biosci (Landmark Ed). 2010; 15: 25-34.
10. Elhenawy W, Debelyy MO, Feldman MF. Preferential packing of acidic glycosidases and proteases into Bacteroides outer membrane vesicles. MBio. 2014; 5(2): e00909- e00914.
11. Ahmadi Badi S, Moshiri A, Fateh A, Rahimi Jamnani F, Sarshar M, Vaziri F, et al. Microbiota-Derived extracellular vesicles as new systemic regulators. Front Microbiol. 2017; 8: 1610.
12. Wexler AG, Goodman AL. An insider's perspective: Bacteroides as a window into the microbiome. Nat Microbiol. 2017; 2: 17026.
13. Schwechheimer C, Kuehn MJ. Outer-membrane vesicles from Gram-negative bacteria: biogenesis and functions. Nat Rev Microbiol. 2015; 13(10): 605-619.
14. Chutkan H, MacDonald I, Manning A, Kuehn MJ. Quantitative and

qualitative preparations of bacterial outer membrane vesicles. Methods Mol Biol. 2013; 966: 259-272.
15. Bishop DG, Work E. An extracellular glycolipid produced by Escherichia coli grown under lysine-limiting conditions. Biochem J. 1965; 96(2): 567-576.
16. Knox KW, Vesk M, Work E. Relation between excreted lipopolysaccharide complexes and surface structures of a lysine-limited culture of Escherichia coli. J Bacteriol. 1966; 92(4): 1206-1217.
17. Brown L, Wolf JM, Prados-Rosales R, Casadevall A. Through the wall: extracellular vesicles in Gram-positive bacteria, mycobacteria and fungi. Nat Rev Microbiol. 2015; 13(10): 620-630.
18. Kulkarni HM, Jagannadham MV. Biogenesis and multifaceted roles of outer membrane vesicles from Gram-negative bacteria. Microbiology. 2014; 160(Pt 10): 2109-2121.
19. Ellis TN, Kuehn MJ. Virulence and immunomodulatory roles of bacterial outer membrane vesicles. Microbiol Mol Biol Rev. 2010; 74(1): 81-94.
20. Kulp A, Kuehn MJ. Biological functions and biogenesis of secreted bacterial outer membrane vesicles. Annu Rev Microbiol. 2010; 64: 163-184.
21. Shen J, Obin MS, Zhao L. The gut microbiota, obesity and insulin resistance. Mol Aspects Med. 2013; 34(1): 39-58.
22. Kang CS, Ban M, Choi EJ, Moon HG, Jeon JS, Kim DK, et al. Extracellular vesicles derived from gut microbiota, especially Akkermansia muciniphila, protect the progression of dextran sulfate sodium-induced colitis. PLoS One. 2013; 8(10): e76520.
23. Claassen I, Meylis J, van der Ley P, Peeters C, Brons H, Robert J, et al. Production, characterization and control of a Neisseria meningitidis hexavalent class 1 outer membrane protein containing vesicle vaccine. Vaccine. 1996; 14(10): 1001-1008.
24. Nakao R, Hasegawa H, Ochiai K, Takashiba S, Ainai A, Ohnishi M, et al. Outer membrane vesicles of Porphyromonas gingivalis elicit a mucosal immune response. PLoS One. 2011; 6(10): e26163.
25. Michael S, Montag M, Dott W. Pro-inflammatory effects and oxidative stress in lung macrophages and epithelial cells induced by ambient particulate matter. Environ Pollut. 2013; 183: 19-29.
26. Kowapradit J, Opanasopit P, Ngawhirunpat T, Apirakaramwong A, Rojanarata T, Ruktanonchai U, et al. In vitro permeability enhancement in intestinal epithelial cells (Caco-2) monolayer of water soluble quaternary ammonium chitosan derivatives. AAPS PharmSciTech. 2010; 11(2): 497-508.
27. Cañas MA, Fábrega MJ, Giménez R, Badia J, Baldomà L. Outer membrane vesicles from probiotic and commensal Escherichia coli activate NOD1-mediated immune responses in intestinal epithelial cells. Front Microbiol. 2018; 9: 498.
28. Sam Daliri S, Samadi Kafil H, Aghazadeh M, Fateh A, Yousefi M, Siadat SD. Extraction and biological evaluation of the membrane vesicles of mycobacterium tuberculosis (CRBIP7. 11) as adjuvant and vaccine candidate. Jundishapur J Microbiol. 2017; 10(3): e39953.
29. Delbaz SA, Siadat SD, Aghasadeghi MR, Piryaie M, Najar Peerayeh S, Mousavi SF, et al. Biological and immunological evaluation of Neisseria meningitidis serogroup A outer Membrane vesicle as vaccine candidates. Jundishapur J Microbiol. 2013; 6(4): 5007.
30. Behrouzi A, Vaziri F, Riazi Rad F, Amanzadeh A, Fateh A, Moshiri A, et al. Comparative study of pathogenic and non-pathogenic Escherichia coli outer membrane vesicles and prediction of host-interactions with TLR signaling pathways. BMC Res Notes. 2018; 11(1): 539.
31. Cecil JD, Sirisaengtaksin N, O'Brien-Simpson NM, Krachler AM. Outer membrane vesicle-host cell interactions. Microbiol Spectr. 2019; 7(1).
32. Stentz R, Horn N, Cross K, Salt L, Brearley C, Livermore DM, et al. Cephalosporinases associated with outer membrane vesicles released by Bacteroides spp. protect gut pathogens and commensals against β-lactam antibiotics. J Antimicrob Chemother. 2015; 70(3): 701-709.
33. Yi J, Liu Q, Kong Q. Advances in outer membrane vesicles of gram-negative bacteria as sub-unit vaccines-A review. Wei Sheng Wu Xue Bao. 2016; 56(6): 911-921.
34. Kim OY, Park HT, Dinh NTH, Choi SJ, Lee J, Kim JH, et al. Bacterial outer membrane vesicles suppress tumor by interferon-γ-mediated antitumor response. Nat Commun. 2017; 8(1): 626.
35. Wassenaar TM, Zimmermann K. Lipopolysaccharides in food, food supplements, and probiotics: should we be worried? Eur J Microbiol Immunol (Bp). 2018; 8(3): 63-69.
36. Mohammadi H, Abedi A, Akbarzadeh A, Mokhtari MJ, Shahmabadi HE, Mehrabi MR, et al. Evaluation of synthesized platinum nanoparticles on the MCF-7 and HepG-2 cancer cell lines. International Nano Letters. 2013; 3(1): 28.

Original Article

Folliculogenesis-Associated Genes Expression in Human Vitrified Ovarian Tissue after Xenotransplantation in γ-Irradiated Mice

Zahra Shams Mofarahe, Ph.D.[1], Marefat Ghaffari Novin, Ph.D.[1], Mojdeh Salehnia, Ph.D.[2]*

1. Department of Biology and Anatomical Sciences, School of Medicine, Shahid Beheshti University of Medical Sciences, Tehran, Iran
2 Department of Anatomical Sciences, Faculty of Medicine, Tarbiat Modares University, Tehran, Iran

Corresponding Address: P.O.BOX: 14115-111, Department of Anatomical Sciences, Faculty of Medicine, Tarbiat Modares University, Tehran, Iran
Email: salehnim@modares.ac.ir

Received: 22/December/2018, Accepted: 28/April/2019

Abstract

Objective: Autograft transplantation of vitrified cortical ovarian tissue is an acceptable clinical technique for fertility preservation in women. Xenograft transplantation into animal models could be useful for evaluating the safety of human vitrified ovarian tissue. This study targeted to evaluate impact of vitrification on expression of the genes associated with folliculogenesis after xenograft transplantation of human vitrified ovarian tissue to γ-irradiated mice.

Materials and Methods: In this experimental study, ovarian biopsies were gathered from six transsexual persons. The cortical section of ovarian biopsies was separated and chopped into small pieces. These pieces were randomly divided into vitrified and non-vitrified groups. In each group some pieces were considered as non-transplanted tissues and the others were transplanted to γ-irradiated female National Medical Research Institute (NMRI) mice. Before and after two weeks of xenograft transplantation, histological assessment and evaluation of the expression of folliculogenesis-associated genes (*FIGLA, GDF-9,* KL and *FSHR*) were performed in both vitrified and non-vitrified groups.

Results: Percentage of the normal follicles and expression of the all examined genes from transplanted and non-transplanted tissue were similar in both vitrified and non-vitrified groups (P>0.05). After transplantation, the normal follicle rate was significantly decreased and among the folliculogenesis-associated genes, expression of *GDF-9* gene was significantly increased, rather than before transplantation in vitrified and non-vitrified tissues (P<0.05).

Conclusion: The vitrification method using dimethyl solphoxide and ethylene glycol (EG) had no remarkable effect on the normal follicular rate and expression of folliculogenesis-associated genes after two weeks human ovarian tissue xenografting. In addition, transplantation process can cause a significant decrease in normal follicular rate and expression of *GDF-9* gene.

Keywords: Gene Expression, Ovarian Tissue, Vitrification, Xenotransplantation

Cell Journal(Yakhteh), Vol 22, No 3, October-December (Autumn) 2020, Pages: 350-357

Citation: Shams Mofarahe Z, Ghaffari Novin M, Salehnia M. Folliculogenesis-associated genes expression in human vitrified ovarian tissue after xenotransplantation in γ-irradiated mice. Cell J. 2020; 22(3): 350-357. doi: 10.22074/cellj.2020.6553.

Introduction

There are a large number of primordial follicles in human ovarian cortical tissue (1). These follicles are more impervious to cryoinjury effects because of their low metabolism and lack of zona and cortical granules (2). Therefore, ovarian tissue cryopreservation is an acceptable method for fertility preservation in women (3, 4). The possibility of harvesting ovarian tissue at any time of the menstrual cycle is one of hallmarks of fertility preservation through ovarian tissue cryopreservation, in comparison with the other methods. Hence, in cancerous patients with limited time for ovulation induction and egg collection or in pre-pubertal girls, ovarian tissue cryopreservation assumes as the only chance for fertility preservation (5). Recently, the simplicity, safety and cost effectiveness of vitrification made it more acceptable technique, although there are different cryopreservation methods (6-10).

Normal development of follicle needs expression of the particular genes involved in the folliculogenesis process (11, 12). Accordingly, it has been revealed that expression of *FIGLA* and *GDF-9* genes in oocyte of primordial and primary follicles respectively, in addition to expression of *KIT LIGAND* (*KL*) and *FSHR* genes in the granulosa cells of primordial and secondary follicles play an essential role in the follicular development (13-16). No significant alteration on the expression profile of these genes has been detected in human vitrified ovarian tissue immediately after warming or following two weeks of *in vitro* culture (17, 18).

Autograft transplantation of vitrified ovarian tissue was a successful clinical procedure because endocrine function as well as fertility was resumed in patients (19, 20). Contradictory findings have been reported regarding the alteration of oocyte and follicular cells gene expression in vitrified ovarian tissue after transplantation (21-23). In this context, xenograft transplantation into animal models proposed as a quality evaluation of human vitrified ovarian tissues before clinical usage (22).

Since there was a lack of study in expression of the genes involved in follicular development of human vitrified ovarian tissue after the transplantation, the goal of this study was to evaluate impact of vitrification on expression of genes involved in folliculogenesis after

xenograft transplantation of human vitrified ovarian tissue to γ-irradiated mice.

Materials and Methods

All reagents and materials were obtained from Sigma-Alderich (Germany) except those mentioned.

Ovarian tissue collection

This experimental study was endorsed by the Ethics Commission of faculty of Medicine of Shahid Beheshti University of Medical Science (Tehran, Iran) and informed consents were obtained for usage of human tissues (no.172). In this comparative research, ovarian tissue samples were obtained during sex reassignment surgery from six transsexual persons aged 20-30 years with informed consent. It should be noted that persons with a history of hormone administration were excluded. The specimens were promptly delivered to the laboratory in Leibovitz'sL-15 medium on ice, as described in the previous studies (17, 18).

Preparation of human ovarian cortical tissue

The ovarian biopsies were transferred to fresh equilibrated Leibovitz'sL-15 medium. Then their cortical tissues were separated and chopped into small pieces (4×2×1 mm) under a sterile condition.

The retrieved ovarian tissue pieces were accidentally separated into vitrified and non-vitrified groups (n=100 pieces in total). In both non-vitrified and vitrified groups, 50 pieces (from at least five women) were regarded as non-transplanted tissues. Among these tissues, 30 pieces were fixed in Bouin's solution for histological assessment and 20 pieces were kept at -80˚C for later molecular evaluation. In both non-vitrified and vitrified groups, the remaining pieces (n=50 pieces from at least five women) were transplanted to 25 γ-irradiated immunosuppressed female mice for two weeks. From these transplanted tissues, 30 pieces were fixed in Bouin's solution for histological assessment and 20 pieces were kept at -80˚C for later molecular evaluation.

Vitrification and warming procedures

The ovarian tissue pieces were vitrified by the described procedure of Kagawa et al. (24) with some modification. In summary, the pieces were initially washed out in Hanks' balanced salt solution (HBSS with HEPES) complemented with 20% human serum albumin (HAS), then immersed in equilibration solution containing HBSS, 7.5% ethylene glycol (EG) and 7.5% dimethyl sulphoxide (DMSO) for 25 minutes. Next, the tissue pieces were placed into the vitrification solution (20% EG, 20% DMSO and 0.5 M sucrose) for 15 minutes. Finally, the tissue pieces were moved into cryovials containing 100 µl vitrification solution set on nitrogen vapor for 30 seconds and then kept in liquid nitrogen for a week.

The pieces were melted by plunging the vials into water bath at 37˚C. Then, they were transferred into HBSS containing 1 M sucrose in for 3 minutes at 37˚C, and incubated in 0.5 M sucrose for 5 minutes at room temperature. Finally, the pieces were equilibrated in α-MEM medium for two hours.

Providing γ-irradiated mice and transplantation of the human ovarian tissue

Female NMRI mice were obtained from Tarbiat Modares University animal house (Tehran, Iran), aged between 8 and 10 weeks, and used in this study. The mice were synchronized and phase of the mice estrous cycle was confirmed by vaginal cytology. The vaginal smear viewed under a light microscope at the ×400 magnification and they were considered for human ovarian transplantation at postures phase. All experimental procedures were accepted by Animal Research Committee of Shahid Beheshti University. In order to suppress the immune system for preventing rejection of the transplanted tissue, the mice (n=25) were irradiated with 7.5 Gy single dose Gama irradiation for 6 minutes (25).

Transplantation of cortical ovarian tissue was preformed 72 hours after irradiation. Intra-peritoneal injection of a combination of ketamine 10 % (75 mg/kg body weight) and xylazine 2 % (15 mg/kg) was administered for anesthesia. Two pieces of human ovarian tissue were subcutaneously transplanted into the back of each mouse. Then the mice were kept under aseptic situation with free availability to food and water. After 14 days of transplantation, the mice were euthanized by cervical dislocation and tissue fragments were retrieved for downstream experiments.

Histological evaluation by hematoxylin and eosin

A total of 15 pieces in each group of the study were fixed in Bouin's solution for 18 hours at room temperature. The samples were processed and embedded in paraffin wax, and they were subsequently serially sectioned at 5 µm thickness. Every tenth section of each piece was mounted on glass slides and colored with hematoxylin and eosin (H&E). Then, each section was inspected for determining the number of follicles, field by field under the ×100 magnification of the light microscope. In order to prevent the re-counting follicles, only follicles with a clear nucleus of oocyte were calculated. The follicles were classified as primordial, primary and secondary according to the previous classification (26). Primordial follicles had one layer of flattened follicular cells. Primary follicles had one layer of cuboidal follicular cells and secondary follicles had two or more layers of cuboidal granulosa cells. Atretic follicles had pyknotic oocyte nucleus, shrunken ooplasm or disorganized follicular cells.

RNA extraction and cDNA synthesis for molecular evaluation

In order to evaluate expression of the some genes related to development of oocyte and follicular cells (including:

FIGLA, *GDF-9*, *KL* and *FSHR* genes) total RNA was extracted from 40 non-transplanted and transplanted fragments in both vitrified and non-vitrified groups using TRIzol reagent (Invitrogen, USA) as indicated by the manufacturer's directions. The RNA specimens were treated with DNase to eliminate any genomic DNA contamination only before proceeding with the cDNA synthesis. Then, RNA concentration was calculated by spectrophotometry. Finally, 1000 ng of the extracted RNA was used for cDNA synthesis by the commercial Kit (Thermo Scientific, EU), according to the indicated manufacturer's directions. The cDNA synthesis reaction was carried out at 42˚C for 60 minutes, and the synthesized cDNA was kept at -20˚C.

Real-time reverse transcriptase-polymerase chain reaction

The primers for real-time reverse transcriptase-polymerase chain reaction (RT-PCR) were formulated (Table 1) utilizing GenBank (http://www.ncbi.nlm.nih.gov) and Primer3 software, then synthesized by Generary Biotech Company (China).

RT-PCR was carried out by the Applied Biosystems (UK) real-time thermal cycler as indicated by QuantiTect SYBR Green RT-PCR Kit (Applied Biosystems, UK). The housekeeping gene, *β-ACTIN*, was considered as internal control. For each specimen, the house keeping gene and the target genes were amplified in the same round. One microliter of cDNA, 1 µl of the mixture of forward and reverse primers and 10 µl SYBR Green Master Mix were used per 20 µl of the reaction volume. After each PCR run, melt curve was analyzed to determine amplification specificity. Real-time heating condition included holding step at 95˚C for 5 minutes, cycling steps (35-40 cycles) at 95˚C for 15 seconds, 58˚C for 30 seconds and 72˚C for 15 seconds which was continued by a melt curve analysis at 95˚C for 15 seconds, 60˚C for 1 minutes and 95˚C for 15 seconds. Then the relative quantification of target genes was calculated by the Pfaffl formula (27). The real-time RT-PCR experiments were performed duplicate for each specimen in at least a three biological repeats.

Statistical analysis

Statistical analysis was performed with the SPSS 19.0 software (SPSS Inc., Chicago, IL, USA). Quantitative variables were displayed as mean ± standard error (SE) and percentage. The follicular counting data and result of real-time RT-PCR were analyzed by paired-samples t test and bootstrap. $P<0.05$ were considered statistically significant.

Results

Histological examination of ovarian cortical tissue

The morphology of non-transplanted and transplanted ovarian cortical tissues in both vitrified and non-vitrified groups was shown in Figure 1. In both vitrified and non-vitrified groups, the morphology of follicles and stromal cells was almost similar, before and after transplantation. The normal follicles had circular oocyte with intact granulosa cells. The atretic follicles were seen in fibrotic and ischemic areas of transplanted tissues. The stromal cells had also a normal appearance in all groups. After 14 days of ovarian xenograft, the growing follicles (secondary follicles) were seen in vitrified and non-vitrified tissues (Fig.1). The follicular integrity and stromal tissue structures of transplanted and non-transplanted tissues were similar in vitrified and non-vitrified groups.

Table 1: Specifications of the primers utilized for real-time reverse transcriptase-polymerase chain reaction (RT-PCR) assay

Target gene	Primer sequence	Accession number	Product size (bp)
β-actin	F: TCAGAGCAAGAGAGGCATCC	NM_001101.3	187
	R: GGTCATCTTCTCACGGTTGG		
FIGLA	F: TCGTCCACTGAAAACCTCCAG	NM_001004311.3	76
	R: TTCTTATCCGCTCACGCTCC		
KL	F: AATCCTCTCGTCAAAACTGAAGG	NM_000899.4	163
	R: CCATCTCGCTTATCCAACACTGA		
GDF-9	F: TCCACCCACACACCTGAAAT	NM_005260	147
	R: GCAGCAAAACCAAAGGAGGA		
FSHR	F: CTGGCAGAAGAGAATGAGTCC	NM_181446.2	157
	R: TGAGGATGTTGTACCCGATGATA		

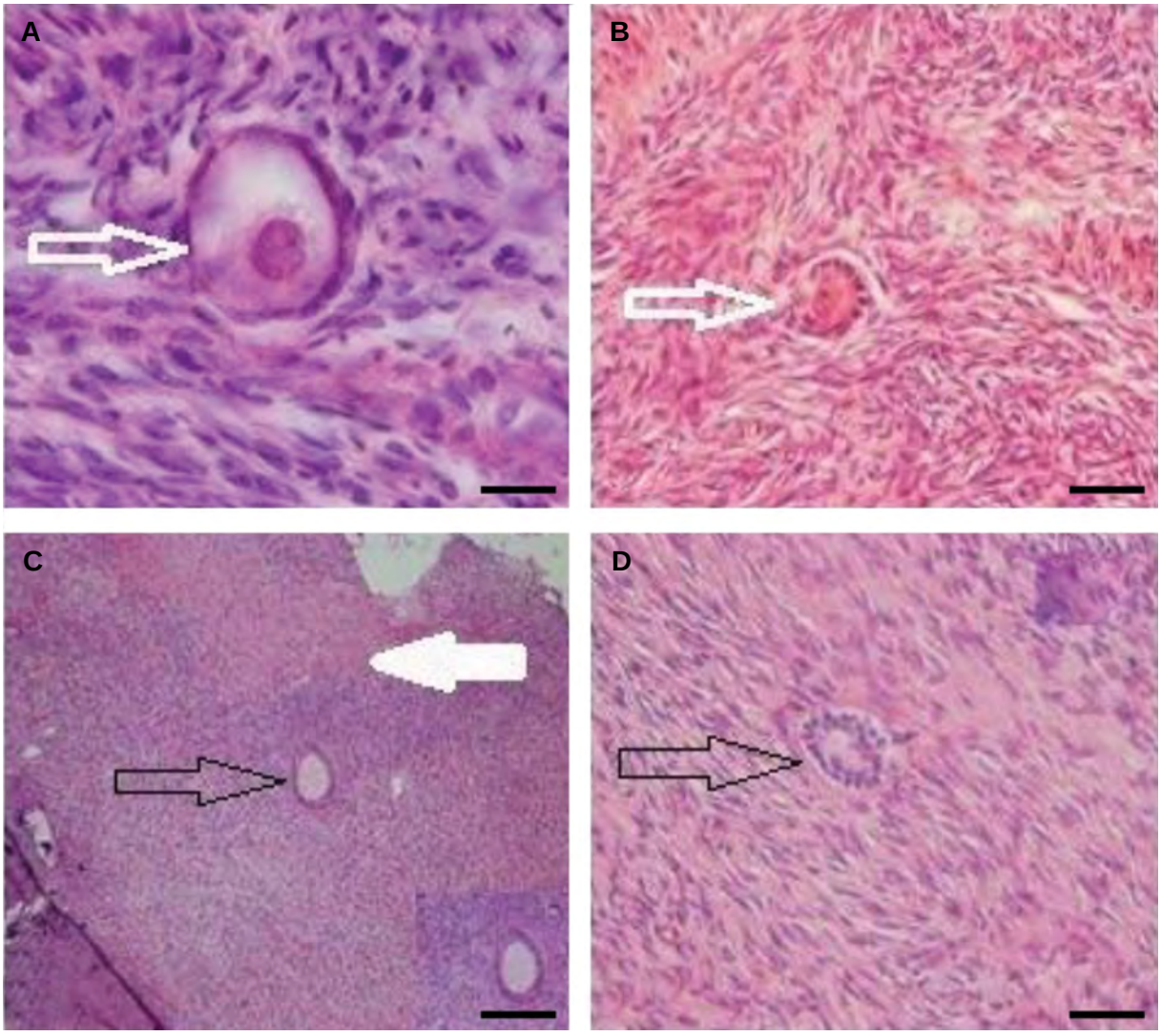

Fig.1: Hematoxylin and eosin staining of non-transplanted and transplanted human ovarian cortical sections in both vitrified and non-vitrified groups. The morphology of primordial and primary follicles was shown white arrow and the secondary follicles demonstrated black arrow. **A.** Vitrified non-transplanted tissues, **B.** Vitrified transplanted tissue, **C.** Non-vitrified non-transplanted group, and **D.** Non-vitrified and non-transplanted group. The atretic follicles were shown in fibrotic and ischemic areas of transplanted tissues (white filled arrow in B) (scale bar: 200 µm).

Percent of normal follicle in the non-transplanted ovarian tissues

A total of 350 follicles were counted in 30 pieces of non-vitrified and vitrified ovarian tissues. The percentages of morphologically normal follicles at different developmental stages in both groups are shown in Table 2. This rate was 86.5% in non-vitrified and 84.3% in vitrified tissues. In non-vitrified tissue, among normal follicles the proportion of primordial, primary and secondary follicles was 62.4%, 22.1% and 2%, respectively. In vitrified group, these percentages were 59%, 23.1% and 2.2%, respectively. There was no statistically significant difference in the percentage of normal follicles between these two groups (P>0.05).

Percentage of normal follicle in the transplanted ovarian tissues

A total of 300 follicles were counted and analyzed in 30 transplanted ovarian cortical pieces in the non-vitrified and vitrified groups. Percentage of the morphologically normal follicles, at different developmental stages in both groups, are shown in Table 2. Proportion of normal follicle was 78.9% in non-vitrified and 75% in vitrified tissues. Among the normal follicles in non-vitrified and vitrified tissues, percentage of the primordial follicles was 14.4% and 15.8%, primary follicles was 55.1% and 52.5%, secondary follicles was 9.4% and 6.7%, respectively. There was no statistically significant difference between these two groups (P>0.05).

Comparison of normal follicle percentage in the non-transplanted and transplanted ovarian tissues

In the both transplanted tissues, compared to the non-transplanted tissues, percentage of normal follicles was significantly decreased (P<0.05). Proportion of primordial follicles was significantly lower and percent of primary and secondary follicles was significantly higher in both transplanted tissues than their non-transplanted counterparts (P<0.05).

Table 2: Percentage of the normal follicles at different developmental stages before and after xenograft transplantation of human ovarian tissue in vitrified and non-vitrified groups

Group	Number of total follicles	Number of normal follicles	Number of primordial follicles	Number of primary follicles	Number of secondary follicles
Non-transplanted vitrified	155	131/155**	135/131**	57/131**	9/131**
		(84.51 ± 1.42)	(58.69 ± 2.61)	(23.24 ± 2.48)	(2.58 ± 0.54)
Non-transplanted non-vitrified	195	169/195*	166/169*	68/169*	13/169*
		(86.66 ± 2.11)	(63.58 ± 5)	21.02 ± 4.68	(2 ± 1.71)
Transplanted vitrified	120	90/120**	19/90**	63/90**	8/90**
		(75 ± 3)	(15.83 ± 1.21)	(52.50 ± 3)	(6.66 ± 1)
Transplanted non-vitrified	180	142/180*	26/142*	99/142*	17/142*
		(78.88 ± 1.33)	(14.44 ± 1.58)	(54.99 ± 2.12)	(9.44 ± 1.50)

Data were presented as mean (%) ± SE. There was no significant difference between the vitrified and non-vitrified groups before and after transplantation in all columns (P>0.05). There were significant differences between transplanted and non-transplanted groups in vitrified (*) and non-vitrified group (**), P<0.05.

Expression of folliculogenesis-associated genes in the non-transplanted ovarian tissues

The ratio expression of *FIGLA*, *GDF-9*, *KL* and *FSHR* genes to *β-ACTIN* gene in non-vitrified group before transplantation were 18.4×10^{-4}, 17.3×10^{-4}, 8.6×10^{-4} and 18.4×10^{-4} while in non-transplanted-vitrified group they were respectively 14×10^{-4}, 13×10^{-4}, 7.3×10^{-4} and 18.7×10^{-4} (Fig.2). There was no statistically significant difference between expression of the all examined genes in both non-transplanted tissues (P>0.05).

Expression of folliculogenesis-associated genes in the transplanted ovarian tissues

The ratio expression of *FIGLA*, *GDF-9*, *KL* and *FSHR* genes to *β-ACTIN* gene in non-vitrified group after transplantation were respectively 16.8×10^{-4}, 484.7×10^{-4}, 45.6×10^{-4}, 123.9×10^{-4} while they were respectively 10.4×10^{-4}, 335.8×10^{-4}, 33.4×10^{-4} and 85.1×10^{-4} in the vitrified group (Fig.2). There was no statistically significant difference between expression of the all examined genes in the both transplanted-vitrified and non-vitrified groups (P>0.05).

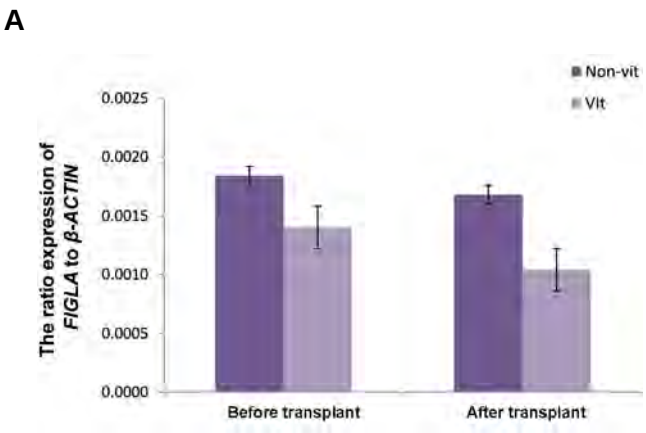

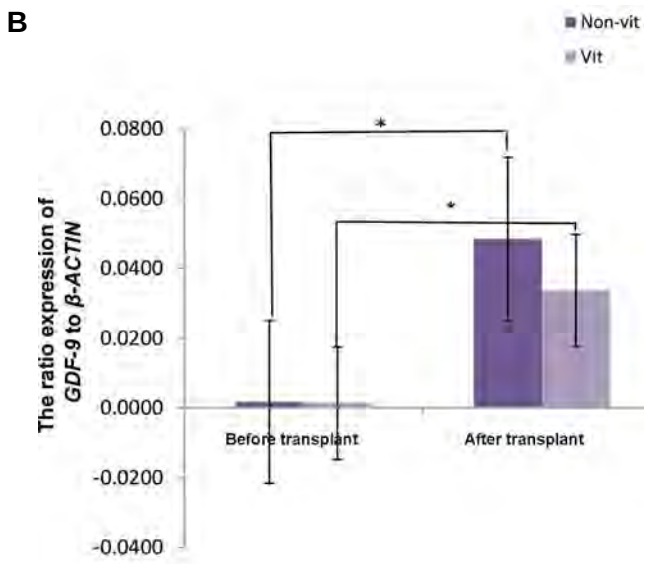

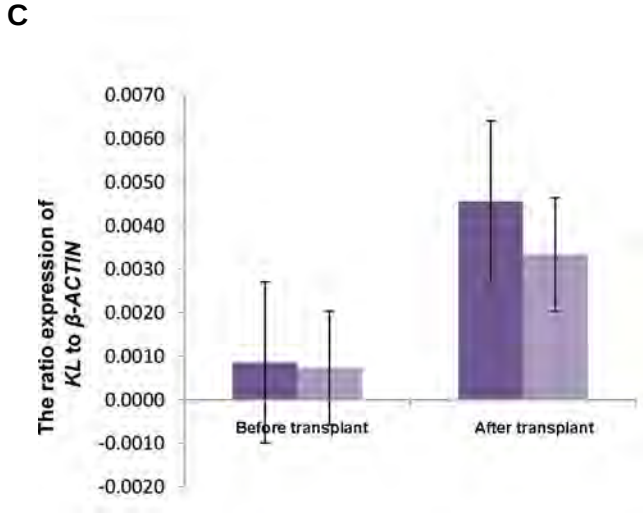

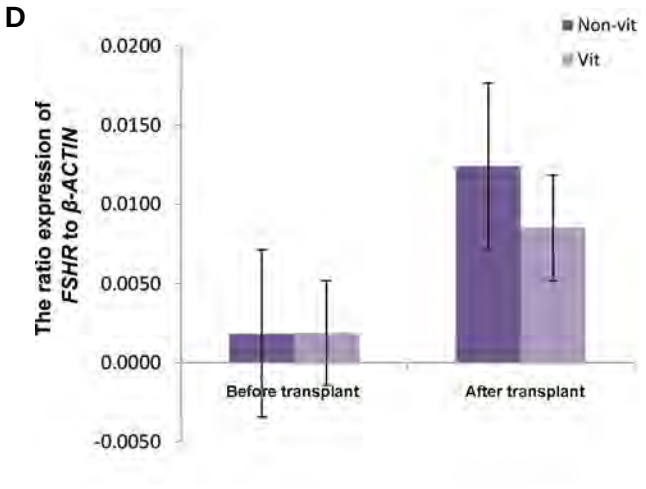

Fig.2: Folliculogenesis-associated genes expression to *β-ACTIN* in non-transplanted and transplanted human ovarian cortical tissues of vitrified and non-vitrified groups. **A.** *FIGLA*, **B.** *GDF-9*, **C.** *KIT LIGAND,* and **D.** *FSHR* genes expression to *β-ACTIN* in the non-transplanted and transplanted tissues in non-vitrified and vitrified groups are shown. There was no statistically significant difference between non-vitrified and vitrified groups. *; The expression of *GDF-9* gene was significantly increased in transplanted tissues in comparison with non-transplantation tissues.

Comparison of folliculogenesis-associated gene expressions in non-transplanted and transplanted ovarian tissues

In the transplanted tissues in comparison with non-transplanted tissues, *FIGLA*, *KL* and *FSHR* gene expression levels were similar in both vitrified and non-vitrified groups (P0.05). But, *GDF-9* gene expression was significantly increased in the transplanted tissue of the vitrified and non-vitrified groups (P<0.05).

Discussion

In this study, we showed that rate of normal follicles at different developmental stages in the cortical ovarian tissue was similar after 14 days of xenograft transplantation in both vitrified and non-vitrified transplanted groups. It seems that method of vitrification had no delayed deleterious effects on normal follicles rate in human ovarian tissue, and primordial and primary follicles were able to resume growth and development after vitrification and transplantation. Therefore, this method is useful for preserving human ovarian cortical tissue. Application of EG and DMSO as penetrable and sucrose as non-penetrable cryoprotectant in the vitrification solution, by reducing tissue damage, had a good effect on preserving ovarian cortical tissue.

Consistent to our findings, David and colleagues showed that integrity of follicles in cryopreserved human ovarian tissue was preserved well after three weeks xenotransplantation (28). Moreover, Nisdle reported that after three weeks xenograft transplantation of human ovarian cortical tissue, there was no significant difference between normal follicle population in the both vitrified and non-vitrified transplanted tissue (29). In contrast with our data, Jafarabadi and colleagues showed that xenotransplantation of vitrified tissue resulted in a much more reduction of the normal follicles in comparison with non-vitrified one. They suggested that vitrification procedure might have harmful effects on the viability and morphology of follicles after transplantation (22). This discrepancy could be due to differences in the vitrification techniques, transplantation site and duration of transplantation.

The success of xenograft transplantation depends on many factors including the vitrification technique, composition of vitrification solution, type of species and transplantation site (30).

According to our obtained data transplantation of vitrified and non-vitrified human ovarian tissues resulted in a significant reduction in the rate of normal follicle apart from vitrification procedure. Moreover, fibrotic areas were observed in the transplanted tissue in both groups. Decreased rate of the normal follicles may be related to occurrence of ischemia during tissue transplantation. Hence, the follicle normality may be more sensitive to the transplantation procedure on its own than vitrification. The revascularization of transplanted tissue takes several days and during this period ischemia has occurred. This ischemia reduced number of follicles and subsequently diminished lifetime of the transplanted tissue (31). One of the most important factors in successful transplantation is rapid re-establishment of blood flow which is essential for survival of ovarian follicles in the transplanted tissue (32). Amorim et al. (7) have reported considerable follicular survival after transplantation of human ovarian cortical tissue to kidney capsule of immunosuppressed mice. In contrast to the above report, which preformed transplantation with a suitable vascular bed for transplanted ovarian tissues, herein, the degeneration of follicles due to ischemia could be attributed to inappropriate vascular bed support. Moreover, Dath et al. (33) reported that intramuscular transplantation of ovarian tissue associated with better survival of ovarian follicles because of a suitable blood supply. Hence, to improve the follicles viability, transplantation site with suitable blood vessels should be selected.

In this study, significant reduction of normal follicle rate and number of primordial follicles were noticed; however, the number of growing follicles (primary and secondary) was significantly increased at the end of transplantation. This may represent the progress of follicular development in transplanted vitrified and non-vitrified tissues in spite of non-suitable vascular bed. Accordingly, we observed similar gene expression levels of *FIGLA*, *GDF-9*, *KL* and *FSHR* in the vitrified and non-vitrified transplanted tissues. It seems that vitrification did not have any significant

effect on mRNA level and ovarian follicles had retained their ability to express developmental genes even after transplantation. Compatible to our data, Jafarabadi and colleagues showed that anti-apoptotic gene expressions were similar in both vitrified and non-vitrified human ovarian tissue after one month transplantation (22). It has also been revealed that expression of *CKIT*, KL and *GDF-9* genes in human cryopreserved and fresh ovarian cortical tissue was similar after three weeks transplantation (28). As we observed, expression of the majority of target genes before and after transplantation in vitrified and non-vitrified tissue was similar and only expression of *GDF-9* gene in vitrified and non-vitrified tissue was significantly increased after transplantation. Increased number of the primary follicles may be related to the activation of primordial follicles following incidence of ischemia and hypoxia in the transplanted ovarian tissue (32). Considering that *GDF-9* gene are expressed in growing ovarian follicles (primary and secondary) (9), its increased expression could be because of elevated number of growing follicles after transplantation. This activation may result in loss of follicular reservoir in transplanted ovarian tissue that subsequently reduces lifespan of the transplanted tissue (32).

Conclusion

The vitrification method using DMSO and EG had no harmful effect on the follicular development and expression of genes related to folliculogenesis after xenografting human ovarian tissue. Moreover, the process of transplantation can cause a significant decrease in normal follicular rate and expression of *GDF-9* gene.

Acknowledgements

There is no financial support and conflict of interest in this study.

Authors' Contributions

Z.S.M.; Performed the experiments, analyzed the data and contributed to writing the manuscript. M.S.; Supervised the study and contributed to doing the experiments, data analysis and writing the manuscript. M.G.N.; Contributed to designing of the study and project development. All authors read and approved the final manuscript.

References

1. Candy CJ, Wood MJ, Whittingham DG. Restoration of a normal reproductive lifespan after grafting of cryopreserved mouse ovaries. Hum Reprod. 2000; 15(6): 1300-1304.
2. Prasath EB. Ovarian tissue cryopreservation: an update. J Hum Reprod Sci. 2008; 1(2): 50-55.
3. Sanfilippo S, Canis M, Smitz J, Sion B, Darcha C, Janny L , et al. Vitrification of human ovarian tissue: a practical and relevant alternative to slow freezing. Reprod Biol Endocrinol. 2015; 13: 67.
4. Kim SY, Kim SK, Lee JR, Woodruff TK. Toward precision medicine for preserving fertility in cancer patients: existing and emerging fertility preservation options for women. J Gynecol Oncol. 2016; 27(2): e22.
5. Pacey AA, Eiser C. The importance of fertility preservation in cancer patients. Expert Rev Anticancer Ther. 2014; 14(5): 487-489.
6. Shi Q, Xie Y, Wang Y, Li S. Vitrification versus slow freezing for human ovarian tissue cryopreservation: a systematic review and meta-anlaysis. Sci Rep. 2017; 7(1): 8538.
7. Amorim CA, Dolmans MM, David A, Jaeger J, Vanacker J, Camboni A, et al. Vitrification and xenografting of human ovarian tissue. Fertil Steril. 2012; 98(5): 1291-8. e1-2.
8. Kondapalli LA, Dillon KE, Sammel MD, Ray A, Prewitt M, Ginsberg JP, et al. Quality of life in female cancer survivors: is it related to ovarian reserve? Qual Life Res. 2014; 23(2): 585-592.
9. Nottola SA, Camboni A, Van Langendonckt A, Demylle D, Macchiarelli G, Dolmans MM, et al. Cryopreservation and xenotransplantation of human ovarian tissue: an ultrastructural study. Fertil Steril. 2008; 90(1): 23-32.
10. Zhou XH, Zhang D, Shi J, Wu YJ. Comparison of vitrification and conventional slow freezing for cryopreservation of ovarian tissue with respect to the number of intact primordial follicles: a meta-analysis. Medicine (Baltimore). 2016; 95(39): e4095.
11. Markholt S, Grøndahl ML, Ernst EH, Andersen CY, Ernst E, Lykke-Hartmann K. Global gene analysis of oocytes from early stages in human folliculogenesis shows high expression of novel genes in reproduction. Mol Hum Reprod. 2012; 18(2): 96-110
12. Bonnet A, Cabau C, Bouchez O, Sarry J, Marsaud N, Foissac S, et al. An overview of gene expression dynamics during early ovarian folliculogenesis: specificity of follicular compartments and bi-directional dialog. BMC Genomics. 2013; 14: 904.
13. Carlsson IB, Laitinen MP, Scott JE, Louhio H, Velentzis L, Tuuri T, et al. Kit ligand and c-Kit are expressed during early human ovarian follicular developmentand their interaction is required for the survival of follicles in long-term culture. Reproduction. 2006; 131(4): 641-649.
14. Hsueh AJ. Fertility: the role of mTOR signaling and KIT ligand. Curr Biol. 2014; 24(21): R1040-R1042.
15. Kishi H, Kitahara Y, Imai F, Nakao K, Suwa H. Expression of the gonadotropin receptors during follicular development. Reprod Med Biol. 2017; 17(1): 11-19.
16. Soyal SM, Amleh A, Dean J. FIGalpha, a germ cell-specific transcription factor required for ovarian follicle formation. Development. 2000; 127(21): 4645-4654.
17. Shams Mofarahe Z, Ghaffari Novin M, Jafarabadi M, Salehnia M, Noroozian M, Ghorbanmehr N. Effect of human ovarian tissue vitrification/warming on the expression of genes related to folliculogenesis. Iran Biomed J. 2015; 19(4): 220-225.
18. Shams Mofarahe Z, Salehnia M, Ghaffari Novin M, Ghorbanmehr N, Fesharaki MG. Expression of folliculogenesis-related genes in vitrified human ovarian tissue after two weeks in vitro culture. Cell J. 2017; 19(1): 18-26.
19. Practice Committee of American Society for Reproductive Medicine. Ovarian tissue cryopreservation: a committee opinion. Fertil Steril. 2014; 101(5): 1237-1243
20. Anderson RA, Wallace WHB, Telfer EE. Ovarian tissue cryopreservation for fertility preservation: clinicaland research perspectives. Hum Reprod Open. 2017; 2017(1): hox001.
21. Agca C, Lucy MC, Agca Y. Gene expression profile of rat ovarian tissue following xenotransplantation into immune-deficient mice. Reproduction. 2009; 137(6): 957-967.
22. Jafarabadi M, Abdollahi M, Salehnia M. Assessment of vitrification outcome by xenotransplantation of ovarian cortex pieces in γ-irradiated mice: morphological and molecular analyses of apoptosis. J Assist Reprod Genet. 2015; 32(2): 195-205.
23. Van Langendonckt A, Romeu L, Ambroise J, Amorim C, Bearzatto B, Gala JL, et al. Gene expression in human ovarian tissue after xenografting. Mol Hum Reprod. 2014; 20(6): 514-525.
24. Kagawa N, Silber S, Kuwayama M. Successful vitrification of bovine and human ovarian tissue. Reprod Biomed Online. 2009; 18(4): 568-577.
25. Johnsen HE, Lanza F. Quality assessment of autologous hematopoietic blood progenitor and stem cell grafting: a prospective registration study. J Biol Regul Homeost Agents. 2002;

16(4): 272-288.
26. Lass A, Silye R, Abrams DC, Krausz T, Hovatta O, Margara R, et al. Follicular density in ovarian biopsy of infertile women: a novel method to assess ovarian reserve. Hum Reprod. 1997; 12(5): 1028-1031.
27. Pfaffl MW. A new mathematical model for relative quantification in real-time RT-PCR. Nucleic Acids Res. 2001; 29(9): e45.
28. David A, Van Langendonckt A, Gilliaux S, Dolmans MM, Donnez J, Amorim CA. Effect of cryopreservation and transplantation on the expression of kit ligand and anti-Mullerian hormone in human ovarian tissue. Hum Reprod. 2012; 27(4): 1088-1095.
29. Nilsson EE, Skinner MK. Kit ligand and basic fibroblast growth factor interactions in the induction of ovarian primordial to primary follicle transition. Mol Cell Endocrinol. 2004;214(1-2):19-25.
30. Fatehi R, Ebrahimi B, Shahhosseini M, Farrokhi A, Fathi R. Effect of ovarian tissue vitrification method on mice preantral follicular development and gene expression. Theriogenology. 2014; 81(2): 302-308.
31. Donnez J, Squifflet J, Van Eyck AS, Demylle D, Jadoul P, Van Langendonckt A, et al. Restoration of ovarian function in orthotopically transplanted cryopreserved ovarian tissue: a pilot experience. Reprod Biomed Online. 2008; 16(5): 694-704.
32. Kim S, Lee Y, Lee S, Kim T. Ovarian tissue cryopreservation and transplantation in patients with cancer. Obstet Gynecol Sci. 2018; 61(4): 431-442.
33. Dath C, Van Eyck AS, Dolmans MM, Romeu L, Delle Vigne L, Donnez J, et al. Xenotransplantation of human ovarian tissue to nude mice: comparison between four grafting sites. Hum Reprod. 2010; 25(7): 1734-1743.

Original Article

Supplementation of Culture Media with Lysophosphatidic Acid Improves The Follicular Development of Human Ovarian Tissue after Xenotransplantaion into The Back Muscle of γ-Irradiated Mice

Zeynab Mohammadi, Ph.D.[1], Nasim Hayati Roodbari, Ph.D.[1], Kazem Parivar, Ph.D.[1], Mojdeh Salehnia, Ph.D.[2]*

1. Department of Biology, Science and Research Branch, Islamic Azad University, Tehran, Iran
2. Department of Anatomy, Faculty of Medical Sciences, Tarbiat Modares University, Tehran, Iran

Corresponding Address: P.O.Box: 14115-111, Department of Anatomy, Faculty of Medical Sciences, Tarbiat Modares University, Tehran, Iran
Email: salehnim@modares.ac.ir

Received: 26/January/2019, Accepted: 23/April/2019

Abstract

Objective: The aim of the present study was to evaluate the effects of lysophosphatidic acid (LPA) supplementation of human ovarian tissue culture media on tissue survival, follicular development and expression of apoptotic genes following xenotransplantation.

Materials and Methods: In this experimental study, human ovarian tissue was collected from eight normal female to male transsexual individuals and cut into small fragments. These fragments were vitrified-warmed and cultured for 24 hours in the presence or absence of LPA, then xenografted into back muscles of γ-irradiated mice. Two weeks post-transplantation the morphology of the recovered tissues were evaluated by hematoxylin and eosin staining. The expression of genes related to apoptosis (*BAX and BCL2*) were analyzed by real time revers transcription polymerase chain reaction (RT-PCR) and detection of BAX protein was done by immunohistochemical staining.

Results: The percent of normal and growing follicles were significantly increased in both grafted groups in comparison to the non-grafted groups, however, these rates were higher in the LPA-treated group than the non-treated group (P<0.05). There was a higher expression of the anti-apoptotic gene, BCL2, but a lower expression of the pro-apoptotic gene, BAX, and a significant lower BAX/ BCL2 ratio in the LPA-treated group in comparison with non-treated control group (P<0.05). No immunostaining positive cells for BAX were observed in the follicles and oocytes in both transplanted ovarian groups.

Conclusion: Supplementation of human ovarian tissue culture medium with LPA improves follicular survival and development by promoting an anti-apoptotic balance in transcription of *BCL2* and *BAX* genes.

Keywords: Apoptosis, Lysophosphatidic Acid, Ovarian Follicle

Cell Journal(Yakhteh), Vol 22, No 3, October-December (Autumn) 2020, Pages: 358-366

Citation: **Mohammadi Z, Hayati Roodbari N, Parivar K, Salehnia M. Supplementation of culture media with lysophosphatidic acid improves the follicular development of human ovarian tissue after xenotransplantaion into the back muscle of γ-irradiated mice. Cell J. 2020; 22(3): 358-366. doi: 10.22074/cellj.2020.6752.**

Introduction

Fertility preservation by using cryopreserved ovarian tissue is critical for patients who are subjected to chemotherapy and radiotherapy or suffer from premature ovarian failure and autoimmune problems (1). The ovarian tissue is cryopreserved by two slow freezing and vitrification techniques. Based on the literature vitrification may be more effective than slow freezing, based on less primordial follicular DNA damage and better preservation of stromal cells (2). *In vitro* culture (IVC) followed by transplantation of cortical ovarian tissue is a potential technique to develop and grow the follicles after cryopreservation. The results obtained from these techniques in human ovarian tissue are very controversial due to their large sizes, dense ovarian stroma and long folliculogenesis period (3-4).

Apoptosis that is induced by oxidative stress or physical and chemical triggers during IVC and transplantation in cryopreserved tissues, affects the quality, growth, survival, and development of ovarian follicles (5-9). The usage of appropriate growth factors, antioxidants and anti-apoptotic factors improves the quality of the tissue during both IVC and grafting procedure (10-13).

Lysophosphatidic acid (LPA) is a bioactive phospholipid that is present in all tissues and plays roles in several cell activities such as proliferation, differentiation and migration (14,15). In ovaries and uterus LPA signaling is involved in early embryo development and preparation of endometrium for embryo-maternal interactions (14,16-21). LPA and its active receptors have been reported to be expressed in uterus, ovaries, and placenta (15, 16). Recent studies on several mammalian species showed that LPA does its function through interactions of its LPAR1-6 receptors (16-22). Out of the six LPA receptors, LPAR4 is highly expressed in the cortex of human ovaries and LPAR1-3 are detected in human granulosa-lutein cells (15).

In addition, the effects of LPA as an anti-apoptotic factor on several cell types have been suggested in the literature (17, 21-23). However, there is poor information regarding its effects for improving the cell quality in IVC of human ovarian tissue. Therefore, the aim of the present study was to evaluate the effects of supplementation of the human ovarian tissue culture media with LPA on tissue survival

and follicular development after xenotransplantation, using morphological and immunohistochemical techniques as well as analysis of the expression of apoptosis-related genes.

Materials and Methods

All reagents used in the following experiments were obtained from Sigma-Aldrich (Germany), unless stated otherwise.

Ovarian tissue collection

In this experimental study, the human ovarian tissues were collected from 8 normal transsexual (female to male) individuals aged 18-35 years old (median 26.1). The tissues were received following laparoscopic surgery under confirmation by Ethics Committee of the Faculty of Medical Science of Tarbiat Modares University (Ref. No. 52/883). The ovarian cortical tissues were cut into approximately 2×1×1 mm pieces under sterile conditions (n=130). These fragments vitrified-warmed and all assessments of this study were performed on these samples. All samples were cryopreserved and stored at liquid nitrogen until they were used.

Experimental design

This experimental study was designed to assess the effect of LPA on human ovarian tissue morphology and expression of some apoptosis-related genes after xenotransplantation. After vitrification and warming of ovarian fragments, the tissues were cultured 24 hours in the presence or absence of LPA, then xenotransplanted into gluteus maximus muscles of γ-irradiated female NMRI mice. Before and after transplantation tissue morphology and follicular counting were assessed by hematoxylin and eosin (H&E) staining. Analysis of expression of the apoptosis-related genes (*BAX* and *BCL2*) was performed by real time revers transcription polymerase chain reaction (RT-PCR). Also immunohistochemical staining for BAX protein was done on recovered transplanted tissue.

Ovarian tissue vitrification and warming

The ovarian cortical fragments (n=125) were vitrified according to the protocol described previously in the solution ethylene glycol, ficol and sucrose named: EFS40% (6). The human ovarian tissues were equilibrated in three changes of vitrification solutions, then they were put into cryovials and stored in liquid nitrogen. For warming the ovarian tissues they were hydrated by serially diluted sucrose (1, 0.5 and 0.25 M phosphate buffer) and equilibrated with culture media for 30 minutes for the following assessments. Some ovarian fragments (n=5 fragments) were fixed in Bouin's solution for evaluation of normal morphology after warming and the other fragments were used for *in vitro* culturing (n=120 fragments).

Ovarian tissue culture

Vitrified-warmed tissue fragments were cultured (n=120 fragments in total) in multi-well culture plates, containing 300 µl/well of α-MEM supplemented with 5 mg/ml human serum albumin (HSA), 0.1 mg/ml penicillin G, 0.1 mg/ml streptomycin, 10 µg/ml insulin-transferrin-selenium, 0.5 IU/ml human recombinant follicle stimulating hormone, with or without 20 µM LPA at 37˚C in humidified chamber with 5% CO_2 (24). Some of these cultured ovarian fragments were used for histological evaluation, follicular counting and molecular analysis before transplantation (n=30 for each group) and the others were transplanted into γ-irradiated mice (n=30 for each group).

γ-irradiated mice preparation and xenotransplantation of human ovarian tissue

The 8-weeks-old NMRI female mice (n=30 mice for each group) were each given a single dose of 7.5 Gy whole body γ-irradiation for 6 minutes (Theratron 780C, Canada). For human ovarian tissue transplantation, the mice were anesthetized by an intra-peritoneal injection of ketamine 10% (75 mg/kg body weight) and xylazine 2% (15 mg/kg) and their back muscles were bilaterally exposed (25). Each tissue fragment that was derived from either LPA-treated or non-treated groups was individually inserted and stitched within each muscle (two ovarian fragments for each mouse), and the wound was sutured. The mice were sacrificed 14 days after transplantation and the recovered tissues were randomly fixed for histological and immunohistochemical analyses (n=15 tissue fragments for each group) or kept at -80˚C for molecular studies (n=15 tissue fragments in each group for triplicates).

Histological evaluation

For the light microscopic study, the fresh (n=5 fragment), vitrified-warmed (n=5 fragment), LPA-treated and non-treated human ovarian fragments before (n=15 fragments for each group) and after transplantation (n=15 fragments for each group) were fixed in Bouin's solution and embedded in paraffin wax. Tissue sections were prepared serially at 5 µm thickness and every 10th section was stained with H&E and observed under a light microscope (near 15-20 sections per each fragment). Another set of tissue sections was prepared for immunohistochemistry.

The follicle classification criteria included: those containing an intact oocyte as well as granulosa cells (normal), those containing pyknotic oocyte nuclei or disorganized granulosa cells (degenerated), those containing only a single layer of flattened granulosa cells (primordial), those with cuboidal granulosa cells in a single layer (primary), and finally those with two or more layers of granulosa cells (growing follicles).

Immunohistochemical staining for BAX

The expression of pro-apoptotic protein BAX in transplanted LPA-treated and non-treated ovarian tissue was confirmed by immunohistochemistry. After paraffin

removal, antigen retrieval was performed by boiling the tissue sections in citrate buffer (10 mM, pH=6) in a microwave oven for 10 minutes at 700 W. Then they were cooled at room temperature and washed in phosphate buffer saline (PBS). The tissue sections were separately incubated in rabbit polyclonal immunoglobulin G (IgG) anti-BAX antibody (SC-493, 1: 100) (Santa Cruz Biotechnology, UK) at 4˚C overnight, then were washed three times in PBS. Then they were incubated with a secondary goat anti-rabbit IgG antibody conjugated with fluorescein isothiocyanate (FITC) (Ab 6721, 1:100, Abcam, UK) diluted in PBS for 2 hours at 37˚C. Tissue sections from adult mouse ovaries were used as positive controls and were stained according to the same protocol. The samples were analyzed under fluorescent microscope (Ziess, Germany).

RNA extraction and cDNA synthesis

Total RNA was extracted from LPA-treated and non-treated ovarian tissue fragments before (n=15 in each group in three repeats) and after (n=15 in each group in three repeats) grafting, using Trizol reagent (Invitrogen, UK) and according to the manufacturer's protocol. The RNA samples were treated with DNase prior to proceeding with the cDNA synthesis. RNA concentration was measured by spectrophotometry. The cDNA synthesis was performed using a commercial Kit (Thermo Scientific, EU) at 42˚C for 60 minutes and the reaction was terminated by heating the samples at 70˚C for 5 minutes. The obtained cDNA was stored at -80˚C until utilized.

Real-time revers transcription polymerase chain reaction

Primers for the apoptosis-related genes, *BAX* and *BCL2*, and housekeeping *β-actin* (Table 1) were designed using the online primer3 software. One-step RT-PCR was performed on the Applied Biosystems (UK) real-time thermal cycler according to QuantiTect SYBR Green RT-PCR kit (Applied Biosystems, UK, Lot No: 1201416). Real-time thermal cycling conditions were set up as follows: holding step at 95˚C for 5 minutes, cycling step at 95˚C for 15 seconds, 60˚C for 30 seconds and it was continued by a melt curve step at 95˚C for 15 seconds, 60˚C for 1 minutes, and 95˚C for 15 seconds. Then, relative quantification of the target genes to housekeeping gene (*β-actin*) was determined by Pfaffl method. The non-template negative control sample was included in each run. These experiments were repeated at least three times.

Statistical analysis

All experiments were repeated in triplicates. All data were presented as mean ± SD and were analyzed, using one-way ANOVA and post hoc Duncan's Multiple Range Test. Statistical analysis was performed with the SPSS 19.0 (Chicago, IL, USA). A $P<0.05$ was considered statistically significant.

Results

Histological observation

The normal morphology of human ovarian tissue after vitrification-warming in comparison to a fresh sample is presented in Figure 1 A and B. As shown in this Figure, the structure of tissue is cryopreserved well and no significant damage is seen in the follicles or stromal cells.

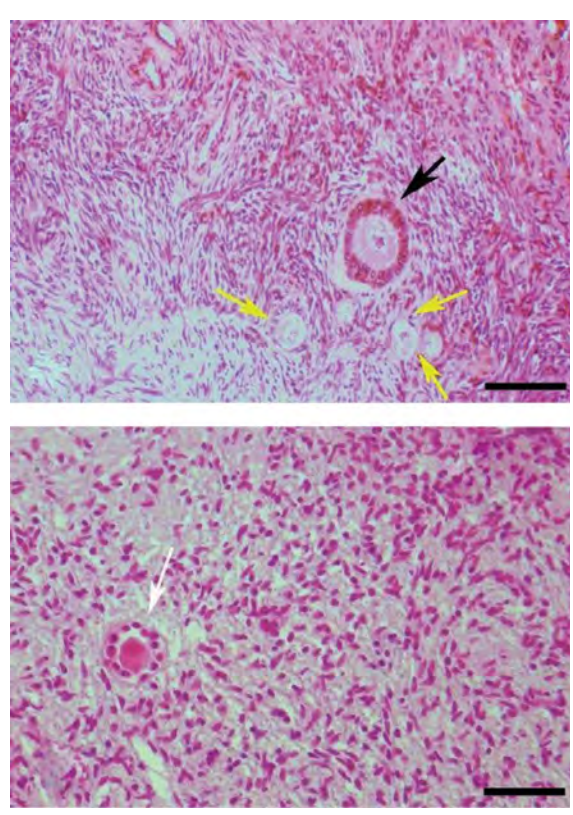

Fig.1: Light microscopic observation of fresh and vitrified human ovarian tissue using hematoxylin and eosin. **A.** The morphology of human ovarian tissue were demonstrated in fresh (scale bar: 60 µm) and **B.** Vitrified-warmed groups (scale bar: 30 µm). The normal primordial (yellow arrows), primary (white arrow) and growing follicles (black arrow) are seen.

Table 1: The characteristics of primers used for the the real time revers transcription polymerase chain reaction

Target gene	Primer sequence (5´-3´)	Accession number	Product size (bp)
BCL2	F: TTGCTTTACGTGGCCTGTTTC	NM_000018.9	94
	R: GAAGACCCTGAAGGACAGCCAT		
BAX	F: CCCGAGAGGTCTTTTTCCGAG	NM_000019.9	155
	R: CCAGCCCATGATGGTTCTGAT		
β-actin	F: TCAGAGCAAGAGAGGCATCC	NM_001101.3	187
	R: GGTCATCTTCTCACGGTTGG		

The light microscopic observations of LPA-treated and non-treated human ovarian fragments after 24 hours of IVC are illustrated in Figure 2 A-D. The normal morphology of the growing follicles with central oocytes are seen and the oocytes are in close contact with the surrounding granulosa cells. Two weeks after grafting, the primordial, primary and growing follicles are detected in tissue sections (Fig.2E-H), however, the detachment between the oocyte and granulosa cells are observed in some follicles in non-treated grafted ovarian sections (Fig.2F).

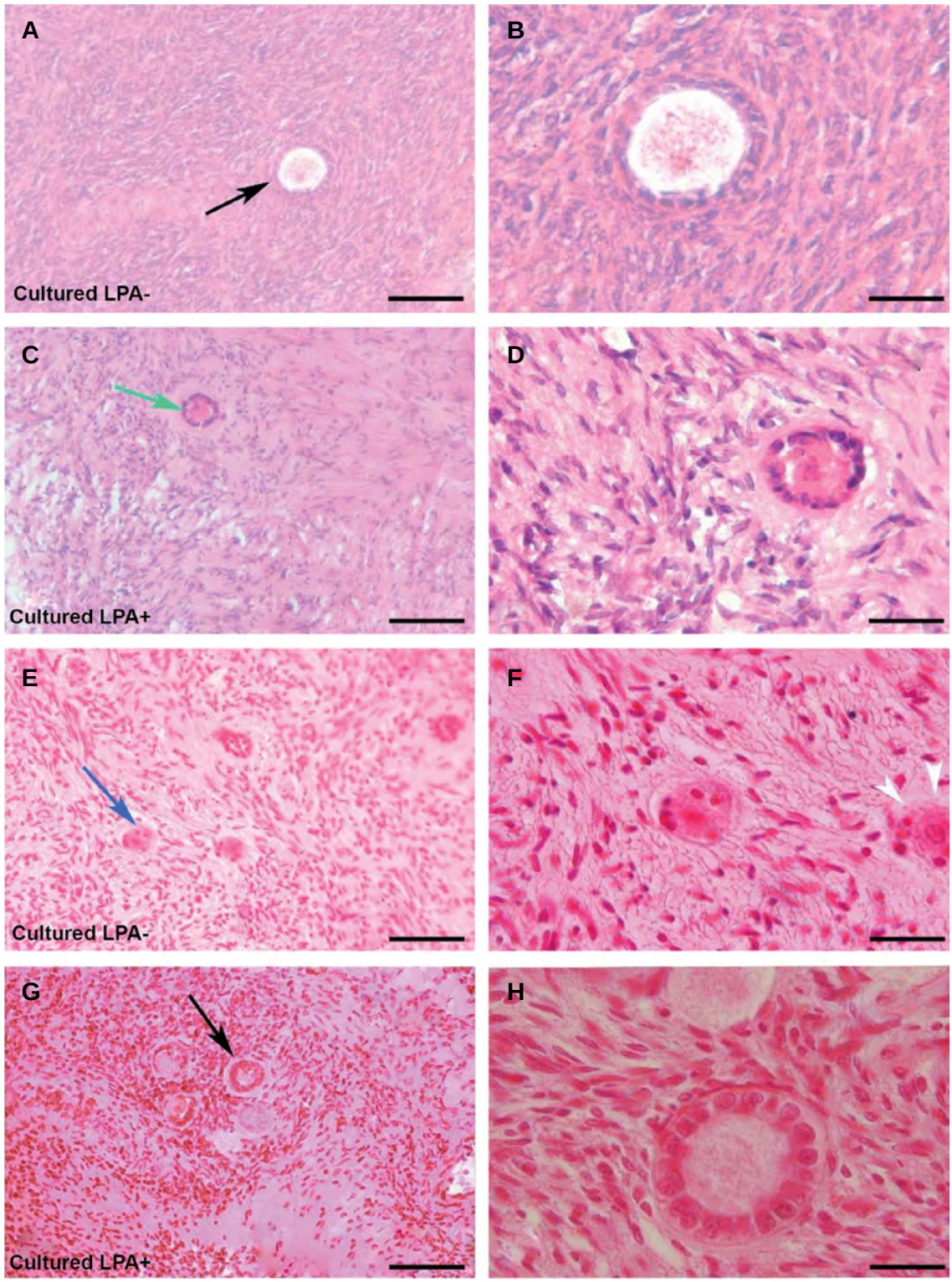

Fig.2: Light microscopic images of the cultured human ovarian tissue and xenografted tissue using hematoxylin and eosin staining. The micrograph of cultured tissues before transplantation **A, B.** In non-treated group and **C, D.** In LPA-treated group. The morphology of tissues after transplantation **E, F.** In non-treated group and **G, H.** In LPA-treated group. The images in the second panel are showing high magnifications of the first panel. The morphology of normal primordial follicles (blue arrows), primary follicle (green arrow) and growing follicle (black arrow) are shown. The white arrow head shows detachment of the follicular cells in the non-treated group after grafting (scale bar: A, C, E, G: 30 µm, B, D, F, H: 20 µm).

The percent of normal follicles in the study groups

The proportion of the follicles at different developmental stages in our study groups is summarized in Table 2. After 24 hours into the cultures of ovarian fragments, the number of normal follicles in the LPA-treated group is significantly higher than those in the not-treated group [88.01 ± 2.62% vs. 81.72 ± 2.31% ($P<0.05$)]. Moreover, 14 days after transplantation, in the LPA-treated group 91.62 ± 0.70% of the follicles presented normal morphology, which was significantly higher ($P<0.05$) than that in the non-treated group (87.97 ± 1.61%).

The percentage of follicles at different developmental stages in study groups

The proportion of the follicles at different developmental stages in all experimental groups are compared and presented in Table 2. The percentage of the primordial follicles in non-treated cultures as well as LPA-treated groups prior to transplantation are 41.78 ± 4.61% and 42.49 ± 1.13%, respectively. Following transplantation the non-treated and treated groups decline significantly to 30.46 ± 6.86 and 21-17 ± 6.01, respectively ($P<0.05$). However, this post-transplantation percentage is significantly lower in the LPA-treated group compared to the non-treated group ($P<0.05$). There is no significant difference between the percentages of the primary follicles in the two study groups (Table 2).

The total percentages of the growing follicles in the LPA-treated group and the non-treated group prior to transplantation are 20.17 ± 2.39 and 19.49 ± 1.65, and are increased after transplantation to 40.95 ± 2.11 and 29.44 ± 1.39, respectively ($P<0.05$). This difference is significantly higher in the LPA-treated group compared to the non-treated group ($P<0.05$, Table 2).

Immunohistochemistry

The representative images of BAX immunohistochemistry in both transplanted ovarian tissue and positive tissue section as control are shown in Figure 3A-C. In spite of the presence of several BAX-positive cells (white arrow) in the follicular and stromal cells of the adult mouse ovarian tissue as positive control (Fig.3C), no other positive labeling for BAX was observed in the follicles and oocytes in neither transplanted ovarian group.

Expression of apoptosis-related genes in studied groups

The expression ratio of *BAX* and *BCL2* genes to the housekeeping gene (*β-actin*) in both study groups is shown in Figure 4. Our results indicate that, the expression ratio of the *BAX* gene in the LPA-treated group is significantly lower than that in the non-treated group ($P<0.05$) both before and after grafting. Nonetheless, the level of *BCL2* gene expression is significantly higher in the LPA-treated group compared to the non-treated ovarian tissue ($P<0.05$) before grafting (Fig.4A, B) also the same result was obtained after grafting ($P<0.05$). Also, the ratio of *BAX* to *BCL2* expression in the LPA-treated group is significantly less than that in the non-treated ovarian tissue ($P<0.05$, Fig.4C).

Table 2: The number of follicles at different developmental stages in all groups of study

Groups (vitrified-ovarian tissue)	Total number of F.	Number of normal F.	Number of degenerated F.	Number of primordial F.	Number of primary F.	Number of growing F.
Cultured-LPA$^-$	90	73 (81.72 ± 2.31)	17 (18.28 ± 0.99)	30 (41.78 ± 4.61)	29 (38.73 ± 4.68)	14 (19.49 ±1.65)
Cultured-LPA$^+$	134	119 (88.01 ± 2.62)^a	15 (11.99 ± 2.62)^a	51 (42.49 ± 1.13)	43 (37.34 ± 3.46)	25 (20.17 ± 2.39)
Cultured-grafted-LPA$^-$	258	227 (87.92 ± 1.61)^a	31 (12.08 ± 1.61)^a	71 (30.46 ± 6.86)^a	90 (40.46 ± 7.49)	67 (29.44 ± 1.39)^a
Cultured-grafted-LPA$^+$	223	204 (91.62 ± 0.70)^{b,c}	19 (8.38 ± 0.70)^{b,c}	41 (21.17 ± 6.01)^c	80 (38.44 ± 4.40)	84 (40.95 ± 2.11)^{b,c}

LPA; Lysophosphatidic acid, F; Follicle, ^{a}; Significant difference with cultured-LPA$^-$ (without LPA) group in the same column ($P<0.05$), ^{b}; Significant differences with cultured-LPA$^+$ (with LPA) group in the same column ($P<0.05$), and ^{c}; Significant differences with cultured-grafted- LPA$^-$ (without LPA) group in the same column ($P<0.05$). The number of follicles at different developmental stages was calculated according to the total number of normal follicles. Data are presented as %mean ± SD.

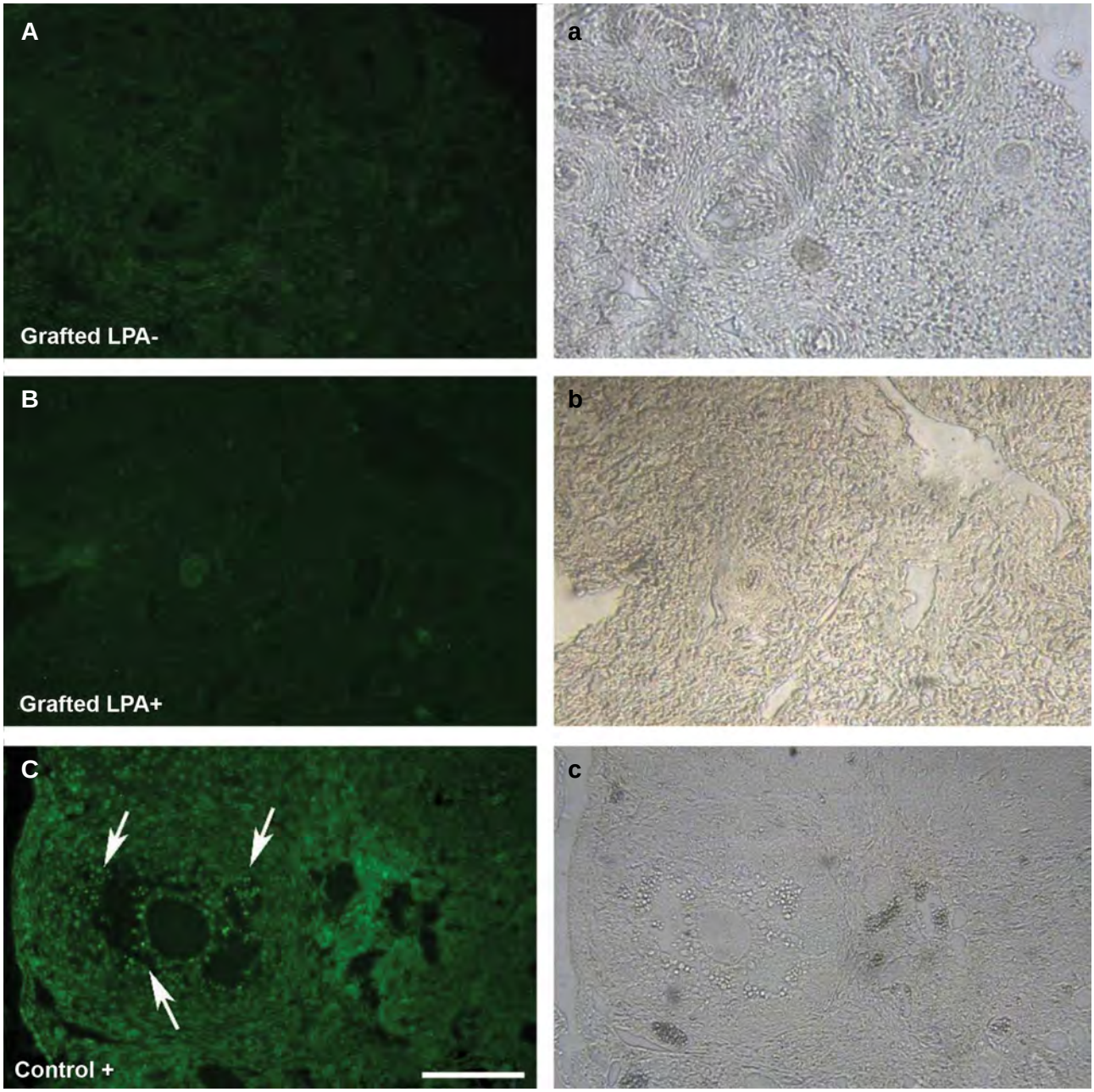

Fig.3: The images of immunohistochemistry of BAX in studied groups. Representative figures of immunostained cells **A, a.** In non-treated group, **B, b.** LPA-treated group after transplantation were demonstrated, and **C, c.** Adult mouse ovarian tissue served as the positive control. White arrows show the BAX-positive cells. The left panel show the phase contrast of the images in the right panel (scale bar: 100 µm). LPA; Lysophosphatidic acid.

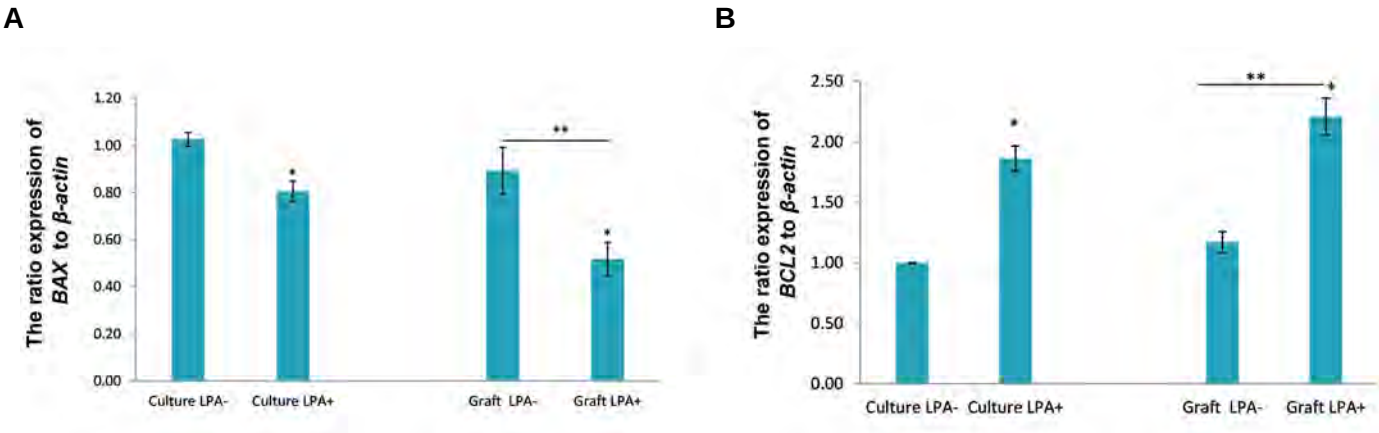

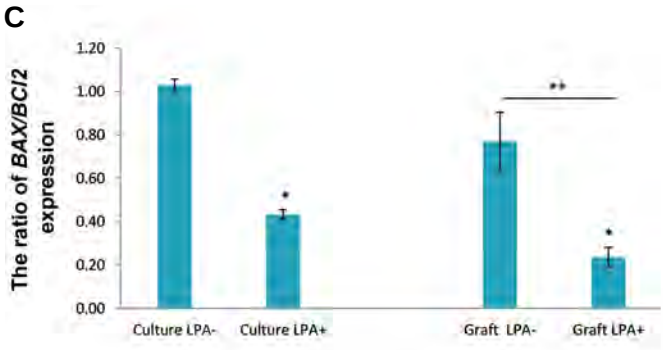

Fig.4: The comparison of the expression ratio of pro-apoptotic and anti-apoptotic genes in studied group. The expression of **A.** *BAX* and **B.** *BCl2* genes to the housekeeping gene (*β-actin*) and the ratio of *BAX/BCL2* expression were presented. LPA; Lysophosphatidic acid, *; Significant difference with the non-treated groups (LPA^-) (P<0.05), and **; Significant differences of both transplanted groups with respected non-transplanted groups (P<0.05).

Discussion

This is to our knowledge the first report to evaluate the effect of LPA on the improvement of development and survival of human ovarian follicles after IVC as well as transplantation of ovarian tissue. Our morphological observations indicate an enhancement in the rate of normal follicles and a decrease in the percentage of degenerated follicles in the LPA-treated group in comparison to the non-treated group. This result shows the beneficial effects of LPA on the preservation of the follicles within the human ovarian tissues during an IVC period and following transplantation. These effects of LPA may be related to its function as an anti-apoptotic factor (17, 21-23). Apoptosis take places within the ovarian cells through two main pathways, including the activation of caspase 8, and the mitochondrial pathway that is controlled by BAX and BCL2 as regulatory proteins (26-28). In agreement with our morphological analysis, immunohistochemical staining showed very low number of BAX positive cells in the transplanted groups, especially in the LPA-treated group. According to the literature, the anti-apoptotic effects of LPA on oocyte, granulosa cells, ovarian cancer cells and corpus luteum are documented (17, 21, 23, 27). In the study by Rapizzi et al. (29) it was shown that LPA induced migration and survival in the cervical cancer cells line, HeLa cells. Similarly, in the bovine corpus luteum, it was demonstrated that LPA inhibited the expression of BAX, therefore contributing to the survival of the cells (23). Sinderewicz et al. (19) and Boruszewska et al. (30) demonstrated that in healthy bovine follicles, LPA interacts with estradiol to stimulate the anti-apoptotic processes of granulosa cells.

In addition, molecular analysis in the present study revealed a significantly higher expression of *BCL2* and lower expression of *BAX* in the LPA-treated group in comparison with the non-treated group. Moreover, we found a significantly lower *BAX/BCL2* ratio in the LPA-treated group compared to the non-treated ones. As *BCL2* and *BAX* have been detected in the granulosa cells, it has been suggested that follicular viability and development may depend on a low level of pro-apoptotic gene expression, which prevents cell death within ovarian tissue.

In agreement to our observations, in the study by Zhang et al. (18) the authors have shown that exposure of blastocyst culture media to LPA reduces the expression of the pro-apoptotic genes, while increasings the expression of anti-apoptotic genes. Similar results were obtained by Boruszewska et al. (17) in their study on bovine oocyte.

Our current data demonstrates that LPA could enhance the follicular growth and development, as the culture media used in our study seems to support the activation and development of growing follicles. The growth of follicles depends mainly on proliferation rate of the granulosa cells. It is proposed that LPA could be involved in proliferation and growth of the follicles directly via its receptors, or indirectly by stimulation of some other factors (16-22). In agreement with these suggestions, it has been previously revealed that in the mitogenic effects of LPA on ovarian, tumor, and amniotic cells, mitogen-activated protein kinase (MAPK)/p38 and phosphoinositol 3-kinase (PI3K)/Akt pathways are involved (31-33). Kim et al. (31) also have found that LPA modulates cellular activity and stimulates proliferation of human amnion cells *in vitro*. These authors also proposed that the LPA produced in leiomyoma may be involved in tumor cell proliferation.

With regard of another suggestion that was well demonstrated previously by Boruszewska et al. (30), it is possible that LPA alone or LPA together with follicle stimulating hormone induced estradiol (E2) are byproducts of *in vitro* cultures of bovine granulosa cells. Thus, the secretion of these hormones causes an increase in the expression of the follicle stimulating hormone receptor and 17β –Hydroxysteroid dehydrogenase (*HSD)* genes that are involved in follicular growth and development. Our results are in agreement with that reported by Abedpour et al. (22, 24), who stated that LPA can improve the developmental and maturational rates of the follicles in cultured mouse ovarian tissue. Related reports show that LPA plays a significant role in activation of the primordial follicles and improves nuclear and cytoplasmic maturation of mouse oocytes via its receptors (33). In 2015 Zhang et al. (18) performed a similar study and demonstrated that LPA had beneficial effects on porcine cytoplasmic oocyte maturation. The work by Boruszewska et al. (17) also revealed that supplementation of bovine oocyte maturation media with LPA increased expression of some oocyte developmental genes such as growth differentiation factor 9 *(GDF9)* and follistatin *(FST)* transcripts. Hwang et al. (34) by treatment of porcine oocytes during *in vitro* maturation with different concentrations of LPA showed that 30 μM LPA promotes and enhances cumulus cell expansion and oocyte nuclear and cytoplasmic maturation, and reduces

the intracellular reactive oxygen species level.

In contrast to our current report, in our previous study we had grafted the vitrified human ovarian tissue, and the rate of normal follicles was significantly decreased in the vitrified grafted tissues. In the present study, however, the tissue was cultured for 24 hours prior to transplantation. It is suggested that during the time of cultivation, especially in the presence of LPA, the harmful effects of cryopreservation are recovered to some extent. In a published study by Rahimi et al. (35), similar to our groups, they observed a higher incidence of apoptosis in grafted vitrified ovarian tissue samples without any supplementary factors added to the transplanted tissue. To prove this suggestion additional assessments are needs.

Moreover, our observations showed the percentage of normal follicles was higher in both transplanted groups compared to their respected non-transplanted tissues at the end of the culture period. An explanation for this result is that in spite of degeneration of some follicles due to ischemia in the grafted tissue, these damaged follicles were disappeared during these two weeks following engraftment. It seems that the total number of the follicles may decline per each tissue section (was not calculated), while we have analyzed the ratio of normal follicles in comparison to the total number of the counted ones.

Conclusion

Supplementation of human ovarian tissue culture media with LPA could improve the follicular survival and development by promoting an anti-apoptotic balance in transcription of *BCL2* and *BAX* genes, leading to increased cell survival.

Acknowledgements

This work was supported by grants from Tarbiat Modarres University and Iran National Science Foundation (97s/3489). The authors have no conflicts of interest relevant to this article.

Authors' Contribution

Z.M.; Performed the experiments, analyzed the data and contributed to writing the manuscript. M.S.; Supervised the study and contributed to doing the experiments, data analysis and writing the manuscript. N.H.R., K.P.; Contributed to designing of the study and project development. All authors read and approved the final manuscript.

References

1. Fisch B, Abir R. Female fertility preservation: past, present and future. Reproduction. 2018; 156(1): F11-F27.
2. Shi Q, Xie Y, Wang Y, Li S.Vitrification versus slow freezing for human ovarian tissue cryopreservation: a systematic review and meta-anlaysis. Sci Rep. 2017; 7(1): 8538.
3. Ramezani M, Salehnia M, Jafarabadi M. Vitrification and in vitro culture had no adverse effect on the follicular development and gene expression of stimulated human ovarian tissue. J Obstet Gynaecol Res. 2018; 44(3): 474-487.
4. Dittrich R, Lotz L, Fehm T, Krüssel J, von Wolff M, Toth B, et al. Xenotransplantation of cryopreserved human ovarian tissue--a systematic review of MII oocyte maturation and discussion of it as a realistic option for restoring fertility after cancer treatment. Fertil Steril. 2015; 103(6): 1557-1565.
5. Rahimi G, Isachenko E, Sauer H, Isachenko V, Wartenberg M, Hescheler J, et al. Effect of different vitrification protocols for human ovarian tissue on reactive oxygen species and apoptosis. Reprod Fertil Dev. 2003; 15(6): 343-349.
6. Salehnia M, Sheikhi M, Pourbeiranvand S, Lundqvist M. Apoptosis of human ovarian tissue is not increased by either vitrification or rapid cooling. Reprod Biomed Online. 2012; 25(5): 492-499.
7. Abdollahi M, Salehnia M, Salehpour S, Ghorbanmehr N. Human ovarian tissue vitrification/warming has minor effect on the expression of apoptosis-related genes. Iran Biomed J. 2013; 17(4): 179-186.
8. Ramezani M, Salehnia M, Jafarabadi M. Short term culture of vitrified human ovarian cortical tissue to assess the cryopreservation outcome: molecular and morphological analysis. J Reprod Infertil. 2017; 18(1): 162-171.
9. Donfack NJ, Alves KA, Araújo VR, Cordova A, Figueiredo JR, Smitz J, et al. Expectations and limitations of ovarian tissue transplantation. Zygote. 2017; 25(4): 391-403.
10. Kedem A, Fisch B, Garor R, Ben-Zaken A, Gizunterman T, Felz C, et al.. Growth differentiating factor 9 (GDF9) and bone morphogenetic protein 15 both activate development of human primordial follicles in vitro, with seemingly more beneficial effects of GDF9. J Clin Endocrinol Metab. 2011; 96(8): E1246-E1254.
11. Kang BJ, Wang Y, Zhang L, Li SW. Basic fibroblast growth factor improved angiogenesis of vitrified human ovarian tissues after in vitro culture and xenotransplantation. Cryo Letters. 2017; 38(3): 194-201.
12. Kang BJ, Wang Y, Zhang L, Xiao Z, Li SW. bFGF and VEGF improve the quality of vitrified-thawed human ovarian tissues after xenotransplantation to SCID mice. J Assist Reprod Genet. 2016; 33(2): 281-289.
13. Fransolet M, Noël L, Henry L, Labied S, Blacher S, Nisolle M, et al. Evaluation of Z-VAD-FMK as an anti-apoptotic drug to prevent granulosa cell apoptosis and follicular death after human ovarian tissue transplantation. J Assist Reprod Genet. 2019; 36(2): 349-359.
14. Ye X. Lysophospholipid signaling in the function and pathology of the reproductive system. Hum Reprod Update. 2008; 14(5): 519-536.
15. Sheng X, Yung YC, Chen A, Chun J. Lysophosphatidic acid signalling in development. Development. 2015; 142(8): 1390-1395.
16. Sinderewicz E, Grycmacher K, Boruszewska D, Kowalczyk-Zięba I, Staszkiewicz-Chodor J, et al. Expression of genes for enzymes synthesizing lysophosphatidic acid, its receptors and follicle developmental factors derived from the cumulus-oocyte complex is dependent on the ovarian follicle type in cows. Anim Reprod Sci. 2018; 192: 242-250.
17. Boruszewska D, Torres AC, Kowalczyk-Zieba I, Diniz P, Batista M, Lopes-da-Costa L, et al. The effect of lysophosphatidic acid during in vitro maturation of bovine oocytes: embryonic development and mRNA abundances of genes involved in apoptosis and oocyte competence. Mediators Inflamm. 2014; 670670.
18. Zhang JY, Jiang Y, Lin T, Kang JW, Lee JE, Jin DI. Lysophosphatidic acid improves porcine oocyte maturation and embryo development in vitro. Mol Reprod Dev. 2015; 82(1): 66-77.
19. Sinderewicz E, Grycmacher K, Boruszewska D, Kowalczyk-Zięba I, Staszkiewicz J, Ślężak T, et al. Bovine ovarian follicular growth and development correlate with lysophosphatidic acid expression. Theriogenology. 2018; 106: 1-14.
20. Sinderewicz E, Grycmacher K, Boruszewska D, Kowalczyk-Zięba I, Woclawek-Potocka I. Lysophosphatidic acid expression in theca cells depends on the type of bovine ovarian follicle. Reprod Domest Anim. 2017; 52(1): 28-34.
21. Sinderewicz E, Grycmacher K, Boruszewska D, Kowalczyk-Zięba I, Staszkiewicz J, Ślężak T, et al. Expression of factors involved in apoptosis and cell survival is correlated with enzymes synthesizing lysophosphatidic acid and its receptors in granulosa cells originating from different types of bovine ovarian follicles. Reprod Biol Endocrinol. 2017; 15(1): 72.
22. Abedpour N, Salehnia M, Ghorbanmehr N. The Effects of Lysophosphatidic Acid on the incidence of cell death in cultured vitrified and non-vitrified mouse ovarian tissue: separation of necrosis and apoptosis border. Cell J. 2018; 20(3): 403-411.
23. Kowalczyk-Zieba I, Boruszewska D, Saulnier-Blache JS, Lopes Da Costa L, Jankowska K, Skarzynski DJ, et al. Lysophosphatidic acid

action in the bovine corpus luteum -an in vitro study. J Reprod Dev. 2012; 58(6): 661-671.
24. Abedpour N, Salehnia M, Ghorbanmehr N. Effect of lysophosphatidic acid on the follicular development and the expression of lysophosphatidic acid receptor genes during in vitro culture of mouse ovary. Vet Res Forum. 2018; 9(1): 59-66.
25. Jafarabadi M, Abdollahi M, Salehnia M. Assessment of vitrification outcome by xenotransplantation of ovarian cortex pieces in γ-irradiated mice: morphological and molecular analyses of apoptosis. J Assist Reprod Genet. 2015; 32(2): 195-205.
26. Brodowska A, Laszczyńska M, Starczewski A. Apoptosis in ovarian cells in postmenopausal women. Folia Histochem Cytobiol. 2007; 45(2): 99-98.
27. Tilly JL, Tilly KI, Kenton ML, Johnson AL. Expression of members of the bcl-2 gene family in the immature rat ovary: equine chorionic gonadotropin-mediated inhibition of granulosa cell apoptosis is associated with decreased bax and constitutive bcl-2 and bcl-xlong messenger ribonucleic acid levels. Endocrinology. 1995; 136(1): 232-241.
28. Tilly JL. Apoptosis and ovarian function. Rev Reprod. 1996; 1(3): 162-172.
29. Rapizzi E, Donati C, Cencetti F, Pinton P, Rizzuto R, Bruni P. Sphingosine 1-phosphate receptors modulate intracellular Ca2+ homeostasis. Biochem Biophys Res Commun. 2007; 353(2): 268-274.
30. Boruszewska D, Sinderewicz E, Kowalczyk-Zieba I, Skarzynski DJ, Woclawek-Potocka I. Influence of lysophosphatidic acid on estradiol production and follicle stimulating hormone action in bovine granulosa cells. Reprod Biol. 2013; 13(4): 344-347.
31. Kim JI, Jo EJ, Lee HY, Kang HK, Lee YN, Kwak JY, et al. Stimulation of early gene induction and cell proliferation by lysophosphatidic acid in human amnion-derived WISH cells: role of phospholipase D-mediated pathway. Biochem Pharmacol. 2004; 68(2): 333-340.
32. Fang X, Gaudette D, Furui T, Mao M, Estrella V, Eder A, et al. Lysophospholipid growth factors in the initiation, progression, metastases, and management of ovarian cancer. Ann N Y Acad Sci. 2000; 905: 188-208.
33. Jo JW, Jee BC, Suh CS, Kim SH. Addition of lysophosphatidic acid to mouse oocyte maturation media can enhance fertilization and developmental competence. Hum Reprod. 2014; 29(2): 234-241
34. Hwang SU, Kim KJ, Kim E, Yoon JD, Park KM, Jin M, et al. Lysophosphatidic acid increases in vitro maturation efficiency via uPA-uPAR signaling pathway in cumulus cells. Theriogenology. 2018; 113: 197-207.
35. Rahimi G, Isachenko E, Isachenko V, Sauer H, Wartenberg M, Tawadros S, et al. Comparison of necrosis in human ovarian tissue after conventional slow freezing or vitrification and transplantation in ovariectomized SCID mice. Reprod Biomed Online. 2004; 9(2): 187-193.

Original Article

Quality of Blastocysts Created by Embryo Splitting: A Time-Lapse Monitoring and Chromosomal Aneuploidy Study

Marjan Omidi, Ph.D.[1], Mohammad Ali Khalili, Ph.D.[1, 2*], Iman Halvaei, Ph.D.[3], Fatemeh Montazeri, Ph.D.[4], Seyed Mehdi Kalantar, Ph.D.[4]

1. Research and Clinical Center for Infertility, Yazd Reproductive Sciences Institute, Shahid Sadoughi University of Medical Sciences, Yazd, Iran
2. Department of Reproductive Biology, Shahid Sadoughi University of Medical Sciences, Yazd, Iran
3. Department of Anatomical Sciences, Faculty of Medical Sciences, Tarbiat Modares University, Tehran, Iran
4. Abortion Research Center, Yazd Institute of Reproductive Sciences, Shahid Sadoughi University of Medical Sciences, Yazd, Iran

Corresponding Address: P.O.Box: 89195-999, Research and Clinical Center for Infertility, Yazd Reproductive Sciences Institute, Shahid Sadoughi University of Medical Sciences, Yazd, Iran
Email: khalili59@hotmail.com

Received: 1/February/2019, Accepted: 20/April/2019

Abstract

Objective: The aim of this study was to screen the potential of human embryos to develop into expanding blastocysts following *in vitro* embryo splitting and then assess the quality of the generated blastocysts based on chromosomal characteristics and using morphokinetics.

Materials and Methods: In this experimental study, a total of 82 good quality cleavage-stage donated embryos (8-14 cells) were used (24 embryos were cultured to the blastocyst stage as controls and 58 embryos underwent *in vitro* splitting). After *in vitro* splitting, the blastomere donor and blastomere recipient embryos were named twin A and twin B, respectively. Morphokinetics and morphological parameters were evaluated using a time-lapse system in the blastocysts developed from twin embryos. Aneuploidy of chromosomes 13, 15, 16, 18, 21, 22, X and Y were analyzed in the twin blastocysts.

Results: Following *in vitro* splitting, of the 116 resulting twin embryos, 80 (69%) developed to the expanded blastocyst (EBL) stage compared to 21 (87.5%) embryos in the control group (P>0.05). The morphokinetics analysis suggested that the developmental time-points were influenced by the *in vitro* splitting. Moreover, the blastocysts developed from A and B twins had impaired morphology compared to controls. Regarding chromosome abnormalities, there was no significant difference in the rate of aneuploidy or mosaicism between the different groups.

Conclusion: This study showed that while no chromosomal abnormalities were seen, *in vitro* embryo splitting may affect the embryo morphokinetics.

Keywords: Aneuploidy, Blastocyst, Mosaicism, Time-Lapse

Cell Journal(Yakhteh), Vol 22, No 3, October-December (Autumn) 2020, Pages: 367-374

Citation: **Omidi M, Khalili MA, Halvaei I, Montazeri F, Kalantar SM. Quality of blastocysts created by embryo splitting: a time-lapse monitoring and chromosomal aneuploidy study. Cell J. 2020; 22(3): 367-374. doi: 10.22074/cellj.2020.6717.**

Introduction

Identical twins resulting from natural splitting of human embryos are accepted by society which are comparable with non-identical twins. Successful pregnancies following *in vitro* embryo splitting have been established in large animals, including sheep (1), cattle (2), horses (3) and pigs (4). The first attempt at *in vitro* human embryo splitting was carried out by Hall et al. (5) in 1993. In their study, the polyploid cleaved embryos underwent *in vitro* splitting and grew to the 32-cell stage. Later, efforts on *in vitro* human embryo splitting resulted in blastocysts which were morphologically suitable for clinical usage such as for "low responders" (6-8).

Successful pregnancy and live birth of healthy animals as well as morphologically normal adequate human blastocysts following *in vitro* embryo splitting increased the possibility of applying this method to infertile couples. However, application of *in vitro* splitting in the clinic requires comprehensive validation of the derived twin embryos. Up to now, the majority of studies have investigated the developmental competence of twin embryos after *in vitro* splitting and the data regarding cellular and molecular assessments in these embryos are very limited (6-9). Recently, Noli and colleagues showed that the majority of the cells in the twin blastocysts expressed inner cell mass (ICM) and trophectoderm (TE) markers simultaneously (8). Later, the same group evaluated the effects of *in vitro* embryo splitting on the miRNA profile of their spent blastocyst medium (SBM). They found the SBM from twin embryos had a significant difference in the amount of miRNAs involved in implantation compared to euploid implanted blastocysts (10). Generally, despite the possible advantages of this method for infertile patients, there is controversy over its clinical use in published studies (11). In addition, the chromosomal state of developed blastocysts from *in vitro* splitting has not been evaluated yet. Time-lapse monitoring (TLM), as a novel technology can be useful for embryo quality assessments through the evaluation of embryo morphology and developmental kinetics (12). The main goal in this study was to analyze the chromosomal status combined with developmental competence using

TLM in human twin embryos created via *in vitro* splitting.

Materials and Methods

The embryos were donated without any financial incentive. Informed consent was obtained from each couple. The Ethical Committee of our institute approved this experimental study since the embryos would not be transferred to the uterus after experimental procedures (IR.SSU.MEDICINE.REC.1395.93).

Embryos

All day-2 or day-3 embryos were cryopreserved from 2011 to 2016 by vitrification using RapidVit™ Cleave kit (Vitrolife, Sweden). Donated embryos were warmed using RapidWarm™ Cleave kit (Vitrolife, Sweden) according to the manufacturer's instructions. The warmed embryos were cultured *in vitro* until development to at least the 8-cell stage. The inclusive embryos with symmetrical blastomeres and no fragmentation or <10% fragmentation were considered as good quality embryos (13).

Embryo micromanipulation and time-lapse monitoring

The good quality 8-14-cell embryos were pre-incubated in 5 µL microdroplets of Ca-Mg-free culture medium (PGD medium, Vitrolife, Sweden) prior to biopsy and covered with mineral oil for 3 minutes at 37˚C in order to facilitate the separation of blastomeres. A 1480 nm infrared diode laser (OCTAX Laser Shot®, MTG, Germany) was used to open a 35-40 µm diameter hole in the zona pellucida (ZP). Half of the blastomeres were taken out using a micropipette with a 30 µm inner diameter (Sunlight Medical, Jacksonville, FL, USA) regardless of the presence or absence of the nucleus. The biopsied blastomeres were then inserted one by one from donor embryos (twin A) into a previously prepared empty ZP to create the recipient embryos (twin B). In this study, the empty ZPs were derived from immature oocytes or discarded embryos (14). After *in vitro* splitting, both twin A and twin B embryos were carefully washed and cultured individually in nine-micro well primo vision plates (Vitrolife, Sweden) which were prepared with 40 µL of G-2™ PLUS media (Vitrolife, Sweden) overlaid with mineral oil and equilibrated overnight in a triple-gas incubator. Images were acquired in seven distinct focal planes every 10 minutes by a primovision time-lapse system (Vitrolife, Sweden). Intact embryos without manipulation (controls) were cultured and developed under the same conditions. Time-lapse images by the primovision system were used for the assessment of embryo development, timing of developmental events, blastocyst morphology and morphometry.

Morphokinetics analysis

The developmental stages after *in vitro* splitting used for morphokinetics parameters were: the existence of more than nine blastomeres (9+), formation of the morula or fully compacted embryo (Mor), the start of blastulation (SB), formation of the blastocyst (BL) and formation of the expanded blastocyst (EBL) (Fig.1). The duration of stages was calculated as follows: compaction (9+ to Mor), start of blastulation (Mor to SB), blastocyst formation (SB to BL) and blastocyst expansion (BL to EBL).

Morphology analysis

Blastocyst morphology was assessed using the images acquired from the time-lapse system. At the blastocyst stage, embryo quality was assessed based on Gardner's classification, which takes into account the expansion grade and the development of the ICM and TE (15). According to this classification, we defined three blastocyst quality classes for full and expanded blastocysts: A) good- (AA, AB, BA and BB), fair- (AC, CA, BC and CB) and poor-quality blastocysts (CC).

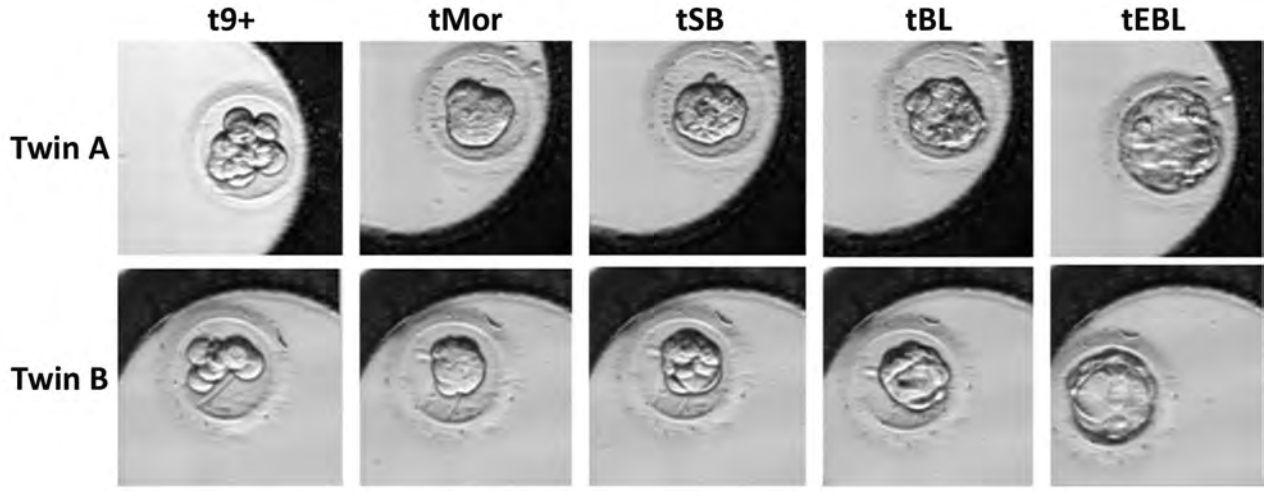

Fig.1: Developmental stages used for morphokinetic analyses using time-lapse monitoring compared between twin A and twin B.
9+; More than nine blastomeres, Mor; Morula or fully compacted embryo, SB; Start of blastulation, BL; Blastocyst, and EBL; Expanded blastocyst.

Morphometric analysis

The diameter (in micrometers) of the expanded blastocysts was measured by EmbryoViewer. The measurements were taken on the images of the blastocysts. The diameter of each blastocyst was calculated as the average of the distance between the outside borders of the TE measured in two directions (vertical and horizontal).

Cytogenetic screening procedures

Trophectoderm biopsy

Embryo biopsies were performed on a pre-warmed stage in a dish prepared with 5 µL droplets of HEPES buffered medium (G-MOPS, Vitrolife, Sweden) overlaid with pre-equilibrated mineral oil. The herniated TE cells were biopsied in the expanded blastocysts developed from A and B twins, through the previously created hole in the ZP. In the control embryos, a 10-20 µm hole was made in the ZP directly opposite the ICM of the blastocysts using a diode laser. Blastocysts were incubated for a further 4 hours to allow blastocoel expansion and herniation of the TE cells. After herniation, 5-10 TE cells were drawn into the biopsy pipette followed by laser-assisted cutting of the target cells.

Fixation

The biopsied TE cells were washed in a hypotonic solution (6 mg/mL bovine serum albumin in 0.1% sodium citrate), then placed in a hypotonic solution for 3 minutes. The TE cells were then placed on a prewashed (with 100% ethanol) microscope slide. After that, an aliquot of fixative (methanol: acetic acid, 3:1) was dropped onto the specimen. Air was then blown across the sample to evaporate the fixative (16).

Fluorescence *in situ* hybridization

The biopsied TE cells were fixed on glass slides as previously described (17). FISH assays of the fixed TE cells took place using two sequential hybridizations. The first hybridization contained probes for chromosomes 13, 18, 21, and X (MetaSystems, Altlussheim, Germany) and the second round was performed using probes for chromosomes 15, 16, 22, and Y (MetaSystems, Altlussheim, Germany). The prepared slides were examined under a fluorescence microscope (Olympus BX51, GSL-10 with BX61, Japan). Classification of embryos after FISH assay results was done according to the criteria published by f Delhanty et al. (18). In this classification, the embryos were categorized into four groups: normal, abnormal non-mosaic, diploid mosaic, and abnormal mosaic.

Statistical analysis

Statistical analysis was performed using SPSS (SPSS version 20, Chicago, IL) and/or GraphPadPrism (GraphPad Software, San Diego, CA, USA). The quantitative and qualitative data were presented as mean ± SD and percentages, respectively. The Shapiro-Wilk test was applied to evaluate the normal distribution of data. t test was used for independent samples and one-way ANOVA (followed by Tukey's test) as parametric and Mann-Whitney U and Kruskal-Wallis as nonparametric were used tests wherever appropriate. The chi-squared test was applied for comparison between qualitative data. $P<0.05$ was considered as significant.

Results

Developmental potential to expanding blastocyst is unaffected following embryo splitting

After warming, there were 82 good quality cleavage-stage embryos. Among these, 58 embryos were split into two groups: group 1 (n=37), including embryos with 8- 9 blastomeres; and group 2 (n=21), including embryos with 10-14 blastomeres. The remaining 24 embryos in the same condition were used as the controls. In general, from 116 resulting twin embryos, 80 (69%) of them were developed to the EBL stage compared to 21 (87.5%) embryos in the control group. Moreover, developmental potential of A and B twins was similar regardless of their groups (70.7% vs. 67.2%, P= 0.688). Furthermore, when comparing twin and control embryos, the number of starting blastomeres appeared to have no significant effect on them reaching each stage.

Next, we compared the developmental potential of the embryos of different origins i.e. control, twin A or twin B. Although overall more embryos in the group 2 were developed to each stage compared to group 1, the only significant difference was in the number of embryos reaching the SB stage between twin B embryos: 73% of embryos in group 1 versus 95.2% of embryos in group 2 (P= 0.038).

Dynamic pattern of twin embryos

Assessment and comparison of the developmental dynamics between twin and control embryos that reached the EBL stage was done regarding two parameters; time of reaching each stage and the duration between the stages. In comparing the time of reaching each stage, there was no significant difference between the control and twin embryos, except for time of reaching more than 9 blastomeres (t9+) in the group 1 (Fig.2A). The time these embryos took to get to this stage was significantly lower in the control embryos (9.80 ± 3.51 hours) compared to twins (twin A: 19.70 ± 7.05 hours and twin B: 20.54 ± 7.03 hours, $P<0.0001$). In a different way, regarding the origin, the differences between the embryos in groups 1 and 2 were significant for the time the embryos took to reach all developmental stages (Fig.2B).

Comparison of twins and control embryos did not reveal a pronounced rhythm in their developmental dynamics regards to the duration of critical stages in embryo development. Although some significant differences were found between twin and control embryos at the compaction and expansion stages (Fig.3A). A and B twins belonging to groups 1 and 2, did not differ in duration between the different stages (Fig.3B).

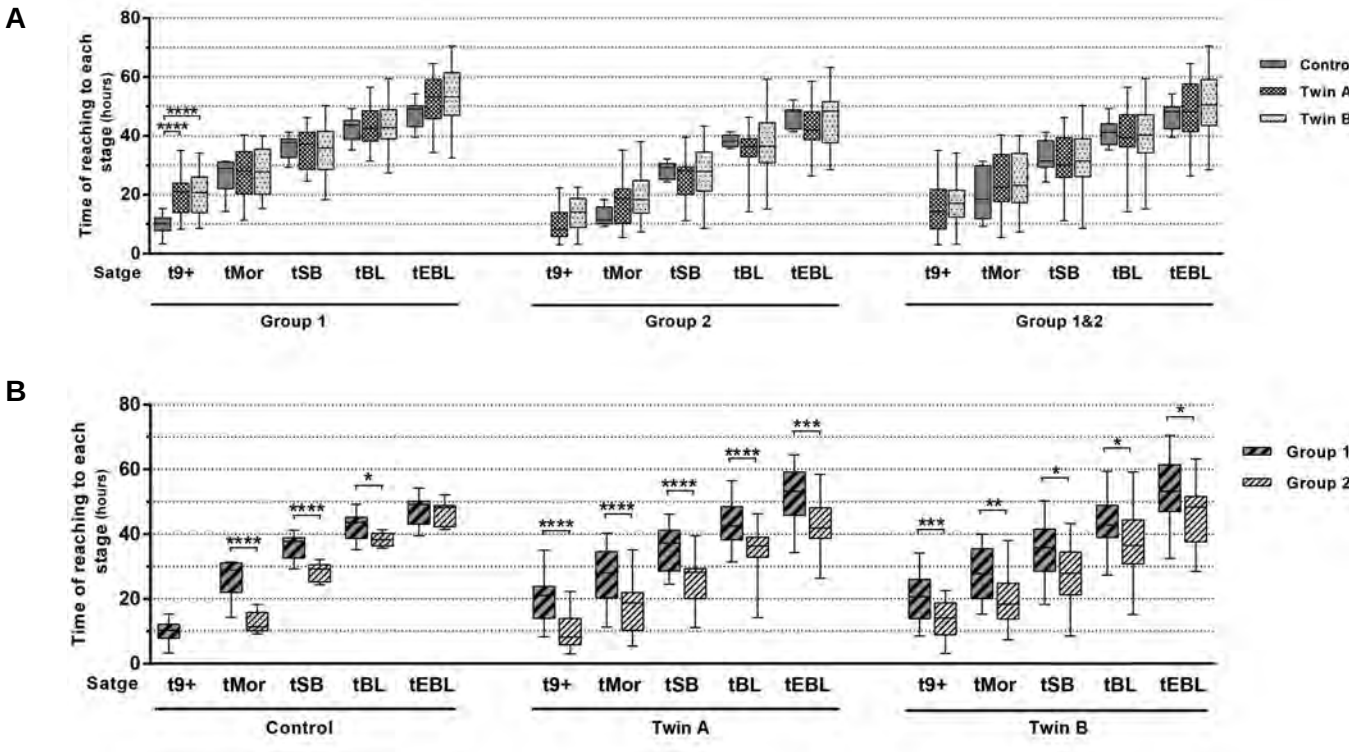

Fig.2: Developmental dynamics of twin embryos. **A.** The time of reaching each developmental stage for twin and control embryos within the group (group 1, 8-9 blastomeres and group 2, 10-14 blastomeres). **B.** Comparison of the time of reaching each developmental stage depending on the number of starting blastomeres in the control, twin A (donor blastomere) and twin B (recipient blastomere) embryos, separately.
9+; More than nine blastomeres, Mor; Morula or fully compacted embryo, SB; Start of blastulation, BL; Blastocyst, EBL; Expanded blastocyst, *; P≤0.05, **; P≤0.01, ***; P≤0.001, and ****; P≤0.0001.

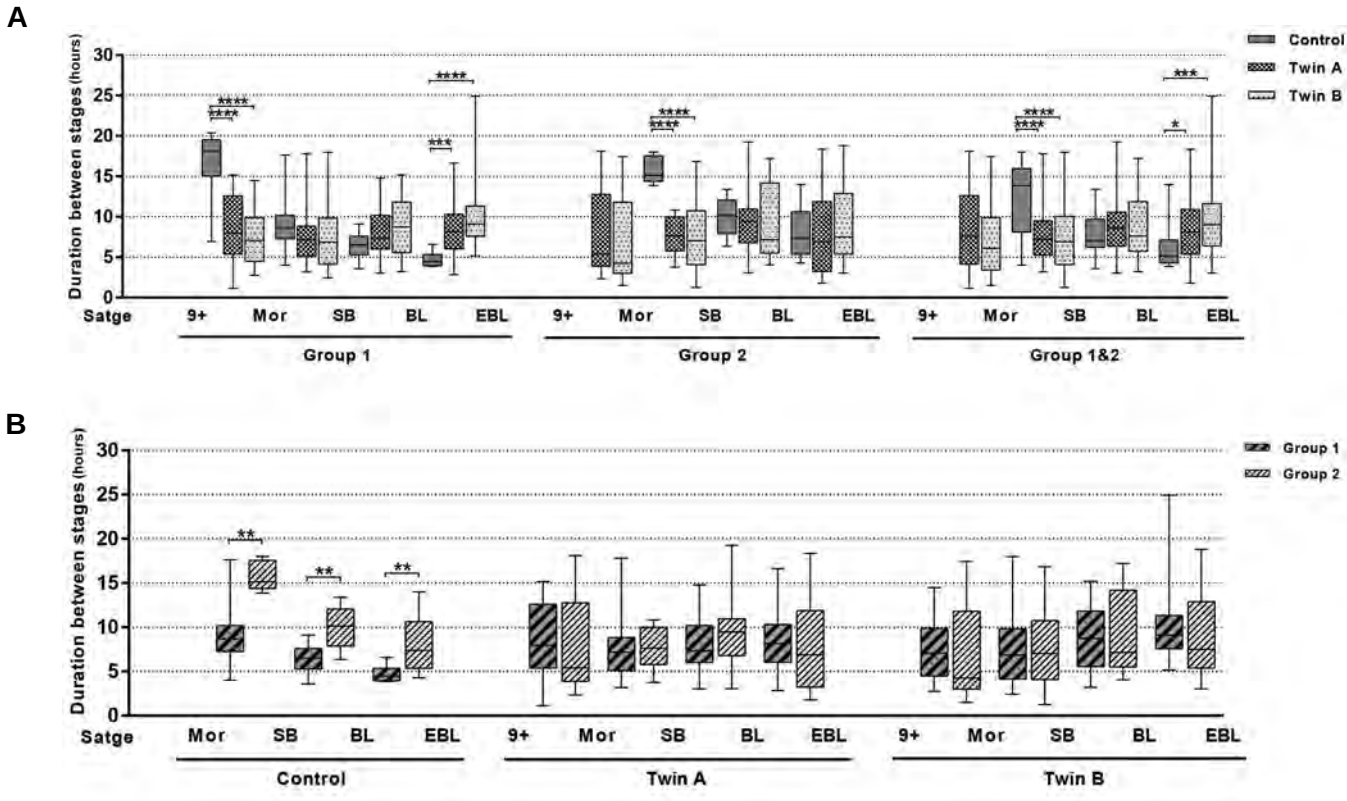

Fig.3: Developmental dynamics of twin embryos. **A.** Comparison of the duration between stages for twin and control embryos within the group (group 1, 8-9 blastomeres and group 2, 10-14 blastomeres). **B.** Comparison of the duration between stages depending on the number of starting blastomeres in the control, twin A (donor blastomere) and twin B (recipient blastomere) embryos, separately.
9+; More than nine blastomeres, Mor; Morula or fully compacted embryo, SB; Start of blastulation, BL; Blastocyst, EBL; Expanded blastocyst, *; P≤0.05, **; P≤0.01, ***; P≤0.001, and ****; P≤0.0001.

Blastocyst morphology and inner cell mass quality following splitting

The findings showed that the proportion of blastocysts with good morphology was significantly higher in the control group (71.4%) compared to A twins (39.6%, P=0.015) and B (28.6%, P=0.001). Although, the rate of fair quality embryos increased in the twins (A: 39.6% and B: 40.5%) after the splitting procedure compared to the control group (23.8%, Table 1). Furthermore, the sub-group analysis displayed an increased rate of grade C ICM and grade B TE in twin embryos (Table 1). Two (4.2%) ICMs in the twin A group were grade A. However, no grade A ICMs were noticed in the B twins.

Decreased size of blastocysts developed from twin embryos

Morphometric analysis showed a significant decrease in the overall size of twin expanded blastocysts compared to controls (mean ± SD (μm): 102.35 ± 5.19 vs. 120.92 ± 4.55, P<0.0001). Regardless of the number of starting blastomeres, the average diameter of blastocysts in A and B twins was 103.53 μm and 101.11 μm, respectively, whereas the average diameter for control embryos was 120.92 μm.

No significant difference in the prevalence of aneuploidy or mosaicism in twin embryos

As presented in Table 2, the aneuploidy prevalence of each chromosome was assessed in total cells of embryos (Fig.4). The blastocysts originated in all groups were similar in total abnormal cells (P=0.179). There was no significant difference between different groups regarding the rate of chaotic genomes (the cells with more than one chromosomal abnormality).

Next, we compared chromosomal abnormalities in the whole blastocysts developed from each group. Our data revealed no significant differences in the abnormality status between twins and control embryos (P=0.845). However, there was a statistically insignificant trend towards a decrease of normal embryos in twins (twin A: 60% and twin B: 57.1%) compared to the controls (71.4%, P>0.05).

Table 1: Morphology of the inner cell mass (ICM) and trophectoderm (TE) of blastocysts following *in vitro* splitting

Variables	Control n=21	Twin A n= 48	Twin B n=42	P value
ICM (%)				
A	9 (42.9)	2 (4.2)	0	<0.0001
B	8 (38.1)	18 (37.5)	14 (33.3)	
C	4 (19)	28 (58.3)	28 (66.7)	
TE (%)				<0.0001
A	16 (76.2)	12 (25)	8 (19)	
B	2 (9.5)	25 (52.1)	19 (45.2)	
C	3 (14.3)	11 (22.9)	15 (35.7)	

The values are presented as the number of embryos (%).

Table 2: Aneuploidy prevalence by chromosome

Chromosome	Control n=272	Twin A n= 502	Twin B n=482	P value
13	8 (2.9)	9 (1.8)	17 (3.5)	0.237
15	1 (0.4)	3 (0.6)	1 (0.2)	0.621
16	11 (4)	23 (4.6)	26 (5.4)	0.682
18	10 (3.7)	23 (4.6)	24 (5)	0.71
21	5 (1.8)	19 (3.8)	24 (5)	0.097
22	0	4 (0.8)	1 (0.2)	0.17
X	2 (0.7)	5 (1)	0	0.1
Y	0	3 (0.6)	0	0.105
Chaotic cells	1 (0.4)	6 (1.2)	3 (0.6)	0.401
Total abnormal cells	36 (13.2)	83 (16.5)	89 (18.5)	0.179

The values are presented as the number of embryos (%).

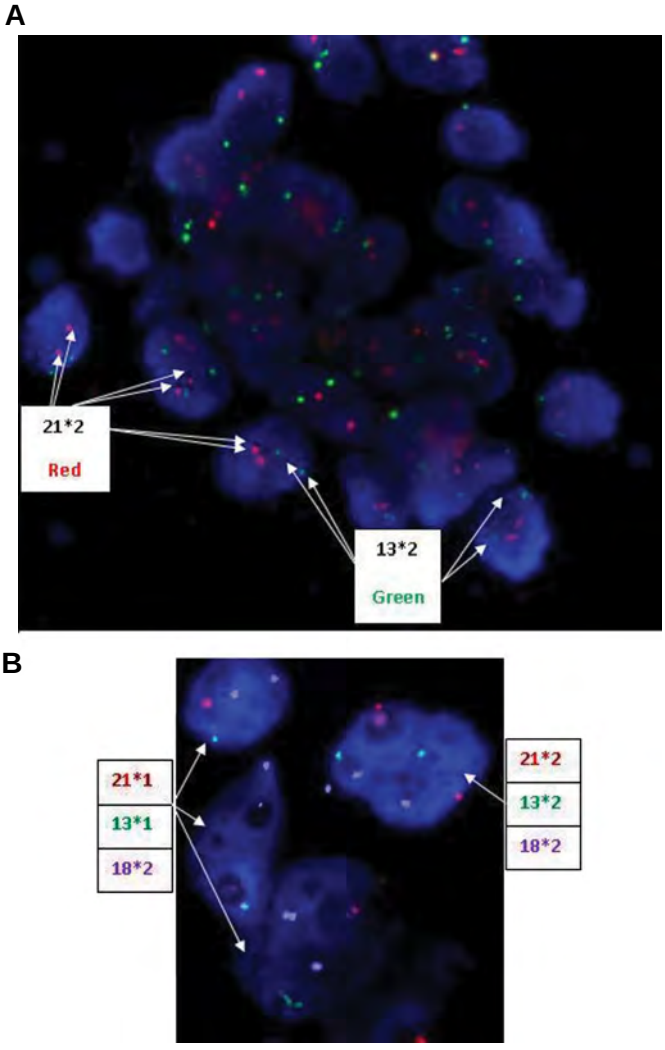

Fig.4: FISH results on blastocyst stage biopsy. **A.** Probe set included 13 (green signal) and 21 (red signal). All of the cells are normal regarding probe 13/21. **B.** Probe set included 13 (green signal), 21 (red signal) and 18 (blue signal). One cell is normal and 3 cells have monosomy 21 and monosomy 13. Overall, the embryo related to B is a mosaic blastocyst.

Discussion

Successful experiments in the development of human twin embryos to the blastocyst stage following *in vitro* splitting (6-8) led us to assess their potential for clinical applications. Developmental analyses presented here have proven that human twin embryos were compatible with non-manipulated embryos, as they were similar in their rates of reaching the EB stage. Increasing the number of blastomeres used for the splitting procedure improved the development to all stages. There was no significant difference in the developmental potential between embryos without blastomere disturbance (twin As) and those in which the blastomeres were inputted into the empty ZP one by one (twin Bs). These findings confirmed the theory that the cell-cell interaction between blastomeres is not essential in order to facilitate the development to the blastocyst stage (8).

Morphokinetic assessments revealed no significant difference in the length of time twin embryos took to reach the EBL stage compared to controls. Interestingly, the blastulation time showed a decreasing trend in the twin embryos in group 2 (10-14 blastomeres) compared to the controls. Moreover, A twins reached each stage faster than B twins; however, the differences were not significant. We hypothesized that manipulated blastomeres need extra time for recovering in order to continue the cell cycle. This hypothesis can be supported by some events, especially in recipient embryos during TLM, such as cytoplasmic waves without sign of division, and blastomere displacing and rotation. Furthermore, all embryos in group 2, regardless of being twins or controls, significantly grew faster to the EBL stage. Since the embryos in group 2 had extended culture from pronuclear stage, they needed less time to develop to the blastocyst stage compared to the group 1. These findings demonstrated a similarity in total time needed for blastocyst development for embryos in either of the groups 1 or 2. There was a wide range between the minimum and maximum times of reaching each stage in the twins compared to controls. Twins exhibited a significantly shorter time duration for the compaction (9+ to Mor) and the start of blastulation (Mor to SB) stages than the control embryos. This result is in accordance with findings of Noli et al. (8), suggesting a kind of 'compensation' for the lower cell number in twin embryos. In a different assessment, twins from both groups did not differ regarding the duration between the stages.

Based on data from the quality assessment of human twin embryos, splitting resulted in smaller blastocysts with a lower quality of ICM and TE compared to non-manipulated embryos. A previous study demonstrated that in spite of increasing the number of blastocysts after splitting, the percentage of good quality blastocysts significantly decreased in the mice model (6). In line with our results, Noli and associates had detected a significant difference in size between twins compared to the controls. In addition, they found that the decreased size of blastocysts developed after *in vitro* splitting was due to the decreased number of blastomeres (8). Nevertheless, an animal model study showed offspring of a normal size following *in vitro* splitting because the regulation of cell number occurs after blastocyst formation (19). Mitalipov et al. (20) also found similar ICM:TE and ICM:total cell ratios between twin blastocysts and controls. The presence of NANOG-only positive cells indicates the development potential of the ICM in twins following the splitting procedure (8). The early embryonic blastomeres are totipotent cells and have the individual capacity to develop into both ICM and TE lineages (21). On the other hand, human embryonic genome activation occurs between the 4- to 8-cell stage, when the cells have flexibility (22-23). So, there is an opinion that the allocation of ICM and TE occurs after embryonic genome activation at the early 8-cell stage before the cells become polarized at both the membrane and cytoplasmic levels. This means that removal of blastomeres after cell polarization does not compromise formation of the ICM. Accordingly, the morning of day 3 was introduced as the best time for blastomere biopsy (24). There are two theories regarding the position of the blastomeres within the embryo and the

appearance of two distinct cells lineages i.e. the TE and ICM; The cell polarity model (25) and the inside-outside hypothesis (26). According to these hypotheses, either the outer blastomeres within the embryo or the blastomeres with a perpendicular plane of cleavage participate in the formation of the TE cells (27). Our morphokinetics data showed a derangement in the position of the blastomeres following the *in vitro* splitting procedure. In this method, a smll number of blastomeres were placed into a large space, resulting in an outer position of all blastomeres and subsequently differentiation to TE cells. Our results in regards to the poor quality or lack of ICM in twin blastocysts suggested that lineage determination may take place through the inside-outside model. In a pilot study, we tried *in vitro* splitting in triploid embryos. Next, the developed blastocysts (n=24) from twin embryos were cultured for derivation of human embryonic stem cell (hESC) lines. After three to five days of blastocyst culture, the initial outgrowths of hESC-like cells were generated. After proliferation and passaging, some of the cells expressed hESC and trophoblastic markers, however, no cell line was established (28).

To the best of our knowledge, this is the first study that evaluates the impact of human embryo *in vitro* splitting on chromosomal abnormality and mosaicism. We found that chromosomes 22, 16, 21, and 15 were the main chromosomes involved in cleavage-stage aneuploidies. We also report an improvement in implantation rate with the evaluation of eight critical chromosomes: X, Y, 13, 15, 16, 18, 21, and 22 (29, 30). Our findings in analysing total abnormal cells and embryos showed no significant differences between twin and control embryos. Furthermore, the data showed that the decrease in the number of normal (euploid) twin blastocysts was simultanious with an increase in the proportion of the mosaic blastocysts with no significant differences. Mosaic embryos as a category between normal (euploid) and abnormal (aneuploid) embryos may be lead to a decreased implantation and pregnancy potential as well as an increased risk of genetic abnormalities (31-33). In trisomic mosaicism, it was shown that the embryos with mosaic trisomies of chromosomes 2, 7, 13, 14, 15, 16, 18, and 21 may be in higher risk of developing a child affected with a trisomy syndrome. Therefore, it was advised that the cycles with total mosaic embryos should be canceled until obtaining euploid embryos (31). According to the data on preimplantation genetic screening (PGS), the rate of aneuploidy in the cleavage-stage embryos was 60%, of which approximately 50% were represented by mosaicism where the nature of abnormality was unknown (34-36). There are some reports showing that oocyte manipulation may increase the risk of aneuploidy in subsequent embryos. It was suggested that abberations in cytoskeletal integrity, such as mitochondrial distribution, may reduce the meiotic competence of the oocyte and lead to subsequent mitotic errors at the cleavage-stage and predispose the embryos to chromosomal abnormalities (37). Also, deviances in activity of motor proteins and spindle formation during handling of oocytes are risk factors for non-disjunction and embryo aneuploidy (38). Our results showed that the embryo micromanipulation during *in vitro* splitting does not increase the risk of aneuploidy in the developed blastocysts. It seems micromanipulation in the oocyte may increase the risk of chromosomal abnormality but micromanipulation at the cleavage-stage does not.

Recent studies have introduced comparative genomic hybridization (CGH) and microarray-CGH as more optimal strategies for aneuploidy detection (39), in spite of some of their limitations (40). It is suggested that further studies be conducted with a higher number of donor embryos for *in vitro* splitting, and the use of chromosomal analyses that evaluate whole chromosomal aneuploidies such as CGH-array or next-generation sequencing. In the next step, epigenetic investigations can be performed to rule out the probable effects of *in vitro* splitting on the epigenetic status of the developed blastocysts.

Conclusion

The current study shows that some developmental time-points were affected by *in vitro* splitting. This technique increased the number of developed blastocysts and no chromosomal abnormalities were found when compared to controls. However, the developed blastocysts from *in vitro* splitting were of low quality. This technique may raise the hope to treat poor responders or cases of advanced maternal age in the assisted reproductive technology (ART) program. This study demonstrates that focus on the embryo's stage at the time of the splitting procedure can improve the outcomes of this technique. These data motivate further attempts of upgrading the *in vitro* splitting program in order to develop more healthy twins.

Acknowledgements

This study was extracted from the Ph.D. thesis of Marjan Omidi. The authors appreciate Yazd Research and Clinical Center for Infertility for all its support. The authors declare no conflicts of interest.

Authors' Contributions

M.O., M.A.K., S.M.K.; Contributed to conception and design. M.O.; Contributed to all experimental work. M.O., S.M.K., F.M.; Contributed to data analysis and conducted. cytogenetic analysis. M.O., I.H.; Contributed to data analysis. M.O., I.H., M.A.K., S.M.K.; Contributed extensively in interpretation of the data and the conclusion. M.O, I.H.; Contributed to write the manuscript. All authors read and approved the final manuscript.

References

1. Willadsen SM. A method for culture of micromanipulated sheep embryos and its use to produce monozygotic twins. Nature. 1979; 277(5694): 298-300.
2. Willadsen SM, Polge C. Attempts to produce monozygotic quadruplets in cattle by blastomere separation. Vet Rec. 1981; 108(10): 211-213.
3. Allen WR, Pashen RL. Production of monozygotic (identical) horse twins by embryo micromanipulation. J Reprod Fertil. 1984;71(2): 607-613.

4. Ash K, Anderson GB, Bondurant RH, Pashen RL, Parker KM, Berger T. Competition between split and nonmanipulated embryos in the production of identical piglets. Theriogenology. 1989; 31(4): 903-910.
5. Hall JL, Engel D, Gindoff PR, Mottla G, Stillman R. Experimental cloning of human polyploid embryos using an artificial zona pellucida. Fertil Steril. 1993; 61: S1.
6. Van de Velde H, Cauffman G, Tournaye H, Devroey P, Liebaers I. The four blastomeres of a 4-cell stage human embryo are able to develop individually into blastocysts with inner cell mass and trophectoderm. Hum Reprod. 2008; 23(8): 1742-1747.
7. Illmensee K, Levanduski M, Vidali A, Husami N, Goudas VT. Human embryo twinning with applications in reproductive medicine. Fertil Steril. 2010; 93(2): 423-427.
8. Noli L, Dajani Y, Capalbo A, Bvumbe J, Rienzi L, Ubaldi FM, et al. Developmental clock compromises human twin model created by embryo splitting. Hum Reprod. 2015; 30(12): 2774-2784.
9. Omidi M, Khalili MA, Agha-Rahimi A, Nottola S, Anbari F, Faramarzi A, et al. Efficacy of the in vitro splitting of human preimplantation embryos from ART programs. Turk J Med Sci. 2019; 19(2).
10. Noli L, Capalbo A, Dajani Y, Cimadomo D, Bvumbe J, Rienzi L, et al. Human embryos created by embryo splitting secrete significantly lower levels of miRNA-30c. Stem Cells Dev. 2016; 25(24): 1853-1862.
11. Halvaei I, Ghazali S, Nottola SA, Khalili MA. Cleavage-stage embryo micromanipulation in the clinical setting. Syst Biol Reprod Med. 2018; 64(3): 157-168.
12. Kaser DJ, Racowsky C. Clinical outcomes following selection of human preimplantation embryos with time-lapse monitoring: a systematic review. Hum Reprod Update. 2014; 20(5): 617-631.
13. Khalili MA, Razavi V, Mardanian F, Esfandiari N. The predictive value of pronuclear morphology screening on embryo development and pregnancy outcome in ART cycles. Middle East Fertil Soc J. 2008; 13(1): 44-51.
14. Halvaei I, Khalili MA, Nottola SA. A novel method for transmission electron microscopy study of cytoplasmic fragments from preimplantation human embryos. Micros Res Tech. 2016; 79(6): 459-462.
15. Gardner DK, Surrey E, Minjarez D, Leitz A, Stevens J, Schoolcraft WB. Single blastocyst transfer: a prospective randomized trial. Fertil Steril. 2004; 81(3): 551-555.
16. McArthur SJ, Leigh D, Marshall JT, de Boer KA, Jansen RPS. Pregnancies and live births following biopsy and PGD analysis of human embryos at the blastocyst stage. Fertil Steril. 2005; 84:1628- 1636.
17. Colls P, Escudero T, Cekleniak N, Sadowy S, Cohen J, Munné S. Increased efficiency of preimplantation genetic diagnosis for infertility using “no result rescue”. Fertil Steril. 2007; 88(1): 53-61.
18. Delhanty JD, Harper JC, Ao A, Handyside AH, Winston RM. Multicolour FISH detects frequent chromosomal mosaicism and chaotic division in normal preimplantation embryos from fertile patients. Hum Genet. 1997; 99(6): 755-760.
19. Escribá MJ, Valbuena D, Remohí J, Pellicer A, Simón C. New techniques on embryo manipulation. J Reprod Immun. 2002; 55(1-2): 149-161.
20. Mitalipov SM, Yeoman RR, Kuo HC, Wolf DP. Monozygotic twinning in rhesus monkeys by manipulation of in vitro-derived embryos. Biol Reprod. 2002; 66(5): 1449-1455.
21. Ethics Committee of the American Society for Reproductive Medicine. Embryo splitting for infertility treatment. Fertil Steril. 2004; 82 Suppl 1: S256-S257.
22. Braude P, Bolton V, Moore S. Human gene expression first occurs between the four-and eight-cell stages of preimplantation development. Nature. 1988; 332(6163): 459-461.
23. Cauffman G, Van de Velde H, Liebaers I, Van Steirteghem A. DAZL expression in human oocytes, preimplantation embryos and embryonic stem cells. Mol Hum Reprod. 2005; 11(6): 405-411.
24. Strauss JF, Barbieri RL. Yen & Jaffe’s reproductive endocrinology. Physiology, pathophysiology, and clinical management. Eighth edition. Elsevier Health Sciences; 2019.
25. Johnson MH, Ziomek CA. The foundation of two distinct cell lineages within the mouse morula. Cell. 1981; 24(1): 71-80.
26. Tarkowski AK, Wróblewska J. Development of blastomeres of mouse eggs isolated at the 4-and 8-cell stage. J Embryol Exp Morphol. 1967; 18(1): 155-180.
27. Carlson BM. Human embryology and developmental biology. Fifth edition. Elsevier Health Sciences; 2014.
28. Omidi M, Aflatoonian B, Tahajjodi SS, Khalili MA. Attempts for Generation of embryonic stem cells from human embryos following in vitro embryo twinning. Stem Cells Dev. 2019; 28(5): 303-309.
29. Munné S, Chen S, Fischer J, Colls P, Zheng X, Stevens J, et al. Preimplantation genetic diagnosis reduces pregnancy loss in women aged 35 years and older with a history of recurrent miscarriages. Fertil Steril. 2005; 84(2): 331-335.
30. Munné S, Wells D, Cohen J. Technology requirements for preimplantation genetic diagnosis to improve assisted reproduction outcomes. Fertil Steril. 2010; 94(2): 408-430.
31. Sachdev NM, Maxwell SM, Besser AG, Grifo JA. Diagnosis and clinical management of embryonic mosaicism. Fertil Steril. 2017; 107(1): 6-11.
32. Vera-Rodriguez M, Rubio C. Assessing the true incidence of mosaicism in preimplantation embryos. Fertil Steril. 2017; 107(5): 1107-1112.
33. Munné S, Wells D. Detection of mosaicism at blastocyst stage with the use of high-resolution next-generation sequencing. Fertil Steril. 2017; 107(5): 1085-1091.
34. Munné S. Preimplantation genetic diagnosis of numerical and structural chromosome abnormalities. Reprod BioMed Online. 2002; 4(2): 183-196.
35. Gianaroli L, Magli MC, Ferraretti AP. The in vivo and in vitro efficiency and efficacy of PGD for aneuploidy. Mol Cell Endocrinol. 2001; 183 Suppl 1: S13-S18.
36. Kuliev A, Verlinsky Y. Meiotic and mitotic nondisjunction: lessons from preimplantation genetic diagnosis. Hum Reprod Update. 2004; 10(5): 401-407.
37. Van Blerkom J, Davis P, Alexander S. Differential mitochondrial distribution in human pronuclear embryos leads to disproportionate inheritance between blastomeres: relationship to microtubular organization, ATP content and competence. Hum Reprod. 2000; 15(12): 2621-2633.
38. Eichenlaub-Ritter U, Shen Y, Tinneberg HR. Manipulation of the oocyte: possible damage to the spindle apparatus. Reprod Biomed Online. 2002; 5(2): 117-124.
39. Mateu E, Rodrigo L, Peinado V, Milán M, Campos I, García-Herrero S, et al. Preimplantation genetic diagnosis for translocations and interchromosomal effect assessed by array CGH. Reprod Biomed Online. 2018; 36 (Suppl 1): e20-e21.
40. Fragouli E, Alfarawati S, Daphnis DD, Goodall NN, Mania A, Griffiths T, et al. Cytogenetic analysis of human blastocysts with the use of FISH, CGH and aCGH: scientific data and technical evaluation. Hum Reprod. 2010; 26(2): 480-490.

Original Article

lncRNA Metastasis-Associated Lung Adenocarcinoma Transcript 1 Promotes Proliferation and Invasion of Non-Small Cell Lung Cancer Cells via Down-Regulating *miR-202* Expression

Guo Tiansheng, B.Sc.#*, Huang Junming, M.Sc.#, Wan Xiaoyun, M.Sc., Chen Peixi, M.Sc., Du Shaoshan, B.Sc., Chen Qianping, B.Sc.

Department of Oncology, Guangzhou Panyu Hospital of Chinese Medicine, Guangzhou, PR China

 # The first two authors equally contributed to this work.

Corresponding Address: Department of Oncology, Guangzhou Panyu Hospital of Chinese Medicine, Guangzhou, PR China
Email: xiehewxj@163.com

Received: 1/March/2019, Accepted: 6/May/2019

Abstract

Objective: Accumulating evidences indicate that long non-coding RNAs (lncRNAs) play key roles in cancer. This study aims to clarify role of the metastasis-associated lung adenocarcinoma transcript 1 (*MALAT1*) in non-small cell lung cancer (NSCLC) and uncover the underlying mechanisms.

Materials and Methods: In this experimental study, *MALAT1* and *miR-202* expression in tissues and cell lines were detected using quantitative real time polymerase chain reaction (qRT-PCR) assay. Cell transfection was conducted using Lipofectamine 3000. Cell proliferation was determined with CCK-8 assay. MMP2 and MMP9 expressions were measured with Western blot. Cell invasive ability was evaluated by Transwell assay. Starbase 2.0 tool was used to predict targets of *MALAT1*. Dual luciferase reporter assay, RNA-binding protein immunoprecipitation assay and RNA pull-down assay were conducted to confirm the potential direct interaction between *MALAT1* and *miR-202*.

Results: *MALAT1* was overexpressed in NSCLC samples and cell lines. High expression of *MALAT1* was related to large tumor size (>3 cm), poor histological grade, advanced cancer and tumor metastasis in NSCLC. *In vitro* assays exhibited that knockdown of *MALAT1* remarkably decreased A549 cell growth and invasion capacity, while overexpression of *MALAT1* significantly enhanced NCI-H292 cell proliferation and invasion ability. Next, we verified that *MALAT1* could act as a competing endogenous RNA (ceRNA) by sponging *miR-202* in NSCLC and there is a negative correlation between *MALAT1* and *miR-202*. Besides, overexpression of *miR-202* inhibited cell proliferation and invasive ability in *MALAT1*-overexpressed cells.

Conclusion: This study demonstrated that lncRNA-*MALAT1* gets involved in NSCLC progression by targeting *miR-202*, indicating that *MALAT1* may serve as a novel therapeutic target for NSCLC treatment.

Keywords: lncRNA-*MALAT1*, *miR-202*, Non-Small Cell Lung Cancer

Cell Journal(Yakhteh), Vol 22, No 3, October-December (Autumn) 2020, Pages: 375-385

Citation: **Tiansheng G, Junming H, Xiaoyun W, Peixi Ch, Shaoshan D, Qianping Ch. lncRNA metastasis-associated lung adenocarcinoma transcript 1 promotes proliferation and invasion of non-small cell lung cancer cells via down-regulating miR-202 expression. Cell J. 2020; 22(3): 375-385. doi: 10.22074/cellj.2020.6837.**

Introduction

Lung cancer is the first cause of cancer deaths worldwide, leading to about 1.6 million patients die per year (1). According to the pathological diagnosis, lung cancer is divided into small-cell lung cancer (SCLC, around 15%) and non-small cell lung cancer (NSCLC, around 85%). Although diagnostic techniques and therapy strategies (such as surgical techniques and targeted treatment) have progressed, the 5-year overall survival rate is still below 15%. Besides, this 15% of patients are accompanied with high recurrence rates (2). Thus, it is necessary to determine oncogenes involved in lung cancer development and progression and explore the underlying mechanism, facilitating development of more effective treatment methods.

Long noncoding RNAs (lncRNAs) are an emerging class of transcripts, which is longer than 200 nucleotides (nt). Although lncRNAs are coded by the genome, they are hardly translated into proteins. Previous researches revealed that lncRNAs serve as new regulators, controlling gene expressions epigenetically and post-transcriptionally. They also play crucial roles in modulating chromatin dynamics, cell growth, differentiation and development (3). Increasing evidences indicated that many lncRNAs are observed to be abnormally expressed in many types of cancer (4). For instance, Wei and Wang (5) found that lncRNA-*MEG3* was downregulated in gastric carcinoma specimens and overexpression of it could repress gastric cancer cell growth and mobility via elevating p53 expression. lncRNA *CPS1-IT1* was reported to serve as tumor suppressor in colorectal cancer and low *CPS1-IT1* expression indicated poor prognosis (6).

The metastasis-associated lung adenocarcinoma transcript 1 (*MALAT1*), also called as nuclear-enriched abundant transcript 2 (*NEAT2*), *HCN*, *LINC00047*, *NCRN00047* and *PRO2853*, is an extensively expressed lncRNA, with the length of around 8000 nt (7). In 2003, *MALAT1* was first found to function as a survival

prognostic factor for stage I lung adenocarcinoma or squamous cell carcinoma patients (8). In recent years, accumulating evidences suggested that *MALAT1* plays a key role in tumorigenesis. In gastric cancer, *MALAT1* was reported to promote tumorigenicity and metastasis through facilitating vasculogenic mimicry and angiogenesis (9). In triple-negative breast cancer, *MALAT1* was found to promote cell proliferation and invasion via decreasing expression of *miR-129-5p* (10). Xie et al. (11) revealed that *MALAT1* suppressed apoptosis and enhanced cell invasion ability via inhibiting *miR-125p* in bladder cancer. In epithelial ovarian cancer, *MALAT1* was found to facilitate cell growth and induce epithelial-mesenchymal transition (EMT) through modulating PI3K/AKT signaling pathway (12). The study performed by Li et al. (13) showed that *MALAT1* is positively correlated with chemoresistance in colorectal cancer patients. Nevertheless, further investigations are still required to identify role and function of *MALAT1* in development and progression of NSCLC.

Previous studies have identified *miR-202* as a tumor suppressor. For instance, in papillary thyroid carcinoma, *miR-202* attenuates cell migration and invasion abilities via inhibiting Wnt signaling pathway (14). In human bladder cancer, *miR-202* suppresses cell growth and metastasis through targeting EGFR (15). Furthermore, *miR-202* was found to reduce expression level of TGFβ receptors and reverse TGFβ1-mediated EMT in pancreatic cancer (16). In NSCLC, *miR-202* decreased cell viability and weakens cell mobility and invasive capacity by suppressing STAT3 activity (17).

In this study, we observed that lncRNA-*MALAT1* was highly expressed in NSCLC tissues and cell lines. Correlation analysis revealed that high *MALAT1* expression was related to large tumor size (> 3 cm), moderate or poor differentiation, advanced tumor stage and metastasis. Biologically functional experiments demonstrated that *MALAT1* promoted NSCLC cell proliferation and invasion. Further molecular mechanisms revealed that *MALAT1* could sponge *miR-202* within NSCLC progression.

Materials and Methods

Patients and tissue samples

Forthy NSCLC tissues as well as corresponding adjacent normal tissues specimens were collected from Guangzhou Panyu Hospital of Chinese Medicine between June 2015 and July 2018. Patients involved in this study had not received any preoperative radiotherapy or chemotherapy. All specimens were identified as NSCLC tissues or normal lung tissues via histopathological observation. After resection, all tissues were dipped in liquid nitrogen promptly and then were stored at -80˚C for further studies. All enrolled patients were informed to sign the written informed consent and this study was approved by the Ethics Committees of Guangzhou Panyu Hospital of Chinese Medicine (license number of ethics statement: 2015HW126).

Cell culture

In this experimental study, normal lung cell BEAS-2B, NSCLC cell lines (A549, NCI-H23, NCI-H292, NCI-H1299 and NCI-H1975) and HEK293T cell were obtained from ATCC. BEAS-2B cell was cultured in BEBM medium (Lonza/Clonetics Corporation, Switzerland) containing 10% fetal bovine serum (FBS, Thermo Fisher Scientific, USA). NSCLC cell lines and HEK293T cell were cultured in RPMI-1640 medium (Thermo Fisher Scientific, USA) supplemented with 10% (v/v) FBS. All cells were maintained in a humidified atmosphere with 5% CO_2 at 37˚C.

RNA extraction and quantitative real time polymerase chain reaction assay

Total RNA was extracted from tissue specimens and cell lines by using TRIzol reagent (Invitrogen, USA) according to manufacturer's protocol and treated with DNase I (Thermo Fisher Scientific, USA) to remove genomic DNA. cDNA was synthesized with the Transcriptor First Strand cDNA Synthesis Kit (Roche, Switzerland). For miRNAs, reverse transcription was conducted with TaqMan Micro-RNA Reverse Transcription Kit (Applied Biosystems, USA). Expression level of lncRNA-*MALAT1* was analyzed on a CFX96 real-time thermocycler (BioRad, USA) by using SsoAdvanced™ Universal SYBR® Green Supermix (BioRad, USA). Detection of *miR-202* was performed using TaqMan microRNA Assay kit (Applied Biosystems, USA) on the CFX96 real-time thermocycler (BioRad, USA). *GAPDH* and *U6* were considered as endogenous control of lncRNA-*MALAT1* and *miR-202* respectively. Relative expression levels were calculated by using $2^{-\Delta\Delta CT}$ method. All primers used in this study are listed below:

MALAT1-
F: 5′-AGTACAGCACAGTGCAGCTT-3′
R: 5′-CCCACCAATCCCAACCGTAA-3′

GAPDH-
F: 5′-GGAGCGAGATCCCTCCAAAAT-3′
R: 5′-GGCTGTTGTCATACTTCTCATGG-3′

miR-202-
F: 5′-CCTCCCAGGCTCACGAGGCT-3′
R: 5′-GGTGCAGGTGCACTGGTGCA-3′

U6-
F: 5′-GCTTCGGCAGCACATATACTAAAAT-3′
R: 5′-CGCTTCACGAATTTGCGTGTCAT-3′.

The sequences of *MALAT1* were quoted from Zuo et al. (10). The sequences of *miR-202* were quoted from Hoffman et al. (18), while the sequences of *GAPDH* and *U6* were designed by ourselves using Pubmed.

Cell transfection

siRNAs oligo targeting *MALAT1*, *miR-202* mimics,

scramble oligonucleotides and pcDNA3.1-*MALAT1* were supplied by GenePharma company (Shanghai, China). Transfection was conducted with Lipofectamine 3000 Reagent (Thermo Fisher Scientific, USA) in accordance with the manufacturer's instruction. The sequence of siRNAs against *MALAT1* were as follows:

si-*MALAT1*: 5′-GAGCAAAGGAAGUGGCUUA-3′
si-NC: 5′-CGUACGCGGAAUA CUUCGAdTdT-3′.

CCK-8 assay

At 24 hours post-transfection, 1×10^3 cells/well were seeded in 96-well plates and cultured overnight. The cell viability was measured with CCK-8 (Beyotime Biotechnology, China) at different time of culture (0, 24, 48 and 72 hours) following the manufacturer's instruction.

Western blot assay

Total protein was extracted from cell pellet using RIPA lysis buffer (Thermo Fisher Scientific, USA) supplemented with protease inhibitors and phosphatase inhibitors (Roche) according to the manufacturer's protocol. Concentration of total protein was determined by using BCA™ Protein Assay Kit (Thermo Fisher Scientific, USA). Then, 40 μg of protein per lane was separated by 8% sodium dodecyl sulfate-polyacrylamide gel electrophoresis (SDS-PAGE) and transferred to polyvinylidene fluoride (PVDF) membranes. 5% skim milk was used to block PVDF membranes for 1 hour at room temperature. Next, membranes were incubated with primary antibodies overnight at 4˚C, followed by incubation of secondary antibodies for 1 hour at room temperature. Next, protein bands were visualized using the enhanced chemiluminescence system (Bio-Rad Clarity Western ECL, USA). Primary antibodies, including MMP2 (1:1000), MMP9 (1:1000) and β-actin (1:1000) and HRP-conjugated secondary antibodies (1:5000) were obtained from Cell Signaling Technology (CST Inc., USA). β-actin was regarded as the internal control.

Transwell invasion assay

24-well Transwell chambers were purchased from Corning (USA). After 24 hours transfection, 1×10^4 suspended cells in 100 μl serum free medium were seeded in upper chambers smeared on Matrigel (BD Biosciences, USA). Bottom chambers were filled with 600 μl medium containing 10% FBS. After 48 hours culture, upper chambers were fixed with 4% formaldehyde and stained with 0.05% crystal violet. Then, a cotton swab was used to rub away cells on the above membrane. The invaded cells through membrane were counted using optical microscopy.

Dual-luciferase reporter gene assay

Firstly, the full-length 3′-UTR of *MALAT1* with *miR-202* binding sites was cloned into the downstream of firefly luciferase gene in pGL3 (Invitrogen, USA) to construct pGL3-*MALAT1* wild type (WT) and mutant (Mut). HEK293T cells were co-transfected with WT-*MALAT1*, Mut-*MALAT1* reporter gene plasmid or pRL-TK plasmids and *miR-202* mimics or miR-NC with Lipofectamine 3000 (Thermo Fisher Scientific, USA). The pRL-TK Vector was intended for use as an internal control reporter vector and may be used in combination with any experimental reporter vector to co-transfect mammalian cells. The pRL-TK Vector contains the herpes simplex virus thymidine kinase (HSV-TK) promoter to provide low to moderate levels of Renilla luciferase expression in co-transfected mammalian cells. 48 hours later, luciferase activity was determined with a dual-luciferase reporter assay system (Promega, USA).

RNA-binding protein immunoprecipitation assay

A Magna RIP RNA binding protein immunoprecipitation kit was obtained from Millipore (Darmstadt, German) and the Ago2 antibody was purchased from Abcam (Cambridge, USA). RIP assay was conducted using the magna RIP RNA binding protein immunoprecipitation kit and Ago2 antibody in accordance with the instruction of manufacturer. qRT-PCR was used to determine expression level of co-precipitated RNAs.

RNA pull-down assay

Biotin-labeled miR-NC and biotin-labeled *miR-202* were synthesized by GenePharma company (Shanghai, China). 48 hours after transfection with biotin-labeled miR-NC or biotin-labeled *miR-202*, the cells were collected to conduct an RNA pull-down experiment using Pierce™ Magnetic RNA Protein Pull-down Kit (Thermo Fisher Scientific, USA) following the manufacturer's instruction. lncRNA-*MALAT1* level was determined using qRT-PCR from the pull-down samples.

Statistical analysis

Statistical analyses were processed with GraphPad Prism 6.0 software (GraphPad software, USA) and all data were expressed as mean ± standard deviation (SD). Student t test or one-way ANOVA was used to determine the differences between two groups or among multiple groups respectively. $P<0.05$ was considered as statistically significant.

Results

Overexpression of lncRNA-*MALAT1* is observed in NSCLC tissues and cell lines

To investigate the role of lncRNA-*MALAT1* in development of NSCLC carcinogenesis, we analyzed lncRNA-*MALAT1* expression in 40 paired NSCLC tissues and pericarcinomatous normal tissues with qRT-PCR. As shown in Figure 1A, the expression level of lncRNA-*MALAT1* was notably higher in NSCLC tissue samples than that in pericarcinomatous normal tissue ($P<0.05$). To further analyze the relationship between lncRNA-*MALAT1* expression and clinical pathological parameters, 40 NSCLC patient samples were classified into two groups in accordance with the median relative quantity of lncRNA-*MALAT1*. The lncRNA-*MALAT1* expression

levels above the median expression were defined as high expression while low expression of lncRNA-*MALAT1* was termed as the expression was below the median level. Results showed that high lncRNA-*MALAT1* expression significantly associate with tumor size (>3 cm), moderate or poor differentiation carcinoma, advanced tumor stage (namely advanced TNM stage, including III and IV stages) and tumor metastases (Fig.1B-E, P<0.05). In addition, we confirmed the expression level of lncRNA-*MALAT1* in NSCLC cell lines. As shown in Figure 1F, up-regulation of lncRNA-*MALAT1* was observed in NSCLC cell lines (A549, NCI-H23, NCI-H292, NCI-H1299 and NCI-H1975) compared to the normal lung cell BEAS-2B, indicating that lncRNA-*MALAT1* may play a promotor role in NSCLC. Furthermore, A549 cell expressed the highest level of lncRNA-*MALAT1* and NCI-H292 cell expressed the lowest level of lncRNA-*MALAT1*, compared to the other cell lines. Hence, A549 cell was chosen for silencing lncRNA-*MALAT1* and overexpression of lncRNA-*MALAT1* was performed on NCI-H292 cell.

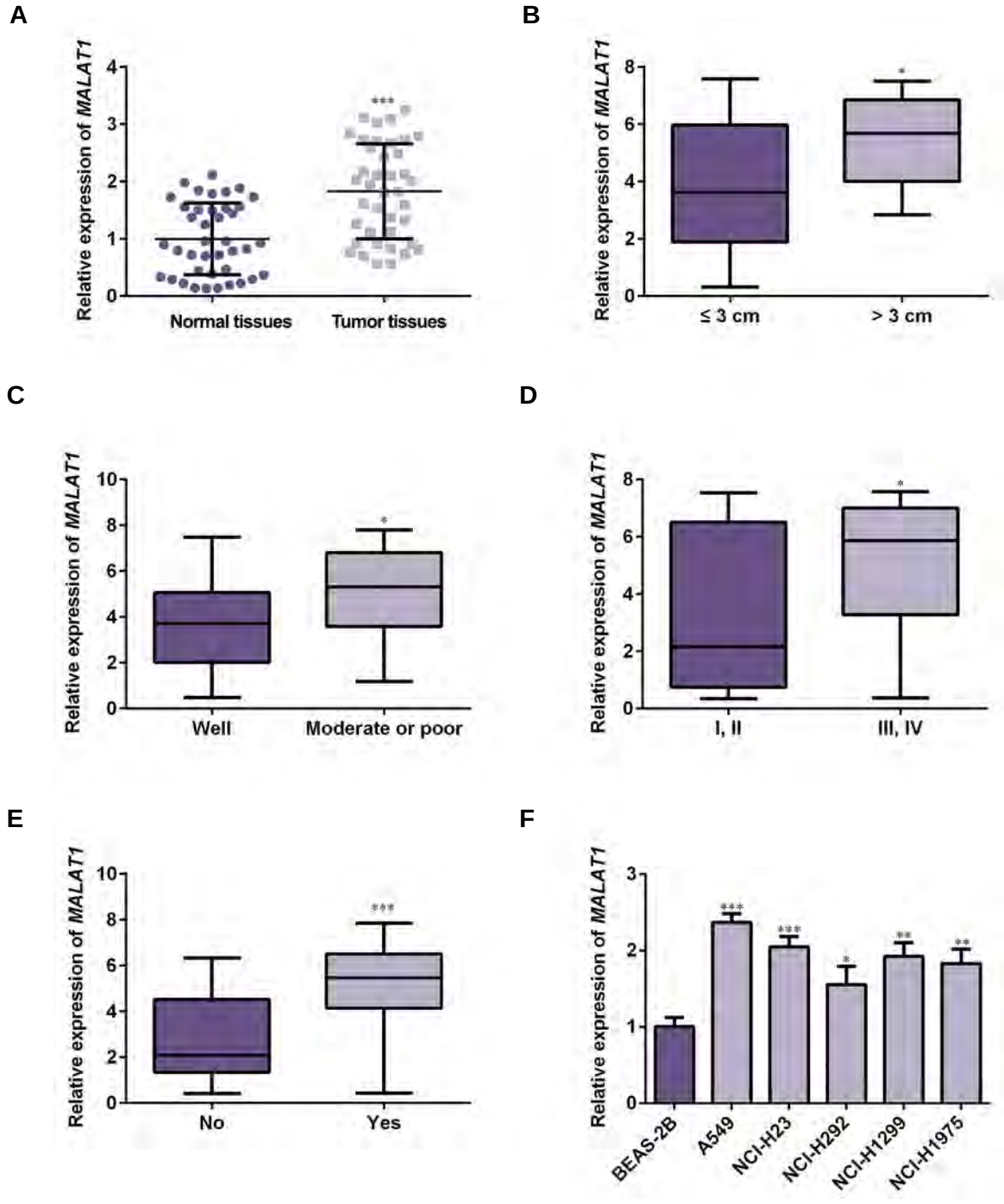

Fig.1: lncRNA-*MALAT1* was up-regulated in NSCLC tissues and cell lines. **A.** lncRNA-*MALAT1* expression in 40 paired NSCLC tissues and normal tissues was detected by qRT-PCR assay. The relationship of lncRNA-*MALAT1* expression with **B.** Tumor size, **C.** Histological grade, **D.** TNM stage and **E.** Tumor metastasis in NSCLC tissues compared to the matched paracancerous tissues (n=40). **F.** Expression level of lncRNA-*MALAT1* in normal lung cell BEAS-2B and NSCLC cell lines (A549, NCI-H23, NCI-H292, NCI-H1299 and NCI-H1975) was determined by qRT-PCR. *; P<0.05, **; P<0.01 and ***; P<0.001, data are expressed as mean ± SD, lncRNA; Long non-coding RNAs, NSCLC; Non-small cell lung cancer, qRT-PCR; Quantitative real time polymerase chain reaction, and TNM; Tumor nude metastasis.

Knocking-down of lncRNA-*MALAT1* inhibits cell growth and invasion

To investigate biological function of *MALAT1* in NSCLC, A549 cells were transfected with siRNAs oligo against *MALAT1*. As the knockdown efficiency of si-*MALAT1*-1 was better than that of si-*MALAT1*-2 (data was not shown), we silenced lncRNA-*MALAT1* expression in A549 cells by transfecting si-*MALAT1*-1 (Fig.2A, P<0.05). CCK-8 assay demonstrated that knockdown of lncRNA-*MALAT1* dramatically suppressed cell proliferation (Fig.2B, P<0.05). Western blot assay revealed that silencing lncRNA-*MALAT1* expression inhibited MMP2 and MMP9 expression (Fig.2C, D, P<0.05). Transwell assay presented that downregulation of lncRNA-*MALAT1* observably restrained cell invasion ability (Fig.2E, F, P<0.05). Collectively, these data demonstrated that knockdown of lncRNA-*MALAT1* inhibits A549 cell proliferation and invasion.

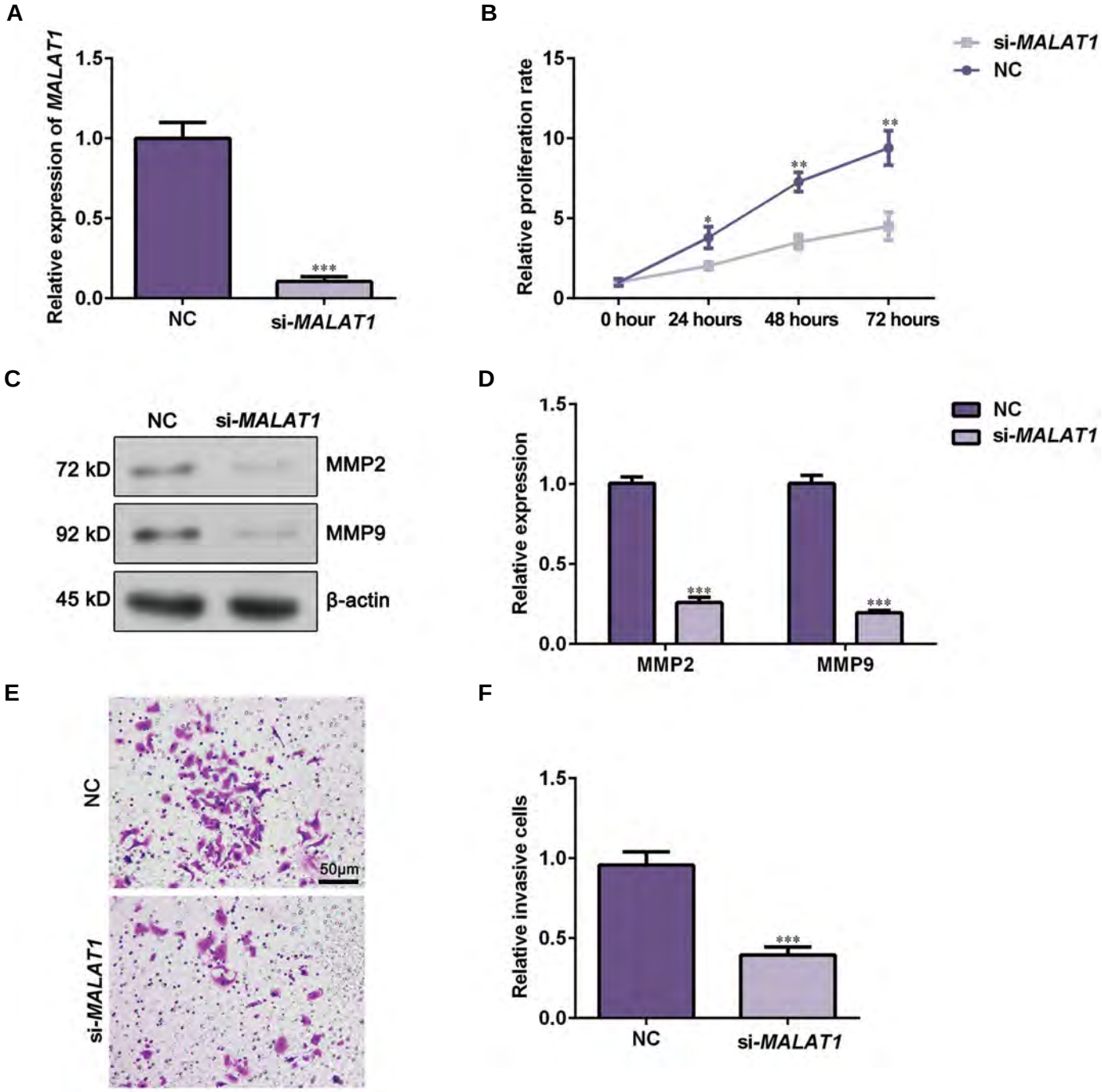

Fig.2: Silencing lncRNA-*MALAT1* repressed A549 cell proliferation and invasion. **A.** A549 cells were transfected with lncRNA-*MALAT1* siRNA oligo and interference efficiency was then detected by qRT-PCR. **B.** Cell viability was determined by CCK-8 assay after transfecting A549 cells with NC or si-*MALAT1*. **C.** Western blot assay was applied to assess MMP2 and MMP9 expression after transfection with si-*MALAT1* or NC. **D.** Data represent the relative protein expression. **E.** Transwell invasion assay was applied to evaluate cell invasive potential after *MALAT1* knocking-down (scale bar: 50 μm). **F.** Relative invasive cell numbers were analyzed with GraphPad Prism 5.0. Data are showed as the mean ± SD (n=3). *; P<0.05, **; P<0.01, ***; P<0.001 versus the NC group, lncRNA; Long non-coding RNAs, and qRT-PCR; Quantitative real time polymerase chain reaction.

Ectopic expression of lncRNA-*MALAT1* promotes cell growth and invasion

To further characterize the biological function of lncRNA-*MALAT1* in NSCLC, we established NCI-H292 cell with overexpression of lncRNA-*MALAT1* (Fig.3A, P<0.05). CCK-8 assay presented that the viability of NCI-H292 cells transfected with lncRNA-*MALAT1* plasmids was significantly increased compared to pcDNA3.1 group (Fig.3B, P<0.05). Western blot assay showed that ectopic expression of lncRNA-*MALAT1* elevated the expression of MMP2 and MMP9 (Fig.3C, D, P<0.05). Besides, Transwell assay revealed that the relative invasion capacity of NCI-H292 cells in *MALAT1*-overexpressed group was notably enhanced compared to pcDNA3.1 group (Fig.3E, F, P<0.05). These data further confirmed lncRNA-*MALAT1* might act as oncogene in NSCLC.

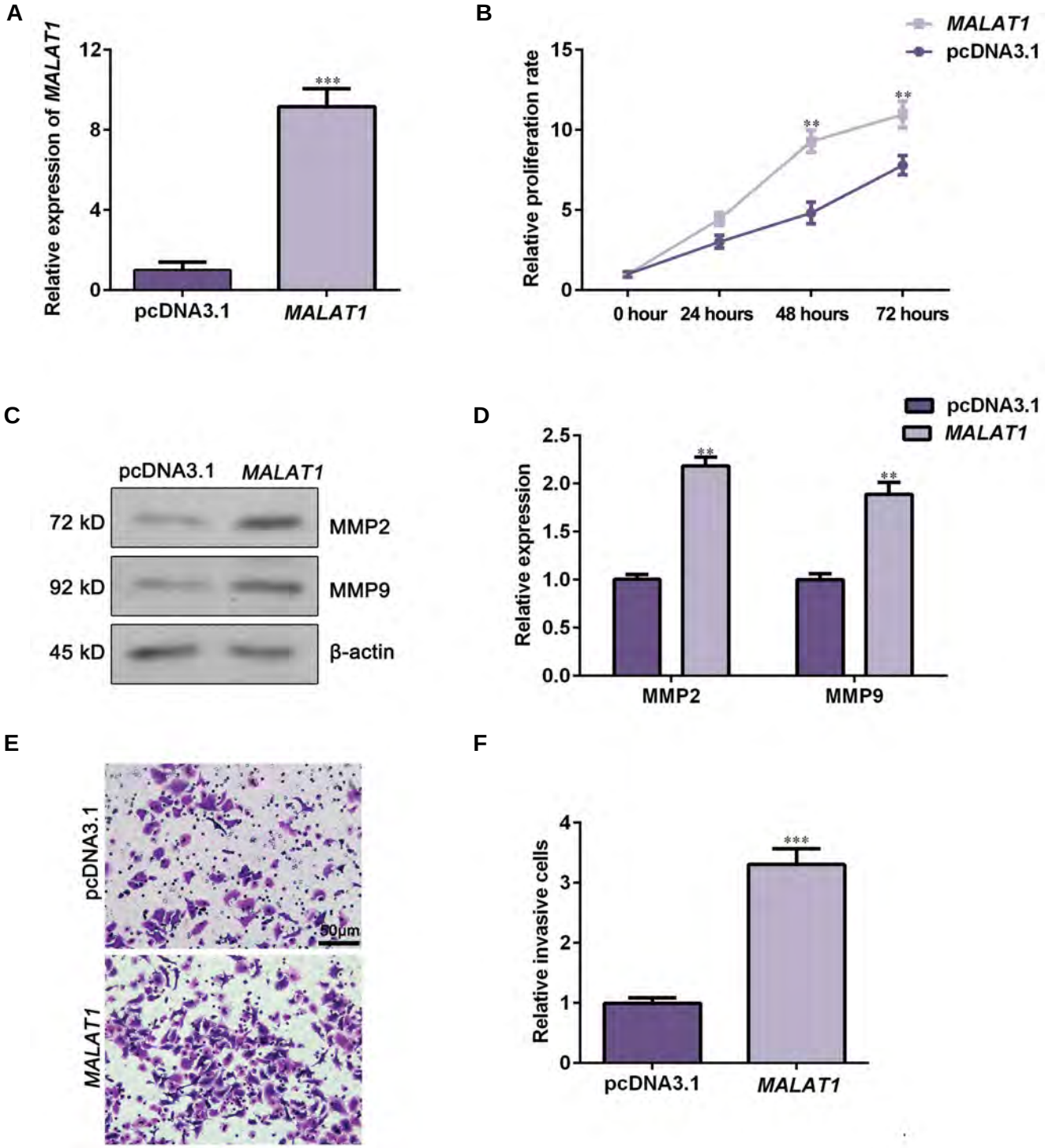

Fig.3: Overexpression of lncRNA-*MALAT1* promoted NCI-H292 cell proliferation and invasion. NCI-H292 cells were transfected with lncRNA-*MALAT1* plasmids or pcDNA3.1. **A.** Relative expression of *MALAT1* was detected by using qRT-PCR, **B.** Cell viability was assessed by CCK-8 assay. **C.** MMP2 and MMP9 expression were evaluated using Western blot assay. **D.** Data represent relative protein expression. **E.** Cell invasion capacity was tested using Transwell invasion assay (scale bar: 50 μm). **F.** Relative invasive cell numbers were analyzed with GraphPad Prism 5.0. Data are represented as the mean ± SD (n=3). **; P<0.01 and ***; P<0.001 versus the pcDNA3.1 group, lncRNA; Long non-coding RNAs, and qRT-PCR; Quantitative real time polymerase chain reaction.

lncRNA-*MALAT1* binds to miR-202 and reduces its expression

As there is complementary sequence of miRNA in lncRNA, they can act as a competing endogenous RNAs, regulating miRNA expressions and biological function (19). To explore the mechanism of lncRNA-*MALAT1* in progressing NSCLC, we used bioinformatics analysis web, Starbase 2.0 (http://starbase.sysu.edu.cn), to predict targets of lncRNA-*MALAT1*. We found that lncRNA-*MALAT1* has a potential binding site to *miR-202* (Fig.4A). We next performed dual luciferase reporter gene assay to confirm if *miR-202* binds to the 3′-UTR of lncRNA-*MALAT1* directly. Luciferase activity was markedly attenuated in HEK293 T cells co-transfected with *MALAT1*-WT plasmids and *miR-202* mimics (P<0.05), while there was no change in the cells co-transfected with *MALAT1*-Mut plasmids and *miR-202* mimics (Fig.4B). This indicates that the 3′-UTR of lncRNA-*MALAT1* complementarily pairs to *miR-202*. Moreover, RIP assay showed that lncRNA-*MALAT1* and *miR-202* were both enriched in the Ago2 pellet compared to the IgG group (Fig.4C, P<0.05). Additionally, RNA pull-down assay presented that endogenous *MALAT1* was pulled-down specifically in the cells overexpressing *miR202* compared to the NC group (Fig.4D, P<0.05). This data suggested that *miR-202* is a suppressive target of lncRNA-*MALAT1*.

LncRNA-*MALAT1* negatively regulates *miR-202* expression in NSCLC tissues

Since lncRNA-*MALAT1* directly binds to *miR-202*, we next explored whether lncRNA-*MALAT1* suppresses expression of *miR-202*. Results of qRT-PCR assay showed that knockdown of lncRNA-*MALAT1* increased *miR-202* expression, while ectopic expression of lncRNA-*MALAT1* decreased expression level of *miR-202* (Fig.5A, B, P<0.05), suggesting that lncRNA-*MALAT1* negatively regulates *miR-202*. Furthermore, we observed that expression level of *miR-202* was markedly downregulated in NSCLC tissues compared to the adjacent normal tissues (Fig.5C, P<0.05). We next analyzed correlation of lncRNA-*MALAT1* and *miR-202* expression levels. Findings show that *miR-202* was negatively related to the expression of lncRNA-*MALAT1* in NSCLC specimens (Fig.5D).

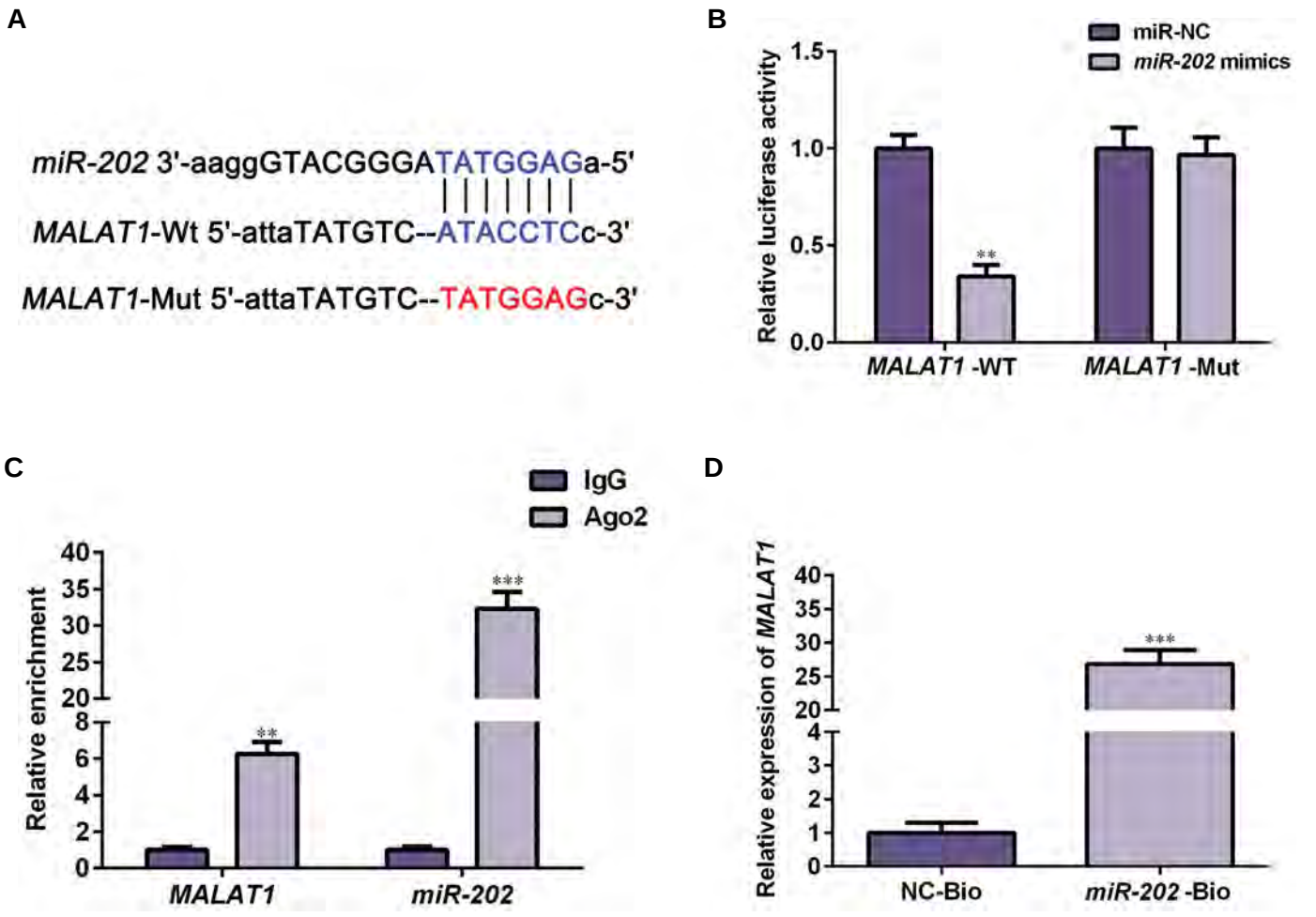

Fig.4: *miR-202* was a direct target of lncRNA-*MALAT1*. **A.** Starbase 2.0 (http://starbase.sysu.edu.cn) was used to identify recognition sequences between *MALAT1* and *miR-202*. **B.** NCI-H292 cells were co-transfected with *miR-202* mimics and *MALAT1*-WT or *MALAT1*-Mut, and then dual-luciferase reporter assay was employed to evaluate luciferase activity. **C.** RIP assay presented that *MALAT1* and *miR-202* expressions were enriched in Ago2 immunoprecipitates compared to IgG immunoprecipitates. **D.** RNA pull-down assay was conducted by transfecting biotin-labeled miR-NC or biotin-labeled *miR-202* into NCI-H292 cells. The endogenous expression level of lncRNA-*MALAT1* was detected by qRT-PCR. Data are expressed as the mean ± SD (n=3). **; P<0.01, ***; P<0.001, lncRNA; Long non-coding RNAs, RIP; RNA-binding protein immunoprecipitation assay, and qRT-PCR; Quantitative real time polymerase chain reaction.

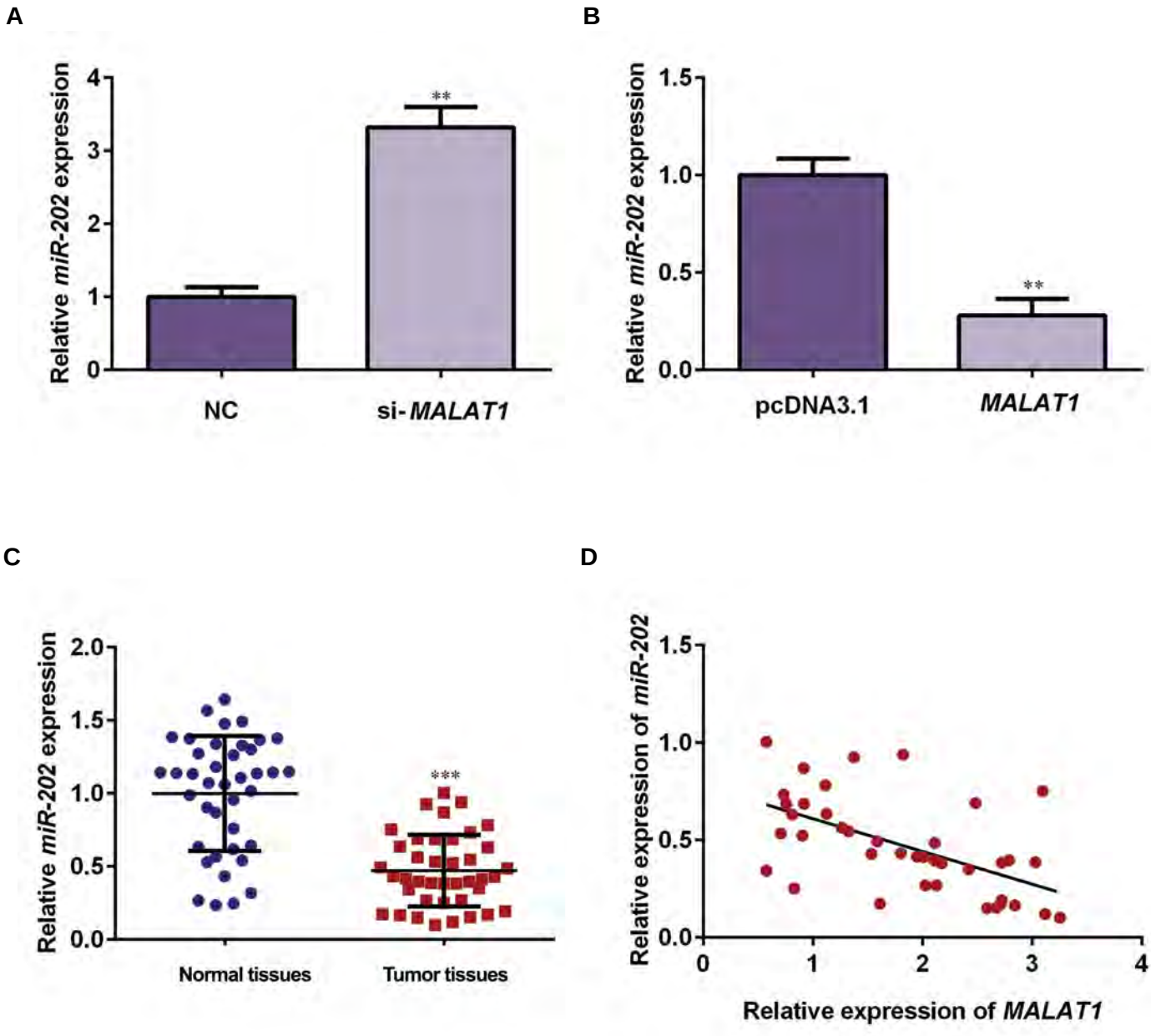

Fig.5: lncRNA-*MALAT1* inhibited *miR-202* expression and down-regulation of *miR-202* was observed in NSCLC tissues and cell lines. **A.** A549 cells were transfected with si-*MALAT1* or si-NC, and then *miR-202* expression was determined by using qRT-PCR. **B.** NCI-H292 cells were transfected with *MALAT1*-overexpressed plasmids or pcDNA3.1, and then *miR-202* expression was determined by qRT-PCR. **C.** *miR-202* expression in 40 cases of NSCLC tissues and matched paracancerous tissues was detected by qRT-PCR assay. **D.** Association of lncRNA-*MALAT1* with *miR-202* was assessed using Pearson's correlation analysis (R^2=0.3236, P<0.05). Relative invasive cell numbers were analyzed with GraphPad Prism 5.0. Data are showed as the mean ± SD. **; P<0.01, ***; P<0.001, lncRNA; Long non-coding RNAs, qRT-PCR; Quantitative real time polymerase chain reaction, and NSCLC; Non-small cell lung cancer.

lncRNA-*MALAT1* promotes NSCLC cells proliferation and invasion via decreasing *miR-202*

Next, we conducted rescue experiments via overexpressing *miR-202* in *MALAT1*-overexpressed cells to investigate whether or not *miR-202* gets involved in *MALAT1*-mediated carcinogenesis. CCK-8 assay revealed that proliferation rate of the cells co-transfected with *MALAT1* and *miR-202* mimics was significantly reduced compared to that of *MALAT1*-overexpressed cells (Fig.6A, P<0.05). In addition, ectopic expression of *miR-202* down-regulated expression levels of MMP2 and MMP9 in *MALAT1*-overexpressed cells, compared to *MALAT1* group (Fig.6B, C, P<0.05). In addition, Transwell invasion assay presented that *miR-202* mimics attenuated cell invasion capacity on *MALAT1*-overexpressed cells (Fig.6D, E, P<0.05). All together, these data demonstrated that lncRNA-*MALAT1* promoted NSCLC cell proliferation and invasion partially by inhibiting *miR-202* expression.

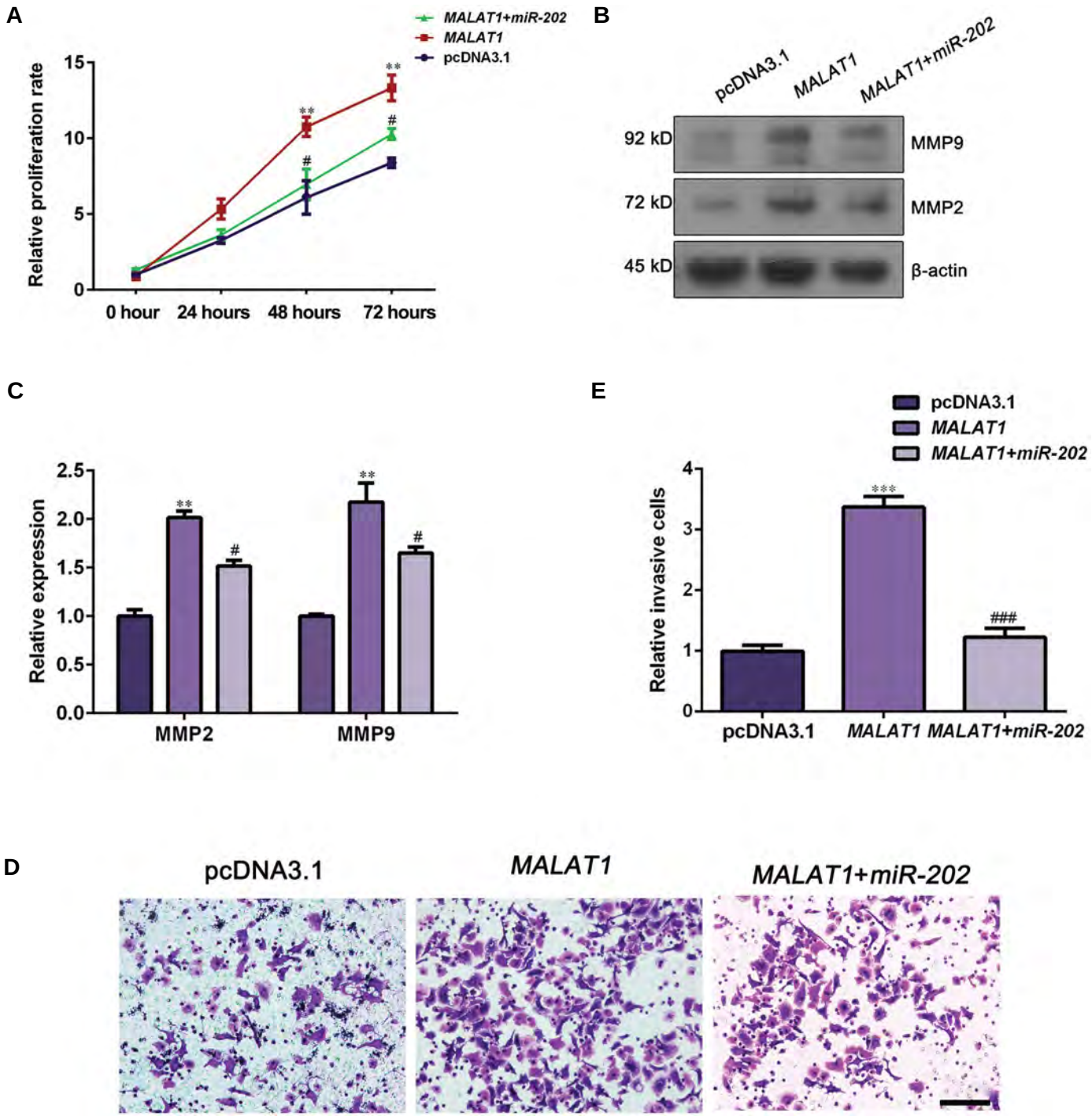

Fig.6: Overexpression of *miR-202* repressed cell growth and invasion in *MALAT1*-overexpressed NCI-H292 cell. NCI-H292 cells were co-transfected with *MALAT1* overexpression plasmids and *miR-202* mimics. **A.** Cell viability was detected using CCK-8 assay. **B.** MMP2 and MMP9 were determined by Western blot assay. **C.** Data represent relative protein expression. **D.** Cell invasion ability was evaluated by Transwell invasion assay (scale bar: 50 μm). **E.** Relative invasive cell numbers were analyzed with GraphPad Prism 5.0. Data are represented as the mean ± SD (n=3). **; P<0.01, ***; P<0.001 versus the pcDNA3.1 group, #; P<0.05, and ###; P<0.001 versus the *MALAT1* group.

Discussion

More and more evidences have shown that the aberrant expression of lncRNAs was observed in lung cancer tissues, indicating that lncRNAs play multiple roles in carcinogenesis of lung cancer (20). For instance, Nie et al. (21) found that lncRNA urothelial carcinoma-associated 1 (*UCA1*) served as an oncogene in NSCLC. High expression of lncRNA-*UCA1* predicted short survival time and multivariate analysis indicated that *UCA1* was an independent risk parameter of prognosis. Chen et al. (22) reported that upregulation of small nucleolar RNA host gene 20 (*SNHG20*) was notably correlated with advanced tumor stage, lymph node metastases and larger tumor size, as well as poorer overall survival chance. Wang et al. (23) revealed that lncRNA-*XIST* contributed to cell proliferation and invasion by inhibition of *miR-186-5p*

in NSCLC. Biological function of lncRNA-*HIT* (HOXA transcript induced by TGFβ) has been investigated in NSCLC. Results demonstrated that lncRNA-*HIT* facilitated NSCLC cell growth through interacting with E2F1 to regulate its target genes (24). Meanwhile, some lncRNAs conferring suppressive function in NSCLC have been recognized. For example, *TUG1* (taurine-upregulated gene 1) functions as a tumor suppressor in NSCLC (25). Considering their roles in tumorigenesis, lncRNAs may hold promise as diagnostic or prognostic biomarkers for lung cancer.

MALAT1 can be used to predict survival chance of stage I lung cancer or squamous cell cancer patients and it is phase and histologically specific to the metastasis of NSCLC patients (8). Accumulating studies have revealed that *MALAT1* not only plays a pivotal role in NSCLC progression, but also promotes other kinds of tumors. Zhang et al. found that serum exosome-derived lncRNA-*MALAT1* facilitated the tumor growth and migration, while it reduced apoptosis rate in NSCLC (26). The study performed by Li et al. (27) showed that *MALAT1* facilitated NSCLC cell growth, colony formation and apoptosis by targeting *miR-124*. In ovarian cancer, *MALAT1* was reported to facilitate cell proliferation and metastasis. It also prevents tumor cells from apoptosis (12). In this study, we found that *MALAT1* was overexpressed in NSCLC tissues and cell lines (A549, NCI-H23, NCI-H292, NCI-H1299 and NCI-H1975) compared to corresponding adjacent normal tissues and normal lung cell BEAS-2B, respectively. This finding was in accordance with previous studies. Further correlation analysis demonstrated that high *MALAT1* expression was positively related to large tumor size, poor histological grade, terminal stage of cancer and tumor metastasis. Knockdown of *MALAT1* inhibited A549 cell growth and invasion, as well as the expression of MMP2 and MMP9. In contrary, overexpression of *MALAT1* elevated NCI-H292 cell proliferation, invasion ability as well as the expression level of MMP2 and MMP9. These data indicated that *MALAT1* functions as oncogene in NSCLC, which is in line with previous studies.

The ceRNA theory proposes that lncRNAs sharing miRNA response elements (MREs) with mRNAs can act as miRNA decoys. It has been reported that lncRNAs can act as ceRNA by sponging miRNAs in cancer progression (28). The underlying molecular mechanisms involved in lncRNAs interacting with miRNAs are as follows: i. lncRNA indirectly inhibits negative regulation of miRNAs on target genes by competing with miRNAs to bind to the 3′-UTR of target gene mRNA, ii. Some lncRNAs form miRNA precursors by intracellular cleavage, which is then processed into specific miRNAs, regulating expression of the target genes, iii. Some lncRNAs function as endogenous miRNA sponges inhibiting miRNA expression (29). For instance, in gastric cancer, lncRNA-*HOTAIR* was reported to serve as a ceRNA to modulate HER2 expression via sponging *miR-331-3p* (30). Huang et al. (31) found that lncRNA-*CASC2* could function as a ceRNA through sponging *miR-18a* in colorectal cancer. In the present study, targets of *MALAT1* were predicted by Starbase 2.0 (http://starbase.sysu.edu.cn). Then we used dual-luciferase reporter gene assay, RIP assay as well as RNA pull-down assay to confirm that *miR-202* was a direct target of *MALAT1*. *MiR-202*, a new tumor suppressor, is down-regulated in gastric cancer (32). In addition, *miR-202* inhibits cell growth and promotes apoptosis in osteosarcoma through decreasing expression of Gli2 (33). *miR-202* also restrains cell proliferation in human hepatocellular cancer via suppressing LRP6 expression post-transcriptionally (34). In prostate cancer, *miR-202* inhibits cell proliferation and metastasis by inhibiting PIK3CA (35). Sun et al. (36) found that *miR-202* can increase therapeutic effect of cisplatin against NSCLC via inhibiting activity of the Ras/MAPK pathway. Zhao et al. (37) revealed that up-regulation of *miR-202* significantly reduces NSCLC cell viability, migration and invasion, and they suggested that STAT3 should be a direct target of *miR-202*. In this study, down-regulation of *miR-202* was observed in NSCLC compared to normal tissues. In addition, there was a negative correlation between *MALAT1* and *miR-202* expression in NSCLC tissues. Overexpression of *miR-202* could reverse oncogenic effect of *MALAT1* in NSCLC, indicating that *miR-202* plays a key role in *MALAT1*-induced cell proliferation and metastasis in NSCLC cells.

The molecular mechanism whereby *MALAT1* contributes to cancer progression appears to be diverse in different cancers. In gastric cancer, *MALAT1* was found to increase cell viability via modulating SF2/ASF (38). In esophageal squamous cell carcinoma, *MALAT1* promotes cell growth and invasion via regulating ATM-CHK2 signaling (39). In colorectal cancer, *MALAT1* facilitates cell growth, mobility and invasion through targeting PRKA kinase anchor protein 9 (AKAP-9) (40). In ovarian cancer, *MALAT1* contributes to cell EMT through modifying PI3K/AKT signaling pathway (12). In the present study, *MALAT1* enhances cell proliferation and metastasis by sponging *miR-202* in NSCLC cell lines. To our knowledge, this is the first report revealing interaction of *MALAT1* with *miR-202* in NSCLC. However, the molecular mechanism of *miR-202* downregulation through *MALAT1* activity requires further study.

Conclusion

This study elucidated that *MALAT1* could facilitate cell growth and invasion via sponging *miR-202* in NSCLC. Thus, our research demonstrated a new axis of *MALAT1*/*miR-202*, suggesting a feasible therapeutic means for NSCLC treatment.

Acknowledgements

There is no financial support and conflict of interest in this study.

Authors' Contributions

G.T., H.J.; Contributed to conception and design. W.X., C.P., D.S., C.Q.; Contributed to all experimental works, data and statistical analyses, and interpretation of data. G.T.; Were responsible for overall supervision. H.J.; Drafted the manuscript, which was revised by G.T. and W.X. All authors read and approved the final manuscript.

Reference

1. Torre LA, Bray F, Siegel RL, Ferlay J, Lortet-Tieulent J, Jemal A. Global cancer statistics, 2012. CA Cancer J Clin. 2015; 65(2): 87-108.
2. Didkowska J, Wojciechowska U, Mańczuk M, Łobaszewski J. Lung cancer epidemiology: contemporary and future challenges worldwide. Ann Transl Med. 2016; 4(8): 150.
3. Bhan A, Mandal SS. LncRNA HOTAIR: A master regulator of chromatin dynamics and cancer. Biochim Biophys Acta. 2015; 1856(1): 151-164.
4. Gibb EA, Brown CJ, Lam WL. The functional role of long non-coding RNA in human carcinomas. Mol Cancer. 2011; 10: 38.
5. Wei GH, Wang X. lncRNA MEG3 inhibit proliferation and metastasis of gastric cancer via p53 signaling pathway. Eur Rev Med Pharmacol Sci. 2017; 21(17): 3850-3856.
6. Zhang W, Yuan W, Song J, Wang S, Gu X. LncRna CPS1-IT1 Suppresses cell proliferation, invasion and metastasis in colorectal cancer. Cell Physiol Biochem. 2017; 44(2): 567-580.
7. Tripathi V, Ellis JD, Shen Z, Song DY, Pan Q, Watt AT, et al. The nuclear-retained noncoding RNA MALAT1 regulates alternative splicing by modulating SR splicing factor phosphorylation. Mol Cell. 2010; 39(6): 925-938.
8. Ji P, Diederichs S, Wang W, Böing S, Metzger R, Schneider PM, et al. MALAT-1, a novel noncoding RNA, and thymosin β4 predict metastasis and survival in early-stage non-small cell lung cancer. Oncogene. 2003; 22(39): 8031-8041.
9. Li Y, Wu Z, Yuan J, Sun L, Lin L, Huang N, et al. Long non-coding RNA MALAT1 promotes gastric cancer tumorigenicity and metastasis by regulating vasculogenic mimicry and angiogenesis. Cancer Lett. 2017; 395: 31-44.
10. Zuo Y, Li Y, Zhou Z, Ma M, Fu K. Long non-coding RNA MALAT1 promotes proliferation and invasion via targeting miR-129-5p in triple-negative breast cancer. Biomed Pharmacother. 2017; 95: 922-928.
11. Xie H, Liao X, Chen Z, Fang Y, He A, Zhong Y, et al. LncRNA MALAT1 inhibits apoptosis and promotes invasion by antagonizing mir-125b in bladder cancer cells. J Cancer. 2017; 8(18): 3803-3811.
12. Jin Y, Feng SJ, Qiu S, Shao N, Zheng JH. LncRNA MALAT1 promotes proliferation and metastasis in epithelial ovarian cancer via the PI3K-AKT pathway. Eur Rev Med Pharmacol Sci. 2017; 21(14): 3176-3184.
13. Li P, Zhang X, Wang H, Wang L, Liu T, Du L, et al. MALAT1 is associated with poor response to oxaliplatin-based chemotherapy in colorectal cancer patients and promotes chemoresistance through EZH2. Mol Cancer Ther. 2017; 16(4): 739-751.
14. Chen J, Yin J, Liu J, Zhu RX, Zheng Y, Wang XL. MiR-202-3p functions as a tumor suppressor and reduces cell migration and invasion in papillary thyroid carcinoma. Eur Rev Med Pharmacol Sci. 2019; 23(3): 1145-1150.
15. Zhang L, Xu J, Yang G, Li H, Guo X. miR-202 Inhibits cell proliferation, migration, and invasion by targeting epidermal growth factor receptor in human bladder cancer. Oncol Res. 2018; 26(6): 949-957.
16. Mody HR, Hung SW, Pathak RK, Griffin J, Cruz-Monserrate Z, Govindarajan R. miR-202 diminishes TGFβ receptors and attenuates TGFβ1-induced EMT in pancreatic cancer. Mol Cancer Res. 2017; 15(8): 1029-1039.
17. Zhao Z, Lv B, Zhang L, Zhao N, Lv Y. miR-202 functions as a tumor suppressor in non-small cell lung cancer by targeting STAT3. Mol Med Rep. 2017; 16(2): 2281-2289.
18. Hoffman AE, Liu R, Fu A, Zheng T, Slack F, Zhu Y. Targetome profiling, pathway analysis and genetic association study implicate miR-202 in lymphomagenesis. Cancer Epidemiol Biomarkers Prev. 2013; 22(3): 327-336.
19. Cesana M, Cacchiarelli D, Legnini I, Santini T, Sthandier O, Chinappi M, et al. A long noncoding RNA controls muscle differentiation by functioning as a competing endogenous RNA. Cell. 2011; 147(2): 358-369.
20. Yang J, Lin J, Liu T, Chen T, Pan S, Huang W, et al. Analysis of lncRNA expression profiles in non-small cell lung cancers (NSCLC) and their clinical subtypes. Lung Cancer. 2014; 85(2): 110-115.
21. Nie W, Ge HJ, Yang XQ, Sun X, Huang H, Tao X, et al. LncRNA-UCA1 exerts oncogenic functions in non-small cell lung cancer by targeting miR-193a-3p. Cancer Lett. 2016; 371(1): 99-106.
22. Chen Z, Chen X, Chen P, Yu S, Nie F, Lu B, et al., Long non-coding RNA SNHG20 promotes non-small cell lung cancer cell proliferation and migration by epigenetically silencing of P21 expression. Cell Death Dis. 2017; 8(10): e3092.
23. Wang H, Shen Q, Zhang X, Yang C, Cui S, Sun Y, et al., The long non-coding RNA XIST controls non-small cell lung cancer proliferation and invasion by modulating miR-186-5p. Cell Physiol Biochem. 2017; 41(6): 2221-2229.
24. Yu L, Fang F, Lu S, Li X, Yang Y, Wang Z. lncRNA-HIT promotes cell proliferation of non-small cell lung cancer by association with E2F1. Cancer Gene Ther. 2017; 24(5): 221-226.
25. Zhang EB, Yin DD, Sun M, Kong R, Liu XH, You LH, et al. P53-regulated long non-coding RNA TUG1 affects cell proliferation in human non-small cell lung cancer, partly through epigenetically regulating HOXB7 expression. Cell Death Dis. 2014; 5: e1243.
26. Zhang R, Xia Y, Wang Z, Zheng J, Chen Y, Li X, et al. Serum long non coding RNA MALAT-1 protected by exosomes is up-regulated and promotes cell proliferation and migration in non-small cell lung cancer. Biochem Biophys Res Commun. 2017; 490(2): 406-414.
27. Li S, Mei Z, Hu HB, Zhang X. The lncRNA MALAT1 contributes to non-small cell lung cancer development via modulating miR-124/STAT3 axis. J Cell Physiol, 2018; 233(9): 6679-6688.
28. Paraskevopoulou MD, Hatzigeorgiou AG. Analyzing miRNA-lncRNA interactions. Methods Mol Biol. 2016; 1402: 271-286.
29. Yu G, Yao W, Gumireddy K, Li A, Wang J, Xiao W, et al. Pseudogene PTENP1 functions as a competing endogenous RNA to suppress clear-cell renal cell carcinoma progression. Mol Cancer Ther. 2014; 13(12): 3086-3097.
30. Liu XH, Sun M, Nie FQ, Ge YB, Zhang EB, Yin DD, et al. Lnc RNA HOTAIR functions as a competing endogenous RNA to regulate HER2 expression by sponging miR-331-3p in gastric cancer. Mol Cancer. 2014; 13: 92.
31. Huang G, Wu X, Li S, Xu X, Zhu H, Chen X. The long noncoding RNA CASC2 functions as a competing endogenous RNA by sponging miR-18a in colorectal cancer. Sci Rep. 2016; 6: 26524.
32. Zhao Y, Li C, Wang M, Su L, Qu Y, Li J, et al. Decrease of miR-202-3p expression, a novel tumor suppressor, in gastric cancer. PLoS One. 2013; 8(7): e69756.
33. Sun Z, Zhang T, Hong H, Liu Q, Zhang H. miR-202 suppresses proliferation and induces apoptosis of osteosarcoma cells by downregulating Gli2. Mol Cell Biochem. 2014; 397(1-2): 277-283.
34. Zhang Y, Zheng D, Xiong Y, Xue C, Chen G, Yan B, et al. miR-202 suppresses cell proliferation in human hepatocellular carcinoma by downregulating LRP6 post-transcriptionally. FEBS Lett. 2014; 588(10): 1913-1920.
35. Zhang S, Cai J, Xie W, Luo H, Yang F. miR-202 suppresses prostate cancer growth and metastasis by targeting PIK3CA. Exp Ther Med. 2018; 16(2): 1499-1504.
36. Sun W, Ping W, Tian Y, Zou W, Liu J, Zu Y. miR-202 Enhances the anti-tumor effect of cisplatin on non-small cell lung cancer by targeting the Ras/MAPK pathway. Cell Physiol Biochem. 2018; 51(5): 2160-2171.
37. Zhao Z, Lv B, Zhang L, Zhao N, Lv Y. miR-202 functions as a tumor suppressor in non-small cell lung cancer by targeting STAT3. Mol Med Rep. 2017; 16(2): 2281-2289.
38. Wang J, Su L, Chen X, Li P, Cai Q, Yu B, et al. MALAT1 promotes cell proliferation in gastric cancer by recruiting SF2/ASF. Biomed Pharmacother. 2014; 68(5): 557-564.
39. Hu L, Wu Y, Tan D, Meng H, Wang K, Bai Y, et al. Up-regulation of long noncoding RNA MALAT1 contributes to proliferation and metastasis in esophageal squamous cell carcinoma. J Exp Clin Cancer Res. 2015; 34: 7.
40. Yang MH, Hu ZY, Xu C, Xie LY, Wang XY, Chen SY, et al. MALAT1 promotes colorectal cancer cell proliferation/migration/invasion via PRKA kinase anchor protein 9. Biochim Biophys Acta. 2015; 1852(1): 166-174.

Original Article

Gene Expression Microarray Data Meta-Analysis Identifies Candidate Genes and Molecular Mechanism Associated with Clear Cell Renal Cell Carcinoma

Ying Wang, Ph.D.[1#*], Haibin Wei, M.Sc.[2#], Lizhi Song, M.Sc.[1], Lu Xu, M.Sc.[1], Jingyao Bao, B.Sc.[1], Jiang Liu, Ph.D.[1*]

1. Institute of Aging Research, School of Medicine, Hangzhou Normal University, Hangzhou, Zhejiang, China
2. Department of Pathology, Zhejiang Cancer Hospital, Hangzhou, Zhejiang, China

#The first two authors equally contributed to this work.

Corresponding Address: Institute of Aging Research, School of Medicine, Hangzhou Normal University, Hangzhou, Zhejiang, China
Emails: flashingdancer@163.com, Jennings_L143@126.com

Received: 1/January/2019, Accepted: 10/June/2019

Abstract

Objective: We aimed to explore potential molecular mechanisms of clear cell renal cell carcinoma (ccRCC) and provide candidate target genes for ccRCC gene therapy.

Material and Methods: This is a bioinformatics-based study. Microarray datasets of GSE6344, GSE781 and GSE53000 were downloaded from Gene Expression Omnibus database. Using meta-analysis, differentially expressed genes (DEGs) were identified between ccRCC and normal samples, followed by Kyoto Encyclopedia of Genes and Genomes (KEGG) pathway and Gene Ontology (GO) function analyses. Then, protein-protein interaction (PPI) networks and modules were investigated. Furthermore, miRNAs-target gene regulatory network was constructed.

Results: Total of 511 up-regulated and 444 down-regulated DEGs were determined in the present gene expression microarray data meta-analysis. These DEGs were enriched in functions like immune system process and pathways like Toll-like receptor signaling pathway. PPI network and eight modules were further constructed. A total of 10 outstanding DEGs including TYRO protein tyrosine kinase binding protein (*TYROBP*), interferon regulatory factor 7 (*IRF7*) and PPARG co-activator 1 alpha (*PPARGC1A*) were detected in PPI network. Furthermore, the miRNAs-target gene regulation analyses showed that miR-412 and miR-199b respectively targeted *IRF7* and *PPARGC1A* to regulate the immune response in ccRCC.

Conclusion: *TYROBP*, *IRF7* and *PPARGC1A* might play important roles in ccRCC via taking part in the immune system process.

Keywords: Clear Cell Renal Cell Carcinoma, Immune Response, Protein-Protein Interaction Network

Cell Journal(Yakhteh), Vol 22, No 3, October-December (Autumn) 2020, Pages: 386-393

Citation: **Wang Y, Wei H, Song L, Xu L, Bao J, Liu J. Gene expression microarray data meta-analysis identifies candidate genes and molecular mechanism associated with clear cell renal cell carcinoma. Cell J. 2020; 22(3): 386-393. doi: 10.22074/cellj.2020.6561.**

Introduction

Clear cell renal cell carcinoma (ccRCC) is a type of RCC developed in adults (1). It has been reported that ccRCC is the most aggressive subtype of RCC (2). Surgery by radical or partial nephrectomy is the main choice for treatment of ccRCC. Although chemotherapy and immunotherapy could be applicable in patients with metastatic ccRCC, the outcome is unsatisfactory (3). Even some of ccRCC are along with the worst prognosis among the common epithelial tumors of the kidney (4). Therefore, exploring molecular biomarkers serving as diagnostic and therapeutic targets, when used alone or in combination with other clinical parameters, are urgently required for better clinical management.

Accumulating evidences suggest that certain differentially expressed genes (DEGs) are closely related to disease progression. Duns et al. (5) showed that histone methyltransferase gene SET domain containing 2 (*SETD2*) is a novel tumor suppressor gene in the process of ccRCC. A chromatin-remodeling gene AT-rich interaction domain 1A (*ARID1A*) is considered to be a new prognostic marker in ccRCC (6). Actually, these genes often play important roles in ccRCC progression via certain function or specific pathways. A recent study indicated that frequent methylation of Kelch like ECH associated protein 1 (*KEAP1*) gene promoter was vital for ccRCC development via KEAP1/ nuclear factor erythroid-2 related factor (NRF2) pathway (7). Moreover, some microRNAs (miRNAs) are abnormally expressed in ccRCC and contribute to tumorigenesis. Urinary miRNAs have been proved to be the predictors of tumor metastasis in ccRCC (8). Yang et al. (9) showed that miR-506 was down-regulated in ccRCC and inhibited cell growth and metastasis via targeting flotillin 1. Although there have been many researches to find genetic biomarkers for ccRCC, characterization progress of the genetic events associated with this cancer is not fully clear yet.

In this study, meta-analysis was used to detect potential DEGs between ccRCC and normal samples based on three microarray datasets. Moreover, functional and pathway enrichment analyses were carried out for these DEGs. Then, protein-protein interaction (PPI) network was investigated. Furthermore, miRNA-target gene interaction network was constructed. We hoped to explore

the underlying molecular mechanisms of ccRCC and provide candidate target genes for ccRCC gene therapy.

Materials and Methods

Microarray data and preprocessing

This is a bioinformatics-based study. Microarray datasets were downloaded from Gene Expression Omnibus database based on the data quantity, sample grouping, microarray platform (Affymetrix) and number of citation. Finally, three datasets were selected: GSE6344, GSE781 and GSE53000. The reasons for selection are as follows: i. Large data quantities, ii. Clear grouping of the experiment (tumor vs. normal), iii. Common microarray platforms (Affymetrix), iv. Consistent sample types (tissue samples). In details, 10 ccRCC and 10 normal tissue samples sequencing on the platform of GPL96 [HG-U133A] Affymetrix Human Genome U133A Array were selected for analysis in microarray dataset GSE6344 (10). For GSE781 (11), 12 ccRCC and 5 normal tissue samples sequenced on the platform of GPL96 [HG-U133A] Affymetrix Human Genome U133A Array were selected. In addition, all samples in GSE53000 (12) (56 ccRCC and 6 normal tissue samples) sequencing on the platform of [HuGene-1_0-st] Affymetrix Human Gene 1.0 ST Array [transcript (gene) version] were used for analysis. Specially, GSE53000 included two samples of lymph node metastasis and one sample of venous thrombus metastasis. Thus, principal component analysis (PCA) was carried out for the 56 ccRCC tissue samples and 6 normal tissue samples. As shown in Figure S1 (Supplementary Online Information at www.celljournal.org), two samples from lymph node metastasis and one sample from venous thrombus metastasis were obviously clustered together, while separated from normal samples. So they could be unified as tumor group for the following analysis. Sample information of the three datasets was shown in Tables S1-S3 (Supplementary Online Information at www.celljournal.org). In order to eliminate the expression value heterogeneity of each gene in different platforms, CEL format of files of three datasets were pooled together and preprocessed using Affy software, including background adjustment, quantiles normalization, summarization and log2 fold change (FC) transformation using Robust Multi-array Average (RMA) algorithm in Affy package (13). The probe identities were converted to gene symbols based on the annotation files downloaded from different platforms. Probes that did not correspond to gene symbols were discarded. For different probes matched to one gene, the average value of different probes was used as the final expression value.

Differentially expressed genes identification

DEGs of ccRCC and normal samples were separately screened based on multiple experimental datasets using MetaDE package in R software (14). The heterogeneity test was performed according to the expression values of each gene under different experimental platforms with the statistical parameters of tau2, Qvalue and Qpval. The tau2=0 [estimated amount of (residual) heterogeneity] and Qpval>0.05 (P values for the test of heterogeneity) represented significant homogeneity. Finally, Benjamini-Hochber adjusted P value (fdr) <0.05, tau2=0 and Qpval >0.05 were considered as the cut-off criteria for DEGs selection. Furthermore, the log2 FC of ccRCC vs. normal >0 represented up-regulated DEGs, while log2 FC of ccRCC vs. normal <0 represented that DEGs were down-regulated.

Functional annotation and pathway enrichment analysis of differentially expressed genes

The clusterProfiler is an online tool applied for enrichment analysis (15). Gene Ontology (GO) functional annotation was used to analyze functions assembled with the up- and down-regulated genes by clusterProfiler. GO functions include molecular function (MF), biological process (BP) and cellular component (CC). To better understand pathways of the involved DEGs, Kyoto Encyclopedia of Genes and Genomes (KEGG) pathway enrichment analysis was performed using clusterProfiler. A P value (the significance threshold of the hypergeometric test) of <0.05 and count (the number of enriched genes) of >2 were used as the cut-off criteria for this analysis.

Constructing protein-protein interaction network and modules analyses

PPI plays a key role in the completion of cellular functions, while they are usually correlated to each other in the form of a PPI network. The Search Tool for the Retrieval of Interacting Genes/Proteins (STRING) is a biological database of predicted and known PPIs. According to this database, the PPI network of DEG-encoding proteins in each group was constructed with the criterion of combined score (medium confidence) >0.4, and it was then visualized by the Cytoscape (version 3.2.0) software (National Institute of General Medical Sciences, USA). Score of nodes in the current network was analyzed using degree centrality, a topology property index. Higher node score presented more important node in the network, suggesting that is more likely the hub node in this network. Furthermore, the MCODE tool (National Institute of General Medical Sciences, USA) (16) in Cytoscape was used to screen the modules from the network.

miRNA-target gene regulatory network construction

The potential ccRCC related miRNAs were explored based on Enrichr database. The miRNA-target gene regulatory network was constructed with the miRNA associating with up- and down-regulated gene based on Cytoscape software (National Institute of General Medical Sciences, USA).

Results

Differentially expressed genes investigation between clear cell renal cell carcinoma and control groups

With fdr <0.05, tau2=0 and Qpval >0.05, 955 DEGs

were identified in ccRCC group compared to that of the normal controls, including 511 up-regulated and 444 down-regulated genes.

Gene ontology function and Kyoto Encyclopedia of Genes and Genomes pathway enrichment analyses

Using clusterProfiler, GO functional enrichment analysis was performed and the results showed that the up-regulated DEGs were significantly enriched in functions like immune system process (GO_BP, P=5.02E^{-18}), intracellular (GO_CC, P=5.86 E^{-06}) and protein binding (GO_MF, P=1.09E^{-18}). Meanwhile, the down-regulated genes were mainly enriched in functions like small molecule metabolic process (GO_BP, P=1.39E^{-39}), cytoplasm (GO_CC, P=1.01E^{-06}) and binding (GO_MF, P=3.81E^{-16}) (Fig.1).

Pathway enrichment analysis showed that the up-regulated genes were enriched in pathways like Toll-like receptor signaling pathway (P=1.94E^{-05}), while the down-regulated genes were enriched in pathways like metabolic pathways (P=1.27E^{-28}). The top five enriched pathways are listed in Table 1.

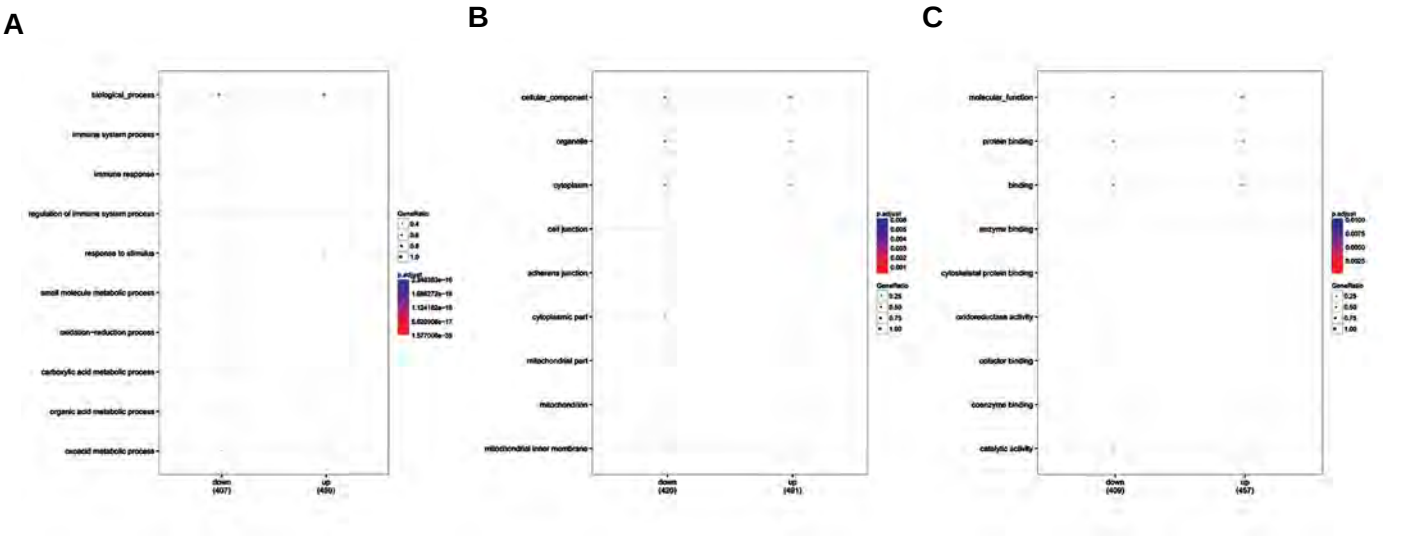

Fig.1: GO functional enrichment analysis for DEGs between ccRCC and normal samples. **A.** Up- and down-regulated genes presented in top none biological processes. **B.** Up- and down-regulated genes presented in top eight cellular functions. **C.** Up- and down-regulated genes presented in top eight molecular functions. GO; Gene ontology, ccRCC; Clear cell renal cell carcinoma, and DEGs; Differentially expressed genes.

Table 1: Top five KEGG pathways enriched by the differentially expressed genes in clear cell renal cell carcinoma

Category	Pathway ID	Pathway	Count	P value
Up	hsa04620	Toll-like receptor signaling pathway	13	1.94E^{-05}
	hsa05133	Pertussis	11	2.13E^{-05}
	hsa04145	Phagosome	14	3.15E^{-04}
	hsa05150	Staphylococcus aureus infection	8	3.18E^{-04}
	hsa04666	Fc gamma R-mediated phagocytosis	10	5.19E^{-04}
Down	hsa01100	Metabolic pathways	113	1.27E^{-28}
	hsa01200	Carbon metabolism	26	9.72E^{-16}
	hsa00190	Oxidative phosphorylation	26	5.04E^{-14}
	hsa05012	Parkinson's disease	26	2.56E^{-13}
	hsa00280	Valine, leucine and isoleucine degradation	15	1.04E^{-11}

P<0.05 was considered to be significantly different. KEGG; Kyoto encyclopedia of genes and genomes.

Protein-protein interaction network and modules investigation

To dig out more effective information, regarding the DEGs mentioned above, PPI network was constructed on the basis of interaction relationship among the proteins. With score=0.4, a total of 2483 PPI pairs and 643 DEG-encoded proteins were identified. According to the score of degree centrality, TYRO protein tyrosine kinase binding protein (TYROBP, degree=68, up-regulation), cathepsin S (CTSS, degree=53, up-regulation), colony stimulating factor 1 receptor (CSF1R, degree=52, up-regulation), Fc fragment of IgE receptor Ig (FCER1G, degree=43, up-regulation), protein tyrosine phosphatase, receptor type C (PTPRC, degree=43, up-regulation), mitogen-activated protein kinase 1 (MAPK1, degree=43, up-regulation), CD53 molecule (CD53, degree=42, up-regulation), Ras-related C3 botulinum toxin substrate 2 (RAC2, degree=42, up-regulation), cluster of differentiation 14 (CD14, degree=41, up-regulation), cytochrome C, and somatic (CYCS, degree=40, down-regulation) were the top 10 proteins encoded by DEGs.

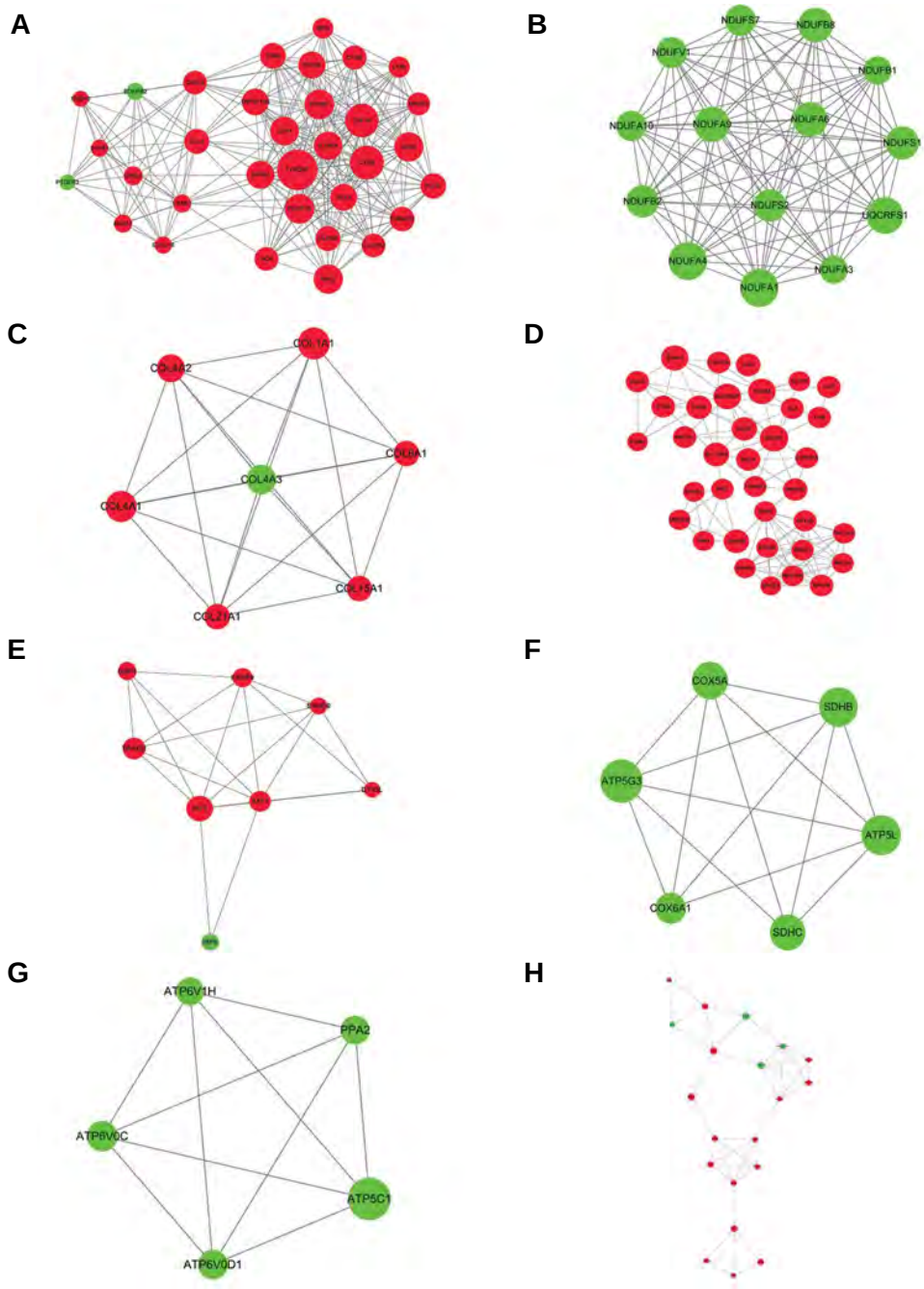

Fig.2: The modules obtained from protein-protein interaction network. **A.** The module "a" was constructed by 33 nodes and 267 interactions. **B.** The module "b" was constructed by 14 nodes and 91 interactions. **C.** The module "c" was constructed by 7 nodes and 21 interactions. **D.** The module "d" was constructed by 36 nodes and 114 interactions. **E.** The module "e" was constructed by 8 nodes and 20 interactions. **F.** The module "f" was constructed by 6 nodes and 14 interactions. **G.** The module "g" was constructed by 5 nodes and 10 interactions. **H.** The module "h" was constructed by 20 nodes and 39 interactions. Green node represents down-regulated gene; red node represents up-regulated gene.

The MOCDE software showed eight modules from PPI network. The detail information was showed in Figure 2. To further investigate crucial pathways involved in the process of ccRCC, the KEGG pathway analysis was performed on DEGs in these modules. Results showed that chemokine signaling pathway ($P=4.88E^{-05}$), Parkinson's disease ($P=3.17E^{-24}$), protein digestion and absorption ($P=3.31E^{-08}$) and ribosome ($P=5.00E^{-08}$) were the most significant pathways enriched by DEG-encoded proteins in the respectively modules a, b, c and d. Meanwhile, NOTCH signaling pathway ($P=3.99E^{-02}$), oxidative phosphorylation ($P=7.89E^{-10}$), oxidative phosphorylation ($P=5.74E^{-08}$) and adipocytokine signaling pathway ($P=2.18E^{-02}$) were the most significant pathways enriched respectively by modules e, f, g and h. The top two KEGG pathways in each module are listed in Table 2.

miRNAs-target gene regulatory network analyses

Here, miRNAs targeted up- and down-regulated genes were investigated based on Enrichr software. Then, the regulatory network was constructed using Cytoscape software. Results showed that there were four miRNAs (including miR-145, miR-199B, miR-199A and miR-412), 94 up-regulated genes [such as interferon regulatory factor 7 (*IRF7*), TYRO protein tyrosine kinase binding protein (*TYROBP*) and *CD14*)], as well as 45 down-regulated genes [such as PPARG coactivator 1 alpha (*PPARGC1A*), dystroglycan 1 (*DAG1*) and klotho (*KL*)] in the present network (Fig.3).

Table 2: Top two KEGG pathways in modules enriched by the differentially expressed genes of clear cell renal cell carcinoma

Module ID	Pathway ID	Pathway name	Count	P value	Genes
a	hsa04062	Chemokine signaling pathway	6	$4.88E^{-05}$	*CXCL9, RAC2, CXCL16, HCK, GNG2...*
	hsa04060	Cytokine-cytokine receptor interaction	6	$3.17E^{-04}$	*CXCL9, IL10RA, CXCL16, TNFSF13B, CSF1R...*
b	hsa05012	Parkinson's disease	14	$3.17E^{-24}$	*NDUFB2, NDUFA3, UQCRFS1, NDUFA9, NDUFB8...*
	hsa00190	Oxidative phosphorylation	14	$3.97E^{-24}$	*NDUFB2, NDUFA3, UQCRFS1, NDUFA9, NDUFB8...*
c	hsa04974	Protein digestion and absorption	4	$3.31E^{-08}$	*COL4A2, OL1A1, COL4A1, COL15A1*
	hsa04512	ECM-receptor interaction	3	$1.15E^{-05}$	*COL4A2, COL1A1, COL4A1*
d	hsa03010	Ribosome	7	$5.00E^{-08}$	*RPL35A, RPS24, RPS15A, RPS16, RPL30...*
	hsa05150	Staphylococcus aureus infection	4	$6.74E^{-05}$	*ITGAM, C1QA, C3AR1, C1QC*
e	hsa04330	Notch signaling pathway	1	$3.99E^{-02}$	*DTX3L*
	hsa04623	Cytosolic DNA-sensing pathway	1	$3.99E^{-02}$	*IRF7*
f	hsa00190	Oxidative phosphorylation	6	$7.89E^{-10}$	*SDHB, COX5A, COX6A1, SDHC, ATP5G3...*
	hsa05012	Parkinson's disease	5	$9.97E^{-08}$	*DHB, COX5A, COX6A1, SDHC, ATP5G3*
g	hsa00190	Oxidative phosphorylation	5	$5.74E^{-08}$	*ATP6V0D1, ATP6V0C, PPA2, ATP5C1, ATP6V1H...*
	hsa05110	Vibrio cholerae infection	3	$3.94E^{-05}$	*ATP6V0D1, ATP6V0C, ATP6V1H*
h	hsa04920	Adipocytokine signaling pathway	3	$2.18E^{-02}$	*MTOR, PPARGC1A, PPARA*

KEGG; Kyoto Encyclopedia of Genes and Genomes.

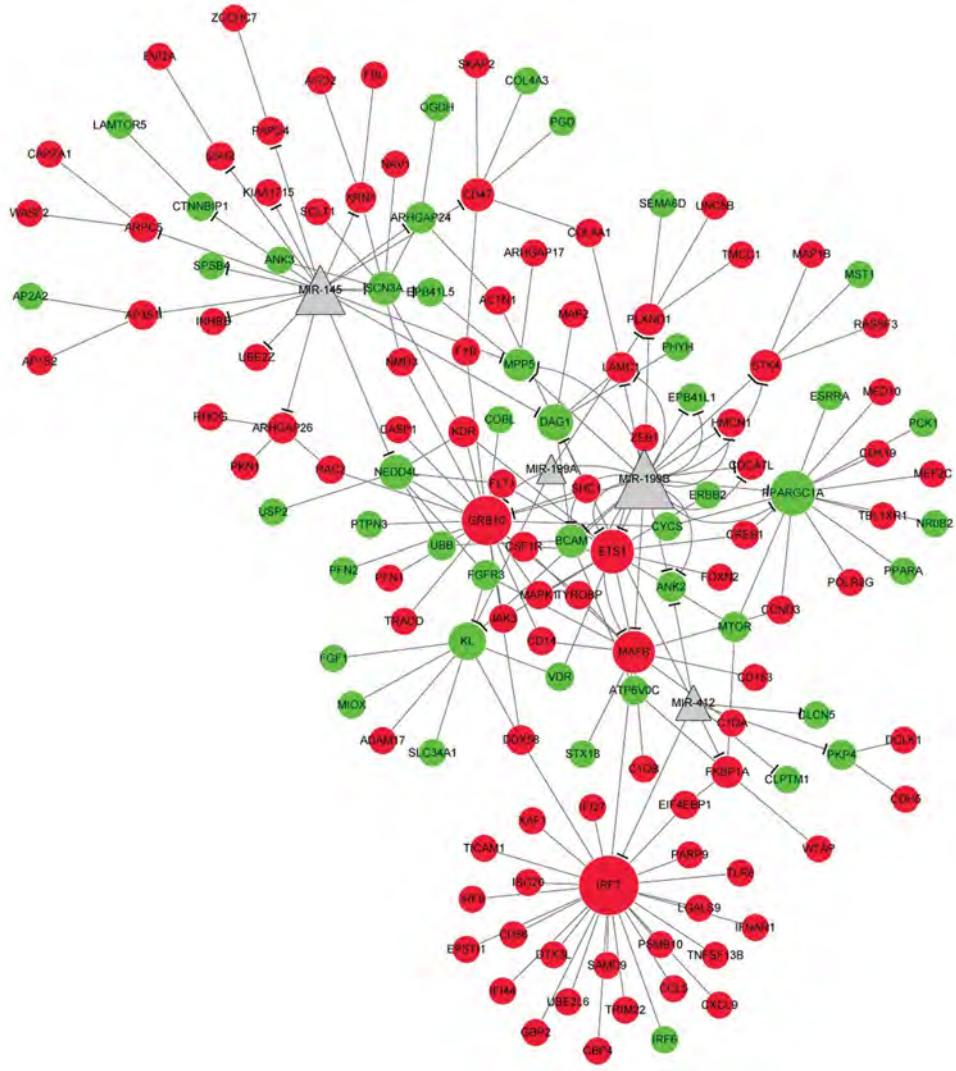

Fig.3: miRNAs-genes regulatory network. Green node represents down-regulated gene, red node represents up-regulated gene and grey triangle represents miRNA.

Discussion

ccRCC is one of the most common RCC identified in adults presenting the worst prognosis among the common epithelial tumors of kidney. In this study, total 955 DEGs were identified in ccRCC from normal samples. GO analysis showed that these DEGs, including up-regulated *TYROBP* and *IRF7*, and down-regulated *PPARGC1A*, were mainly enriched in functions like immune system and small molecule metabolic processes. KEGG enrichment analysis demonstrated that these DEGs were significantly enriched in the pathways like Toll-like receptor signaling pathway as well as metabolic pathways. Furthermore, *IRF7* was predicted to be targeted by miR-412 and *PPARGCA1* could be targeted by miR-199B.

Immune system protects host body against disease. Aberration of immune system could lead to inflammatory diseases, autoimmune diseases and cancer (17). Importantly, ccRCC has shown extensive responses to immune checkpoint blockade therapies (18). Based on an in-depth immune profiling study, Chevrier et al. (19) identified that *CD38* and *CD204* involved in the tumor microenvironment modulate cancer progression. Previous study has presented that orchestration of immune checkpoints has prognostic value in ccRCC (20), but detailed mechanism of the checkpoints in ccRCC is yet unclear.

TYROBP is the encoding gene of a transmembrane signaling polypeptide, which possesses an immunoreceptor tyrosine-based activation motif in its cytoplasmic domain (21). Previous study reported that TYROBP associated with the killer cell immunoglobulin-like receptor family and it served as an activating signal transduction element in cells (22). *TYROBP* is reported to be related to Alzheimer's pathology (21). Deficiency of *TYROBP* is neuroprotective in a mouse model with early Alzheimer's pathology. Meanwhile, the bone remodeling and brain function also depend on the integrity of *TYROBP* signal (23). In addition, it has been documented that TYROBP presents a general function in inflammatory responses in microglia via the Jun NH2-terminal kinase (JNK)

signaling pathway (24). However, very rare studies focus on *TYROBP* correlation with ccRCC. In the current study, functional enrichment analysis showed that *TYROBP* was significantly enriched in the BP of immune system, indicating that *TYROBP* might also play critical role in the pathogenic inflammatory response of ccRCC. However, further analysis of *TYROBP* is still required to reveal the exact mechanism involved in pathogenesis of ccRCC.

IRF7, encoded interferon regulatory factor, is a member of type I interferon regulatory transcription factor family, which plays a critical role in the innate immunity (25). *IRF7* silencing promotes bone metastasis of breast cancer via immune escape way (26). Coit et al. (27) have documented that *IRF7* plays critical role in renal involved in lupus via regulating demethylation of DNA in naive $CD4^+$ T cells. It was also reported that *IRF7* can serve as a therapeutic target against renal tissue damage caused by bacterial infection (28). In the current study, functional enrichment analysis revealed that *IRF7* was significantly enriched in the Toll-like receptor signaling pathway and immune response biological process. Toll-like receptor signaling pathway has been reported to play crucial roles in the inflammation, infection and cancer (29). Moreover, *IRF7* was predicted to be targeted by miR-412 in ccRCC. miR-412 is a mature type of miR-142, contributing to important functions in inflammatory and immune response among different diseases (30). Taken together, we speculated that miR-412 might present a critical role in the immune response of ccRCC via targeting *IRF7* in Toll-like receptor signaling pathway.

PPARGCA1 is the encoding gene of PPARG co-activator 1α, which is a co-regulator of mitochondrial biogenesis and oxidative phosphorylation. Cho et al. (31) have documented that genetic variation of *PPARGCA1* regulates diet-associated inflammation in colorectal cancer. Moreover, polymorphisms of *PPARGCA1* and lower expression of *PPARGCA1* are risk factors in the pathogenesis of non-alcoholic fatty liver disease, characterized by abnormal inflammatory response during etiology (32). In the current study, down-regulation of *PPARGCA1* was identified in ccRCC samples and functional enrichment showed that *PPARGCA1* was significantly enriched in the immune response biological process. Further analysis showed that *RRARGCA1* was regulated by miR-199b. miR-199b is down-regulated in several solid tumors (33). Hou et al. (34) have documented that down-regulation of miR-199b strongly correlated with poor survival of HCC patients. In addition, miR-199b associated with poor survival of ovarian cancer patients, and loss of miR-199b results in hypermethylation in ovarian cancer (35). These evidences indicated that miR-199b might contribute to the pathogenesis of ccRCC via regulating *PPARGCA1* expression.

Conclusion

Abnormal immune response might be an important mechanism of ccRCC. *TYROBP, IRF7* and *PPARGCA1* might play important roles in ccRCC via taking part in the immune system. Furthermore, miR-199B and miR-412 might serve critical roles in the regulation of immune response via targeting *PPRARGCA1* and *IRF7*, respectively. Considering these findings, miR-199b and miR-412 might be used as the prognostic target for ccRCC gene therapy.

Acknowledgements

There is no financial support and conflict of interest in this study.

Authors' Contributions

Y.W., H.W.; Contributed to the design of research, acquisition of data, analysis and interpretation of data, statistical analysis and drafting the manuscript. L.S., L.X., J.B.; Contributed to the analysis and interpretation of data and statistical analysis. J.L.; Contributed to the design of research. All authors read and approved the final manuscript.

References

1. Hakimi AA, Reznik E, Lee CH, Creighton CJ, Brannon AR, Luna A, et al. Commentary on: "An integrated metabolic atlas of clear cell renal cell carcinoma." Urol Oncol. 2017; 35(9): 579-580.
2. Cohen HT, McGovern FJ. Renal-cell carcinoma. N Engl J Med. 2005; 353(23): 2477-2490.
3. Thomas JS, Kabbinavar F. Metastatic clear cell renal cell carcinoma: a review of current therapies and novel immunotherapies. Crit Rev Oncol Hematol. 2015; 96(3): 527-533.
4. Frew IJ, Moch H. A clearer view of the molecular complexity of clear cell renal cell carcinoma. Annu Rev Pathol. 2015; 10: 263-289.
5. Duns G, van den Berg E, van Duivenbode I, Osinga J, Hollema H, Hofstra RM, et al. Histone methyltransferase gene SETD2 is a novel tumor suppressor gene in clear cell renal cell carcinoma. Cancer Res. 2010; 70(11): 4287-4291.
6. Lichner Z, Scorilas A, White NM, Girgis AH, Rotstein L, Wiegand KC, et al. The chromatin remodeling gene ARID1A is a new prognostic marker in clear cell renal cell carcinoma. Am J Pathol. 2013; 182(4): 1163-1170.
7. Fabrizio FP, Costantini M, Copetti M, la Torre A, Sparaneo A, Fontana A, et al. Keap1/Nrf2 pathway in kidney cancer: frequent methylation of KEAP1 gene promoter in clear renal cell carcinoma. Oncotarget. 2017; 8(7): 11187-11198.
8. Shu X, Hildebrandt MAT, Reis RBd, Ye Y, Gu J, Wood CG, et al. Abstract 1527: Urinary miRNAs as predictors of tumor metastasis in localized patients with clear cell renal cell carcinoma: a pilot study. Cancer Res. 2016; 76(14 Suppl): 1527.
9. Yang FQ, Zhang HM, Chen SJ, Yan Y, Zheng JH. Correction: MiR-506 is down-regulated in clear cell renal cell carcinoma and inhibits cell growth and metastasis via targeting FLOT1. PLoS One. 2015; 10(5): e0129404.
10. Gumz ML, Zou H, Kreinest PA, Childs AC, Belmonte LS, Legrand SN, et al. Secreted Frizzled-related protein 1 loss contributes to tumor phenotype of clear cell renal cell carcinoma. Clin Cancer Res. 2007; 13(16): 4740-4749.
11. Lenburg ME, Liou LS, Gerry NP, Frampton GM, Cohen HT, Christman MF. Previously unidentified changes in renal cell carcinoma gene expression identified by parametric analysis of microarray data. BMC Cancer. 2003; 3: 31.
12. Gerlinger M, Horswell S, Larkin J, Rowan AJ, Salm MP, Varela I, et al. Genomic architecture and evolution of clear cell renal cell carcinomas defined by multiregion sequencing. Nat Genet. 2014; 46(3): 225-233.
13. Gautier L, Cope L, Bolstad BM, Irizarry RA. affy--analysis of Affymetrix GeneChip data at the probe level. Bioinformatics. 2004; 20(3): 307-315.
14. Qi C, Hong L, Cheng Z, Yin Q. Identification of metastasis-associated genes in colorectal cancer using metaDE and survival analysis. Oncol Lett. 2016; 11(1): 568-574.
15. Yu G, Wang LG, Han Y, He QY. clusterProfiler: an R package for

comparing biological themes among gene clusters. OMICS. 2012; 16(5): 284-287.
16. Bader GD, Hogue CW. An automated method for finding molecular complexes in large protein interaction networks. BMC Bioinformatics. 2003; 4: 2.
17. O'Byrne KJ, Dalgleish AG. Chronic immune activation and inflammation as the cause of malignancy. Br J Cancer. 2001; 85(4): 473-483.
18. Giraldo NA, Becht E, Pagès F, Skliris G, Verkarre V, Vano Y, et al. Orchestration and prognostic significance of immune checkpoints in the microenvironment of primary and metastatic renal cell cancer. Clin Cancer Res. 2015; 21(13): 3031-3040.
19. Chevrier S, Levine JH, Zanotelli VRT, Silina K, Schulz D, Bacac M, et al. An immune atlas of clear cell renal cell carcinoma. Cell. 2017; 169(4): 736-749. e18.
20. Stone L. Kidney cancer: orchestration of immune checkpoints has prognostic value in ccRCC. Nat Rev Urol. 2015; 12(4): 182.
21. Ma J, Jiang T, Tan L, Yu JT. TYROBP in Alzheimer's disease. Mol Neurobiol. 2015; 51(2): 820-826.
22. Campbell KS, Colonna M. DAP12: a key accessory protein for relaying signals by natural killer cell receptors. Int J Biochem Cell Biol. 1999; 31(6): 631-636.
23. Tomasello E, Vivier E. KARAP/DAP12/TYROBP: three names and a multiplicity of biological functions. Eur J Immunol. 2005; 35(6): 1670-1677.
24. Zhong L, Zhang ZL, Li X, Liao C, Mou P, Wang T, et al. TREM2/DAP12 complex regulates inflammatory responses in microglia via the JNK signaling pathway. Front Aging Neurosci. 2017; 9: 204.
25. Kocić G, Radenkovic S, Cvetkovic T, Cencic A, Carluccio F, Musovic D, et al. Circulating nucleic acids as possible damage-associated molecular patterns in different stages of renal failure. Ren Fail. 2010; 32(4): 486-492.
26. Bidwell BN, Slaney CY, Withana NP, Forster S, Cao Y, Loi S, et al. Silencing of Irf7 pathways in breast cancer cells promotes bone metastasis through immune escape. Nat Med. 2012; 18(8): 1224-1231.
27. Coit P, Renauer P, Jeffries MA, Merrill JT, Mccune WJ, Maksimowiczmckinnon K, et al. Renal involvement in lupus is characterized by unique DNA methylation changes in naïve CD4+ T cells. J Autoimmun. 2015; 61: 29-35.
28. Puthia M, Ambite I, Cafaro C, Butler D, Huang Y, Lutay N, et al. IRF7 inhibition prevents destructive innate immunity-A target for nonantibiotic therapy of bacterial infections. Sci Transl Med. 2016; 8(336): 336ra59.
29. Chen K, Huang J, Gong W, Iribarren P, Dunlop NM, Wang JM. Toll-like receptors in inflammation, infection and cancer. Int Immunopharmacol. 2007; 7(10): 1271-1285.
30. Sharma S. Immunomodulation: A definitive role of microRNA-142. Dev Comp Immunol. 2017; 77: 150-156.
31. Cho YA, Lee J, Oh JH, Chang HJ, Sohn DK, Shin A, et al. Genetic variation in PPARGC1A may affect the role of diet-associated inflammation in colorectal carcinogenesis. Oncotarget. 2017; 8(5): 8550-8558.
32. Yoneda M, Hotta K, Nozaki Y, Endo H, Uchiyama T, Mawatari H, et al. Association between PPARGC1A polymorphisms and the occurrence of nonalcoholic fatty liver disease (NAFLD). BMC Gastroenterol. 2008; 8: 27.
33. Mudduluru G, Ceppi P, Kumarswamy R, Scagliotti GV, Papotti M, Allgayer H. Regulation of Axl receptor tyrosine kinase expression by miR-34a and miR-199a/b in solid cancer. Oncogene. 2011; 30(25): 2888-2899.
34. Hou J, Lin L, Zhou W, Wang Z, Ding G, Dong Q, et al. Identification of miRNomes in human liver and hepatocellular carcinoma reveals miR-199a/b-3p as therapeutic target for hepatocellular carcinoma. Cancer Cell. 2011; 19(2): 232-243.
35. Liu MX, Siu MK, Liu SS, Yam JW, Ngan HY, Chan DW. Epigenetic silencing of microRNA-199b-5p is associated with acquired chemoresistance via activation of JAG1-Notch1 signaling in ovarian cancer. Oncotarget. 2014; 5(4): 944-958.

Original Article

Endoplasmic Reticulum Stress Induces miR-706, A Pro-Cell Death microRNA, in A Protein Kinase RNA-Like ER Kinase (PERK) and Activating Transcription Factor 4 (ATF4) Dependent Manner

Xiu Wang, M.D.[1#*], Yi Han, M.D., Ph.D.[2#], Guodong Hu, M.D.[2], Jianbo Guo, M.D., Ph.D.[3], Hongyu Chen, M.D.[2]

1. Department of Anesthesiology, The Fourth Affiliated Hospital of China Medical University, Shenyang, Liaoning, China
2.The Second Department of Urology, Shenyang Red Cross Hospital, Shenyang, People's Republic of China (CHN)
3. The Third Department of General Surgery, The Fourth affiliated Hospital of China, Medical University, Shenyang, Liaoning, China

#The first two authors equally contributed to this work.

***Corresponding Address: Department of Anesthesiology, The Fourth Affiliated Hospital of China Medical University, Shenyang, Liaoning, China**
Email: a6860330@yahoo.com*

Received: 9/April/2019, Accepted: 22/June/2019

Abstract

Objective: Endoplasmic reticulum (ER) stress causes an adaptive response initiated by protein kinase RNA-like ER kinase (PERK), Ire1 and ATF6. It has been reported that these upstream regulators induce microRNAs. The current study was designed to find a novel microRNA that mediates ER stress components and finally contributes to cell fate decision.

Materials and Methods: In this experimental study, miR-706 levels were checked under different conditions of ER stress induced by Thapsigargin, Tunicamycin or low glucose media. PERK and ATF4 were knocked-down by administration of lentivirus-mediated short hairpin RNA to explore the effect of ER stress related proteins on miR-706 expression. The effect of miR-706 on caspase activity and apoptosis inhibitor 1 (*CAAP1*) levels were examined by using mimic-miR-706. The role of CAAP1 in inhibiting cell death (measured by Annexin V staining) and contributing to patient overall survival (measured by Kaplan-Meier estimate) were further confirmed by anti-miR-706 and CAAP1 knock-down.

Results: We showed that Thapsigargin or Tunicamycin triggered ER stress leading to the induction of miR-706. miR-706 induction is dependent on PERK and its downstream regulator ATF4, as knocking-down of PERK and ATF4 suppressed miR-706 induction in response to ER stress. Knocking-down of miR-706 reduces cell death triggered by ER stress, indicating that miR-706 is pro-cell death microRNA. We further identified *CAAP*1 as a miR-706 target in regulating ER stress initiated cell death.

Conclusion: Collectively, our results pointed to an ER signaling network consisting of proteins, microRNA and novel target.

Keywords: Activating Transcription Factor 4, Caspase Activity and Apoptosis Inhibitor 1, Endoplasmic Reticulum Stress, miR-706, Protein Kinase RNA-Like ER Kinase

Cell Journal(Yakhteh), Vol 22, No 3, October-December (Autumn) 2020, Pages: 394-400

Citation: **Wang X, Han Y, Hu G, Guo J, Chen H. Endoplasmic reticulum stress induces miR-706, a pro-cell death microRNA, in a protein kinase RNA-like ER kinase (PERK) and activating transcription factor 4 (ATF4) dependent manner. Cell J. 2020; 22(3): 394-400. doi: 10.22074/cellj.2020.6873.**

Introduction

Unfolded protein response (UPR) or endoplasmic reticulum (ER) stress is a signaling pathway elicited in response to various stimuli such as hypoxia during low oxygen pressure in tumors, virus infection and other stresses which disturb cell homeostasis (1-3). During UPR, unfolded proteins are accumulated in the ER lumen and these then interact with binding immunoglobulin protein (BiP, also known as GRP-78) (4-6). In homeostatic cell, BiP is bound to three upstream regulators of UPR, as protein kinase RNA-like ER kinases (PERKs), IRE1 and ATF6 (7, 8). In the presence of unfolded proteins, BiP is released from these UPR regulators and binds to unfolded proteins. This triggers activation of PERK, Ire1 and ATF6 by oligomerization (9, 10). Ire1 is composed of a domain that senses stress and it is in the lumen of the ER. This protein has a single transmembrane domain as well as the cytosolic domain that contains a protein kinase sub-domain and RNase sub-domain (11). Ire1 triggers expression of X-box binding protein 1 (Xbp1) transcription factor (12).

PERK activation leads to translational suppression via eIF2 alpha serine 51 phosphorylation and this causes ATF4 production (13). ATF4 is a transcription factor which in turn induces pro-apoptotic protein CHOP (14-17). PERK plays important role in diabetes, cancer and Alzheimer's disease (14, 18-20). PERK has dual seemingly contradictory activities. When the stress is brief, PERK induces anti-apoptotic components like miR-211, while the stress is prolonged, it induces pro-apoptotic CHOP (16).

microRNAs (miR) are almost 22 nucleotides RNAs

coding no protein. However, they perform diverse functions in a variety of biological processes by post-transcriptional regulation of gene expression (21-24). Regulation of microRNAs by all three branches of UPR (PERK, IRE1 and ATF6) has been well documented in the past decades (25, 26). Here, we show that PERK induces miR-706 and this microRNA promotes cell death in the later stages of cell stress. The miR-706 dependent cell death is regulated by the PERK/ATF4 signaling through targeting caspase activity and apoptosis inhibitor 1 (CAAP1).

Materials and Methods

Cell cultures

In this experimental study, NIH3T3 mouse embryonic fibroblasts (CRL1658, ATCC, USA) and AML12 mouse hepatic cells (CRL-2254™, ATCC) were cultured in Dulbecco's Modified Eagle Medium (DMEM, Invitrogen, USA) supplemented with 10% fetal bovine serum (Sigma-Aldrich, USA) at 37˚C in a humidified atmosphere of 5% CO_2. The cells were passaged every two days at 1:6 ratios. The cells were treated with 500 nM Thapsigargin (Sigma-Aldrich, USA) or 100 ng/ml Tunicamycin (Sigma-Aldrich, USA) unless otherwise noted. Human lung cancer cell line H1299 (CRL5803, ATCC), human ovarian cancer line SKOV3 (HTB-77, ATCC), human ovarian surface epithelial cell line HOSE (Beinachuanglian, PRC) and human lung fibroblast HFL1 (CCL153, ATCC) cells were cultured in RPMI 1640 (Invitrogen, USA) with 10% fetal bovine serum.

Knocking-down of PERK, ATF4 and CAAP1

Short hairpin RNA targeting PERK, ATF4 or CAAP1 from Dharmacon (USA) was transfected together with packaging plasmids (respectively pMDL, pVSVG or pRSV-Rev) into 293T cells by Lipofectamine 2000 (ThermoFisher, USA). For lentiviral transduction, NIH3T3 cells were incubated with 2 ml virus and 10 μg/ml polybrene (Sigma-Aldrich, USA) for three hours (27).

Mimic and antisense miR-706

Mimic miR-706 (MmiR3117-MR03) was purchased from Genecopoeia (USA). Oligos targeting miR-706 (MmiR-AN1135-SN-20, Genecoepoeia) were transfected using Lipofectamine 2000 as previously reported (28).

Quantitative reverse transcription polymerase chain reaction and Western blot

Ambion microRNA purification kit (Ambion, USA) and microRNA reverse transcription kit (Applied Biosystems, USA) were used for total RNA preparation and RNA reverse transcription. Quantitative reverse transcription PCR (qRT-PCR) was performed on an Applied Biosystems 7900 apparatus (Applied Biosystems, USA). Primers for miR-706, *ATF4,* and *CHOP* included:

miR-706-
F: 5′-ACACTCCAGCTGGGACAGAAACCCTGTCTC-3′
R: 5′-TGGTGTCGTGGAGTCG-3′

ATF4-
F: 5′-TCCTGAACAGCGAAGTGTTG-3′
R: 5′-ACCCATGAGGTTTCAAGTGC-3′

CHOP-
F: 5′-CTGCCTTTCACCTTGGAGAC-3′
R: 5′-CGTTTCCTGGGGATGAGATA-3′.

Western blot was also conducted as previously reported (29). The antibodies are: CAAP1 (NBP1-94020, Novus Biologicals, USA) and GAPDH (14C10, Cell Signaling Technology, USA).

Measurement of cell death

Cells were trypsinized, spun and stained with APC-annexin V (30) (BD Biosciences, USA) according to the manufacturer's protocol. The samples were run on FACS Canto (BD Biosciences, USA) to collect APC-annexin V fluorescence (31).

Results

miR-706 is an endoplasmic reticulum stress-dependent microRNA

To determine if ER stress triggers miR-706, NIH3T3 cells were incubated with Thapsigargin for 5 and 10 hours. We used these time points as they are early enough to induce in full gear pro-apoptotic machinery (23, 24). Total RNA was purified and qRT-PCR analysis was done using miR-706 primers. We observed that in NIH3T3 cells, miR-706 expression was elevated in response to ER stress (Fig.1A, left panel). To confirm this result, NIH3T3 cells were further treated with Tunicamycin which has different mechanism of ER stress induction than Thapsigargin. Compared to the control cells, Tunicamycin treated cells showed significant extent amount of miR-706 induction (Fig.1A, right panel). These results imply that miR-706 is an ER stress-responsive microRNA.

We next treated hepatic cell line AML12 with Thapsigargin for ER stress induction. In these cells, there was also remarkable elevation of miR-706 expression (Fig.1B). To check whether physiological stimulus induces this microRNA, NIH3T3 cells were cultured in media with low glucose concentration (0.5 mM). We observed induction of miR-706 in low glucose media (Fig.1C). These findings confirmed that ER stress induces expression of miR-706.

miR-706 is a PERK-dependent microRNA

Next, we investigated if miR-706 induction by ER-stress is PERK dependent. PERK wild-type and knock-down NIH3T3 cells were cultured and treated with Thapsigargin for 10 hours. Total RNA was purified from PERK wild-type and PERK knock-down cells. qRT-PCR using the specific primers showed that miR-

706 was up-regulated 5.7 fold in PERK wild-type cells; this induction was remarkably suppressed in PERK knocked-down cells (Fig.2A). Since the activation of PERK leads to ATF4 translation inhibition and *CHOP* transcription (1), activity of PERK knock-down in our study was confirmed by assessing grade of down-regulation of *ATF4* and *CHOP* transcriptions (Fig.2B). Knock-down of other branches of ER stress (IRE1 and ATF6) did not have significant effect on miR-706 induction (data not shown). These results demonstrate that miR-706 is governed in a PERK-dependent way in response to ER stress.

miR-706 is an ATF4-dependent microRNA

ATF4 regulates transcription of many pro-survival and in case of prolonged stress, pro-apoptotic proteins like CHOP (32). To investigate downstream regulation of miR-706 synthesis, we treated ATF4 wild-type and ATF4 knock-down NIH3T3 cells with Thapsigargin for 0 and 10 hours. miR-706 expression was induced in ATF4 wild-type cells. ATF4 knock-down cells did not show any induction of miR-706 expression (Fig.3). These findings illustrate the crucial role of ATF4 in the ER/ miR-706 axis.

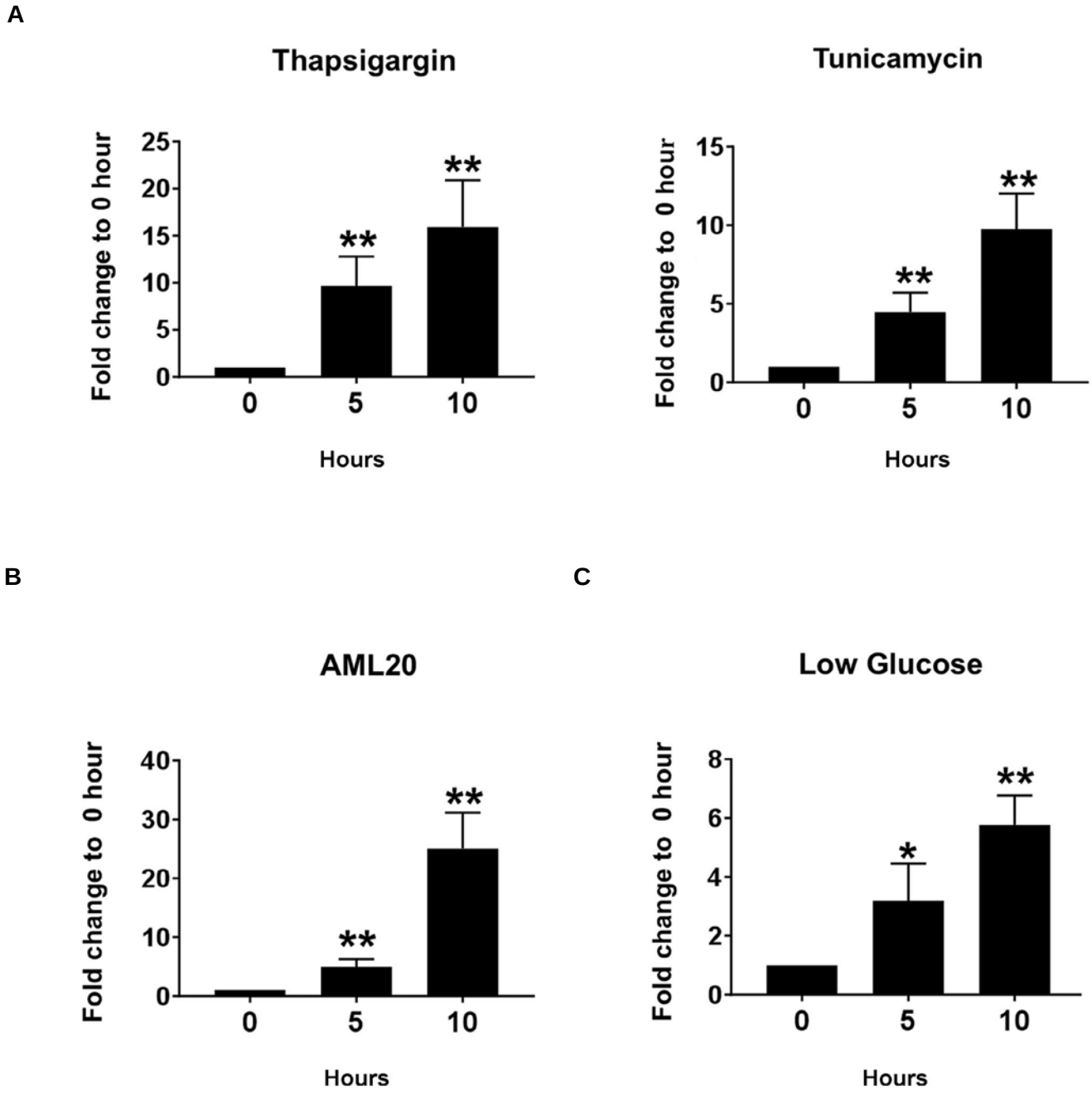

Fig.1: ER stress induces miR-706. **A.** NIH3T3 cells were treated with Thapsigargin or Tunicamycin at the indicated times. miR-706 expression was determnied by qRT-PCR. **B.** AML12 mouse hepatic cells were treated with Thapsigargin at the indicated times. miR-706 expression was determnied by qRT-PCR. **C.** NIH3T3 cells were put in low glucose media for the indicated times. miR-706 expression was determnied by qRT-PCR. *; P<0.05, **; P<0.01 compared to the control, and qRT-PCR; Quantitative reverse transcription polymerase chain reaction.

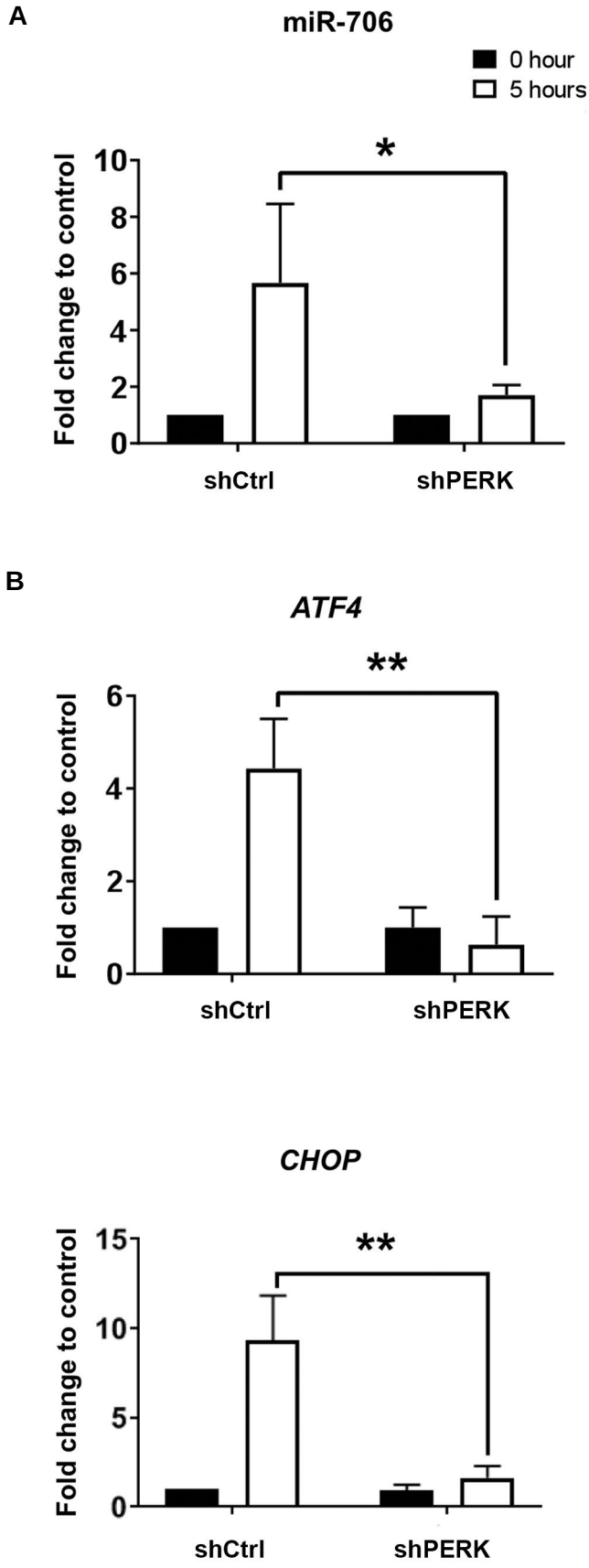

Fig.2: miR-706 induction in response to ER stress is dependent on PERK. NIH3T3 cells tranfected with shControl (shCtrl) or shPERK were treated with Thapsigargin for five hours. **A.** miR-706 expression level was analyzed by qRT-PCR. **B.** *ATF4* and *CHOP* expression were measured by qRT-PCR as a read-out for PERK and ATF4 activity. *; P<0.05, **; P<0.01, and qRT-PCR; Quantitative reverse transcription polymerase chain reaction.

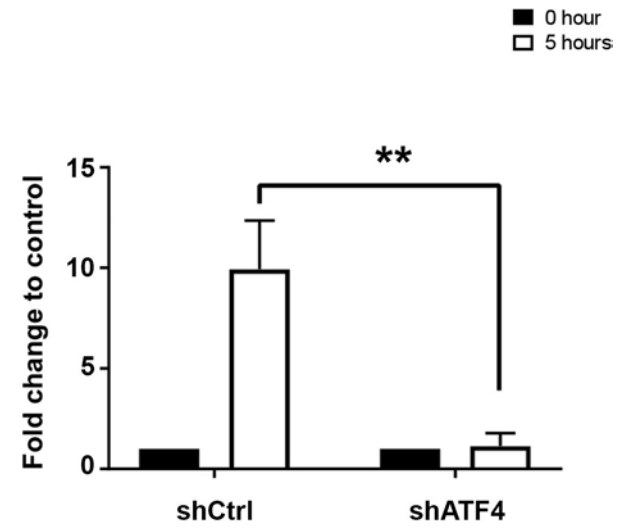

Fig.3: ATF is necessary for miR-706 induction in response to ER stress. ATF4 was knocked-down in NIH3T3 cells and treated with Thapsigargin for five hours. miR-706 expression were determnied by qRT-PCR . **; P<0.01 and qRT-PCR; Quantitative reverse transcription polymerase chain reaction.

miR-706 directly targets CAAP1

Using Targetscan analysis, microRNA target prediction showed that miR-706 is predicted to target anti-apoptotic caspase activity and apoptosis inhibitor 1 (CAAP1) (Fig.4A). Therefore, we used mimic miR-706 to overexpress miR-706 and then determine CAAP1 level. Figure 4B demonstrated that CAAP1 expression was attenuated in response to miR-706 overexpression. In addition, we checked the *CAAP1* level in antisense miR-706 transduced cells. Figure 4C indicated down-regulation of *CAAP1* expression by anti- miR-706 in Thapsigargin treated cells. These data supported our hypothesis that CAAP1 is a miR-706 target.

miR-706 promotes cell death following ER stress through CAAP1

Since miR-706 is induced by PERK and the latter molecule has dual pro-survival as well as pro-apoptotic functions (23), we studied whether miR-706 plays any role in cell fate. An oligo targeting miR-706 was designed and NIH3T3 cells were transduced. These cells were then treated with Thapsigargin for 24 hours. As a control, scrambled oligo was used. Total cell death in the scrambled and antisense miR-706 transduced cells was detected using Annexin V staining. We observed that compared to the scrambled transfected cells, cell death in the antisense miR-706 transduced cells was remarkably reduced, indicating that miR-706 is a pro-cell death microRNA. The cells in which miR-706 was inhibited and CAAP1 was knocked-down showed significant, even if partial, reversal of antisense miR-706 mediated protection (Fig.4D, E). These results indicated the fundamental role of CAAP1 in mediating miR-706 pro-apoptotic functions.

CAAP1 suppression contributes to tumor cell survival

Increasing evidence suggests that chronic ER stress is induced in numerous human cancers such as lung cancer, breast cancer, hepatocellular carcinoma, melanoma, lymphoma (33-35). We then chose human lung cancer and ovarian cancer cell lines to further examine the effect of CAAP1 on cell survival. Western blot and the quantification results showed obvious down-regulation of CAAP1 protein in both human ovarian cancer cell line SKOV3 and lung cancer cell line H1299, in contrast to their normal control cells (Fig.5A, B). We next examined the impact of CAAP1 on tumor progression. Analysis from the online database (http://kmplot.com/) indicates that human ovarian and lung cancer patients with higher CAAP1 expression show significantly prolonged overall survival (Fig.5C). These evidences further confirmed our findings that CAAP1 is a key factor in the cell death initiated by ER stress.

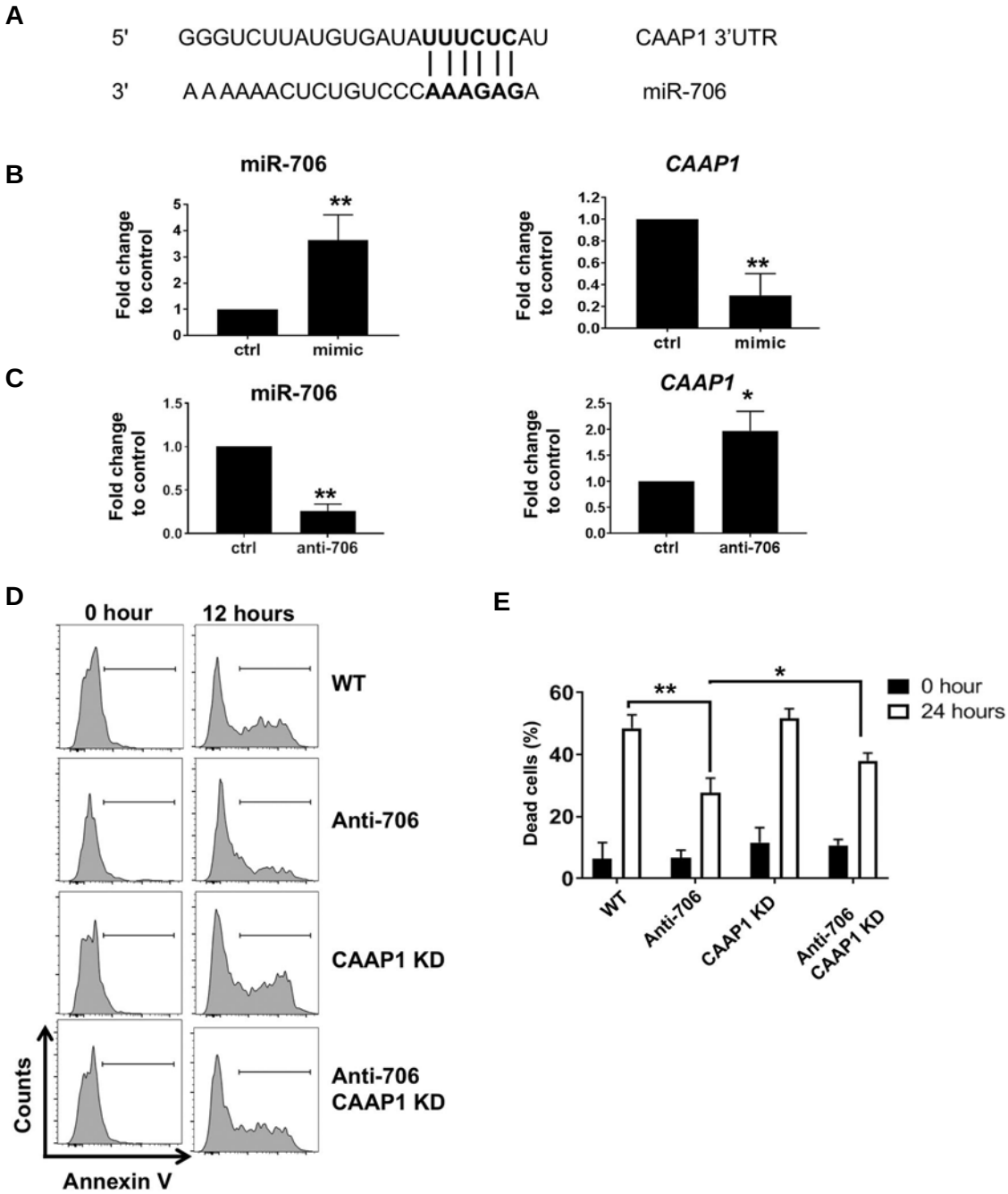

Fig.4: miR-706 tiggers ER stress dependent cell death trough CAAP1. **A.** Target scan prediction showing predicted binding of miR-706 and CAAP1 3´UTR. **B.** NIH3T3 cells were transfected with scrambled microRNA (control; ctrl) or mimic miR-706 (mimic). Total RNA was purified and *CAAP1* expression was determined using qRT-PCR. **C.** NIH3T3 cells were transduced with antisense miR-706 (anti-706) and then incubated with Thapsigargin for 24 hours. Total RNA was purified and *CAAP1* expression was determined using qRT-PCR. **D.** NIH3T3 cells were transduced with scrambled microRNA (ctrl), antisense miR-706 (anti-706) or antisense miR-706 and shCAAP1. The cells were then incubated with Thapsigargin for 24 hours. Cell death was assesed by Annexin V staining. **E.** Quantification of panel C. *; P<0.05, **; P<0.01 compared to control, and qRT-PCR; Quantitative reverse transcription polymerase chain reaction.

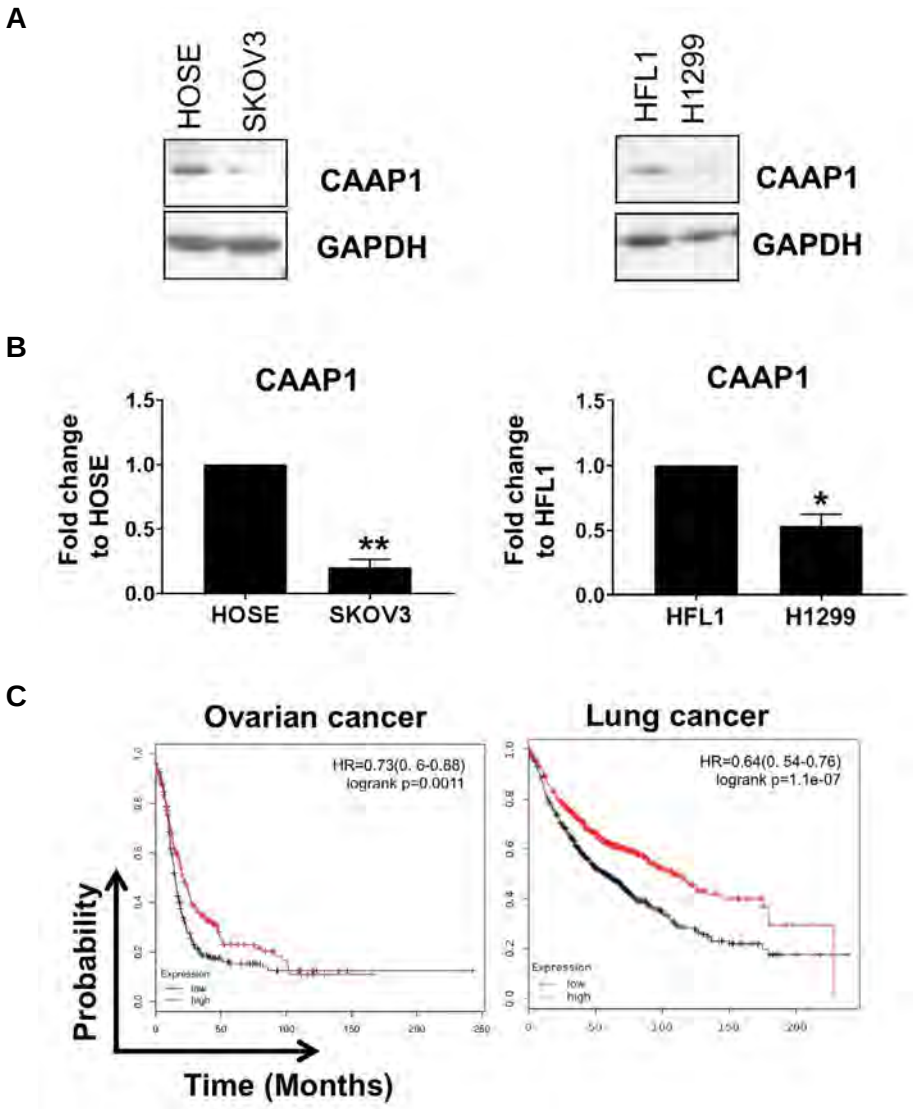

Fig.5: CAAP1 is critical for cell survival in tumor conditions that induce ER stress. **A.** CAAP1 protein levels are higher in the ovarian and lung cancer cell lines (SKOV3 and H1299) compared to their normal control cell lines (HOSE and HFL1). **B.** Quantification of panel A. *; P<0.05 or **; P<0.01 compared to HOSE or HFL1 cells respectively. **C.** High CAAP1 levels confer better survival in gastric, ovarian and lung cancer patients (analysis from the online database http://kmplot.com/). Log-rank P values and hazard ratios are shown at the up right corner.

Discussion

UPR or UPR has been shown to regulate several microRNAs. PERK up-regulates miR-30-c-2* which in turn represses Xbp-1. CHOP (36), as a downstream activator of PERK, induces miR-708, which in turn suppresses rhodopsin (25). PERK also induces miR-216b in a CHOP-dependent manner, while it suppresses c-Jun and thereby induces apoptosis (24) . Ire1 has been shown to degrade pre-microRNAs -125b and -96 with implications for cell death (26). In this work, for the first time, we identified a novel microRNA, miR-706, in response to ER stress and confirmed its critical role in governing cell fate.

ER stress signaling has dual purposes. In the initial stage, UPR signaling tries to preserve homeostasis by suppressing protein synthesis, launching antioxidant response and inducing pro-survival signals such as miR-211 (23). In the later stage, when it is clear that ER stress has caused damage beyond repair, UPR switches to pro-apoptotic signaling. Pro-apoptotic signals include CHOP. Interestingly, both pro-apoptotic and pro-survival signals can be initiated by the same transcription factors. ATF4, a transcription factor, initially induces pro-survival miR-211 and at later it induces pro-apoptotic CHOP. In the current study, we show one microRNA playing a role in ER stress signaling mediated cell death. miR-706 was induced rapidly following ER stress in a PERK and ATF4 dependent manner. Lack of this microRNA suppressed cell death and this phenomenon was reversed, at least in part, by knocking-down of CAAP1. CAAP1 has been demonstrated to be an anti-apoptotic protein (37). Our finding provides further molecular evidence for the ER-stress causing cell death.

miR-706 protects oxidative stress induced hepatic fibrogenesis through blocking PKCα/TAOK1 signaling (38). Lian et al. (39) reported that miR-706 inactivates caspase-3 and caspase-9 and thus inhibit apoptosis induced by vesicular stomatitis virus. However, its role in UPR has never been reported. Our work, for the first time, implies the necessity of PERK/ATF4/ miR-706/ CAAP1 axis in ER stress induced cell death.

Blast search with mmu-miR-706 showed that it is closely matched with Homo sapiens uncharacterized LOC105372576. In future, role of this microRNA in human physiology in the context of ER stress could be investigated.

Conclusion

Our results identified the fundamental role for miR-706 in regulating cell death induced by ER stress and suggested that miR-706 might be a novel therapeutic target for human cancers. We also provided evidence that CAAP1 is the direct target of miR-706 in response to PERK/AFT4 pathway mediated ER stress.

Acknowledgements

This study did not receive support from any grant. We thank all the colleagues for their kind help on the work. There is no conflict of interest in this study.

Authors' Contributions

X.W.; Designed the work. G.H., Y.H., J.G.; Conducted experiments and analyzed data. H.C., X.W.; Interpreted the data and wrote the manuscript. All authors read and approved the final manuscript.

References

1. Cubillos-Ruiz JR, Bettigole SE, Glimcher LH. Tumorigenic and immunosuppressive effects of endoplasmic reticulum stress in cancer. Cell. 2017; 168(4): 692-706.
2. Madden E, Logue SE, Healy SJ, Manie S, Samali A. The role of the unfolded protein response in cancer progression: from oncogenesis to chemoresistance. Biol Cell. 2019; 111(1): 1-17.
3. Hetz C. The unfolded protein response: controlling cell fate decisions under ER stress and beyond. Nat Rev Mol Cell Biol. 2012; 13(2): 89-102.
4. Dauer P, Sharma NS, Gupta VK, Durden B, Hadad R, Banerjee S, et al. ER stress sensor, glucose regulatory protein 78 (GRP78) regulates redox status in pancreatic cancer thereby maintaining "stemness". Cell Death Dis. 2019; 10(2): 132.
5. Ventura R, Mordec K, Waszczuk J, Wang Z, Lai J, Fridlib M, et al. Inhibition of de novo palmitate synthesis by fatty acid synthase induces apoptosis in tumor cells by remodeling cell membranes, inhibiting signaling pathways, and reprogramming gene expression. EBioMedicine. 2015; 2(8): 808-824.
6. Niu Z, Wang M, Zhou L, Yao L, Liao Q, Zhao Y. Elevated GRP78 expression is associated with poor prognosis in patients with pancreatic cancer. Sci Rep. 2015; 5: 16067.
7. Bertolotti A, Zhang Y, Hendershot LM, Harding HP, Ron D. Dynamic interaction of BiP and ER stress transducers in the unfolded-protein response. Nat Cell Biol. 2000; 2(6): 326-332.
8. Shen JS, Chen X, Hendershot L, Prywes R. ER stress regulation of ATF6 localization by dissociation of BiP/GRP78 binding and unmasking of golgi localization signals. Dev Cell. 2002; 3(1): 99-111.
9. Cakir I, Nillni EA. Endoplasmic Reticulum Stress, the Hypothalamus, and Energy Balance. Trends Endocrinol Metab. 2019; 30(3): 163-176.
10. Kitamura M. The unfolded protein response triggered by environmental factors. Semin Immunopathol. 2013; 35(3): 259-275.
11. Tirasophon W, Welihinda AA, Kaufman RJ. A stress response pathway from the endoplasmic reticulum to the nucleus requires a novel bifunctional protein kinase/endoribonuclease (Ire1p) in mammalian cells. Gene Dev. 1998; 12(12): 1812-1824.
12. Bettigole SE, Glimcher LH. Endoplasmic reticulum stress in immunity. Annu Rev Immunol. 2015; 33: 107-138.
13. Liu CY, Schröder M, Kaufman RJ. Ligand-independent dimerization activates the stress response kinases IRE1 and PERK in the lumen of the endoplasmic reticulum. J Biol Chem. 2000; 275(32): 24881-24885.
14. Harding HP, Zhang YH, Ron D. Protein translation and folding are coupled by an endoplasmic-reticulum-resident kinase. Nature. 1999; 397(6716): 271-274.
15. Lu PD, Harding HP, Ron D. Translation reinitiation at alternative open reading frames regulates gene expression in an integrated stress response. J Cell Biol. 2004; 167(1): 27-33.
16. Vattem KM, Wek RC. Reinitiation involving upstream ORFs regulates ATF4 mRNA translation in mammalian cells. Proc Natl Acad Sci USA. 2004; 101(31): 11269-11274.
17. Blais JD, Filipenko V, Bi M, Harding HP, Ron D, Koumenis C, et al. Activating transcription factor 4 is translationally regulated by hypoxic stress. Mol Cell Biol. 2004; 24(17): 7469-7482.
18. Bi M, Naczki C, Koritzinsky M, Fels D, Blais J, Hu N, et al. ER stress-regulated translation increases tolerance to extreme hypoxia and promotes tumor growth. Embo J. 2005; 24(19): 3470-3481.
19. Bobrovnikova-Marjon E, Grigoriadou C, Pytel D, Zhang F, Ye J, Koumenis C, et al. PERK promotes cancer cell proliferation and tumor growth by limiting oxidative DNA damage. Oncogene. 2010; 29(27): 3881-3895.
20. Zinszner H, Kuroda M, Wang X, Batchvarova N, Lightfoot RT, Remotti H, et al. CHOP is implicated in programmed cell death in response to impaired function of the endoplasmic reticulum. Gene Dev. 1998; 12(7): 982-995.
21. Bartel DP. MicroRNAs: genomics, biogenesis, mechanism, and function. Cell. 2004; 116(2): 281-297.
22. Upton JP, Wang L, Han D, Wang ES, Huskey NE, Lim L, et al. IRE1 alpha cleaves select microRNAs during ER stress to derepress translation of proapoptotic caspase-2. Science. 2012; 338(6108): 818-822.
23. Chitnis NS, Pytel D, Bobrovnikova-Marjon E, Pant D, Zheng H, Maas NL, et al. miR-211 is a prosurvival microRNA that regulates chop expression in a PERK-dependent manner. Mol Cell. 2012; 48(3): 353-364.
24. Xu Z, Bu Y, Chitnis N, Koumenis C, Fuchs SY, Diehl JA. miR-216b regulation of c-Jun mediates GADD153/CHOP-dependent apoptosis. Nat Commun. 2016; 7: 11422.
25. Behrman S, Acosta-Alvear D, Walter P. A CHOP-regulated microRNA controls rhodopsin expression. J Cell Biol. 2011; 192(6): 919-927.
26. Maurel M, Chevet E. Endoplasmic reticulum stress signaling: the microRNA connection. Am J Physiol Cell Physiol. 2013; 304(12): C1117-C1126.
27. Crompton BD, Carlton AL, Thorner AR, Christie AL, Du J, Calicchio ML, et al. High-throughput tyrosine kinase activity profiling identifies FAK as a candidate therapeutic target in Ewing sarcoma. Cancer Res. 2013; 73(9): 2873-2883.
28. Zhang J, Ren H, Yuan P, Lang W, Zhang L, Mao L. Down-regulation of hepatoma-derived growth factor inhibits anchorage-independent growth and invasion of non-small cell lung cancer cells. Cancer Res. 2006; 66(1): 18-23.
29. Li Y, Chitnis N, Nakagawa H, Kita Y, Natsugoe S, Yang Y, et al. PRMT5 is required for lymphomagenesis triggered by multiple oncogenic drivers. Cancer Discov. 2015; 5(3): 288-303.
30. Vermes I, Haanen C, Steffens-Nakken H, Reutelingsperger C. A novel assay for apoptosis. Flow cytometric detection of phosphatidylserine expression on early apoptotic cells using fluorescein labelled Annexin V. J Immunol Methods. 1995; 184(1): 39-51.
31. Koopman G, Reutelingsperger CP, Kuijten GA, Keehnen RM, Pals ST, van Oers MH. Annexin V for flow cytometric detection of phosphatidylserine expression on B cells undergoingapoptosis. Blood. 1994; 84(5): 1415-1420.
32. Han J, Backa SH, Hur J, Lin YH, Gildersleeve R, Shan J, et al. ER-stress-induced transcriptional regulation increases protein synthesis leading to cell death. Nat Cell Biol. 2013; 15(5): 481-490.
33. Bu Y, Yoshida A, Chitnis N, Altman BJ, Tameire F, Oran A, et al. A PERK-miR-211 axis suppresses circadian regulators and protein synthesis to promote cancer cell survival. Nat Cell Biol. 2018; 20(1): 104-115.
34. Wang M, Kaufman RJ. The impact of the endoplasmic reticulum protein-folding environment on cancer development. Nat Rev Cancer. 2014; 14(9): 581-597.
35. Hart LS, Cunningham JT, Datta T, Dey S, Tameire F, Lehman SL, et al. ER stress-mediated autophagy promotes Myc-dependent transformation and tumor growth. J Clin Invest. 2012; 122(12): 4621-4634.
36. Wu YL, Hsu NY, Cheau-Feng Lin F, Lee H, Cheng YW. MiR-30c-2*negative regulated MTA-1 expression involved in metastasis and drug resistance of HPV-infected non-small cell lung cancer. Surgery. 2016; 160(6): 1591-1598.
37. Zhang Y, Johansson E, Miller ML, Jänicke RU, Ferguson DJ, Plas D, et al. Identification of a Conserved anti-apoptotic protein that modulates the mitochondrial apoptosis pathway. PLoS One. 2011; 6(9): e25284.
38. Yin R, Guo D, Zhang S, Zhang X. miR-706 inhibits the oxidative stress-induced activation of PKC alpha/TAOK1 in liver fibrogenesis. Sci Rep. 2016; 6: 37509.
39. Lian H, Liu W, Liu Q, Jin H, Sun Y, Li J, et al. A laboratory-attenuated vesicular stomatitis virus induces apoptosis and alters the cellular microRNA expression profile in BHK cells. Arch Virol. 2010; 155(10): 1643-1653.